Intensification and Optimization of Bio-glycerol conversion into Valuable Chemicals using Electromagnetic Radiation promoted Reactor

Thesis Submitted by

Poulami Karan

Doctor of Philosophy (Engineering)

Chemical Engineering Department
Faculty Council of Engineering & Technology
Jadavpur University
Kolkata, India

2023

Dedicated to

My Family

JADAVPUR UNIVERSITY
KOLKATA 700032, INDIA

INDEX No: 23/16/E

1. Title of the Thesis: Intensification and Optimization of Bio-glycerol conversion into Valuable Chemicals using Electromagnetic Radiation promoted Reactor

2. Name, Designation & Institution of the Supervisor:

Prof. (Dr.) Rajat Chakraborty

Professor

Chemical Engineering Department

Jadavpur University

3. List of Publications:

1. **P. Karan**, P. Mukhopadhyay, R. Chakraborty, *Intensification of monostearin (phase change material) synthesis in infrared radiated rotating reactor: Optimization and heterogeneous kinetics*, Energy Conversion and Management (Elsevier) 138 (**2017**) 577-586. (**Impact factor: 10.4**)
2. **P. Karan**, P. Mukhopadhyay, R. Chakraborty, *Quartz halogen-ultrasonication integrated rotating reactor for efficient photocatalytic-thermocatalytic synthesis of glyceryl monocaprin: Kinetics of heterogeneous esterification*, Asia-Pacific Journal of Chemical Engineering (Wiley Online Library)15(1) (**2020**) e2379. (**Impact factor: 1.8**)
3. **P. Karan**, R. Chakraborty, *E-waste derived silica-alumina for eco-friendly and inexpensive Mg-Al-Ti photocatalyst towards glycerol carbonate (electrolyte) synthesis: Process optimization and LCA*, Waste Management (Elsevier) 140 (**2022**) 213-224. (**Impact factor: 8.1**)
4. **P. Karan**, R. Chakraborty, *Intensification of Autocatalytic Methyl Oleate Synthesis in Continuous Flow Rotating Recycle Reactor under Hybrid Radiation: Process Optimization and Scale-up*, Chemical Engineering Journal (Elsevier) (**2022**) 140032.

(**Impact factor: 15.1**)

5. **P. Karan,** V.P. Vu, R. Chakraborty, and S.H. Lee. "Barnacle carapace-chitosan supported highly-efficient nano Al-W alloy electrocatalyst for sustainable bio-glycerol valorization: Environmental impact and cost analyses." Chemical Engineering Journal Advances 16 (**2023**): 100560. (**Cite score: 4.6**)

4. List of Patents: None

5. List of Presentations in National/International Conferences:

1. **P. Karan,** R. Chakraborty; 2016; "Utilization of Waste Biomass derived Bioglycerol fo r Synthesis of Industrially Important Products, International Conference on Solid Waste Management", (6th IconSWM 2016), Kolkata, November 24-26.

2. **P. Karan,** P. Mukhopadhyay, R. Chakraborty, 2016, "Recent trends in Synthesis of Fat ty Acid Esters applied as Phase Change Energy Storage Materials", National Conferenc e on Renewable Energy (NCRE 2016), Kolkata, July 27-28

3. **P. Karan,** R. Chakraborty, 2017, "Enhanced Production of Glycerol Monocaprate usin g waste resources in Semi-batch reactor", National Conference on Sustainable Advance d Technologies for Environmental Management, IIEST, Shibpur, June 28-30

4. **P. Karan,** P. Pradhan, R. Chakraborty, 2020; "Optimization of Biodiesel Production fr om Used Rice Bran Oil Employing Waste Derived-hydroxyapatite Supported Vanadiu m Catalyst", International Conference on Water, Energy, and Environmental Sustainabi lity (WEES2020), Durgapur, January 13-15**.**

"STATEMENT OF ORIGINALITY"

I, **Poulami Karan** registered on **28/09/2016 (Ref No D-7/E/552/16)** do hereby declare that this thesis entitled "**Intensification and Optimization of Bio-glycerol Conversion into Valuable Chemicals using Electromagnetic Radiation Promoted Reactor**" contains literature survey and original research work done by the undersigned candidate as part of Doctoral studies.

All information in this thesis have been obtained and presented in accordance with existing academic rules and ethical conduct. I declare that, as required by these rules and conduct, I have fully cited and referred all materials and results that are not original to this work.

I also declare that I have checked this thesis as per the "Policy on Anti Plagiarism, Jadavpur University, 2019", and the level of similarity as checked by iThenticate software is **7%**.

Poulami Karan

Signature of Candidate:

Date: 26.09.2023

Certified by Supervisor

Rajat Chakraborty 26.09.2023

(Signature with date, and seal)

Prof. Rajat Chakraborty
Chemical Engineering Department
Jadavpur University
Kolkata-700032

CERTIFICATE FROM THE SUPERVISOR

This is to certify that the thesis entitled ***"Intensification and Optimization of Bio-glycerol Conversion into Valuable Chemicals using Electromagnetic Radiation Promoted Reactor"*** *submitted by Smt.* ***Poulami Karan****, who got her name registered on* ***28/09/2016 (Ref No****: D-7/E/552/16) for the award of Ph.D. (Engineering) degree of Jadavpur University is absolutely based upon her own work under the supervision of* ***Prof. (Dr.) Rajat Chakraborty****, Chemical Engineering Department, Jadavpur University, and that neither her thesis nor any part of the thesis has been submitted for any degree/diploma or any other academic award anywhere before.*

Rajat Chakraborty 26.09.2023

Signature of the Supervisor and date with Office Seal

Prof. Rajat Chakraborty
Chemical Engineering Department
Jadavpur University
Kolkata-700032

ACKNOWLEDGEMENT

This Ph.D. dissertation is completed under the guidance, support, care, and the help from a lot of important ones in my life. I would like to extend my deepest sense of gratitude to all of them. Foremost, I would like to praise and thank GOD, the almighty, for His showers of blessings throughout my research work to complete the research successfully.

First of all, I would like to express my profound gratitude towards my supervisor Prof. Rajat Chakraborty (Head of the Department, Department of Chemical Engineering, Jadavpur University), for his invaluable guidance throughout my research work and kind care of my personal life. He was a constant source of inspiration to seek out the solution to many challenging problems and to work hard for the success of the project. I personally feel that his suggestions, which reshaped my career and outlook in life, cannot be restricted by the limits of some literary words, and his untiring cooperation during my Ph.D. submission.

I would like to thank my senior colleagues and laboratory alumni, Dr. Piasy Pradhan, Dr. Punam Mukhopadhyay. I am also thankful to my fellow lab mates Mr. Sourav Barman, Miss Sohini Roy Choudhury, and Miss. Ritika Samanta for their constant encouragement and support, for the stimulating discussions, and for all the fun we have had during my Ph.D. life. Also, I would like to express my deep and sincere gratitude to Prof. Changwoon Nah, Prof. Soo-Hyoung Lee, and his lab group Dinh Cung Tien Nguyen, Van-Phu Vu in School of Semiconductor and Chemical Engineering, Jeonbuk National University, Republic of Korea for giving me the opportunity to do research and providing immense support during my Ph.D. I am obliged to all my friends with whom I am associated during my Ph.D. and from whom I have enriched my knowledge, vision, and perception and a*ll their names couldn't be enlisted in such a short space. My special recognition goes out to*

the excellent non-teaching staff of the Chemical Engineering Department, Jadavpur University who were extremely helpful and made every official process easier to navigate.

I would like to express my heartfelt gratitude to my parents (Dr. Pabitra Kumar Karan, and Mrs. Paramita Karan) and brother (Dr. Prithwish Karan) for believing in me and being my pillar of strength and always teaching me how to never lose hope and keep going. Words fall short at this moment to express my gratitude to my parents. I am also thankful to my parents-in-law for their unhesitating support, love, and faith that encouraged me to achieve my goal. It is my privilege to owe my deepest sense of gratitude to my husband Dr. Sarbaranjan Paria, as his constant motivation has always helped me to achieve academic excellence and complete this milestone in my career, without whom I would not conquer all the challenges I met.

Finally, I acknowledged the Department of Chemical Engineering, Jadavpur University for providing the essential facilities required for my Ph.D. completion. I am also thankful to University Grant Commission Major Research Project (UGC-MRP) and Council of Scientific and Industrial Research (CSIR) for providing the fellowship [(F.No. 43-161/2014 (SR)] and [09/096(0975)/2019-EMR-I] in this period.

Kolkata

2023 *Poulami Karan*

Preface

The present thesis, entitled “Intensification and Optimization of Bio-glycerol Conversion into Valuable Chemicals using Electromagnetic Radiation Promoted Reactor” deals with the dedication toward green chemistry and to phasing out inefficient fossil fuel, causing the most serious threat to mankind due to greenhouse gas emissions. The main approach of the global community is to enhance the value of the burgeoning amounts of glycerol obtained from the biodiesel industry. Due to its unique structure, and renewability feature, glycerol has been pondered as a platform chemical for the advanced production of energy storage materials, food additives, biofuel additives, and clean H_2, through various pathways like esterification, transesterification, and oxidation via catalytic processes. In this regard, many researchers have made efforts to valorize glycerol using various pathways. Previous literature revealed the application of homogeneous catalysts for glycerol conversion employing thermally heated reactor systems. However, because of the corrosive nature and appearance of side reactions, homogeneous catalysis becomes economically unfavorable. To overcome this problem, a special priority has arisen on the use of commercially available heterogeneous solid catalysts but also in developing bulk non-precious photo/electro metal-based solid acid/base catalysts. To understand the effect of support over the bulk catalysts, biowaste, and e-waste are used to prepare sustainable support material that enhances the catalytic activity. Furthermore, to get the desired yield/selectivity of the product in a shorter reaction time and moderate reaction temperature, electromagnetic radiation has been applied to replace conventional heating systems. To this aim, the application of electromagnetic radiation in the esterification and transesterification reaction has augmented the reaction with a faster reaction rate and less activation energy, implying negligible mass and heat transfer resistance. Considering the effect of process parameters influencing the reaction condition, a statistical optimization tool has been

assessed. It reveals that the interactive effects among the process factors exist in governing the process response. However, heterogeneous surface reaction kinetic models have been measured through non-linear fitting of experimental data. In addition, various reactor configurations have been ascribed to intensify the rate of reaction. To fulfill the purpose of circular economy, techno-economic assessment has been considered to evaluate the ecological and economic footprint accompanying the upgradation of glycerol.

CONTENTS

LIST OF FIGURES

LIST OF TABLES

LIST OF ABBREVIATION

Glycerol	GL	Amberlyst 15	A15
Glycerol monostearin	MSN	Nano titania	NT-P25
Glyceryl monocaprin	GMC	Amberlyst 15-Nanotitania	ATO
Glycerol oxidation reaction	GOR	Conventionally energized mechanically stirred reactor	CEMR
Hydrogen evolution reaction	HER	Gas chromatography-mass spectroscopy	GC-MS
Capric acid	CA	Waste-printed circuit board	WPCB
Oleic acid	OA	WPCB derived silica	SA_{WPCB}
Potato dextrose broth	PDB	Solar-simulated quartz halogen lamp radiated batch reactor	SSQHLBR
Stearic acid	SA	Box-Behnken design	BBD
Taguchi experimental design	TED	Thermally heated batch reactor	THBR
Dimethyl carbonate	DMC	Modified rotating packed bed reactor	MPBR
Fatty acid methyl ester	FAME	Recycle ratio	RR
Conventional heating	CH	Methyl oleate	MO
Infrared radiation	IR	Liquid hourly space velocity	LHSV
Ultrasound energized rotating reactor	USERR	Chitin/Chitosan	CS/CH
Quartz halogen-energized rotating reactor	QHERR	Multiwalled carbon nanotube	MWNT
Far infrared radiated reactor	FIRR	Functionalized multiwalled carbon nanotube	FMWNT
Stirred batch reactor	SBR	Linear sweep voltammetry	LSV
Rotating batch reactor	RBR	Cyclic voltammetry	CV
Langmuir Hinshelwood	LH	Electrochemically active surface area	ECSA
Eley Rideal	ER	Electrochemical impedance spectroscopy	EIS
Pseudo homogeneous	PH	Nuclear magnetic resonance	NMR
Quartz halogen radiation	QHR	Waste pork lard-derived glycerol	WPLG
Ultrasonication	US	Life cycle impact assessment	LCIA
Microwave	MW	Hydrogen	H_2
Near-infrared radiation	NIR	Solar simulated radiation	SSR
Quartz halogen radiator -US-energized rotating reactor	QHRUERR	Terrestrial Ecosystem	TETPinf
Global warming potential	GWP 100	Particulate matter formation	PMFP
Glyceryl monooleate	GMO	Water depletion	WDP
Human toxicity	HTPinf	Life cycle costing	LCC
Agricultural land occupation	ALOP	Life cycle assessment	LCA

CHAPTER 1

Introduction

Concern about clean energy and clean air are the exigencies for the growing global population and socioeconomic prosperity. The major priority for finding sustainable and renewable energy resources will lead to a decline in the use of non-renewable energy resources. In this context, renewable green energy sources like biofuels have manifested the potential to replenish permanent solutions to current worldwide energy challenges [1]. Although renewable resources can meet global energy demands, the substitutions for petro-diesel fuel demand a carbon atom derived from biomass. With India's primary energy demand set to double by 2040, the use of biodegradable and nontoxic biodiesel is one of the potential carbon-neutral liquid biofuels that are braced to compete with and replace petroleum-based diesel fuel to a large extent and is considered to be a practical solution for producing renewable fuels. This fuel helps to reduce the environmental impact as the end product is 95 percent carbon-free on average. Moreover, in the combustion of biodiesel lower amount of sulfur content, fewer hydrocarbons (HC) and carbon monoxide (CO) are emitted [2]. As per the statistical report, the top global biodiesel-producing countries in 2021 are mentioned in Figure 1.1 [3]. The surplus amount of low-value glycerol (GL) production i.e., 10 wt.% as by-product during biodiesel formation blemishes the biodiesel industry. In 2020 due to the COVID-19 pandemic, biodiesel market experienced a downturn. However, in the next 3 years, biodiesel production is forecasted to turn out at 40 million tons per year with the formation of about 6.3 million tons of impure GL by 2025 [4]. Therefore, it is imperative to find a solution. Nevertheless, among the bio-based platform chemicals, GL represents an exceptional example that has significant potential regarding conversion to valuable fine chemicals either in traditional thermochemical methods or photo or electrochemical routes. Figure 1.2 shows the global crude GL industry report. Asia-Pacific contributed 54.1% market share in 2021 and is estimated to grow at a compound annual growth rate (CAGR) of 1.9% during

the year 2031 [5].

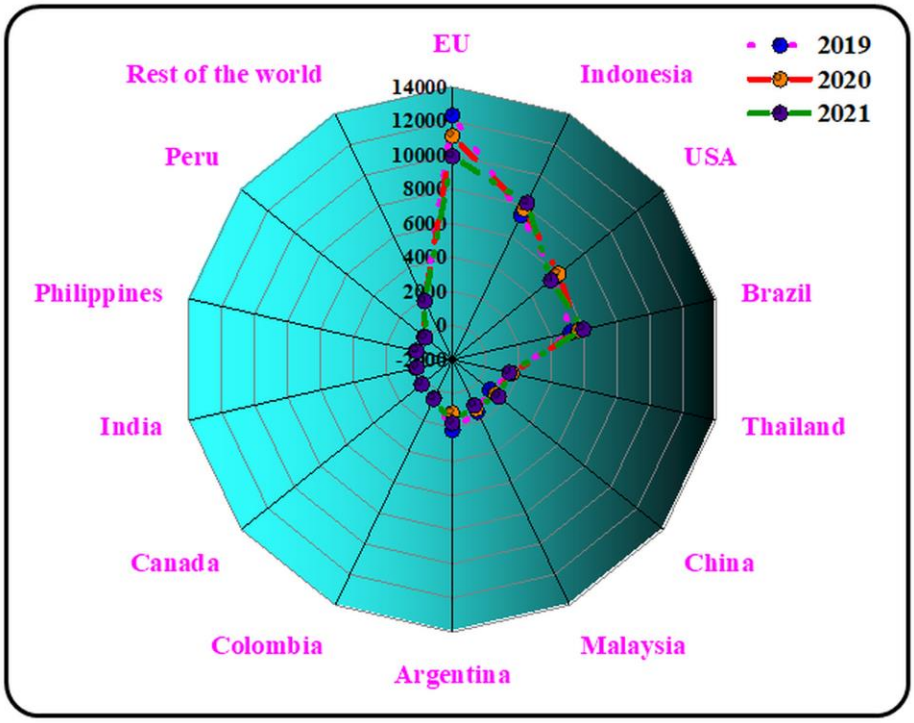

Figure 1.1. Worldwide FAME biodiesel production (in 1000 metric tons) countries in the year 2019 to 2021

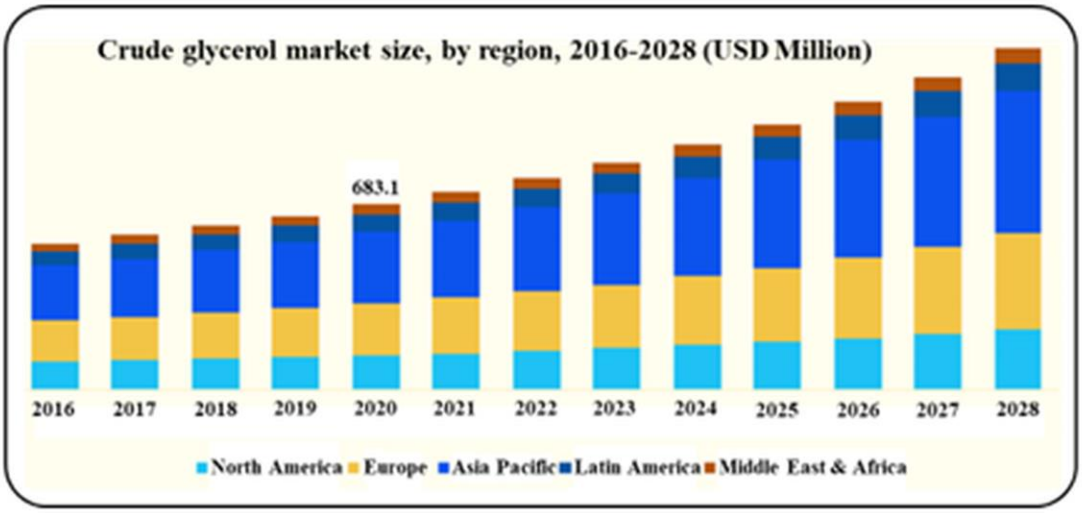

Figure 1.2. Global crude GL market report, 2021-2028 [6]

The high performance of top GL-producing Asian countries leads to a competitive environment concerning production technologies with certain production capacities.

Moreover, Europe is the key producer of biodiesel and GL in the world. GL is propane-1,2,3-triol, confining three hydroxy (OH) groups: two identical primary OH and one secondary OH [7]. Finding specific applications in fuel additives, thermal energy storage, and energy conversion [8]; several scenarios have been evolved to convert GL into fine chemicals. To valorize GL, a diverse selection of processes like esterification [9], transesterification/carbonylation [10], GL oxidation [11], and reduction [12] have been studied in making the shift from a lab-scale research attempt to commercialization. The electrochemical glycerol oxidation reaction (GOR) is another encouraging method adapted by GL in the anode paired with simultaneous production of H_2 at the cathode.

In the formation of valuable products through esterification, and transesterification, various process parameters are required. Thermal heating reveals non-uniformity in temperature distribution from the bulk surface to the reaction mixture making the process inappropriate with lengthy reaction time, thus making the process more energy intensive. During thermal catalysis, an excess number of chemical oxidants, solvents, high temperature, specialized infrastructure, and a large number of undesired by-products, reduces the yield, thus limiting the traditional thermal catalysis. For this reason, nowadays non-conventional heating systems are used to intensify the production process. On the contrary, to identify the ecological and economic bottlenecks in the scale-up study of the process, theoretical simulations, and life cycle assessment (LCA) have been assessed as more sensible implements to estimate the industrial plausibility of a given technology and to compare emerging with existing technologies.

The present thesis focuses on the preparation of industrially important GL value-added products like MSN, GMC, and GC through esterification and transesterification,

respectively. Glyceric acid and hydrogen have also been obtained through GOR and hydrogen evolution reaction. In this regard, various photo and electrocatalysts have been employed. Apart from the photo and electrocatalyst, another important factor is the green catalyst synthesis with the use of sustainable support material derived from waste printed circuit board, and sea wastes (crustacean shell). This approach has not only reduced the operating costs but also mitigates the environmental burden to a larger extent. To overcome the energy-intensive reactions e.g., long reaction time, and high reaction temperature requirement, a successful application of non-conventional energy sources (electromagnetic irradiation, and ultrasonication) has been accomplished. Likewise, to exaggerate the product yield/ selectivity, various types of reactor systems (stirred batch reactor, rotating batch reactor, ultrasound-assisted batch reactor, continuous flow rotating reactor under recycle mode, electrocatalytic batch reactor) have been assessed. To intensify the overall reaction rate of the process, heterogeneous kinetic model has been implemented. Notably, theoretical simulations (COMSOL, ASPEN plus) have been conducted for a greater understanding of the underlying procedure and scale-up of the study. To determine the ecological and economic aspects, LCA coupled with life cycle costing has been implicated in GL valorization.

1.1 Various GL Resources

GL is available in two forms viz. crude form and refined form. Synthetic GL was developed from propylene in several ways, even if typically, uneconomical. Concerning source, the GL market is categorized into hydrolysis reaction, saponification, and transesterification during biodiesel production, etc. The purity of crude GL usually ranges from 40-85%, depending on the feedstock that was used to generate biodiesel [13]. Currently, waste resources are employed as feedstocks like

animal fat, and waste cooking in place of edible and non-edible oils [14]. Owing to increased awareness about personal cleanliness on account of COVID-19 pandemic, the demand for GL has increased. However, the problem behind the production of GL from waste-based feedstocks contains high impurity that has been perceived as a serious threat to the biodiesel manufacturing unit accompanying the disposal cost, and purification cost. The purification steps are shown in Figure 1.3. These techniques are not environmentally feasible due to the abandoned release of volatile organic compounds (VOC) and other harmful gaseous emissions (CO, CO_2, SO_X, NO_X, CH_4), wastewater release, hazardous waste release, etc., leading to high risks to human life and environment. Hence, to overcome this barrier, embellishing a sustainable strategy would be fruitful for GL valorization. Moreover, effectuating circular economy models in fuel industry often comprises the use of waste streams, where waste valorization plays a pivotal role. From LCA perspective ("end-of-life"), the reduction in impacts categories like global warming, ozone depletion, ionizing radiation, terrestrial acidification, fossil fuel depletion, and human ecotoxicity are attributed to reduced environmental damage.

1.2 Routes for GL Valorization

Recently, GL is considered as one of the pertinent compounds due to its unique structure, non-toxicity, renewability feature, and chemical and physical properties. In the valorization of GL, various chemical processes such as esterification, carbonylation/transesterification, partial oxidation, reduction, reforming, and etherification have been proposed as mentioned in Figure 1.4. This is worth mentioning that GL has been valorized industrially viz. the Epicerol® technology developed by Solvay [15].

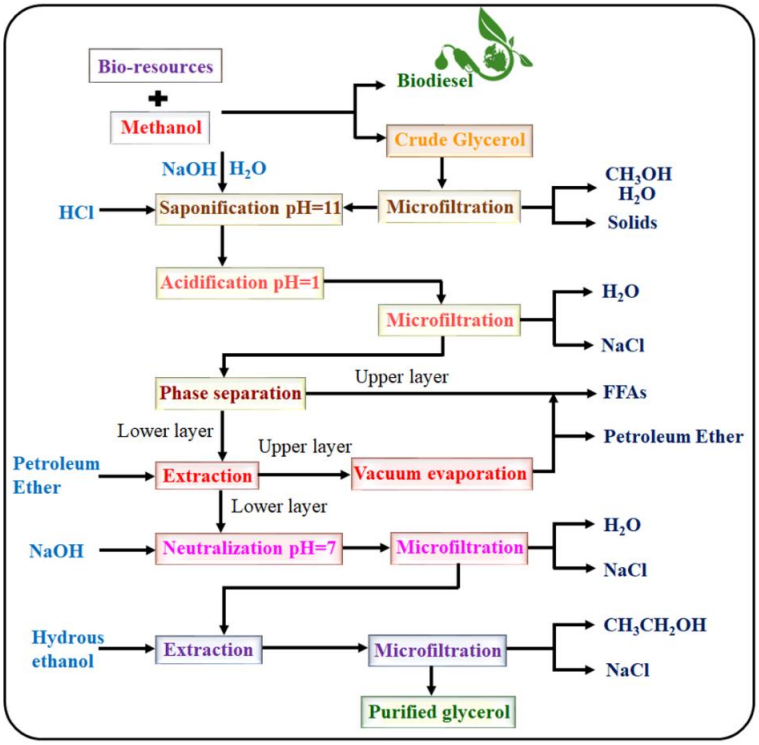

Figure 1.3. Crude GL purification

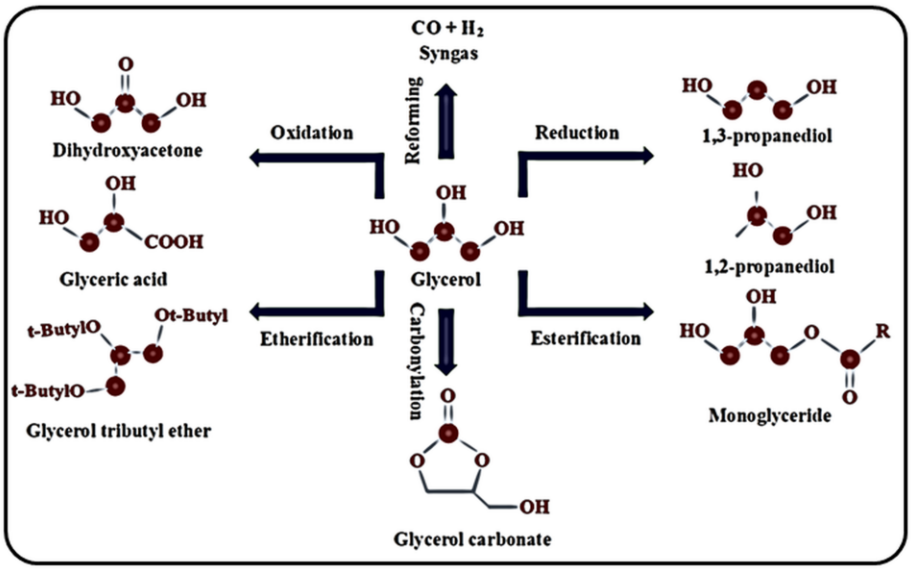

Figure 1.4. High-valued chemicals obtained from GL valorization

1.2.1 Esterification of GL

In the past years, fatty acid esters have been getting remarkable industrial interest. Conventionally, fatty acid esters are used as food additives, spin finish, and textiles;

paint, and ink additives [16]. In addition, GL esters have attracted attention in energy storage applications, and biofuel additives. Esterification is defined as a reaction concerning alcohol with carboxylic acid in the presence of an acid catalyst. Over the last few decades, many researchers have dedicated their research efforts to transforming lower-value GL into valuable chemicals using saturated and unsaturated fatty acids using the esterification technique as depicted in Table 1.1.

Table 1.1 Esters obtained using different fatty acids.

Fatty acid	Feedstock	Catalyst	Reaction condition	Acid conversion/ yield	Reactor type	Product	Ref.
Capric acid	GL	*Candida antarctica*	60°C, 6 h	96.9%	Batch reactor	Glycerol caprate	[17]
Caprylic acid	GL	*Rhizomucor Miehie, Candida Antarctica*	50°C, 7 h	94.8%	Ultrasonic batch reactor	Tricaprylin	[18]
Lauric acid	GL	HSO3SBA-15	160°C, 7 h	95%	stirred batch reactor	Glycerol monolaurate	[19]
Palmitic acid	GL	Candida antarctica lipase B	50°C, 24 h	81%	Batch reactor	Monoglyceride	[20]
caprylic acid	GL	Ionic liquid (tetramethyl ammonium dihydrogen phosphate)	5 min, 150 °C, 5 wt.% catalyst dosage, GL/ caprylic acid =6:1	87.7% caprylic acid conversion, 78.4% yield	Batch reactor	Glycerol monocaprylate	[21]
Stearic acid	GL	Novozyme 435	75°C, 5 h	67.56%	Batch reactor	Distearate	[22]
Acetic acid	GL	Amberlyst 36	80 °C, acetic acid/GL= 3:1, 41 bar pressure, flow rate 0.5 mL/min	-	Continuous reactor	Acetin	[23]
Acetic acid	GL	ion exchange resin Dowex Monosphere 650C	240 min, 4 wt.% catalyst concentration, 120 °C, acetic acid/GL = 9:1	99.6% conversion, 88% selectivity	Batch reactor	Diacetylglycerol and triacetylglycerol mixture	[24]

Esterification is a reversible reaction and is equilibrium-limited due to the formation of the water as a by-product. On the other hand, a GL molecule consists of three

hydroxyl groups, mono, di, and triglyceride are formed during GL esterification. Esterification is conventionally carried out with homogeneous acid catalysts. Another alternative includes a biocatalytic route using enzymes (lipases from *Carica papaya*, *Candida rugosa*) [25] as a catalyst. In comparison with the homogeneous catalyst, it possesses a high product yield and the amount of waste generated from the reaction is much lower. However, the limitations of the biocatalysts are their high cost, longer reaction time required to produce high monoglyceride selectivity and non-recyclability. There are a lot of difficulties in GL esterification. Owing to the occurrence of three -OH groups in GL, it results in the mixture of mono, di, and triglyceride. The use of the catalysts leads to difficulty in separating the desired product from the mixture. Esterification can also take place in the unavailability of the catalyst. This phenomenon could be accredited to the autocatalytic reaction. Several studies have been reported on autocatalysis [26, 27]. Besides, heterogeneous acid catalysts have been engaged to enhance the catalytic activity while increasing the selectivity of the mono/di/tri-glyceride at the same time. Therefore, the synthesis of green and eco-friendly heterogeneous solid acid catalysts is the utmost need for improving the desired product yield. From the viewpoint of sustainability, Okoye et al. [28] has prepared a sulphonated carbon catalyst employing biodiesel-derived GL as a source for the synthesis of di and triacetin applied as oxygenated fuel additives. The heterogeneous solid acid catalyst has been synthesized in one step method via partial sulphonation and carbonization. GL acetylation attained 88% combined selectivity of diacetin and triacetin by employing the optimal catalyst.

1.2.2 Carbonylation/Transesterification of GL

To make the biodiesel production process economically practicable, GC is considered a multifunctional compound with emerging applications in the improvement of a

variety of industrial reactions. Recently, GC has attracted huge attention due to its several applications such as a non-volatile solvent in paint industry, electrolytes in energy storage materials, etc. as mentioned in Figure 1.5.

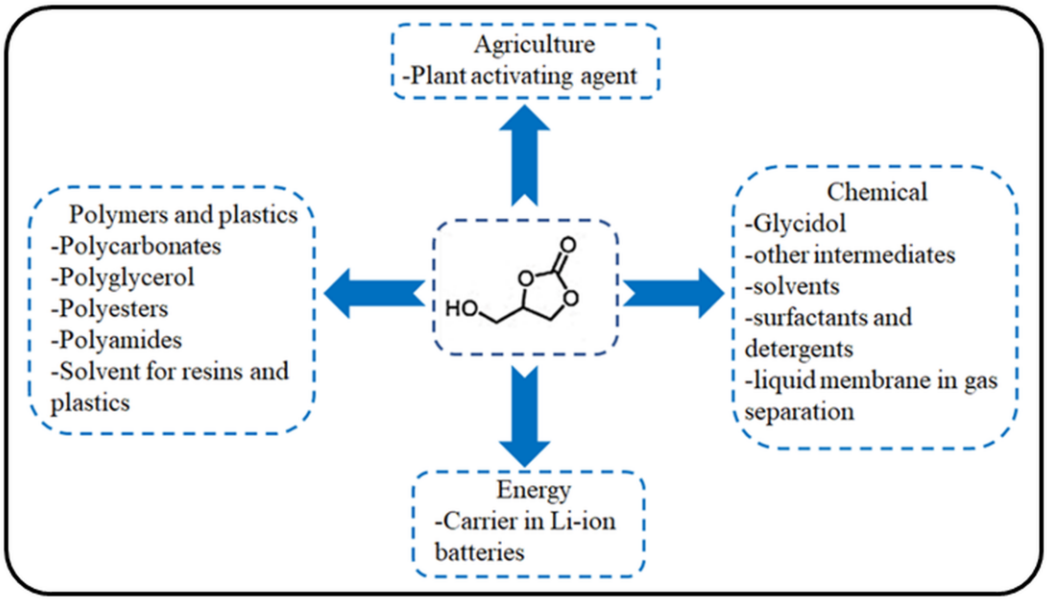

Figure 1.5. Industrial applications of GL carbonate

Over the last sixty years, a relatively large number of journal publications have been continuously released where GL carbonate has given rise to the development of new plausible methods for green chemistry in the activation and utilization of GL as evident in Figure 1.6. GC (4-(hydroxymethyl)-1,3-dioxolane-2-one or GL 1,2-carbonate) is a promising chemical compound, due to biodegradability, non-flammability (fp> 204°), water-soluble, viscous liquid (85.4 mPa.s at 25°C), and high boiling point. It is a quintet cyclic carbonate with different chemical reactivity because of its two diverse functional groups [29]. The global GC market is estimated to expand at a CAGR of 7% to reach US$ 2.4 billion by 2030. The market in the Asia Pacific region is anticipated to expand at a CAGR of more than 7.5% between 2020 and 2030 [30].

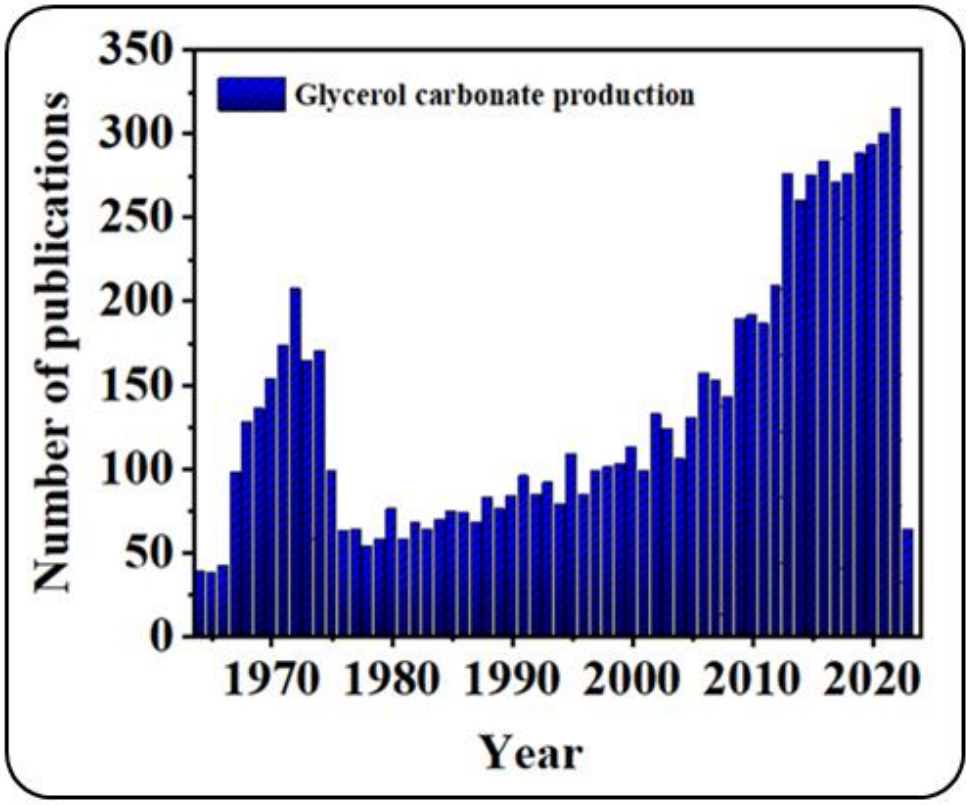

Figure 1.6. Number of publications on GC [31]

On the other side, GC offers less volatile organic compound solvent properties. This feature makes GC a green chemical. So far, different routes have been attributed to synthesizing GC. Direct routes comprise carboxylation (CO_2) and oxidative carboxylation (O_2+CO_2). Meanwhile, indirect routes encompass di-carbonates or alkyl carbonates, urea, and phosgene. Many studies have been investigated in direct and indirect synthesis of GC as depicted in Table 1.2. From Table 1.2, it could be detected that though GL conversion or yield/selectivity of GC was high. However, high pressure, high temperature, and long reaction time made the process unsuitable for industrial application. Though the usage of CO_2 helps in controlling the emission to the environment, GC synthesized through the reaction of GL with CO_2 has some limitations. Mainly due to thermodynamic limitations the yield produced from the reaction is very low and needs further optimization to become a technical route to

produce GC in a large expanse. Alternatively, the reaction of GL with carbon monoxide led to higher yields with a large number of by-products.

Table 1.2. GC production from various reactants

Reactions	Reactant	Catalyst	Reaction conditions	Conversion	Yield/Selectivity	Ref.
Carboxylation	GL and CO_2	Cu/La_2O_3	150°C, 7.0 MPa, 12 h	33.4%	45.4%	[32]
Oxidative carbonylation	GL, carbon monoxide, and oxygen	$PdCl_2$ (phen)/KI	2.0 MPa CO, 1.0 MPa O2, 140°C, 2 h	92%	99%	[33]
Glycerolysis of urea	GL and urea	γ-ZrP	418 K, 3 h, catalyst loading 0.6-1.5% w/w	80%	100%	[34]
Transesterification	GL and DMC	Novozym 435	60°C, 14 h, DMC/GL=1.5:1, 22.02% catalyst loading	94.85%	-	[35]
Transesterification	GL and DMC	K-zeolite	DMC/GL= 3:1, 4 wt.% catalyst loading, 75 °C, 90 min	100%	96%	[36]
Transesterification	GL and dialkyl carbonate	Ionic liquids	120°C, 2 h, dialkyl carbonate/GL= 2:1	93.50%	88.70%	[37]

Unfortunately, this synthesis route demonstrates the inherent difficulty in carrying out the reaction on laboratory and industrial scales due to the toxicity of carbon monoxide. In agreement with urea, the formation of huge amounts of ammonia as a by-product makes the reaction pathway non-environmentally benign and toxic and limits its industrial implementation. In comparison with the direct route, the indirect route i.e., the transesterification route for GC synthesis shows significant attraction due to higher activity and selectivity of the product, shorter reaction time, and higher conversion, requires no organic solvent, eco-friendly and intrinsically safe [38]. Furthermore, transesterification route using various carbonate sources aids a new alternative route for GL conversion. In recent years, among the organic and/or non-cyclic carbonates, researchers have focused on the use of DMC as a green alternative

route to produce GC. Typically, at moderate reaction conditions, GC is produced with simple by-product methanol (Figure 1.7), which is easy to recover and recycle for producing biodiesel, FAME via esterification of triglycerides [39]. For GL transesterification with dimethyl carbonate, the catalyst plays a pivotal role in the reaction. A large selection of homogeneous and heterogeneous base catalysts is found suitable for GC synthesis.

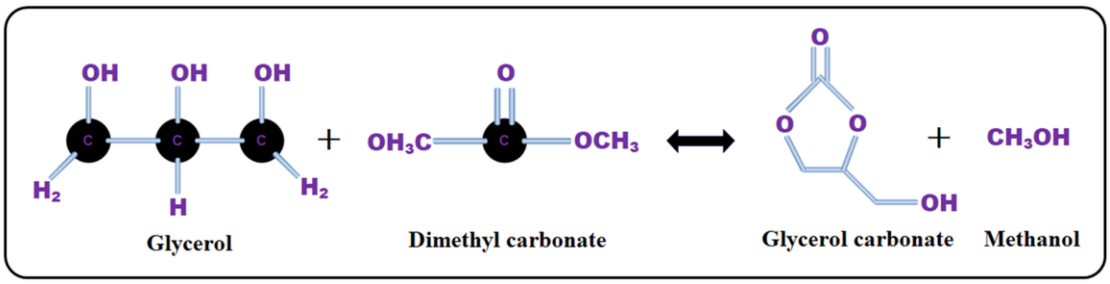

Figure 1.7. Transesterification of GL with DMC to produce GC

1.2.3 GL Oxidation

GL can be operated in two processes, like direct GL fuel cells, by producing electrical energy. The other process is electrolysis, where GL is converted to value-added chemicals on the anode with simultaneous production of hydrogen (H_2) or oxygen reduction at the cathode (Figure 1.8). In recent years, oxidation of GL to fine chemicals has won immense interest by representing GL as an important feedstock due to the polyhydroxy ($3OH^-$) groups in the backbone of GL. The most common GL-oxygenated derivates as shown in Figure 1.9. During oxidation, the primary hydroxyl group is first converted to aldehyde and then to carboxylic acid. In the formation of aldehyde over a heterogeneous catalyst, three steps are involved. Firstly, the alcohol adsorbed on the metal surface, constructing an adsorbed metal alkoxide.

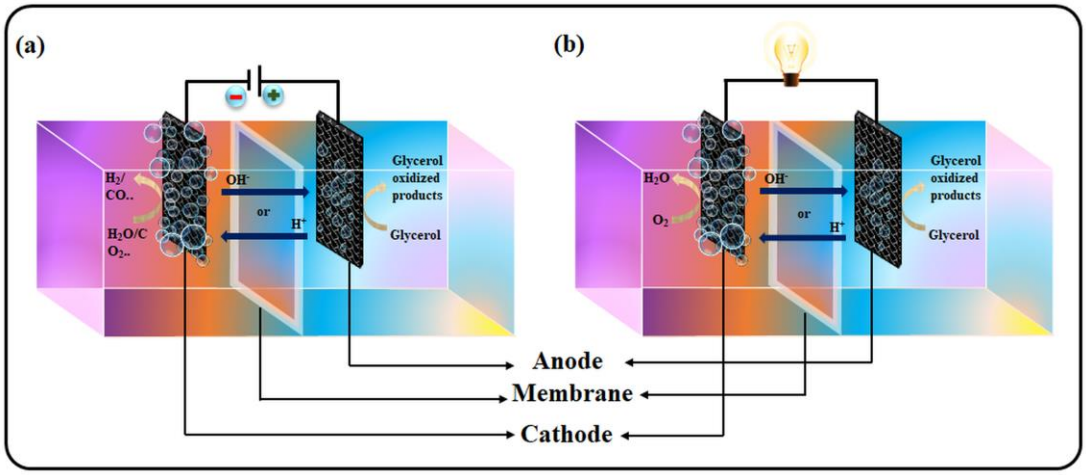

Figure 1.8. Schematic of GL (a) electrolysis cell and (b) fuel cell

Next, β-hydride exclusion took place to form a carbonyl species and a metal hydride. Finally, the metal-hydride is oxidized by dioxygen to revive the metal surface. Moreover, the oxidation of an aldehyde to carboxylic acid is supposed to progress through a geminal diol intermediate [40]. The reaction rate and selectivity of the oxidation depends on the oxidant source or by fermentation processes [41].

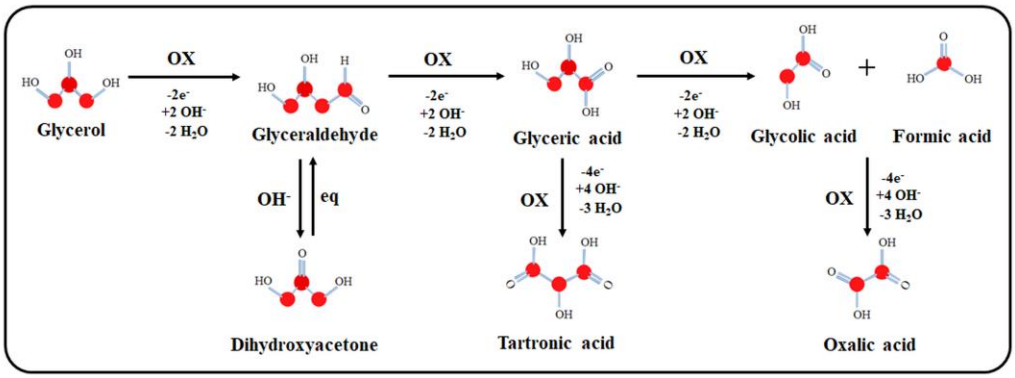

Figure 1.9. Products obtained by the oxidation of GL

1.3 Catalyst for Reaction Intensification

1.3.1 Homogeneous Catalysis

Esterification is conventionally happening in the presence of homogeneous acid catalysts (H_2SO_4, HNO_3, $HClO_4$, H_3PO_4). Meanwhile, the

carbonylation/transesterification reaction is facilitated by highly efficient alkaline active site catalysts viz., KOH, K_2CO_3, NaOH. In the presence of homogeneous catalysts, the reaction becomes corrosive, and separation of the catalyst from the reaction mixture becomes difficult and requires a special treatment process for waste acid, resulting in higher production costs. However, these homogeneous acid/alkali catalysts could not be reused further. The excessive use of water and energy consumption along with hazardous waste resulted in a series of environmental pollution [42].

1.3.2 Heterogeneous Catalysis

Heterogeneous acid/alkali catalysts have played a unique role due to their recyclability or time-on-stream in continuous reactors (good stability), easy separation from the reaction mixture, carried availability of the support, less corrosive, cheaper, and environment-friendly [43] for overcoming the limitations of homogeneous catalysts. These properties enhance the catalytic activity while increasing the substantial GL conversion. In addition, for the process intensification heterogeneous catalysts are suitable to use in various reactor configurations to engender large-scale production and industrial commercialization [44]. Therefore, the advancement of green and eco-friendly heterogeneous solid acid catalysts is the utmost need for improving the desired product yield. Among the many, zeolites, mesoporous silicas, carbon, metal-organic frameworks, metal oxide have been reported as promising heterogeneous catalysts for GL esterification. On the other hand, several solid base catalysts like CaO, KNO_3/CaO, Li/ZnO, and KF-modified hydroxyapatite have been used in the production of GC [45]. However, these catalysts have some limitations, like long preparation time and rapid deactivation rate. Therefore, the high surface area and stability of the catalyst are highly needed to defeat the existing barrier.

1.3.2.1 (a) Surface Acidity: Lewis & Brønsted Acidic Sites

Based on the structural characteristics, acidic sites on oxide surfaces can be classified into two types Brønsted and Lewis. A proton transfer takes place at the Brønsted site (H^+) from the solid to the adsorbed molecule as an ion appears and an ion-dipole interaction with the solid occurs, while Lewis acid sites (M) accept electrons from the adsorbed molecule and a coordinate bond with the surface is found. Mostly, an acid catalyst is categorized for its interaction with the adsorbed species if the number of adsorption sites, the strength of adsorption, the nature of the interaction, and the chemical nature of the adsorbed species are determined. There are several methods to determine surface acidity such infrared (IR) pyridine adsorption method and temperature-programmed desorption of ammonia method [46]. Among them, Fourier transform infrared spectrometer using pyridine adsorption is used to determine the type and quantity of the acid sites. Firstly, degassing is carried out in a vacuum at 250 °C for 3 h, then manifesting to the pyridine vapor after cooling down to 25 °C.

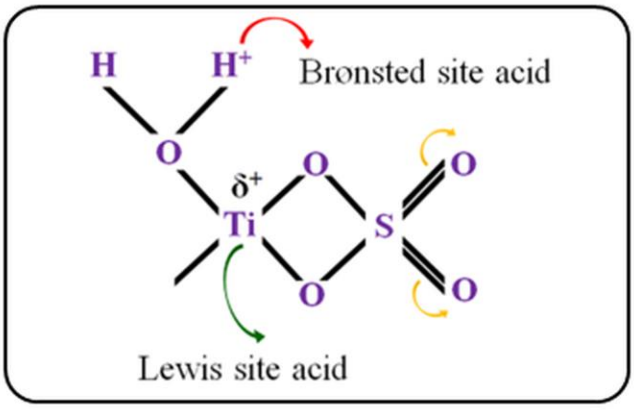

Figure 1.10. Schematic of the Lewis and Brønsted acid sites present in the sulfated titania

The amount of Brønsted acid and Lewis acid sites were analyzed based on the integral area of the adsorption bands at nearly 1540 cm^{-1} at 1450 cm^{-1}, respectively [47].

Ropero-Vega et al. have reported that both Lewis and Brønsted acid sites can be assessed on sulfated titania according to the schematic presented in Figure 1.10. The acid strength is notably increased due to the inductive effect on the S=O bonds. A study of the acidic properties of the catalyst sulfated titania revealed that the presence of Brønsted and Lewis acids both demonstrated high catalytic activity in terms of the conversion of oleic acid (82.2%). Higher selectivity of ester (100%) was attained while Lewis acid (titania sulfated with sulfuric acid) was chosen as catalyst [48].

1.3.2.1 (b) Surface Basicity: Lewis & Brønsted Basic Sites

The basic sites can mostly be ascribed to the presence of interlayer OH^- groups and surface O^{2-} species, which can be allocated as Brønsted and Lewis-type basic sites, respectively. In addition, the presence of the surface hydroxyl groups advocates charge compensation anions and strongly improves the accessibility of the Brønsted-type basic sites, whereas the presence of surface O^{2-} species upon calcination expedites the formation of surface Lewis basic sites. Being basic in nature, mixed oxide-based materials have been utterly applied for GC synthesis in the past few years [49]. For metal oxides, the lattice oxygen on the surface is viewed as Lewis basic sites. The basic properties of these mixed oxides are controlled by the configuration of metal cations in the precursor hydrotalcite. Remarkably, the catalytic activity of calcined hydrotalcite can also be boosted by rehydration in an inert atmosphere, which results in regeneration of the original layered structure, with Brønsted basic sites OH^- as the charge compensating anions in the interlayer. Accordingly, the adjustment of the type of basic sites and surface base strength makes hydrotalcite versatile precursors for preparing solid base catalysts for a comprehensive base-catalyzed reaction [50].

1.3.2.1 (c) Heterogenous Photocatalyst

The concept of photocatalysis is encouraged by natural photosynthesis. When a material uses solar energy to drive thermodynamically rising reactions (positive Gibbs free energy change, $\Delta G > 0$), the process should be observed as photosynthesis. The material used in such a situation must be known as a "photocatalyst" only if the photon is assessed as a reactant. Meanwhile, the material does not change the reaction thermodynamics but only changes the kinetics by establishing new reaction paths through the absorption of optical energy, the material is marked as a photocatalyst. Among the various classes, molecular photocatalysts, traditional semiconducting photocatalysts, quantum dot photocatalysts, and traditional semiconductor-based photovoltaic-assisted catalysts are implementing photocatalysis [51]. Heterogeneous photocatalysis has been elucidated by using a band structure of electronic energy in photocatalysts. Electrons and holes are engendered from the conduction band and valence band, respectively. An electron in a filled valence band is irradiated by photons whose energy is greater than the bandgap, ensuing electron excitation to the conduction band and leaving holes in the valence band. A n-type semiconductor, leaving electrons in the lattice photogenerated holes in the valence band occurs at the interface to perform the oxidation reactions. On the other hand, a p-type photocathode is used, where electrons would be used on the photoelectrode for the reduction reactions. Although photoexcited electrons are easily transferred to the surface, the transfer of holes is challenging. With contact of p-type and n-type semiconductors, the different p- and n-type electronic structures are accomplished by collecting electrons at the coupling interface on the p-type side and holes in the n-type ingredient, resulting in band bending and Fermi level equilibration. There are several advantages and challenges for the photocatalysis system. The advantages of photocatalysis are

effective textural property, high density of active sites, suitable for large-scale operations, and short charge diffusion distance to reduce bulk charge recombination.

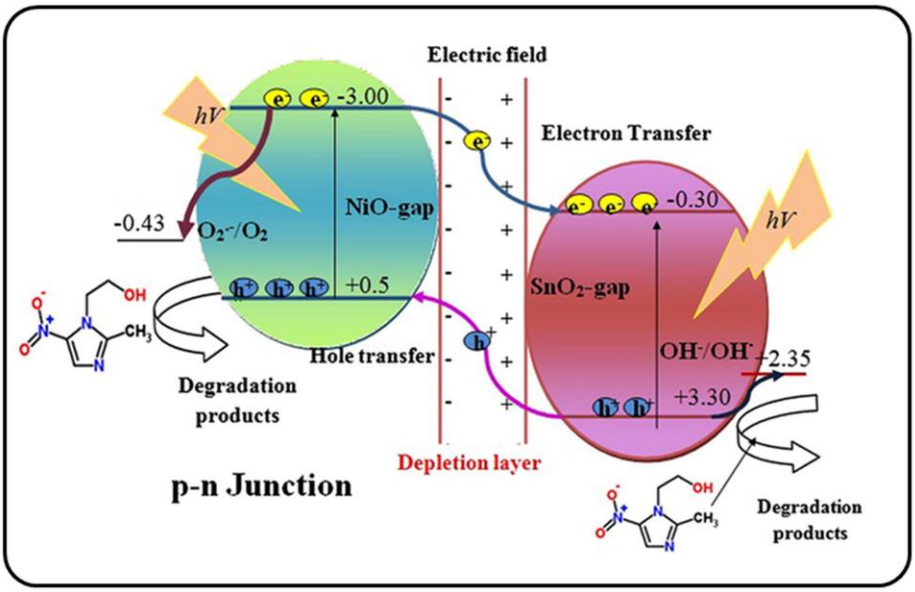

Figure 1.11 Representation of electron/hole production and charge separation in NiO-SnO_2 system Adapted from ref. [52] copyright 2017, with permission from Elsevier.

The challenges mainly include serious surface charge recombination because of the close vicinity of reduction and oxidation sites, poor photocatalytic stability, and product crossover due to the close vicinity of redox sites [53]. Nowadays, photocatalysts are gaining massive attention in the application of GL valorization. Corro et al. reported biodiesel from free fatty acids present in jatropha oil was first esterified with methanol using a highly active SiO_2-supported ZnO heterogeneous photocatalyst under UV irradiation at room temperature [54].

1.3.2.1 (d) Heterogenous Electrocatalyst

An electrocatalyst is a catalyst that engrosses in electrochemical processes. In electrocatalysis, bonds are broken and shaped by electron (e^-) and ion transport at electrode surfaces. Both stability and selectivity must be evaluated for selecting an electrocatalyst and modifying its characteristics. Thermodynamically, a catalyst

lowers the activation energy desired for a chemical reaction. The activation energy of electrochemical reactions is proportional to the potential or voltage at which the reaction takes place. Accordingly, electrocatalysts usually adjust the voltage where reduction and oxidation occur. Several forms of metal-containing catalysts are involved in electrochemistry while dealing with fuel cell or electrolysis engineering. The primary basis of these catalysts is to accelerate the half-reaction rate in a fuel cell. Predominantly, a widespread application of electrocatalysts employed in a fuel cell is based on platinum nanoparticles. However, nowadays, transition metal-based electrocatalysts are employed due to their great activity, textural property, good electrical conductivity stability, and durability. Furthermore, the use of support material has been proven as an effective strategy in lowering the usage of noble metal along with improving the catalytic activity integrated with comparatively large electrochemical surface area and high porosity, double layer capacitance [55]. Li et al. [52] have synthesized a bifunctional catalyst namely nickel-molybdenum-nitride nanoplates on carbon fiber cloth (Ni-Mo-N/CFC) support, for the concurrent high purity hydrogen (FE: 99.7%) and value-added formate products (94~98%) formation under 0.1 M GL dissolved in 1 M KOH. Both HER and GOR performance has concurrently exhibited at a relatively low cell voltage of 1.36 V at 10 mA cm^{-2} current density, which shows the superiority over the alkaline assisted water electrolysis by lowering the potential (260 mV).

1.3.2.1 (e) Catalyst Support

The supported catalysts demonstrate improved stability and higher activity in comparison with the bulk metal catalysts. A suitable catalyst support material should accomplish the following requirements: (i) high surface area so that the support materials can deliver a maximum substrate area for good dispersion of the catalyst

particles (ii) high stability (iii) good catalyst-support interaction (iv) morphology of the surface (v) mesoporous structure (vi) easy recovery of the catalyst (vi) good corrosion resistance. [56, 57] There are various non-carbonaceous and carbonaceous support materials like titania, alumina, silica, conducting polymers, mesoporous carbon, carbon nanotubes, graphene, and carbon fibers possessed in the experiments owing to their high surface area, high electrical conductivity, and relatively good stability. Bulk Ni-Fe catalyst showed a specific surface area of 112.71 m^2 g^{-1}, while in the presence of support material MCM-41, Ni-Fe/MCM-41 catalyst exhibited the highest surface area, narrowest pore size distribution, and pore volume, at 478.80 m^2 g^{-1}, 2.75 nm, and 0.539 cm^3 g^{-1}, respectively. Owing to the presence of support material, high reducibility, and moderate metal support interaction i.e., the uniform dispersion of Fe-Ni oxides on the surface of the support matrix exhibited more active sites during catalytic reactions [58, 59]. However, the costs of such catalytic supports raise the operational expenses, thus making the final product cost-intensive. Therefore, in making the production process relatively cost-effective, naturally, available resources or wastes could be the ideal alternative to produce effectual and sustainable catalyst support.

1.3.2.1 (f) Catalyst Support: Waste printed circuit Board as a source of metal precursor

Electronic waste (e-waste) is one of the fastest-growing waste streams due to the ever-growing production of electrical gadgets and a decline in the average lifespan of various electronic appliances across the globe. Printed circuit board (PCB) is the core component of every electrical and electronic appliance comprising about 3–6% of the total weight of the appliances. Waste Printed Circuit Boards (WPCBs) are a serious concern, as the entire amount of electronic waste will spread 110 million tons by 2030

[60]. Although e-waste has been a life-threatening issue for the ecosystem. Recycling and recovering precious metals are some of the most decisive tasks for safeguarding natural resources and enabling these wastes to be recast as an opportunity rather than a problem. Various initiatives have been appraised for such solid waste management. The composition of PCBs is assorted and heterogeneous in terms of materials, typically consisting of around 28% metallic and 72% non-metallic parts [61]. Non-metallic fractions include fiberglass a combination of 50% silica, 30% alumina, and 20% calcium oxide. Bazargan et al. [62] reported combination of acid treatment with thermal treatment has proven to be a simple yet essential method for the fabrication of porous silica from the non-metallic fraction of WPCB.

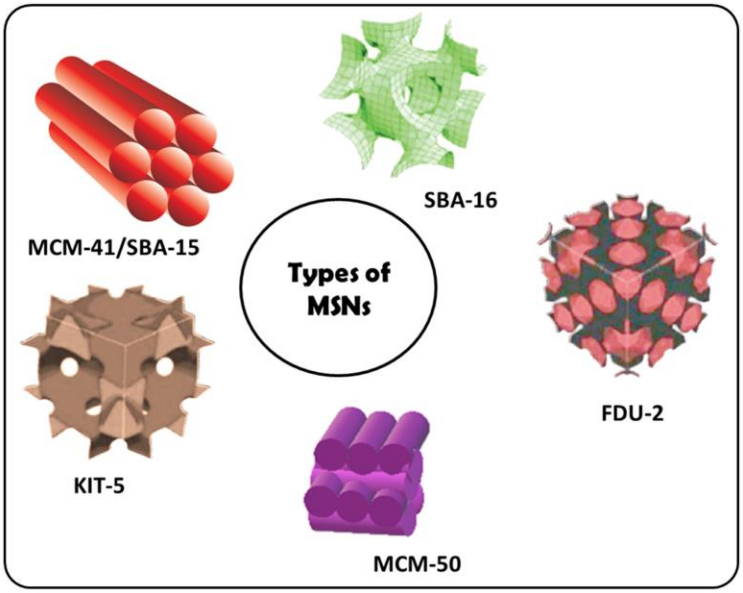

Figure 1.12. Different types of mesoporous silica nanoparticles (MSNs). Adapted from ref. [63] copyright 2022, with permission from Elsevier.

During the last few decades, silica has acquired a lot of attention owing to its constructive properties like very mesoporous structure, high adsorption capacity, and the flexibility of promoting various forms like powders, rods, spheres, discs, and so on [64] as shown in Figure 1.12. Therefore, e-waste valorization for extracting silica

is an important waste treatment technique for preparing economically viable support material for catalyst synthesis.

1.3.2.1 (g) Catalyst Support: Crustacean Waste as a Source of Chitosan

Crustacean waste consists of shells and other inedible fractions and represents an underutilized source of chitin. Exploration and developments in the field of crustacean-waste-derived chitin, extraction of chitosan, and its utilization, manifesting applications considering the improvement of biotechnology-derived chitosan have gained enormous attention in recent years [61]. Chitin is a naturally abundant and renewable polymer. There are various sources from where chitin can be obtained (Figure 1.13a). Being a biopolymer, chitosan has excellent properties such as biodegradability, biocompatibility, and nontoxicity. Chitin is a copolymer of N-acetyl-D-glucosamine and D-glucosamine units linked with β-(1-4) glycosidic bonds, where N-acetyl-D-glucosamine units are major in the polymeric chain. The deacetylated form of chitin refers to chitosan as shown in Figure 1.13a [65]. During the deacetylation process, the acetyl group present in chitin is converted into hydroxyl (-OH) and amino ($-NH_2$) groups in the chitosan. Chitosan is a bio-based polymer like cellulose, showing cationic behavior in acidic solutions and strong attraction toward metal ions. The international chitosan market size was valued at USD 10.88 billion in 2022 and is appraised to expand at a CAGR of 20.1% from 2023 to 2030 (Figure 1.13b) [66]. The growing shrimp industry in developing economies, including India, China, and Thailand, is anticipated to open new opportunities for chitosan manufacturers. Moreover, various studies have been found using chitosan due to its anti-corrosive nature. Although the stability of the polymer against biodegradation is of great concern for application, it can be reinforced by cross-linking treatment with significant improvement in polymer stability. The chemically and physically modified

chitosan has promising prospects for catalytic reactions including oxidation, reductive hydrogenation, and synthesis of fine chemicals. Moreover, chitosan can be used as a support for the preparation of heterogeneous catalysts [67]. Zhao et al. [68] reported chitosan support was an attractive candidate for the preparation of ZnCo-ZIF@Chitosan-3-800 electrocatalyst demonstrating exceptional catalytic stability, and methanol tolerance, and prospects to use in fuel cells.

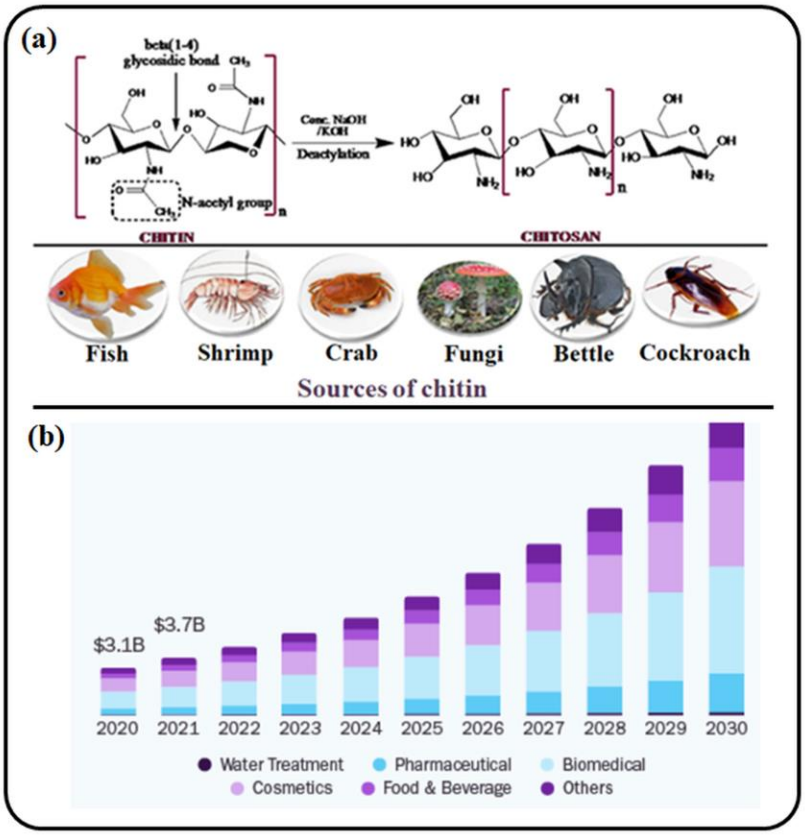

Figure 1.13. (a) Synthesis of chitosan and various sources of chitin, Adapted from ref. [65] copyright 2020, with permission from Elsevier. (b) Global chitosan market [66]

1.4 Reaction Intensification using Electromagnetic Energy

Infrared radiation (IR) signifies energy spectra over 0.001–1.7 eV corresponding to the range of energies separating the quantum states of molecular vibrations. The penetration depth of IR in reaction mass at the molecular level caused robust

molecular collision due to bending and stretching vibration of bonds, facilitating faster transfer of thermal energy into the reactant molecules which results in significantly enhanced activation of reactive species compared to conventional heating system. The penetration depth of IR is deeper than visible light and is more intensely absorbed than MW. Hence, electromagnetic radiation energy (Figure 1.14) is one such which drastically enhances the catalytic activity with the amplification of reaction rate, reduces reaction time, and temperature, and improves desired product selectivity can be recognized as an efficient, labor-saving, and economical method for valuable chemical synthesis.

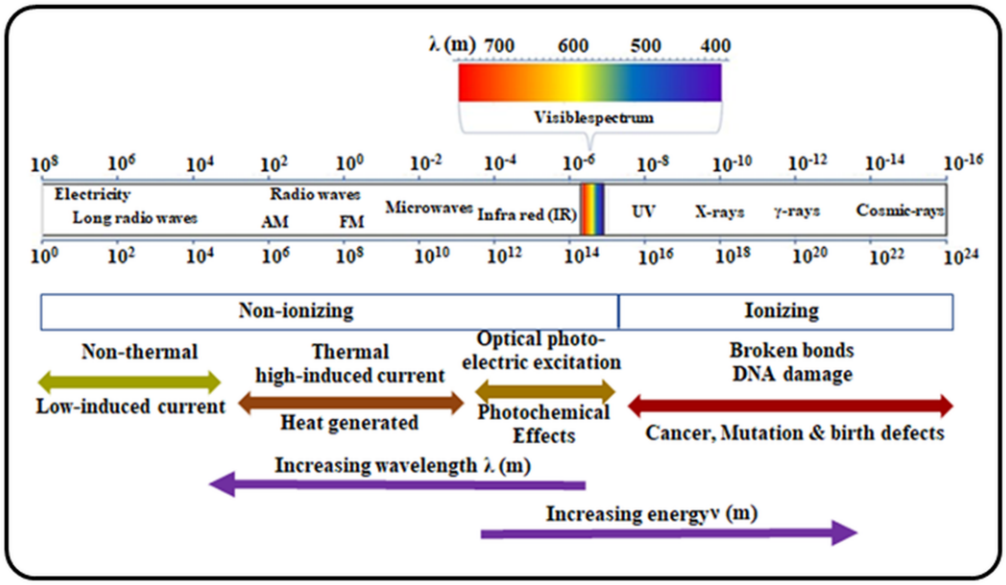

Figure 1.14. Electromagnetic radiation spectrum

Based on the absorption of electromagnetic irradiation by the nanomaterials, a new concept has been introduced. The concept of electromagnetic irradiation may be advantageous in various sectors viz. energy production, nuclear waste processing, radiation chemistry, chemical synthesis, radiotherapy, catalysis, and sensing [69]. Table 1.3 represents the application of different electromagnetic irradiations and their associated risks in chemical reactions.

Table 1.3. Application of different electromagnetic irradiation and its associated risks in chemical reactions.

Radiation	Application	Catalysis/ Reaction	Risks	References
UV Rays	Water purification, killing bacteria, creating fluorescent effects, curing inks and resins, phototherapy, and suntanning.	Biodiesel synthesis through esterification/transesterification reaction using La^{3+}/ZnO-TiO_2. 35°C temperature, irradiation time: 3 h, reaction time: 3 h, FFA conversion: 96.14%	Causes skin cancer, Sunburn, and eye disease.	[70]
Infrared (IR)	heat sensors, thermal imaging, and night vision equipment	Formaldehyde decomposition using graphene-based layered MnO_2 hybrid catalyst.	An extremely high temperature of IR can cause corneal damage.	[71]
Micro Wave (MW)	Cooking, diathermy and cancer treatment, remote sensing, radio astronomy, communication, radar.	Methyl butyrate esters, Amberlyst-15, 50-70°C, 60 min, conversion: 92.6%	It does not have the same risk as ionizing radiation. High-level exposure can cause skin burns or cataracts.	[72]
Radio Frequency (RF)	Broadcasting radio and television signals. Heating and drying applications include ceramics and foam.	Biodiesel Production from microalgae.	Carcinogenic.	[73]

1.5 Reaction Intensification using Various Reactor Systems

The reactor system is highly responsible for converting feedstock to desired products and the product separation techniques are significant factors to be considered before industrialization. The design, construction, and operation of catalytic reactor configurations are controlled by the physicochemical properties of reactants, and operating conditions, and based on product volume per day [1]. Table 1.4 depicts the usage of different reactor systems and their drawbacks in chemical reactions.

Table 1.4. Various reactor configurations and their usage in chemical reactions

Reactor configurations	Reaction conditions	Catalyst used	Application	Salient outcomes	Challenges	Ref.
Batch Glass reactors	DMC: GL=2:1, temperature: 80°C, reaction time: 60 min, catalyst dosage: 1 wt%	0.3KF/La-Zr	Transesterification: GC synthesis	Highly catalytic performance, 90% GC yield, after 3 times of usage: 54.14% yield	The longer reaction time implies a higher net-energy requirement for GC synthesis	[74]
Membrane reactors	Temperature: 50-70°C, Ethanol: acetic acid mole=1:1.5, Polydimethylsiloxane used as membrane material	Amberlyst 15 and sulfuric acid	Esterification: Ethyl acetate synthesis	100% conversion, Temperature has a strong influence on the esterification kinetics and pervaporation Ethyl acetate production rate was higher with sulfuric acid	Corrosive	[75]
Microwave reactors	Microwave power: 280-320 W, feed composition: oleic acid: methanol mole ratio=0.11-0.13, catalyst dosing: 0.5-0.7 g/mL, optimization process: box-Behnken design	Desilicated Hβ (high Brønsted acidity)	Esterification of oleic acid with methanol, ethanol, and isopropanol as a biofuel additive	91% oleic acid conversion and 86% selectivity of methyl oleate were observed at optimal conditions. Oleaic acid with methanol esterification showed lower activation energy calculated from the kinetic data.	Microwave heating is non-uniform.	[76]
Ultrasonic reactors	Ultrasound probe was used using different ultrasound pulses and amplitudes. 2 h, flow rate: 0.16 mL/min, 30-50°C, acetic acid to isoamyl	Lipozyme 435 enzyme immobilized on a polymer support	Esterification: Isoamyl acetate	At 50°C, ultrasound has enhanced the mass transfer at minimum cavitation activity Molecular sieves were used to remove the resulting water to	The increase in the ultrasound power causes negative effect of cavitation which stresses the enzyme. Difficult to commercialize due to non-uniform	[77]

	alcohol mole ratio: 1: 2			obtain the best possible performance.	irradiation	
Semi-batch reactors	Acetic acid mole ratio: 1:1, feed flow rate: 115 ml/min, total reflux: 0.5 h, reflux rate: 200 mole/h	Amberlyst 36	Reactive distillation: Methyl Acetate	The highest yield of methyl acetate at stage 4 (74.74%) with highest mass fraction of pure methyl acetate 97.36% at 0.82 h	High labor cost per unit product, Difficult to scale-up	[78]
Continuous reactors	132 mL packed bed glass reactor (L/D=9), reaction temperature : 58°C, reaction time in batch conditions: 60 min, reaction equilibrium reached at 400 min after continuous operation started	cation exchange resin (Purolite CT725)	Biodiesel	A satisfactory agreement between the experimental data and the proposed model was obtained. The packed bed reactor was modeled as a CSTR due to the high ratio of recycling volumetric flow to the reactor volumetric flow. The reactor followed non-ideal behavior and the reaction process is dominated by the chemical reaction and not by the diffusion of reactants towards the solid catalyst.	Recovery and reuse of the powder catalysts are difficult, unconverted feedstocks stick or block the pipelines, and pressure drop during the circulating flow of reactants through the catalyst bed is another drawback	[79]

1.6 Techno-Economic Assessment

In a declaration following the G20 summit held in New Delhi, India; the member countries affirmed their dedication to tripling global renewable energy capacity by positioning it as a central pillar in global efforts to combat climate change. Moreover,

they emphasized the requirement of renewable clean energy technologies by 2030 and pledged to phase out inefficient fossil fuel subsidies with the achievement of net-zero emissions by 2050 (G20 summit, 2023) [80]. Among the proposed strategies, there is a shift from the currently practiced linear, "take, make, and dispose" economy to a circular, "reduce, reuse, recycle, recover, redesign, and remanufacturing" economy [81]. Biodiesel-derived GL has been valorized to feed the global market with fine chemicals like GL oleate, GL acetate, GC, and formic acid as fuel additive and renewable H_2 through chemo-catalytic technologies. In the context of sustainable development, it is an utmost necessity to assess environmental concerns like global warming, human health, ozone depletion, and marine toxicity. Many scientific studies deal with the LCA to compare the environmental impact of the existing conventional technology with the emerging technologies to mitigate greenhouse gas emissions.

1.7 Summary

Chapter I has portrayed the urgency of the evolution from a fossil-based energy system to a renewable and sustainable biodiesel manufacturing unit. In the production of biodiesel, a huge amount of GL has been formed as a byproduct. However, the surplus amount of bio-GL portrays a major obstruction in the biodiesel production chain resulting in new challenges to its sustainable use. Thus, there is an utmost need to convert bio-GL into fine chemicals and their applications in various sectors. The photocatalytic and electrocatalytic conversion of bio-GL to esters, carbonates, and oxidized products are good alternative where a GL-based energy storage material, food additives not only elevates the biofuel industry but also enhance the market value of bio-GL world-wide.

Therefore, in Chapter 2, preceding articles on GL/monohydric alcohol-based esters, carbonates, and oxidized products have been discussed. For the development of value-

added products, various types of viable resin catalysts inexpensive metal catalysts and economically sustainable waste-derived support materials to augment the catalytic activity, non-conventional energy sources for the enhancement of the reaction rate, selection of optimum process conditions to maximize the desired product yield/selectivity have been considered. Moreover, to make the process sustainable, environmental impact assessment has been studied. To intensify the process, various reactor configurations are incorporated with the reactor scale-up prediction in theoretical simulation have been assessed and compared with the previous literature.

References

[1] P.U. Okoye, A. Longoria, P. Sebastian, S. Wang, S. Li, B. Hameed, A review on recent trends in reactor systems and azeotrope separation strategies for catalytic conversion of biodiesel-derived glycerol, Science of The Total Environment 719 (2020) 134595.

[2] M.S. Houache, K. Hughes, E.A. Baranova, Study on catalyst selection for electrochemical valorization of glycerol, Sustainable Energy & Fuels 3(8) (2019) 1892-1915.

[3] https://www.statista.com/statistics/1297107/fame-biodiesel-production-worldwide-by-key-country. Accessed on September 2023

[4] T. Attarbachi, M.D. Kingsley, V. Spallina, New trends on crude glycerol purification: A review, Fuel 340 (2023) 127485.

[5] https://www.alliedmarketresearch.com/glycerol-market-A16434. Accessed on September 2023. Accessed on September 2023.

[6] https://www.polarismarketresearch.com/industry-analysis/crude-glycerine-market. Accessed on September 2023

[7] R.S. Varma, C. Len, glycerol valorization under continuous flow conditions-recent advances, Current Opinion in Green and Sustainable Chemistry 15 (2019) 83-90.

[8] M.K. Estahbanati, M. Feilizadeh, F. Attar, M.C. Iliuta, Current developments and future trends in photocatalytic glycerol valorization: process analysis, Reaction Chemistry & Engineering 6(2) (2021) 197-219.

[9] I. Díaz, C. Márquez-Alvarez, F. Mohino, J.n. Pérez-Pariente, E. Sastre, Combined alkyl and sulfonic acid functionalization of MCM-41-type silica: part 2. Esterification of glycerol with fatty acids, Journal of Catalysis 193(2) (2000) 295-302.

[10] J.R. Ochoa-Gómez, O. Gómez-Jiménez-Aberasturi, B. Maestro-Madurga, A. Pesquera-Rodríguez, C. Ramírez-López, L. Lorenzo-Ibarreta, J. Torrecilla-Soria, M.C. Villarán-Velasco, Synthesis of glycerol carbonate from glycerol and dimethyl carbonate by transesterification: Catalyst screening and reaction optimization, Applied Catalysis A: General 366(2) (2009) 315-324.

[11] M.S. Houache, R. Safari, U.O. Nwabara, T. Rafaïdeen, G.A. Botton, P.J. Kenis, S. Baranton, C. Coutanceau, E.A. Baranova, Selective Electrooxidation of glycerol to Formic Acid over Carbon Supported $Ni_{1-x}M_x$ (M= Bi, Pd, and Au) Nanocatalysts and Coelectrolysis of CO_2, ACS Applied Energy Materials 3(9) (2020) 8725-8738.

[12] Y. Nakagawa, M. Tamura, K. Tomishige, Catalytic materials for the hydrogenolysis of glycerol to 1, 3-propanediol, Journal of Materials Chemistry A 2(19) (2014) 6688-6702.

[13] V. Naranje, R. Swarnalatha, O. Batra, S. Salunkhe, Technological Assessment on Steam Reforming Process of Crude GL to Produce Hydrogen in an Integrated Waste Cooking-Oil-Based Biodiesel Production Scenario, Processes 10(12) (2022) 2670.

[14] C.V. Rodrigues, K.O. Santana, M.G. Nespeca, A.V. Rodrigues, L.O. Pires, S.I. Maintinguer, Energy valorization of crude glycerol and sanitary sewage in hydrogen generation by biological processes, International Journal of Hydrogen Energy 45(21) (2020) 11943-11953.

[15] A.L. Olson, M. Tunér, S. Verhelst, A concise review of glycerol derivatives for use as fuel additives, Heliyon (2023) e13041.

[16] A. Sakthivel, R. Nakamura, K. Komura, Y. Sugi, Esterification of glycerol by lauric acid over aluminium and zirconium containing mesoporous molecular sieves in supercritical carbon dioxide medium, The Journal of Supercritical Fluids 42(2) (2007) 219-225.

[17] Y. Xia, Y. Fang, K. Zhang, G. Shi, J. Brown, Enzymatic synthesis of partial glycerol caprate in solvent-free media, Journal of Molecular Catalysis B: Enzymatic 23(1) (2003) 3-8.

[18] S.B. More, J.T. Waghmare, P.R. Gogate, Ultrasound pretreatment as a novel approach for intensification of lipase catalyzed esterification of tricaprylin, Ultrasonics Sonochemistry 36 (2017) 253-261.

[19] L. Hermida, A.Z. Abdullah, A.R. Mohamed, Synthesis of monoglyceride through GL esterification with lauric acid over propyl sulfonic acid post-synthesis functionalized SBA-15 mesoporous catalyst, Chemical Engineering Journal 174(2-3) (2011) 668-676.

[20] M. Kapoor, M.N. Gupta, Obtaining monoglycerides by esterification of glycerol with palmitic acid using some high activity preparations of Candida antarctica lipase B, Process Biochemistry 47(3) (2012) 503-508.

[21] C. Zong, R. Wang, H. Qin, L. Chen, Z. Qi, Intensified synthesis of glycerol monocaprylin using ionic liquids by temperature-responsive esterification, Journal of Molecular Liquids 359 (2022) 119255.

[22] M. Blanco, D. Zamora, M. Mir, R. Mulero, Study of the lipase-catalyzed esterification of stearic acid by glycerol using in-line near-infrared spectroscopy, Industrial & Engineering Chemistry Research 48(15) (2009) 6957-6960.

[23] M. Aghbashlo, M. Tabatabaei, H. Rastegari, H.S. Ghaziaskar, Exergy-based sustainability analysis of acetins synthesis through continuous esterification of glycerol in acetic acid using Amberlyst® 36 as catalyst, Journal of Cleaner Production 183 (2018) 1265-1275.

[24] D.M. Reinoso, G.M. Tonetto, Bioadditives synthesis from selective glycerol esterification over acidic ion exchange resin as catalyst, Journal of Environmental Chemical Engineering 6(2) (2018) 3399-3407.

[25] E.D. Cavalcanti, E.C. Aguieiras, P.R. da Silva, J.G. Duarte, E.P. Cipolatti, R. Fernandez-Lafuente, J.A.C. da Silva, D.M. Freire, Improved production of biolubricants from soybean oil and different polyols via esterification reaction catalyzed by immobilized lipase from Candida rugosa, Fuel 215 (2018) 705-713.

[26] B. De, Comparison of bio-and autocatalytic esterification of oils using mono-and diglycerides, Journal of the American Oil Chemists' Society 83(5) (2006) 443-448.

[27] M.d.S. Gomes, M.R. Santos, A.B. Salviano, F.G. Mendonca, I.R. Menezes, M. Jurisch, G.D. Rodrigues, R. Augusti, P.S. Martins, R.M. Lago, Biphasic

reaction of glycerol and oleic acid: Byproducts formation and phase transfer autocatalytic effect, Catalysis Today 344 (2020) 227-233.

[28] P. Okoye, A. Abdullah, B. Hameed, Synthesis of oxygenated fuel additives via glycerol esterification with acetic acid over bio-derived carbon catalyst, Fuel 209 (2017) 538-544.

[29] S. Sahani, S.N. Upadhyay, Y.C. Sharma, Critical review on production of glycerol carbonate from byproduct glycerol through transesterification, Industrial & Engineering Chemistry Research 60(1) (2020) 67-88.

[30] https://www.transparencymarketresearch.com/glycerol-carbonate-market.html

[31] https://pubmed.ncbi.nlm.nih.gov. Accessed March 2023

[32] J. Zhang, D. He, Surface properties of Cu/La_2O_3 and its catalytic performance in the synthesis of glycerol carbonate and monoacetin from glycerol and carbon dioxide, Journal of Colloid and Interface Science 419 (2014) 31-38.

[33] J. Hu, J. Li, Y. Gu, Z. Guan, W. Mo, Y. Ni, T. Li, G. Li, Oxidative carbonylation of glycerol to glycerol carbonate catalyzed by $PdCl_2$ (phen)/KI, Applied Catalysis A: General 386(1-2) (2010) 188-193.

[34] M. Aresta, A. Dibenedetto, F. Nocito, C. Ferragina, Valorization of bio-glycerol: New catalytic materials for the synthesis of glycerol carbonate via glycerolysis of urea, Journal of Catalysis 268(1) (2009) 106-114.

[35] K. Lanjekar, V.K. Rathod, Utilization of glycerol for the production of glycerol carbonate through greener route, Journal of Environmental Chemical Engineering 1(4) (2013) 1231-1236.

[36] Y. Algoufi, B. Hameed, Synthesis of glycerol carbonate by transesterification of glycerol with dimethyl carbonate over K-zeolite derived from coal fly ash, Fuel Processing Technology 126 (2014) 5-11.

[37] Z.I. Ishak, N.A. Sairi, Y. Alias, M.K.T. Aroua, R. Yusoff, Production of glycerol carbonate from glycerol with aid of ionic liquid as catalyst, Chemical Engineering Journal 297 (2016) 128-138.

[38] Y. Ji, Recent development of heterogeneous catalysis in the transesterification of glycerol to glycerol carbonate, Catalysts 9(7) (2019) 581.

[39] J. Keogh, G. Deshmukh, H. Manyar, Green synthesis of glycerol carbonate via transesterification of glycerol using mechanochemically prepared sodium aluminate catalysts, Fuel 310 (2022) 122484.

[40] S.E. Davis, M.S. Ide, R.J. Davis, Selective oxidation of alcohols and aldehydes over supported metal nanoparticles, Green Chemistry 15(1) (2013) 17-45.

[41] A. Villa, N. Dimitratos, C.E. Chan-Thaw, C. Hammond, L. Prati, G.J. Hutchings, glycerol oxidation using gold-containing catalysts, Accounts of Chemical Research 48(5) (2015) 1403-1412.

[42] H. Esmaeili, A critical review on the economic aspects and life cycle assessment of biodiesel production using heterogeneous nanocatalysts, Fuel Processing Technology 230 (2022) 107224.

[43] M.R. Arcanjo, I.J. da Silva Jr, C.L. Cavalcante Jr, J. Iglesias, G. Morales, M. Paniagua, J.A. Melero, R.S. Vieira, glycerol valorization: Conversion to lactic acid by heterogeneous catalysis and separation by ion exchange chromatography, Biofuels, Bioproducts and Biorefining 14(2) (2020) 357-370.

[44] S.M. Gade, V.B. Saptal, B.M. Bhanage, Perception of glycerol carbonate as green chemical: Synthesis and applications, Catalysis Communications (2022) 106542.

[45] S. Jaiswal, S. Maurya, Y.C. Sharma, Studies on role of support metal in glycerol conversion to glycerol carbonate through Mg/MnO_2 and Mg/CuO heterogeneous catalyst, Molecular Catalysis 546 (2023) 113243.

[46] G. Corro, F. Bañuelos, E. Vidal, S. Cebada, Measurements of surface acidity of solid catalysts for free fatty acids esterification in Jatropha curcas crude oil for biodiesel production, Fuel 115 (2014) 625-628.

[47] J. Tan, T. Lu, J. Zhang, B. Xie, M. Chen, X. Zhu, Highly efficient and recyclable catalysts $SnCl_2$–$xH_3PW_{12}O_{40}$/AC with Brønsted and Lewis acid sites for terephthalic acid esterification, Journal of the Taiwan Institute of Chemical Engineers 86 (2018) 18-24.

[48] J. Ropero-Vega, A. Aldana-Pérez, R. Gómez, M. Niño-Gómez, Sulfated titania [TiO_2/SO_4^{2-}]: A very active solid acid catalyst for the esterification of free fatty acids with ethanol, Applied Catalysis A: General 379(1-2) (2010) 24-29.

[49] M. Marimuthu, P. Marimuthu, A.K. SK, S. Palanivelu, V. Rajagopalan, Tuning the basicity of Cu-based mixed oxide catalysts towards the efficient conversion of glycerol to glycerol carbonate, Molecular Catalysis 460 (2018) 53-62.

[50] P. Liu, M. Derchi, E.J. Hensen, Promotional effect of transition metal doping

on the basicity and activity of calcined hydrotalcite catalysts for glycerol carbonate synthesis, Applied Catalysis B: Environmental 144 (2014) 135-143.

[51] X. Yang, D. Wang, Photocatalysis: from fundamental principles to materials and applications, ACS Applied Energy Materials 1(12) (2018) 6657-6693.

[52] H. Derikvandi, A. Nezamzadeh-Ejhieh, Synergistic effect of pn heterojunction, supporting and zeolite nanoparticles in enhanced photocatalytic activity of NiO and SnO_2, Journal of Colloid and Interface Science 490 (2017) 314-327.

[53] G. Corro, U. Pal, N. Tellez, Biodiesel production from Jatropha curcas crude oil using ZnO/SiO_2 photocatalyst for free fatty acids esterification, Applied Catalysis B: Environmental 129 (2013) 39-47.

[54] J. Goel, S. Basu, Effect of support materials on the performance of direct ethanol fuel cell anode catalyst, International Journal of Hydrogen Energy 39(28) (2014) 15956-15966.

[55] Y. Li, X. Wei, L. Chen, J. Shi, M. He, Nickel-molybdenum nitride nanoplate electrocatalysts for concurrent electrolytic hydrogen and formate productions, Nature Communications 10(1) (2019) 5335.

[56] S. Samad, K.S. Loh, W.Y. Wong, T.K. Lee, J. Sunarso, S.T. Chong, W.R.W. Daud, Carbon and non-carbon support materials for platinum-based catalysts in fuel cells, International Journal of Hydrogen Energy 43(16) (2018) 7823-7854.

[57] S. Sharma, B.G. Pollet, Support materials for PEMFC and DMFC electrocatalysts—A review, Journal of Power Sources 208 (2012) 96-119.

[58] D. Yao, C. Wu, H. Yang, Y. Zhang, M.A. Nahil, Y. Chen, P.T. Williams, H. Chen, Co-production of hydrogen and carbon nanotubes from catalytic pyrolysis of waste plastics on Ni-Fe bimetallic catalyst, Energy Conversion and Management 148 (2017) 692-700.

[59] D. Yao, H. Yang, Q. Hu, Y. Chen, H. Chen, P.T. Williams, Carbon nanotubes from post-consumer waste plastics: Investigations into catalyst metal and support material characteristics, Applied Catalysis B: Environmental 280 (2021) 119413.

[60] S. Yousef, M. Tatariants, V. Makarevičius, S.-I. Lukošiūtė, R. Bendikiene, G. Denafas, A strategy for synthesis of copper nanoparticles from recovered metal of waste printed circuit boards, Journal of Cleaner Production 185 (2018) 653-664.

[61] M. Kaya, Recovery of metals from electronic waste by physical and chemical recycling processes, International Journal of Chemical and Molecular Engineering 10(2) (2016) 259-270.

[62] A. Bazargan, D. Bwegendaho, J. Barford, G. McKay, Printed circuit board waste as a source for high purity porous silica, Separation and Purification Technology 136 (2014) 88-93.

[63] B.C. Ekeoma, M. Yusuf, K. Johari, B. Abdullah, Mesoporous silica supported Ni-based catalysts for methane dry reforming: A review of recent studies, International Journal of Hydrogen Energy 47(98) (2022) 41596-41620.

[64] H. Amiri, M. Aghbashlo, M. Sharma, J. Gaffey, L. Manning, S.M. Moosavi Basri, J.F. Kennedy, V.K. Gupta, M. Tabatabaei, Chitin and chitosan derived from crustacean waste valorization streams can support food systems and the UN Sustainable Development Goals, Nature food 3(10) (2022) 822-828.

[65] S. Kumari, R. Kishor, Chitin and chitosan: origin, properties, and applications, Handbook of Chitin and Chitosan, Elsevier2020, pp. 1-33.

[66] https://www.grandviewresearch.com/industry-analysis/global-chitosan-market

[67] E. Guibal, Heterogeneous catalysis on chitosan-based materials: a review, Progress in Polymer Science 30(1) (2005) 71-109.

[68] X. Zhao, L. Liu, W. Yang, Q. Pan, ZIFs@ chitosan derived efficient bimetallic carbon-based catalyst for oxygen reduction, Industrial & Engineering Chemistry Research 61(18) (2021) 6156-6162.

[69] N.N. Cheng, Z. Starkewolf, R.A. Davidson, A. Sharmah, C. Lee, J. Lien, T. Guo, Chemical enhancement by nanomaterials under X-ray irradiation, Journal of the American Chemical Society 134(4) (2012) 1950-1953.

[70] M. Guo, W. Jiang, C. Chen, S. Qu, J. Lu, W. Yi, J. Ding, Process optimization of biodiesel production from waste cooking oil by esterification of free fatty acids using La^{3+}/ZnO-TiO_2 photocatalyst, Energy Conversion and Management 229 (2021) 113745.

[71] J. Wang, G. Zhang, P. Zhang, Graphene-assisted photothermal effect on promoting catalytic activity of layered MnO_2 for gaseous formaldehyde oxidation, Applied Catalysis B: Environmental 239 (2018) 77-85.

[72] P. Dange, V. Rathod, Equilibrium and thermodynamic parameters for heterogeneous esterification of butyric acid with methanol under microwave irradiation, Resource-Efficient Technologies 3(1) (2017) 64-70.

[73] Y. Ma, S. Liu, Y. Wang, S. Adhikari, T.A. Dempster, Y. Wang, Direct biodiesel production from wet microalgae assisted by radio frequency heating, Fuel 256 (2019) 115994.

[74] X. Song, D. Pan, Y. Wu, P. Cheng, R. Wei, L. Gao, J. Zhang, G. Xiao, Synthesis of glycerol carbonate over porous La-Zr based catalysts: The role of strong and super basic sites, Journal of Alloys and Compounds 750 (2018) 828-837.

[75] A. Hasanoğlu, Y. Salt, S. Keleşer, S. Dinçer, The esterification of acetic acid with ethanol in a pervaporation membrane reactor, Desalination 245(1-3) (2009) 662-669.

[76] V.R. Umrigar, M. Chakraborty, P.A. Parikh, H.P. Kohli, Optimization of process parameters for oleic acid esterification using microwave reactor: Catalytic activity, product distribution and reactor energy model, Energy Nexus 7 (2022) 100127.

[77] I. Calinescu, A. Vartolomei, I.-A. Gavrila, M. Vinatoru, T. Mason, A reactor designed for the ultrasonic stimulation of enzymatic esterification, Ultrasonics Sonochemistry 54 (2019) 32-38.

[78] S. Akkaravathasinp, P. Narataruksa, C. Prapainainar, The effect of feed location of a semi-batch reactive distillation via esterification reaction of acetic acid and methanol: Simulation study, Energy Procedia 79 (2015) 778-783.

[79] R. Hernández-Montelongo, J.P. García-Sandoval, A. González-Álvarez, D. Dochain, E. Aguilar-Garnica, Biodiesel production in a continuous packed bed reactor with recycle: A modeling approach for an esterification system, Renewable Energy 116 (2018) 857-865.

[80] https://solarquarter.com/2023/09/11/g20-summit-commitment-to-triple-renewable-energy-capacity-by-2030-and-reduce-fossil-fuel-use/

[81] P. Ghisellini, S. Ulgiati, Circular economy transition in Italy. Achievements, perspectives and constraints, Journal of Cleaner Production 243 (2020) 118360.

CHAPTER 2

Literature Survey

2.1 GL Esterification using Various Supported Acid Catalysts

In view of "green chemistry" usage of biomass or industrial wastes to prepare the catalytic materials is becoming progressively attractive from both academic and ecological points of view due to its valuable advantages. Kong et al. [1] prepared a novel hydrophobic ZrO_2-SiO_2 supported Me&Et-$PhSO_3H$ acid catalyst for the catalytic GO formation. The total surface area of 79.75 m^2/g with a lower pore volume of 0.025 cm^3/g measured by using the BET equation, the catalyst has shown high acidity of 0.62 mmol/g due to the modification with trimethoxymethylsilane and 2-(4-chlorosulfonylphenyl) ethyltrimethoxysilane. All the reactions were conducted at 1:1 mole ratio of GL to OA concentrations without using any solvent. At optimum reaction conditions considering 100 °C temperature, 3 wt.% of catalyst concentration, and 8 h of time duration, the selectivity of GO has been obtained at 84.5% with 39% GL conversion. Although the increases in hydrophobicity of the catalyst can decrease the acidity of the designed catalyst, this work evidenced that the hydrophobicity has a substantial impact on GO yield and reaction rate. Keogh et al. [2] developed a tin-exchanged tungstophosphoric acid catalyst supported on K-10 montmorillonite clay for the esterification of GL with acetic acid. The textural property of the support K-10 clay has promoted the catalytic activity having a BET surface area of 161.1 m^2/g with lower pore volume (0.22 cm^3/g). At optimal reaction conditions such as GL (0.054 mol), acetic acid (0.54 mol), 10 wt. % catalyst loading, 800 rpm, 110 °C, and 120 min were studied, and the high yield of glycerol triacetin was 51.9% with 100% of GL conversion. Langmuir-Hinshelwood (LH) dual-site kinetic model was best fitted with the experimental results. Reddy et al. [3] systematically investigated $WO_3/TiO_2{-}ZrO_2$ and $MoO_3/TiO_2{-}$ ZrO_2 solid acids for triacetin synthesis. The high dispersion of MoO_3 species on the surface of $TiO_2{-}ZrO_2$ results in a high concentration of acid sites

induced by synergistic metal–support interactions. Therefore, complete GL conversion with 80% triacetin selectivity was obtained over $MoO_3/TiO_2–ZrO_2$ solid acid. However, Raman spectroscopy analysis demonstrated that the surface-active sites were blocked due to the geometrically different WO_x sites in the $WO_3/TiO_2–ZrO_2$ catalyst, which is a key reason for the low catalytic efficacy of $WO_3/TiO_2–ZrO_2$ solid acid in GL esterification. The $MoO_3/TiO_2–ZrO_2$ solid acid showed ability with insignificant change in the conversion and selectivity of up to five cycles. Zhu et al. [4] found GL acetylation over zirconia-supported heteropolyacids catalysts using $H_4SiW_{12}O_{40}/ZrO_2$ with active Brønsted sites and hydrothermal stability. The optimum catalyst (0.3 g) has outperformed at 120 °C temperature and 4 h of reaction time in the esterification with the production of bio-additives viz. glyceryl diacetate and glyceryl triacetate having 61.3 and 32.3% selectivity, respectively. Moreover, by preventing deactivation, the catalyst remained consistent in four consecutive reaction cycles. From Table 2.1, it can be observed that various supported solid acid catalysts have been prepared to synthesize the GL esters.

Table 2.1 Preparation of various GL esters using sustainable supported catalysts

Product	Reactant	Catalyst	Reaction conditions	Conversion	Yield/Selectivity	Ref.
GO	GL with OA	MCM-48 uses rice husk ash (RHA) as a silica	140 °C, 4 h	48.05% OA conversion	64.34% selectivity	[5]
Monoglyceride	GL with OA	propyl sulfonic functionalized SBA-15	160 °C, 6 h, 1.2 wt.% catalyst, OA/ GL=1 :1	95% OA conversion		[6]
Monopalmitin	GL with palmitic acid	SBA-15 supported sulfated zirconia	3 h, 170 °C using 2 wt. % of catalyst	86% palmitic acid conversion	43% yield	[7]
Triacetylglycerol	GL with acetic acid	Zr-modified hierarchical mordenite	3 h, 100 °C, 0.1 g catalyst GL/acetic acid=1:10	93.5% GL conversion	69.2% selectivity	[8]
Diacylglycerols	GL with OA	diatomite-loaded SO_4^{2-}/TiO_2	OA/ GL=2:1, 0.1% catalyst loading, 6 h, 210 °C	82% OA conversion	100% selectivity	[9]
Monoglyceride	GL with	ZnO/β-zeolite	0.5 wt%	80% OA	70-80%	[10]

	OA		catalyst, 150 °C, GL/ OA 4:1	conversion	selectivity	
GLlaurate	GL with lauric acid	Arenesulfonic acid functionalized ethyl-bridged-organosilica nanotubes Ar/$PrSO_3H$–Si(Et)Si	GL/ lauric acid= 3:1, 100 °C, 4 wt% catalyst, 1.5 h	95.6% lauric acid conversion	93.7% yield	[11]
triacetin, GLmonolaurate, and GLdilaurate	GL with acetic acid or lauric acid	rod-like nitrogen-containing carbon-based sulfonic acid functionalized ionic liquids, [$PrSO_3HN$][SO_3CF_3]/C	GL /acetic acid=1:6, 1 wt% catalyst, 120 °C, 1atm, GL/lauric acid =3:1, 2 wt% catalyst, 140 °C, 1atm		74.8, 94.7, 91.2% of yield	[12]
GLmonolaurate	GL with lauric acid	Silica gel-supported sulfonic acid functionalized ionic liquid	amount of catalyst 2.0 wt%, GL/ lauric acid=4.1, 145 °C, 45 min	66.9%	83.9% yield	[13]
Triacetin	GL with acetic acid	Molybdophosphoric-supported SiAl nanotubes	GL/ acetic acid=1:3; 75 mg of catalyst; 80°C, 10 h	17%	100% selectivity	[14]
Mono, di and triacetin	GL with acetic acid	Biomass-derived carbon-supported yttrium oxide	GL/ acetic acid=1:12, 130°C, 0.5 g of catalyst, 5 h	99.8% GL conversion	11.1, 60.2, 29.6% selectivity	[15]
Mono, di and triacetin	GL with acetic acid	25% niobic acid supported tungstophosphoric acid	GL/ acetic acid=1:5, 4 h, 120°C	98% conversion	100% selectivity	[16]
Triacetyl glyceride	GL with acetic acid	NiO-supported TiO_2 catalyst	GL/acetic acid=1:10; 40 mg catalyst loading; 150 °C; 15 min	90.2% GL conversion	65.9% selectivity	[17]

2.2 GL Transesterification using Various Supported Catalysts

To make the biodiesel industry economically practicable, GC is considered a multifunctional compound with emerging applications in the improvement of a variety of industrial reactions. Among the fine chemicals derived from GL, GC has attracted much attention in recent years due to its several applications such as a non-

volatile solvent in the paint industry, fuel additive, and electrolyte. In comparison with acid catalysts, basic catalysts showed high reactivity. Moreover, the catalytic activity has been increased with moderate acid and basic strength. Arora et al. [18] explored lithium-ion-impregnated coal fly ash-supported thermally stable catalysts. At 90 °C temperature with 2 h of reaction time, the catalyst yielded 91.74% of GC. Waste steel slag-derived S-CaMgAl mixed metal oxide has been prepared and used to catalyze GLwith DMC (Scheme 2.1). Table 2.2 depicts the synthesis and application of various sustainable supported catalysts for GC synthesis.

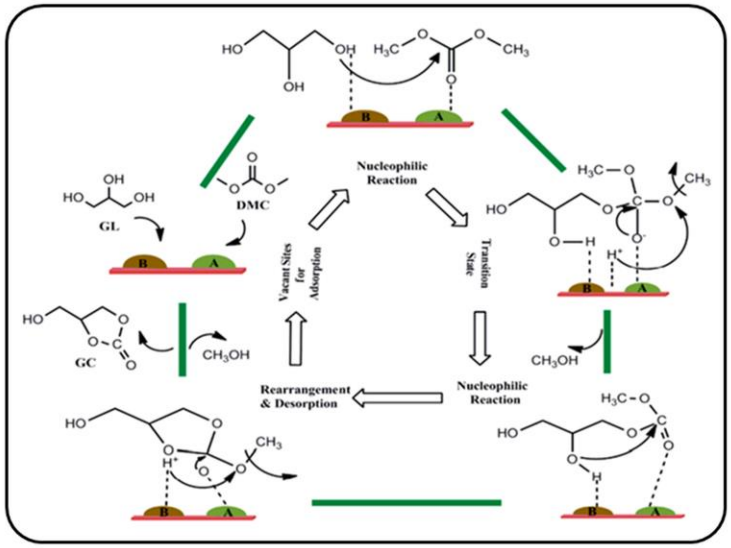

Scheme 2.1. Plausible transesterification reaction mechanism for GL with DMC to yield GC. Adapted from ref. [19]. Copyright 2019, with permission from ACS.

In the reaction, the GC yield reached 96.2% under 3 wt.% catalyst, 1:3 molar ratio of GL and DMC, 75 °C temperature, and 90 min of reaction time. In such cases, no additional solvents are required to ensure the reaction [20]. Phu et al. [21] found that activated red mud supported 50% Zn/Al oxide catalyst has an efficient catalyst for GC synthesis with the selectivity of 84.2% from GL and urea. Furthermore, waste red mud obtained from aluminum industry was applied as a greener catalyst for the efficient production of GC. Catalytic characterizations revealed that 500 °C for red

mud calcination influenced the maximum concentration of active $NaAlO_2$ and Ca_2SiO_4 sites, thus producing the highest catalytic activity with 92.02% GC yield at optimum reaction conditions (90 min, 90°C). However, due to leaching the catalyst has been deactivated after four reaction cycles [22]. Hu et al. [23] reported that cobalt-based zeolitic imidazolate framework-67 (ZIF-67) was developed for GC synthesis using GL with CO_2. Although the conversion and yield were too low i.e., 32, and 29%, respectively, the selectivity was achieved at 92%, at optimum reaction temperature and duration of 210 °C for 12 h, respectively under a pressure of 3 bar of CO_2 CH_3CN as a dehydrating agent. Figure 2.2 shows the FE-SEM and TEM images of ZIF-67. ZIF-67 possesses a uniform rhombic dodecahedral structure with particle sizes of approximately 300-400 nm. Moreover, high specific surface area (~1250 m^2g^{-1}), moderate Lewis acidity and basicity, ligand-to-metal electron transfer, high thermal stability, and well crystallinity made the catalyst favorable for the reaction. Nevertheless, the longer reaction time high temperature, and pressure make the reaction cost intensive [24]. Table 3 represents the GC synthesis using supported catalysts.

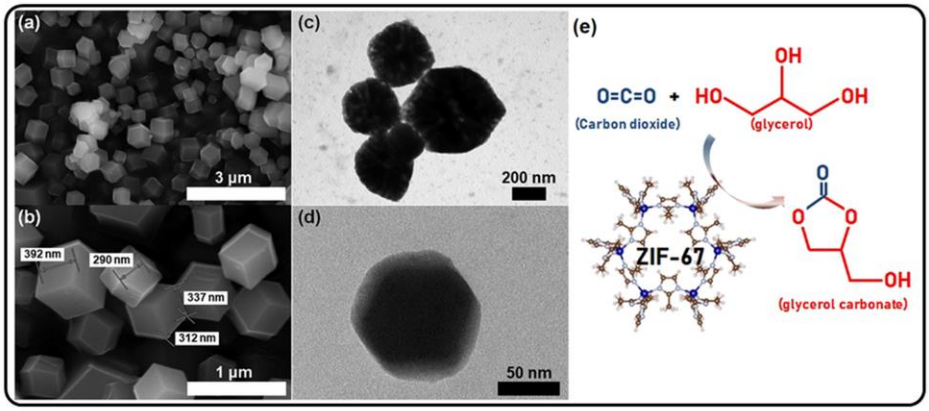

Figure 2.2.(a,b) FE-SEM and (c,d) TEM images of ZIF-67 (e) structure of ZIF-67, and reaction pathway. Adapted from ref. [23]. Copyright 2021, with permission from Elsevier.

Table 2.2. Preparation of GCs using various sustainable supported catalysts

Product	Reactant	Catalyst	Reaction conditions	Conversion	Yield/Selectivity	Ref.
GC	GL with DMC	Li/ZnO	4 h, 95°C, 5 wt.% of catalyst, DMC/ GL=3:1	97.40%	95.84%	[25]
GC	GL with DMC	K-zeolite derived from coal fly ash	DMC/GL=l:1, catalyst loading of 4 wt.% and reaction temperature of 75 °C	100%	96%	[26]
GC	GL with DMC	Strontium–aluminum catalyst	60 min, GL/DMC mole ratio=1:2, 70 °C, 3 wt.% catalyst loading	99.4%	100%	[27]
GC	GL with DMC	Disposable diapers waste-based catalyst (DBDWS-500)	GL/DMC=1:4, 2 wt% catalyst, 75 °C, 2 h	95.6%	97.9%	[28]
GC	GL with DMC	LiNO3/$Mg_4AlO_{5.5}$	80°C, 1.5 h, 5 wt.% catalyst loading, DMC/GL mole ratio=3:1, solvent-free	100%	96.28%	[29]

2.3 Non-CH Energy Source for GL Valorization

Recently, new technologies have rapidly emerged as an efficient tool to intensify the esterification process. The use of non-CH systems considering ultrasonication, and electromagnetic radiation (Figure 2.3) namely MW, IR have been found to be energy efficient rendering not only faster reaction rate and the enhancement in mass and heat transfer, but also shorter reaction time, lower operating temperature has resulted in high product yields/selectivity. The results have been collected and published in the field of esterification, transesterification, and oxidation using heterogeneous supported catalysts under electromagnetic radiation. Karnjanakom et al. [30] found that the production of triacetin over SO_3H-GL-carbon catalyst employed with ultrasound (80 W power) demonstrated 100% selectivity in mild reaction conditions (GL: acetic acid mole ratio=8:1, 100 °C, 150 min, ultrasonic duty cycle = 70%). Ultrasound-assisted acetylation reaction followed the first-order reaction kinetics with a lower activation energy of 51.08 kJ/mol. Moreover, in comparison with other

commercial catalysts, SO_3H-GL-carbon catalyst exhibited the highest reaction rate with excellent reusability for 10 consecutive cycles. Interestingly, the efficacy of ultrasonic cavitation phenomena was higher compared with the CH system, attributed to the physical effects in terms of intense turbulence and microstreaming generated during the cavitation could play a governing role in GL acetylation, resulting in faster reaction and higher triacetin product. MW irradiated system involves the direct delivery of energy to the materials via molecular interaction in the range of 300MHz and 300 GHz frequencies and wavelengths ranging from 0.001 to 1 m [31]. MW irradiation depends on the polarity and dielectric properties of the material. Kong et al. [32] reported GL with OA esterification using a MW reactor. At optimal reaction conditions of 191°C, 0.3 wt.% of Brønsted-based methane sulfonic acid catalyst, and 104 min of reaction time OA conversion was 53.5% higher in MW assisted reactor than CH reactor under solvent-free conditions.

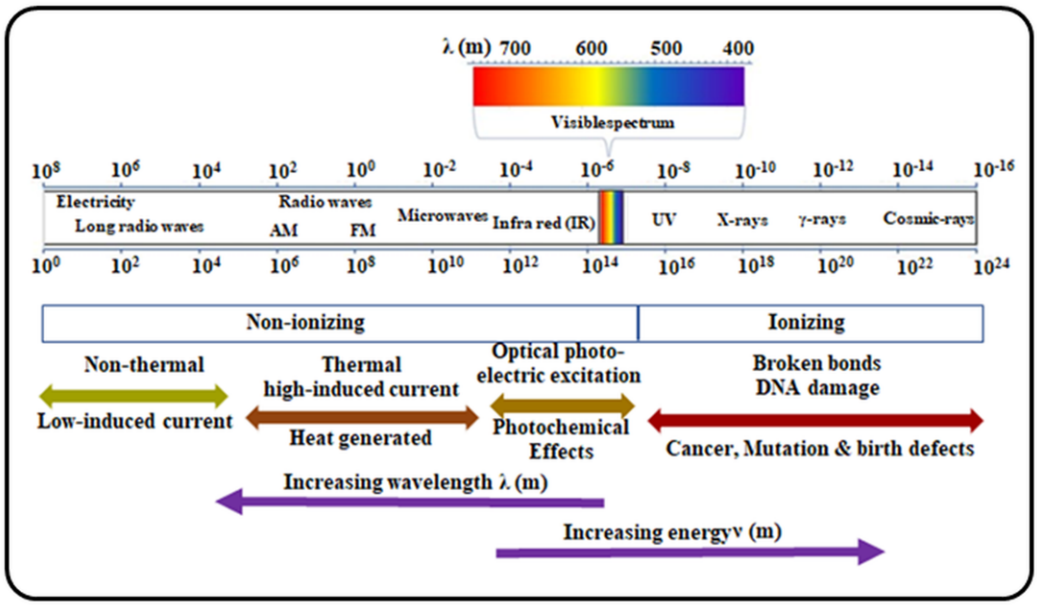

Figure 2.3. Electromagnetic radiation spectrum

Luque et al. [33] investigated mono, di, and triacetylglycerol synthesis from GL and acetic acid using Starbon-400-SO_3H supported palladium material with the selectivity

of 82% of monoester, 66% diester, and 80% triester by employing 300 W MW irradiated reactor within only 10, 15 and 30 min of reaction time, respectively. *Musa acuminate* peel ash, a biowaste-derived solid base catalyst was considered for GC synthesis using GL with DMC, using MW irradiation. The catalyst being biowaste was abundantly available, cheap, biodegradable, renewable, and sustainable. Moreover, the high basicity ($11.0 \leq pH \leq 12.2$), high surface area (539 m^2 g^{-1}), and mesoporous nature (3.38 nm pore dia) of the catalyst showed superiority by promoting the conversion of GL to GC(99%) under MW irradiation (50 W) with greater selectivity (99.5%) as compared to CH (18% conversion and 98.5% selectivity) under the mild reaction conditions (1:2 molar ratio of GL/DMC, catalyst loading of 6 wt.%, temperature of 75 °C and time of 15 min) with great stability up to 6 consecutive cycles [34]. Das et al. [35] demonstrated *Mangifera indica* peel calcined ash MIPCA, a biomass-derived heterogeneous solid base catalyst is investigated for GL transesterification synthesize GC under MW irradiation. The SEM and TEM images of MIPCA catalyst revealed many collates with microporous and mesoporous surfaces, as well as a spongy character as shown in Figure 2.4 a,b,e. Under the optimum reaction conditions of 3:1 M ratio of DMC: GL, 6 wt.% catalyst concentration, 80 °C temperature, and 50 min time, MW irradiation exhibits high conversion (98.1±0.6%) and improved selectivity (100%). Elemental mapping of the catalyst MIPCA shows the presence of potassium, K (red, Figure 2.4c), and calcium, Ca (green, Fig. 2.4d). The polycrystalline nature of the particles was further confirmed by the SAED imaging (Figure 2.4f).

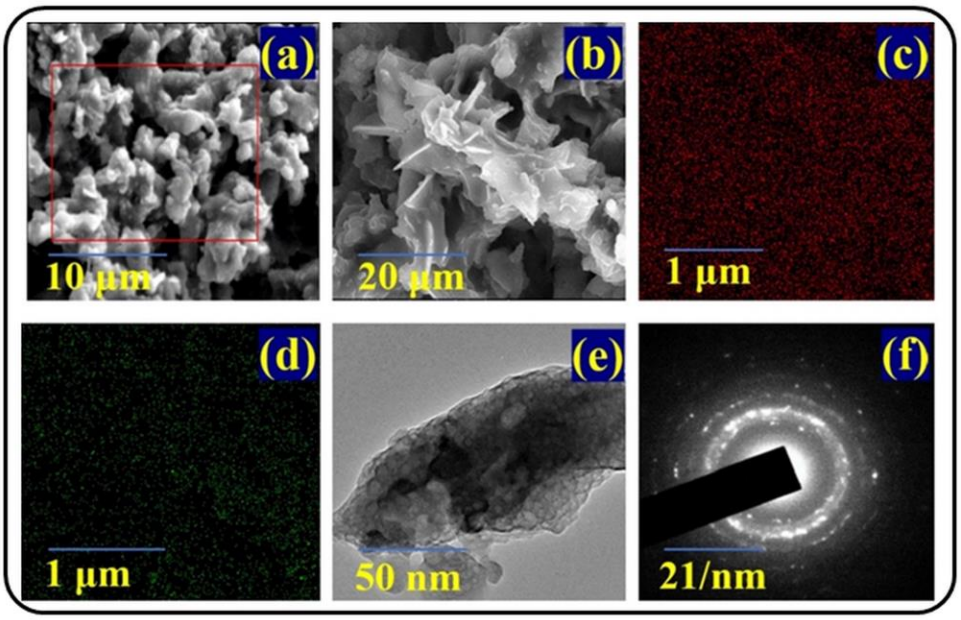

Figure 2.4. SEM images (a, b) of prepared catalyst MIPCA. Scale bars: 10 µm (a), 20 µm (b), and elemental mapping of the catalyst MIPCA showing the presence of Potassium (c), Calcium (d), and TEM image (e) of prepared catalyst along with SAED imaging (f). Scale bars: 50 nm (e), 21/nm (f). Adapted from ref. [35]. Copyright 2022, with permission from Elsevier.

IR represents energy spectra over 0.001-1.7 eV which correspond to the range of energies separating the quantum states of molecular vibrations. IR penetration depth was much deeper than visible light and is more intensely absorbed than MWs. It interacts with molecules to set them into molecular bending stretching vibration causing severe molecular collisions and facilitating faster transfer of electrons from the bulk phase to the catalyst surface resulting in significantly enhanced activation of reactive species compared to CH systems. Very few articles have been published with the aid of IR as a light source to intensify the esterification, and transesterification reaction. Chakraborty et al. [36] have demonstrated GL esterification with acetic acid to maximize the yield of di and/triacetin using a sustainable pork bone-derived hydroxyapatite supported antimony oxide catalyst under an IR-assisted batch reactor.

Notably, to achieve the di and/triacetin yield of 89%, the infrared radiated batch reactor consumes 1/6 times of energy in comparison to the CH batch reactor at a minimum reaction time of 2 h. Due to the addition of the support, the mesoporous catalyst possessed 40 m^2/g of specific surface area with a surface acidity of 4.251 mmol KOH/g catalyst. Noticeably, he developed a catalyst that rendered good stability and reusability for eight successive experimental cycles giving 99±1% GL conversion consistently. It is worth mentioning, that the synthesized product di and/triacetin offered its application as palm biodiesel additive evinced emission reduction by 50% and 20% for CO and HC respectively, with 2 degrees depression in pour point. Mukhopadhyay et al. [37] have established inexpensive slaughterhouse waste, lamb bone derived hydroxyapatite supported cobalt oxide solid acid catalyst for the GL esterification with OA under infrared radiated semi-batch reactor. Among the series of catalysts prepared employing both CH and IR, the infrared radiated batch reactor promoted optimal catalyst demonstrated remarkable catalytic properties considering BET specific surface area of 164.68±0.2 m^2/g and 7.16 mmol/g of acid-site concentration. Moreover, the catalyst revealed high efficacy in the monooleate synthesis with the selectivity of 95±4% at a much lesser reaction time of 80 min.

Mostly the previous literature relevant to GL esters and carbonates not only depends on the nature of the catalyst but also the operating parameters viz. reaction temperature and reaction time to obtain the desired product yield/selectivity. However, scanty articles have been published using non-CH systems.

2.4 Precious Free Non-Noble Metal Electrocatalyst for GOR

While most of the research has been focused on the synthesis of noble metal-based catalysts for GOR, and HER. Nevertheless, so many drawbacks pertinent to the noble metals such as high cost, scarcity, and poor stability, relatively small currents and

easily over-oxidize into CO_2 at high potentials. From the economic and ecological point of view, emerging efforts have been devoted to synthesizing progressive non-noble metal-based catalysts for selective oxidation in place of noble metals. Carrettin et al. [38] have reported that the supported Pt, Pd, and Au catalysts could oxidize GL to glyceric acid with high selectivity using an autoclave with O_2 at 3 bar pressure, 60 °C temperature 3 h of reaction time in the presence of sodium hydroxide (NaOH). No GL conversion has been achieved for Au/C in the absence of NaOH whereas for Pd/C and Pt/C, slow oxidation was observed. These manufacturing processes are cost-intensive and non-environmentally benign due to high pressure, and temperature, and require of long reaction time. Moreover, the rate and selectivity of GL oxidation normally depend on the choice of catalyst, type of oxidation sites, applied potential, the number of oxidized sites at steady state, accompanying side reactions (decarboxylation ($-CO_2$), decarbonylation (-CO) [39] and strongly depends on the pH of the solution. The full reaction of one mole of GL produces three moles of CO_2 gas, which is undesirable. In particular, the partial or selective oxidation reaction can not only avoid the formation of greenhouse gases but also obtain selective value-added products for industrial applications [40]. The most studied monometallic catalysts are Pd, Pt, and Au. However, major challenges associated with selective oxidation by using these monometallic catalysts concern the control of selectivity of the desired products formed during oxidation, deactivation due to overoxidation, and poisoning of the metal surface [41]. In comparison with monometallic catalysts, alloying of multiple metals like Au-Pt, Pt-Bi, and Au-Pd catalysts has significantly improved the oxidation process toward product selectivity. Dou et al. [42] have developed a stable bimetallic Pt_9Sn_1/C nanocatalyst for the oxidation of GL to glyceric acid (50% yield). Compared with the monometallic Pt/C nanocatalyst, Pt_9Sn_1/C has demonstrated two times higher activity, ensuing lower activation energy and high $TOF_{surface}$ (938 h^{-1}) are

attained at a reaction time of 2 h at 60 °C in acidic medium. Shen et al. [43] reported a one-pot approach to the efficient oxidation of GL to lactic acid in presence of Au-Pt/TiO_2 catalyst and O_2 at atmospheric pressure. Au-Pt/TiO_2 catalyst led to enhanced activity and high TOF (527 h^{-1}) through glyceraldehyde and dihydroxyacetone intermediates formed from GL oxidative dehydrogenation in NaOH solution and readily converted to lactic acid (85.6% selectivity) and glyceric acid (10.6%). In contrast, the results for monometallic Pt/TiO_2, Au/TiO_2 catalysts surface have accounted dramatic decrease in their activity. Notably, the interaction between Au and Pt has efficiently prevented the agglomeration of Au particles and the poisoning of Pt sites by O_2, leading to the observed superior stability of the Au–Pt/TiO_2 catalysts in GL oxidation. Ning et al. [44] have optimized the catalytic performance of Bi and Sb-promoted Pt supported on N-doped carbon nanotubes in the production of dihydroxy acetone through GL selective oxidation at neutral pH. In the presence of bimetallic catalysts, the selectivity on the oxidation process of the secondary OH group of GL has induced the production of 1, 3-dihydroxy acetone resulting in a high reaction rate and the alloying of the multi metals significantly diminished deactivation of the catalysts on reuse. During thermal catalysis, an excess number of chemical oxidants, high temperature, specialized infrastructure, and a large number of undesired by-products, reduce the yield, thus limiting the traditional thermal catalysis. In the case of biological enzyme catalysis, the high cost of enzymes, and difficulties in purification and separation of the product after reactions are the major drawbacks. Therefore, GL electrooxidation at a low temperature, atmospheric pressure, lower potentials than the electrooxidation of water [45], straightforward reaction conditions, and the use of renewable electricity make the process environmentally friendly. The GL oxidation process involves a complex mechanism with several steps: GL adsorption, electron transfer, reaction with oxygenated species and product desorption. These steps are

intimately associated with variables like temperature, pH of the electrolyte, nature of the catalyst, surface structure and potential, which bring to the oxidation reaction the possibility of yielding, and selectivity of compounds. The electrochemical oxidation of GL has confined its application in the fine chemical industry and as fuel-cell devices as dangerous and toxic chemicals are substituted by electric current [46]. Moreover, GL electrolysis might be a promising technique for hydrogen production in the future. In the net zero emissions scenario, strong hydrogen demand growth and adoption of cleaner technologies for its production will allow hydrogen and hydrogen-based fuels to prevent up to 60 Gt of CO_2 emissions in 2021-2050 (*https://www.marketsandmarkets.com*). In view of water splitting and chemical-assisted water splitting like urea, ammonia, hydrazine, and methanol are added as sacrificial agents for electrochemical oxidation, GL electrolysis not only produces more valuable chemicals at the anode but also reduces the cell voltage input to produce H_2 at the cathode by the consumption of low-value GL. Other than GL-oxidized products, formic acid is one of the major products applied as fuel in fuel cells [47]. Up to now, various studies have been published emphasizing only noble metals, viz. gold, platinum, palladium, and silver electrodes for the HER and GOR [39, 48]. Unfortunately, CO like toxic species produced during the oxidation of alcohols is strongly adsorbed on the surface of noble catalysts to occupy its active sites, penchant to undergo poisoning of catalyst [49]. Thus, catalysts containing noble metals are highly undesirable. Herein, the aim of the present study focuses on the recent progress in electrocatalytic GL valorization by generating value-added chemicals in GL fuel cells during GL oxidation and production of hydrogen at lower energy cost by using precious free non-noble metal catalysts.

2.5 Bifunctional Non-Precious Metal Electrocatalyst for GL Oxidations and H_2 Generation

While most of the research has been focused on the synthesis of noble metal-based catalysts for GOR, and HER. Nevertheless, so many drawbacks pertinent to the noble metals such as high cost, scarcity, poor stability, relatively fewer currents, and easily over-oxidize into CO_2 at high potentials. From the environmental and economic point of view, emerging efforts have been devoted to synthesizing progressive non-precious metal-based catalysts for selective oxidation in place of noble metals. Recently, Houache et al. [50] reported an unsupported $Ni_{90}Bi_{10}$ nano-catalyst for GOR over OER performed in an alkaline (KOH) electrolyte solution. From the cyclic voltammetry curve, it was exhibited that the $Ni_{90}Bi_{10}$ double shell-core structure has shown the highest mass activity and peak value at 92.6 mA cm^{-2} at an onset potential of 0.44 V compared to monometallic Ni. After 2 weeks of aging, the catalyst has shown two times better catalytic activity than the fresh catalyst toward GL oxidation. This phenomenon could be attributed to the oxidation mechanism from indirect to direct electron transfer. From *in-situ* polarization modulation infrared-reflection absorption spectroscopy (PM-IRRAS) and high-performance liquid chromatography (HPLC) measurements, it was observed that the NiBi served as a potential catalyst where Bi adatom selectively influenced the formation of tartronate. Ni-based catalysts show notable electrocatalytic performance, durability in alkaline solutions, and anti-poison ability, emphasizing a promising candidate for GOR. However, a small adsorption peak of CO_2 has been detected at 2352 cm^{-1} as observed from the PM-IRRAS analysis. Various attempts have been made to reduce the overpotentials and augment the electrolysis efficiencies, with no evidence of CO_2 formation. Hence, to improve the performance of the electrocatalysts, numerous strategies such as

cumulative surface area and enhancing the intrinsic catalytic activity have been focused. A variety of carbonaceous materials have been employed in electrocatalysts to improve their electrocatalytic activity and durability, including graphene, graphitic carbon nitride, and nitrogen-doped carbon. Shabnam et al. [51] have investigated nickel nanoparticle-based electrocatalysts supported on nitrogen-doped graphene (Ni-NGr) for catalyzing GL. The advantage of the catalyst is the presence of nitrogen-doped graphene as support material has more surface defects with increased surface area in comparison with pristine graphene, which has increased the conductivity, electrocatalytic activity, and faster electron transfer effect toward glycerate formation in 0.05 M GL with 0.5 M NaOH solution. Among various heteroatom dopants, nitrogen is estimated as an attractive potential element applied for doped materials since it can not only supply the metallic nanoparticles with anchored sites but also modulate the electronic property of graphene to deliver multidirectional electron transfer routes. Additionally, the graphene embedded with nitrogen atoms was favorable for supplying more active sites for the oxidation of small organic molecules, as well as greatly strengthening the connections between metal nanoparticles and graphene when compared to pristine graphene. These categories revealed substantial improvement in catalytic activity and long-term duration [52]. Accordingly, the construction of three-dimensional porous structures (i.e., metal foams), offers a huge surface area that allows rapid, multi-dimensional electron transport causing rapid reaction kinetics for GOR. The mechanism of GL indirect oxidation over the electrocatalyst has been mentioned step by step as follows.

$$M(OH)_2 + OH^- \rightarrow MOOH + H_2O + e^- \quad (1)$$

$$MOOH + RCH_2OH + OH- \rightarrow M(OH)_2 + H_2O + RCHO + e^- \quad (2)$$

$$RCHO + 3OH^- \rightarrow RCOO^- + 2H_2O + 2e^- \quad (3)$$

In the preliminary step, the oxidation of M^{II} to M^{III} took place (Eq. 1). M represents metal. This transformation occurred in concomitance with the GL oxidation mediated by the generated metal oxyhydroxide, regenerating the $M(OH)_2$ according to Eq. 2. At higher potentials, the aldehydes formed from Eq. 2 could be further oxidized to carboxylates (Eq. 3). The concept of bi-metal, trimetallic and multi-metal-based catalysts have been studied in recent years. NiCuFe-ANPs/ERGO/CE multi-metallic alloy has been electrodeposited on the support of electrochemically reduced graphene oxide (ERGO) and carbon ceramic electrode (CE) to illustrate the GL oxidation in comparison with the binary alloy-based electrocatalysts like NiCu and NiFe. The ternary alloy nanocomposite in the presence of ERGO has influenced the growth of the oxidation peak current density by decreasing the onset potential. Moreover, at a lower potential of 0.8 V the current density approaches 170.35 mA cm^{-2} with the lowest degradation rate in current density among all prepared electrocatalysts as evident from chronoamperometry. Thus, the multi-metallic catalyst has effectively been recognized as an efficient catalyst due to its stability and anti-poisoning effect [53].

Hydrogen (H_2) is a highly promising renewable carbon-neutral sustainable energy carrier having high gravimetric energy density, non-toxicity, non-polluting, and feasible alternative to diminishing fossil fuels [54]. Tafel slope is used to interpret the HER process. Two different mechanisms govern electrochemical hydrogen storage. Firstly, adsorption on the exterior and secondly insertion into bulk of sample. Decisive mechanisms that govern the HER sorption are three-step processes, namely Volmer, Tafel, and Heyrovsky reactions. The preliminary step involved is the charge transfer mechanism occurring at the electrode/electrolyte interface mentioned in Eq. 4 [55]

$$H_2O + M + e^- \leftrightarrow MH_{ads} + OH^- \quad (4)$$

Eq. 4 represents the volmer reaction (Tafel slope ~ 120 mV dec^{-1}) where reduction of water to hydroxyl ion occurs and even adsorption of hydrogen atoms onto the electrode surface. Atoms are adsorbed by host material leading to the formation of subsurface hydrogen (H_{SS}).

$$MH_{ads} \leftrightarrow MH_{SS} \quad (5)$$

These subsurface hydrogen atoms are then, finally diffused into bulk as H_{abs}.

$$MH_{SS} \leftrightarrow MH_{abs} \quad (6)$$

Sidewise Tafel reaction (Tafel slope ~ 30 mV dec^{-1}) also takes place where adsorbed hydrogen atoms recombine to gaseous hydrogen.

$$2MH_{ads} \leftrightarrow H_2(g) + 2M \quad (7)$$

Heyrovsky reaction (Tafel slope ~ 40 mV dec^{-1}) occurs where hydrogen atoms form hydrogen molecules by dissociation of hydrogen atoms from water molecules.

$$MH_{ads} + H_2O + e^- \leftrightarrow M + H_2(g) + OH^- \quad (8)$$

Even though highly efficient H_2 can be produced through water electrolysis, the sluggish kinetics of OER with cathodic HER could risk a danger of explosion by the resultant mixture of H_2/O_2 produced by gas crossover during the water decomposition [56]. Alternatively, upgrading GL through GOR with the use of the abovementioned non-precious metal catalysts has been attributed high selectivity product and high yield rate instead of relatively low value-added O_2. Economically feasible, low-cost, high-activity bifunctional electrocatalysts are highly appreciable for promoting GL

electrolysis to meet the future demand for formic acid in the anode along with hydrogen in the cathode. The vast application of non-precious catalysts in the alkaline medium has made them attractive candidates due to their electrocatalytic activity, anti-poisoning capabilities, and long-term stability. In these regards, transition metal nitrides and other bimetal derivatives have shown immense involvement in a variety of catalytic applications. Their electronic structures provide noble metal-like properties whereas their metallicities lead to high conductivities in catalysis. Li et al. [57] have synthesized a transition metal-based nitride electrocatalyst namely nickel-molybdenum-nitride nanoplates on carbon fiber cloth (Ni-Mo-N/CFC) as a bifunctional catalyst for the concurrent high-purity H_2 (FE: 99.7%) and formate products (94~98%) formation in 0.1 M GL dissolved in 1 M KOH. Both HER and GOR performance has concurrently exhibited at a rather low cell voltage of 1.36 V for a current density of 10 mA cm^{-2}. The cell voltage for GOR was 260 mV lower than the alkaline-assisted water electrolysis. Besides, after 20 cycles of CV scans, and 12 h of stability study employing chronopotentiometry, almost 90% of Mo being leached into the electrolyte. Ni-Mo-N/CFC showed an electrochemical double-layer capacitance (C_{dl}) value of 0.302 F cm^{-2}. However, the loss of Mo could lead to the formation of catalytic defects, resulting in more exposed active sites and enhanced electrocatalytic activity. Liu and coworkers [58] have synthesized hetero-structured bifunctional Ni_3N-$Ni_{0.2}Mo_{0.8}N$ nanowire arrays on carbon cloth surfaces by integrating hydrothermal and nitridation methods. A two-electrode assembly, with the bifunctional activity of the catalyst, renders a current density of 10 mA cm^{-2} at an applied cell voltage of only 1.40 V in 1 M KOH with 0.1 M GL. The Tafel slope for GOR and HER for the catalyst exhibits small values of 95.7 mV dec^{-1} and 86.8 mV dec^{-1} respectively, while the C_{dl} value obtained through cyclic voltammetry (CV) measurements in non-faradaic region is 96.8 mF cm^{-2}, which was significantly larger

than the other catalysts. A parallel formation of formate (FE: 96%, as depicted in ^{1}H NMR spectra) and hydrogen (FE: 100%, as depicted from gas chromatograph) under an alkaline solution showing long-term durability of 20-h with insignificant potential loss has been recognized as a highly stable electrocatalyst. Surface immobilized $Cobalt_{10\%}$ doped copper vanadate exhibited bifunctional reactivity for both HER and GOR in alkaline solution during cathodic and anodic scans. In the presence of 0.2 M GL and 0.2 M KOH electrolyte, the as-prepared catalyst demonstrated a steep increase in the oxidation current at 1.39 V for the current density of 10 mA cm^{-2}. During this dual-active catalysis, lower overpotentials of 176 mV and 160 mV for the HER and GOR, respectively, were required for 10 mA cm^{-2} current density by creating reaction hot spots on the surface of the material leading to unique electrocatalytic proficiencies. From 1H NMR spectra it has been determined that the highly reaction glyceraldehyde has readily converted to glycerate and the glycerate intermediate, resulting in the formation of formate with an FE of 79.8% at 1.6 V. The Tafel slope value of 94 mV dec^{-1} (governed by Volmer-Heyrovsky mechanism) demonstrated high HER performance indicating an excellent FE of 93.7%. Thus, the chronoamperometry stability study has significantly validated no current density decay during the GL electrolysis for 4 h [59]. Several researchers have performed GL electrolysis in both acidic and neutral media in comparison with the alkali medium. Especially, the results obtained from the alkaline media exhibited higher current densities compared to acidic and neutral solutions. A facile synthesis of cost-effective earth-abundant MnO_2 supported on the carbon paper was developed for the electrooxidation of the GL in coordination with hydrogen production in 0.005 M H_2SO_4 with 0.2 M GL. Especially, at a lower potential of 1.36 V vs. RHE, GOR has achieved the current density of 10 mA cm^{-2} which is 270 mV lower than that of OER. The highly active catalyst was stable for longer than 865 h without any decay. Formic

acid was detected from ex-situ NMR and in-situ FTIR with a selectivity of 61-68%. The formic acid has further oxidized to CO_2 and carbon monoxide. Moreover, H_2 has been produced at the cathode as proved by the gas chromatograph [60]. Nevertheless, the formation of CO_2 makes the process ineffective. Fan et al. [61] developed a new strategy like electrochemical neutralization energy where a flow alkali/acid hybrid electrolytic cell has been constructed by coupling alkali (KOH) anodic GOR with acidic (H_2SO_4) cathodic HER where non-precious Mn-$CoSe_2$/CFC material was used as a bifunctional catalyst. The electrode has lowered the GL oxidation potential at 1.27 V vs. RHE for the current density of 10 mA cm^{-2}. Mn-$CoSe_2$/CFC has achieved a high selectivity to formate with FE% of 80% in the wide potential window of 1.22 to 1.37 V vs. RHE. The Turnover frequency (TOF) of the Mn-$CoSe_2$/CFC for GOR and HER were found to be around 3.40 h^{-1} at 1.45 V vs. RHE and 17.64 h^{-1} at -0.3 V vs. RHE, respectively. Moreover, the flow hybrid electrolyzer could stably run for more than 10 days at a current density of 100 mA cm^{-2} as shown in Figure 2.5. Few researchers have explored transition metal phosphides in the field of GL electrolysis.

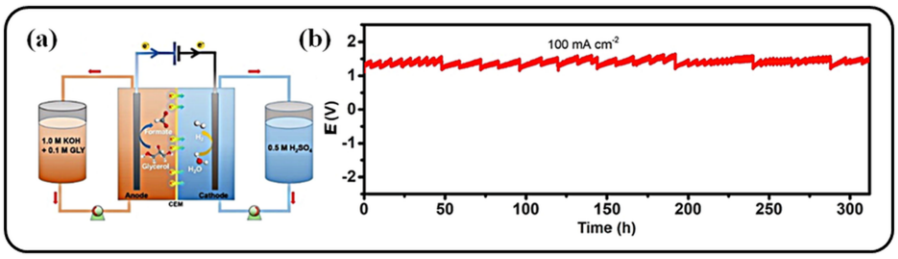

Figure 2.5. (a) Schematic illustration of acid-base neutralization electrolytic cell. (b) Long-term stability test of Mn-$CoSe_2$/CFC at a current density of 100 mA cm^{-2}. Adapted from ref. [61]. Copyright 2022, with permission from Elsevier.

Table 2.3 represents the various bifunctional catalyst syntheses for GL valorization with simultaneous H_2 generation. However, in the future, more GL electrolysis studies are required with lower onset potential and higher current density along with high

stability of the non-precious metal-based catalysts for commercialization.

Table 2.3. Various non-precious bifunctional photo/electrocatalysts are used for GL oxidation reaction and hydrogen evolution simultaneously with their effect on production selectivity.

Catalyst	Process	Onset potential	Current density	Electrolyzer	Reaction conditions	Product	FE%	Ref.
Pt_{SA}-NiCo LDHs/NF by electrodeposition	Electrolysis	1.37 V	100 mA cm^{-2}	1 M KOH + 0.1 M GL	Room temperature	H_2, Formate by ^{13}C NMR and H_2	H_2 100% Formate 88.7 %	[62]
Self-supported Ni_2P-CoP/NF by electrodeposition -phosphidation	Electrolysis	1.3 V	10 mA cm^{-2}	0.5 M KOH + 1 M GL	Room temperature	Formate and H_2 by online GC-TCD	H_2 100% Formate 89.6 %	[63]
Nitrogen-doped cobalt oxide, Pt-coated silicon nanowire	Solar-assisted co-electrolysis	0.27 V	10 mA cm^{-2}	1 M KOH+1 M GL	Solar light irradiation	H_2, Formic acid by ^1H NMR	Formic acid 96.2 %	[64]
CoNiFe-LDHs decorated Ta_3N_5	Solar driven photo-electrocatalysis	0.51 V_{RHE}	1.52 mA cm^{-2}	10 v% GL+1 M NaOH	Visible-light irradiation	H_2, Formate	H_2 100%, Formate 100%	[65]
Mo-$BiVO_4$	Photo-electrolysis	2.0 V vs. RHE	3.8 mA cm^{-2}	10 mL GL+0.01 M phosphate buffer	Visible-light irradiation	Formic acid by ^1H NMR	H_2 100%	[66]
$BiVO_4$/Tannic acid coordinates with Ni and Fe ion	Photoelectrolysis	1.23 V vs. RHE	5.26 mA cm^{-2}	0.1 M Na_2SO_4/ H_2SO_4 solution + 0.1 M GL	Light irradiation	H_2 by Gas chromatography	H_2 93%, Formic acid 94%,	[67]

2.6 Kinetic Analyses

To correlate the experimental results theoretically, classical kinetic models have played a crucial role. In free fatty acids esterification, both reactants are adsorbed on a surface-active site of the solid catalyst, assuming the surface reaction is a rate-limiting

step of esterification. Previously, many researchers have explained the heterogeneous kinetic models based on Langmuir Hinshelwood, Eley-Rideal, and Pseudohomogenous mechanisms. Fukumura et al. [68] reported Eley-Rideal type catalytic reaction model is best fitted for continuous monoacetin synthesis in an expanded-bed column reactor packed with proton type cation exchange resin Amberlyst 16 catalyst by neglecting the intra and extraparticle mass transfer hindrances [86]. Chaemchuen et al. [69] found the Eley Rideal and Langmuir Hinshelwood models in their methyl oleate esterification. Ketzer [70] obtained that the esterification results were best fitted with the Pseudo-homogenous model among the other models for esterification kinetics in methyl acetate synthesis in packed bed reactor operation. Abdullah et al. [71] established multiple kinetic models viz. simple power-law model, and mechanism-based models namely nucleophilic substitution, Langmuir-Hinshelwood, and Eley-Rideal kinetic models for the esterification of GL with lauric acid. Among them, nucleophilic substitution and Langmuir Hinshelwood kinetic models were found to be best fitted showing high accuracy. Moreover, the activation energy of the reaction was 35.62 kJ/mol.

2.7 Reaction Rate Intensification using Various Reactor Configurations

In recent years, from the economic and environmental viewpoint, GL valorization through various oxidation, esterification, and transesterification can be executed in continuous flow reactors for developing futuristic applications via sustainable processes in green chemistry and engineering, especially for a possible industrial scale-up. Nowadays, the continuous production process has become a more effective system in easing the barrier to batch reactors for the development of fine chemicals. Generally, the continuous flow reactor has proved to be a fascinating system to produce biodiesel [72]. Very few research work is composed of the results published

in the field of esterification, transesterification, and oxidation of GL using continuous flow reactor configurations. Vitiello et al. [73] reported a styrene-divinylbenzene acid resin (sPSB-SA) has been performed in the esterification of OA with GL in a steel batch reactor and a packed bed rotating loop reactor. Due to the high recirculation flows, the fluid-solid mass transfer resistance was limited, allowing the reaction to proceed in a kinetic regime. Moreover, to avoid the blockage of the catalyst loaded in the tubular reactor volume, the recycle loop was considered. To achieve the high OA conversion of 21%, the optimum reaction conditions for the esterification were GL: OA mole ratio = 1:3, 180 °C temperature and 180 min of reaction time, and catalyst 1 wt % vs. acid content. The heterogenous sulfonic acid (non-reticulated resin) demonstrated high stability up to 10 reaction cycles compared to homogeneous sulfuric acid at high temperature (180 °C) and good resistance to deactivation. Further, the viscosity test showed good lubricant base oil properties. To valorize GL with acetic acid in the presence of Amberlyst 36 resin catalyst, the exergetic performance of a continuous reactor has evolved. From the exergetic point of view exergy analysis has successfully recognized with exergetic productivity index and functional exergetic efficiency were found to be 0.42 and 25.38%, respectively under the optimum operating parameters viz., mole ratio of acetic acid to GL (3:1), reaction temperature (80 °C), pressure (41 bar) [74]. Nevertheless, the use of ion exchange resin catalysts in a continuous flow reactor suffers from a high swelling ratio, which causes plugging or a very high-pressure drop in the reactor. Alvarez et al. [75] obtained GC using α-Al_2O_3 supported MgAl hydrotalcite catalyst and DMSO solvent in a continuous flow reactor. Moreover, the stronger Brønsted basic sites showed better performance with the favor of complete conversion of GL. Although after 8 h on stream, a small deactivation occurred with the drop of GL conversion i.e., 88% and 20% drop of glycerol decarbonate product, 90% selectivity of GC could be reached at about 80%

conversion with good stability as a function of time. The fine size of the powder material might cause small voidage in the reactor bed due to direct packing of catalyst, which resulted in insufficient mixing of the reactants. Table 2.4 illustrates the continuous production of various valuable chemicals. Being esterification is a reversible reaction, water is produced as by-product. The presence of water generally limits the conversion/selectivity of ester formation. The conversion rate of esterification can be favored by the adsorption of water produced during the reaction. It was found that by addition of molecular sieves adsorbent in the reaction can efficiently remove the water formed in the esterification. By now, a lot of literature has been found where the effect of the addition of molecular sieves that have enhanced the yield in the esterification has been reported [72].

Table 2.4. Catalysts used for GL valorization in continuous flow reactor system.

Product	Process	Reactant	Catalyst	Heating type	Reaction condition	Salient outcome	Ref.
GC	Continuous flow reactor	GL with urea	Mg-Al mixed oxide, Brønsted-type basicity	CH	10 mbar, 423 K, 1 h on stream, GL/urea=1, LHSV=12 h^{-1}, γ-butyrolactone as solvent	65% GC yield in a continuous flow, 20% active decay, 100 h on stream	[76]
Acetin	Continuous flow reactor	GL with acetic acid	Without catalyst	Electrical heating	117 °C, feed flow rate of 0.6 mL min^{-1}, acetic acid/ GL= 1.1, 1 bar	normalized exergy destruction = 3.1, universal exergetic efficiency = 37.5%, and functional exergetic efficiency = 20.8%,	[77]
Monoacetin	Continuous flow reactor	GL with acetic acid	Water behaved as a catalyst,	CH	Reversible reaction, 3% water present, 100 °C, acetic acid/ GL= 1, feed flow rate of 0.6 mL min^{-1}, and 1 bar	53% GL conversion, 93% monoacetine selectivity, surface area=710 m^2 g^{-1}	[78]
Triacetin	Continuous	GL with acetic acid	Amberlyst 36	CH	100 °C, acetic acid/	80% selectivity,	[79]

	flow reactor, entrainer-based azeotropic distillation				GL= 7, 1 bar, and feed flow rate of 0.5 mL min^{-1} over 3g Amberlyst 36	100% conversion	
GL carbonate	Fixed bed continuous reactor	DMC with GL	$LaFeO_3$	CH	DMC/GL=4:1, 240 °C,	71% yield, 100% selectivity, 100 h on stream stability, basicity=1.41 mmol g^{-1}	[80]
Glycidol	packed-bed continuous flow reactor	GL, gas phase reaction	20 wt.% Cs–ZSM-5 zeolite (1500)	CH	1atm, 10 wt% GL, 350 °C, carrier gas N_2 (20 mL min^{-1}), 3 h on stream	$GHSV_{total}$ = 1 250 h^{-1}, 27 h time-on-stream, 40.4% yield, 86.3% GL conversion, basicity=17.3 $\mu mol_{CO2}/g_{catalyst}$	[81]
H_2	fixed-bed reactor	GL with water	Ni–Mg–Al	CH	1 atm, 650 °C, 1.0 g catalyst supported by quartz wool, nitrogen flow of 3×10^{-3} m^3 min^{-1}, L/dp > 100; Pe > 55	Surface area=126.777 m^2 g^{-1}, selectivity 78.5%, 88% conversion	[82]
Formic acid	Batch and continuous flow fixed bed reactor on pilot plant	GL:H_2O_2	Al modified Si	CH	GL/H_2O_2=1:1, 300 mg of catalyst and 9 mL silicon carbide (100 mesh), flow rate 1.0 mL min^{-1}, 150 °C, 7 h	GL conversion=80%, formic acid selectivity= 65%, surface area=698 m^2 g^{-1}	[83]
H_2	fixed-bed reactor	GL with water	spinel NiO/$NiAl_2O_4$ and CaO-based sorbent	CH	550 °C,	H_2 gas composition 98%, Surface area=56.6 m^2 g^{-1}	[84]
Glycerol dioleate	continuous flow packed-bed millireactor	GL with OA	*Candida antartica* l ipase	CH	2×10^{-5} mL min^{-1} flow rate, 45 °C, 0.15 g of lipase, 77 min of residence time, OA/GL=1.6:1	OA conversion 85%, glycerol dioleate selectivity 74%, 9 successive reaction cycles	[85]

2.8 Life Cycle Assessment

Bories et al. [86] developed GC and its use in clay formulations. They have investigated the impacts of the formulation through LCA using ReCiPe v1.10 method. The advantage of incorporation of GC in clay brick matrix confirmed 15-20% reduction in 17 midpoint environmental impacts and on 3 damage categories. Reyes et al. [87] found in the production of 1 MJ of H_2 through GL electrochemical reforming using a solar PV system coupled to the electrochemical process, the GWP impact, i.e., carbon footprint would be reduced by around 92.1% (0.0151 kg CO_2 eq/MJ H_2) in comparison with the fossil fuel energy and on damage categories viz., 22.61% on human health, 8% on ecosystem, and 39.39% on resources were improved. Moreover, in the green energy production low-cost anode material (7.5 USD$/kg H_2) was used.

References

[1] P.S. Kong, P. Cognet, Y. Pérès, J. Esvan, W.M.A.W. Daud, M.K. Aroua, Development of a novel hydrophobic ZrO_2–SiO_2 based acid catalyst for catalytic esterification of glycerol with oleic acid, Industrial & Engineering Chemistry Research 57(29) (2018) 9386-9399.

[2] J. Keogh, C. Jeffrey, M.S. Tiwari, H. Manyar, Kinetic Analysis of Glycerol Esterification Using Tin Exchanged Tungstophosphoric Acid on K-10, Industrial & Engineering Chemistry Research (2022).

[3] P.S. Reddy, P. Sudarsanam, G. Raju, B.M. Reddy, Synthesis of bio-additives: Acetylation of glycerol over zirconia-based solid acid catalysts, Catalysis Communications 11(15) (2010) 1224-1228.

[4] S. Zhu, Y. Zhu, X. Gao, T. Mo, Y. Zhu, Y. Li, Production of bioadditives from glycerol esterification over zirconia supported heteropolyacids, Bioresource Technology 130 (2013) 45-51.

[5] B.M. Kurji, A.S. Abbas, MCM-48 from rice husk ash as a novel heterogeneous catalyst for esterification of glycerol with oleic acid: Catalyst preparation, characterization, and activity, Case Studies in Chemical and Environmental Engineering (2023) 100382.

[6] M.A. Maquirriain, L. Tonutti, C. Querini, B. Dalla Costa, M.L. Pisarello, Glycerine esterification with free fatty acids using SBA-15 functionalized catalysts: Effect of hydrophobicity, Applied Catalysis A: General 650 (2023) 119014.

[7] M.H.M. Yusoff, A.Z. Abdullah, Catalytic behavior of sulfated zirconia supported on SBA-15 as catalyst in selective glycerol esterification with palmitic acid to monopalmitin, Journal of the Taiwan Institute of Chemical Engineers 60 (2016) 199-204.

[8] M. Popova, H. Lazarova, Y. Kalvachev, T. Todorova, A. Szegedi, P. Shestakova, G. Mali, V.D. Dasireddy, B. Likozar, Zr-modified hierarchical mordenite as heterogeneous catalyst for glycerol esterification, Catalysis Communications 100 (2017) 10-14.

[9] Z. Zhang, H. Huang, X. Ma, G. Li, Y. Wang, G. Sun, Y. Teng, R. Yan, N. Zhang, A. Li, Production of diacylglycerols by esterification of oleic acid with glycerol catalyzed by diatomite loaded SO_4^{2-}/TiO_2, Journal of Industrial and Engineering Chemistry 53 (2017) 307-316.

[10] D. Singh, P. Patidar, A. Ganesh, S. Mahajani, Esterification of oleic acid with glycerol in the presence of supported zinc oxide as catalyst, Industrial & Engineering Chemistry Research 52(42) (2013) 14776-14786.

[11] Q. Zhang, C. Zhang, Q. Wu, J. Liu, D. Song, Y. Guo, Sustainable production of biodiesel and transformation of glycerol to glycerol laurate esters over inner diameter-controlled sulfonic acid functionalized ethyl-bridged-organosilica nanotubes, Applied Catalysis A: General 611 (2021) 117973.

[12] Y. Sun, J. Hu, S. An, Q. Zhang, Y. Guo, D. Song, Q. Shang, Selective esterification of glycerol with acetic acid or lauric acid over rod-like carbon-based sulfonic acid functionalized ionic liquids, Fuel 207 (2017) 136-145.

[13] X. Han, G. Zhu, Y. Ding, Y. Miao, K. Wang, H. Zhang, Y. Wang, S.-B. Liu, Selective catalytic synthesis of glycerol monolaurate over silica gel-based sulfonic acid functionalized ionic liquid catalysts, Chemical Engineering Journal 359 (2019) 733-745.

[14] A.B. Neto, A.C. Oliveira, E. Rodriguez-Castellón, A.F. Campos, P.T. Freire, F.F. Sousa, M. Josué Filho, J.C. Araujo, R. Lang, A comparative study on porous solid acid oxides as catalysts in the esterification of glycerol with acetic acid, Catalysis Today 349 (2020) 57-67.

[15] A.F. Uchenna, R. Irmawati, Y.H. Taufiq-Yap, S.M. Izham, U.I. Nda-Umar, Glycerol acetylation over yttrium oxide (Y_2O_3) catalyst supported on palm kernel shell-derived carbon and parameters optimization studies using response surface methodology (RSM), Arabian Journal of Chemistry 16(8) (2023) 104865.

[16] M. Balaraju, P. Nikhitha, K. Jagadeeswaraiah, K. Srilatha, P.S. Prasad, N. Lingaiah, Acetylation of glycerol to synthesize bioadditives over niobic acid supported tungstophosphoric acid catalysts, Fuel Processing Technology 91(2) (2010) 249-253.

[17] J.N. Appaturi, R.J. Ramalingam, M. Selvaraj, S. Chia, S.H. Tan, F. Khoerunnisa, T.C. Ling, E.-P. Ng, Selective synthesis of triacetyl glyceride biofuel additive via acetylation of glycerol over NiO-supported TiO_2 catalyst enhanced by non-microwave instant heating, Applied Surface Science 545 (2021) 149017.

[18] S. Arora, V. Gosu, V. Subbaramaiah, B. Hameed, Lithium loaded coal fly ash as sustainable and effective catalyst for the synthesis of glycerol carbonate from glycerol, Journal of Environmental Chemical Engineering 9(5) (2021) 105999.

[19] B. Das, K. Mohanty, Exploring the promotional effects of K, Sr, and Mg on the catalytic stability of red mud for the synthesis of glycerol carbonate from renewable glycerol, Industrial & Engineering Chemistry Research 58(35) (2019) 15803-15817.

[20] G. Liu, J. Yang, X. Xu, Synthesis of hydrotalcite-type mixed oxide catalysts from waste steel slag for transesterification of glycerol and dimethyl carbonate, Scientific Reports 10(1) (2020) 10273.

[21] H. Nguyen-Phu, C.-y. Park, W.S. Eun, Activated red mud-supported Zn/Al oxide catalysts for catalytic conversion of glycerol to glycerol carbonate: FTIR analysis, Catalysis Communications 85 (2016) 52-56.

[22] B. Das, K. Mohanty, A green and facile production of catalysts from waste red mud for the one-pot synthesis of glycerol carbonate from glycerol, Journal of Environmental Chemical Engineering 7(1) (2019) 102888.

[23] C. Hu, M. Yoshida, H.-C. Chen, S. Tsunekawa, Y.-F. Lin, J.-H. Huang, Production of glycerol carbonate from carboxylation of glycerol with CO_2 using ZIF-67 as a catalyst, Chemical Engineering Science 235 (2021) 116451.

[24] H.T. Kwon, H.-K. Jeong, A.S. Lee, H.S. An, J.S. Lee, Heteroepitaxially grown zeolitic imidazolate framework membranes with unprecedented propylene/propane separation performances, Journal of the American Chemical Society 137(38) (2015) 12304-12311.

[25] X. Song, Y. Wu, F. Cai, D. Pan, G. Xiao, High-efficiency and low-cost Li/ZnO catalysts for synthesis of glycerol carbonate from glycerol transesterification: The role of Li and ZnO interaction, Applied Catalysis A: General 532 (2017) 77-85.

[26] Y. Algoufi, B. Hameed, Synthesis of glycerol carbonate by transesterification of glycerol with dimethyl carbonate over K-zeolite derived from coal fly ash, Fuel Processing Technology 126 (2014) 5-11.

[27] Y. Algoufi, U. Akpan, G. Kabir, M. Asif, B. Hameed, Upgrading of glycerol from biodiesel synthesis with dimethyl carbonate on reusable Sr–Al mixed oxide catalysts, Energy Conversion and Management 138 (2017) 183-189.

[28] S. Wang, J. Wang, P. Sun, L. Xu, P.U. Okoye, S. Li, L. Zhang, A. Guo, J. Zhang, A. Zhang, Disposable baby diapers waste derived catalyst for synthesizing glycerol carbonate by the transesterification of glycerol with dimethyl carbonate, Journal of Cleaner Production 211 (2019) 330-341.

[29] Z. Liu, J. Wang, M. Kang, N. Yin, X. Wang, Y. Tan, Y. Zhu, Structure-activity correlations of $LiNO_3/Mg_4AlO_{5.5}$ catalysts for glycerol carbonate synthesis from glycerol and dimethyl carbonate, Journal of Industrial and Engineering Chemistry 21 (2015) 394-399.

[30] S. Karnjanakom, P. Maneechakr, C. Samart, G. Guan, Ultrasound-assisted acetylation of glycerol for triacetin production over green catalyst: A liquid biofuel candidate, Energy Conversion and Management 173 (2018) 262-270.

[31] A.A.F. da Costas, A.d.N. de Oliveira, R. Esposito, A. Auvigne, C. Len, R. Luque, R.C.R. Noronha, L.A.S. do Nascimento, Glycerol and microwave-assisted catalysis: recent progresses in batch and flow devices, Sustainable Energy & Fuels (2023).

[32] P. San Kong, M.K. Aroua, W.M.A.W. Daud, P. Cognet, Y. Pérès, Enhanced microwave catalytic-esterification of industrial grade glycerol over Brønsted-based methane sulfonic acid in production of biolubricant, Process Safety and Environmental Protection 104 (2016) 323-333.

[33] R. Luque, V. Budarin, J.H. Clark, D.J. Macquarrie, Glycerol transformations

on polysaccharide derived mesoporous materials, Applied Catalysis B: Environmental 82(3-4) (2008) 157-162.

[34] B. Changmai, I.B. Laskar, S.L. Rokhum, Microwave-assisted synthesis of glycerol carbonate by the transesterification of glycerol with dimethyl carbonate using Musa acuminata peel ash catalyst, Journal of the Taiwan Institute of Chemical Engineers 102 (2019) 276-282.

[35] A. Das, D. Shi, G. Halder, S.L. Rokhum, Microwave-assisted synthesis of glycerol carbonate by transesterification of glycerol using Mangifera indica peel calcined ash as catalyst, Fuel 330 (2022) 125511.

[36] R. Chakraborty, P. Mukhopadhyay, B. Kumar, Optimal biodiesel-additive synthesis under infrared excitation using pork bone supported-Sb catalyst: Engine performance and emission analyses, Energy Conversion and Management 126 (2016) 32-41.

[37] P. Mukhopadhyay, R. Chakraborty, Infrared radiation promoted preparation of cost-effective lamb bone supported cobalt catalyst: Efficacy in semi-batch monoolein synthesis, Catalysis Communications 94 (2017) 73-76.

[38] S. Carrettin, P. McMorn, P. Johnston, K. Griffin, C.J. Kiely, G.J. Hutchings, Oxidation of glycerol using supported Pt, Pd and Au catalysts, Physical Chemistry Chemical Physics 5(6) (2003) 1329-1336.

[39] B. Katryniok, H. Kimura, E. Skrzyńska, J.-S. Girardon, P. Fongarland, M. Capron, R. Ducoulombier, N. Mimura, S. Paul, F. Dumeignil, Selective catalytic oxidation of glycerol: perspectives for high value chemicals, Green Chemistry 13(8) (2011) 1960-1979.

[40] N. Tuleushova, Y. Holade, D. Cornu, S. Tingry, Glycerol electro-reforming in alkaline electrolysis cells for the simultaneous production of value-added chemicals and pure hydrogen–Mini-review, Electrochemical Science Advances (2022) e2100174.

[41] D. Liang, J. Gao, J. Wang, P. Chen, Y. Wei, Z. Hou, Bimetallic Pt—Cu catalysts for glycerol oxidation with oxygen in a base-free aqueous solution, Catalysis Communications 12(12) (2011) 1059-1062.

[42] J. Dou, B. Zhang, H. Liu, J. Hong, S. Yin, Y. Huang, R. Xu, Carbon supported Pt9Sn1 nanoparticles as an efficient nanocatalyst for glycerol oxidation, Applied Catalysis B: Environmental 180 (2016) 78-85.

[43] Y. Shen, S. Zhang, H. Li, Y. Ren, H. Liu, Efficient synthesis of lactic acid by

aerobic oxidation of glycerol on Au–Pt/TiO_2 catalysts, Chemistry–A European Journal 16(25) (2010) 7368-7371.

[44] X. Ning, Y. Li, H. Yu, F. Peng, H. Wang, Y. Yang, Promoting role of bismuth and antimony on Pt catalysts for the selective oxidation of glycerol to dihydroxyacetone, Journal of Catalysis 335 (2016) 95-104.

[45] A. Marshall, R. Haverkamp, Production of hydrogen by the electrochemical reforming of glycerol–water solutions in a PEM electrolysis cell, International Journal of Hydrogen Energy 33(17) (2008) 4649-4654.

[46] M.S. Ahmad, M.H. Ab Rahim, T.M. Alqahtani, T. Witoon, J.-W. Lim, C.K. Cheng, A review on advances in green treatment of glycerol waste with a focus on electro-oxidation pathway, Chemosphere 276 (2021) 130128.

[47] L. Fan, B. Liu, X. Liu, N. Senthilkumar, G. Wang, Z. Wen, Recent progress in electrocatalytic glycerol oxidation, Energy Technology 9(2) (2021) 2000804.

[48] T. Li, D.A. Harrington, An overview of glycerol electrooxidation mechanisms on Pt, Pd and Au, ChemSusChem 14(6) (2021) 1472-1495.

[49] P.J. Kulesza, I.S. Pieta, I.A. Rutkowska, A. Wadas, D. Marks, K. Klak, L. Stobinski, J.A. Cox, Electrocatalytic oxidation of small organic molecules in acid medium: Enhancement of activity of noble metal nanoparticles and their alloys by supporting or modifying them with metal oxides, Electrochimica acta 110 (2013) 474-483.

[50] M.S. Houache, K. Hughes, R. Safari, G.A. Botton, E.A. Baranova, Modification of nickel surfaces by bismuth: Effect on electrochemical activity and selectivity toward glycerol, ACS Applied Materials & Interfaces 12(13) (2020) 15095-15107.

[51] L. Shabnam, S.N. Faisal, A.K. Roy, V.G. Gomes, Nickel-Nanoparticles on Doped Graphene: A Highly Active Electrocatalyst for Alcohol and Carbohydrate Electrooxidation for Energy Production, ChemElectroChem 5(23) (2018) 3799-3808.

[52] H. Xu, B. Yan, K. Zhang, J. Wang, S. Li, C. Wang, Y. Shiraishi, Y. Du, P. Yang, Ultrasonic-assisted synthesis of N-doped graphene-supported binary PdAu nanoflowers for enhanced electro-oxidation of ethylene glycol and glycerol, Electrochimica Acta 245 (2017) 227-236.

[53] K. Rahmani, B. Habibi, Electrofabrication of the ternary NiCuFe alloy nanoparticles/ERGO nanocomposite: effective electrooxidation of the glucose

and glycerol in alkaline media, ChemistrySelect 5(26) (2020) 7990-8001.

[54] J. Zhang, T. Wang, P. Liu, Z. Liao, S. Liu, X. Zhuang, M. Chen, E. Zschech, X. Feng, Efficient hydrogen production on MoNi4 electrocatalysts with fast water dissociation kinetics, Nature Communications 8(1) (2017) 15437.

[55] M. Kaur, K. Pal, Review on hydrogen storage materials and methods from an electrochemical viewpoint, Journal of Energy Storage 23 (2019) 234-249.

[56] B. You, X. Liu, N. Jiang, Y. Sun, A general strategy for decoupled hydrogen production from water splitting by integrating oxidative biomass valorization, Journal of the American Chemical society 138(41) (2016) 13639-13646.

[57] Y. Li, X. Wei, L. Chen, J. Shi, M. He, Nickel-molybdenum nitride nanoplate electrocatalysts for concurrent electrolytic hydrogen and formate productions, Nature Communications 10(1) (2019) 5335.

[58] X. Liu, Z. Fang, X. Teng, Y. Niu, S. Gong, W. Chen, T.J. Meyer, Z. Chen, Paired formate and H_2 productions via efficient bifunctional Ni-Mo nitride nanowire electrocatalysts, Journal of Energy Chemistry 72 (2022) 432-441.

[59] V. Tripathi, S. Jain, D. Kabra, L.S. Panchakarla, A. Dutta, Cobalt-doped copper vanadate: a dual active electrocatalyst propelling efficient H 2 evolution and glycerol oxidation in alkaline water, Nanoscale Advances 5(1) (2023) 237-246.

[60] Y. Li, X. Wei, S. Han, L. Chen, J. Shi, MnO_2 Electrocatalysts Coordinating Alcohol Oxidation for Ultra-Durable Hydrogen and Chemical Productions in Acidic Solutions, Angewandte Chemie 133(39) (2021) 21634-21642.

[61] L. Fan, Y. Ji, G. Wang, Z. Zhang, L. Yi, K. Chen, X. Liu, Z. Wen, Bifunctional Mn-doped $CoSe_2$ nanonetworks electrode for hybrid alkali/acid electrolytic H2 generation and glycerol upgrading, Journal of Energy Chemistry 72 (2022) 424-431.

[62] H. Yu, W. Wang, Q. Mao, K. Deng, Z. Wang, Y. Xu, X. Li, H. Wang, L. Wang, Pt single atom captured by oxygen vacancy-rich NiCo layered double hydroxides for coupling hydrogen evolution with selective oxidation of glycerol to formate, Applied Catalysis B: Environmental 330 (2023) 122617.

[63] D. Wu, J. Hao, W. Wang, Y. Yu, X.Z. Fu, J.L. Luo, Energy-saving H2 Generation Coupled with Oxidative Alcohol Refining over Bimetallic Phosphide Ni2P− CoP Junction Bifunctional Electrocatalysts, ChemSusChem 14(24) (2021) 5450-5459.

[64] Z. Ke, N. Williams, X. Yan, S. Younan, D. He, X. Song, X. Pan, X. Xiao, J. Gu, Solar-assisted co-electrolysis of glycerol and water for concurrent production of formic acid and hydrogen, Journal of Materials Chemistry A 9(35) (2021) 19975-19983.

[65] Q. Wang, X. Ma, P. Wu, B. Li, L. Zhang, J. Shi, CoNiFe-LDHs decorated Ta_3N_5 nanotube array photoanode for remarkably enhanced photoelectrochemical glycerol conversion coupled with hydrogen generation, Nano Energy 89 (2021) 106326.

[66] D.K. Bora, M. Nadjafi, A. Armutlulu, D. Hosseini, P. Castro-Fernández, R. Toth, Photoelectrochemical glycerol oxidation on Mo-$BiVO_4$ photoanodes shows high photocharging current density and enhanced H_2 evolution, Energy Advances 1(10) (2022) 715-728.

[67] Y. Han, M. Chang, Z. Zhao, F. Niu, Z. Zhang, Z. Sun, L. Zhang, K. Hu, Selective Valorization of Glycerol to Formic Acid on a $BiVO_4$ Photoanode through NiFe Phenolic Networks, ACS Applied Materials & Interfaces 15(9) (2023) 11678-11690.

[68] T. Fukumura, T. Toda, Y. Seki, M. Kubo, N. Shibasaki-Kitakawa, T. Yonemoto, Catalytic synthesis of glycerol monoacetate using a continuous expanded bed column reactor packed with cation-exchange resin, Industrial & Engineering Chemistry Research 48(4) (2009) 1816-1823.

[69] S. Chaemchuen, P.M. Heynderickx, F. Verpoort, Kinetic modeling of oleic acid esterification with UiO-66: from intrinsic experimental data to kinetics via elementary reaction steps, Chemical Engineering Journal 394 (2020) 124816.

[70] F. Ketzer, F. de Castilhos, An assessment on kinetic modeling of esterification reaction from oleic acid and methyl acetate over USY zeolite, Microporous and Mesoporous Materials 314 (2021) 110890.

[71] P. Hoo, A.Z. Abdullah, Kinetics modeling and mechanism study for selective esterification of glycerol with lauric acid using 12-tungstophosphoric acid post-impregnated SBA-15, Industrial & Engineering Chemistry Research 54(32) (2015) 7852-7858.

[72] J. Gupta, M. Agarwal, A. Dalai, An overview on the recent advancements of sustainable heterogeneous catalysts and prominent continuous reactor for biodiesel production, Journal of Industrial and Engineering Chemistry 88

(2020) 58-77.

[73] R. Vitiello, F. Taddeo, V. Russo, R. Turco, A. Buonerba, A. Grassi, M. Di Serio, R. Tesser, Production of sustainable biochemicals by means of esterification reaction and heterogeneous acid catalysts, ChemEngineering 5(3) (2021) 46.

[74] M. Aghbashlo, M. Tabatabaei, H. Rastegari, H.S. Ghaziaskar, Exergy-based sustainability analysis of acetins synthesis through continuous esterification of glycerol in acetic acid using Amberlyst® 36 as catalyst, Journal of Cleaner Production 183 (2018) 1265-1275.

[75] M.G. Álvarez, M. Plíšková, A.M. Segarra, F. Medina, F. Figueras, Synthesis of glycerol carbonates by transesterification of glycerol in a continuous system using supported hydrotalcites as catalysts, Applied Catalysis B: Environmental 113 (2012) 212-220.

[76] G.M. Lari, A.B. de Moura, L. Weimann, S. Mitchell, C. Mondelli, J. Pérez-Ramírez, Design of a technical Mg–Al mixed oxide catalyst for the continuous manufacture of glycerol carbonate, Journal of Materials Chemistry A 5(31) (2017) 16200-16211.

[77] M. Aghbashlo, M. Tabatabaei, H. Rastegari, H.S. Ghaziaskar, E. Valijanian, Exergy-based optimization of a continuous reactor applied to produce value-added chemicals from glycerol through esterification with acetic acid, Energy 150 (2018) 351-362.

[78] H. Rastegari, H.S. Ghaziaskar, From glycerol as the by-product of biodiesel production to value-added monoacetin by continuous and selective esterification in acetic acid, Journal of Industrial and Engineering Chemistry 21 (2015) 856-861.

[79] H. Rastegari, H.S. Ghaziaskar, M. Yalpani, A. Shafiei, Development of a continuous system based on azeotropic reactive distillation to enhance triacetin selectivity in glycerol esterification with acetic acid, Energy & Fuels 31(8) (2017) 8256-8262.

[80] P.P. Pattanaik, P.M. Kumar, N. Raju, N. Lingaiah, Continuous synthesis of glycerol carbonate by transesterification of glycerol with dimethyl carbonate over Fe–La mixed oxide catalysts, Catalysis Letters 151 (2021) 1433-1443.

[81] A. Kostyniuk, D. Bajec, P. Djinović, B. Likozar, One-step synthesis of glycidol from glycerol in a gas-phase packed-bed continuous flow reactor over HZSM-5 zeolite catalysts modified by $CsNO_3$, Chemical Engineering

Journal 394 (2020) 124945.

[82] C. Wang, B. Dou, H. Chen, Y. Song, Y. Xu, X. Du, T. Luo, C. Tan, Hydrogen production from steam reforming of glycerol by Ni–Mg–Al based catalysts in a fixed-bed reactor, Chemical Engineering Journal 220 (2013) 133-142.

[83] P. Chagas, C.C. Oliveira, A.A. Leitão, L.L. Lima, M.F. Portilho, L.C. Oliveira, Waste glycerol conversion on pilot scale continuous process by Al-modified mesoporous SiO_2 catalysts, Journal of Environmental Chemical Engineering 10(2) (2022) 107286.

[84] B. Dou, B. Jiang, Y. Song, C. Zhang, C. Wang, H. Chen, B. Du, Y. Xu, Enhanced hydrogen production by sorption-enhanced steam reforming from glycerol with in-situ CO2 removal in a fixed-bed reactor, Fuel 166 (2016) 340-346.

[85] N.N. Abd Razak, P. Cognet, Y. Pérès, L.T. Gew, M.K. Aroua, Kinetics and hydrodynamics of Candida antartica lipase-catalyzed synthesis of glycerol dioleate (GDO) in a continuous flow packed-bed millireactor, Journal of Cleaner Production 373 (2022) 133816.

[86] C. Bories, E. Vedrenne, A. Paulhe-Massol, G. Vilarem, C. Sablayrolles, Development of porous fired clay bricks with bio-based additives: Study of the environmental impacts by Life Cycle Assessment (LCA), Construction and Building Materials 125 (2016) 1142-1151.

[87] E. Peralta-Reyes, D. Vizarretea-Vasquez, R. Natividad, A. Aizpuru, E. Robles-Gomez, C. Alanis, A. Regalado-Mendez, Electrochemical reforming of glycerol into hydrogen in a batch-stirred electrochemical tank reactor equipped with stainless steel electrodes: Parametric optimization, total operating cost, and life cycle assessment, Journal of Environmental Chemical Engineering 10(4) (2022) 108108.

CHAPTER 3

Research Gap

Bio-GL is the major by-product of the biodiesel industry and its excess amount creates disposal challenges for the chemical industry. The GL disposal challenge has affected the commercialization of biodiesel production. Thus, the conversion of wastes into high-value-added chemicals is small compared to the volume generated through fuel but its utilization nonetheless is highly desirable for sustainability.

3.1 Selection of Operating Parameters

Preceding literature revealed the conversion of GL to value-added products considering monostearin, glyceryl monocaprin, GC, GC by-product methanol to methyl oleate, glyceric acid and their application in various sectors. However, most of the previous work pertinent to the aforementioned products portrayed the requirement of high reaction temperature, high pressure, and long reaction time coupled with lower yield/selectivity of the product, *difficulties in the purification of desired products as synthesized through the homogeneous catalytic process*. These factors make the process economically unattractive. Therefore, intensification of the reaction process is an utmost necessity not only to reduce the reaction time and the reaction temperature to get higher yield but also to minimize the energy consumption and overall production cost.

3.2 Catalytic Reactor Configuration

Catalytic reactors are playing a vital role in chemical process industries, especially by advancing chemical conversions in an environmentally and economically sustainable pathway. However, scientific investigations exposed that CH reactor configurations still fall short of meeting industry demands for optimal performance, stability, and energy consumption. To overcome these bottlenecks, an advanced design paradigm is necessary to achieve advanced reactors (integration of the reactor with additional

facilities/alternative energy sources/mode of operation) that play a crucial role in overcoming the heat and mass transfer resistances in heterogeneously catalyzed systems for the maximization of valuable products at augmented reaction rate.

3.3 Cost-Intensive Catalyst Supports

Progress in the aspect of GL valorization in GC and GL oxidized products has been limited by several challenging issues including catalyst and catalyst support selection. The catalyst support is essential, enabling large contact surface area, porosity, anticorrosive, heat and mass transfer rate, kinetic parameters like activation energy, and kinetic rate constant. Previous studies illustrated the kinetics of GL conversion to GC remains a challenge due to its separation and recycling challenges coupled with the complexities of corrosion in the reactor, thermodynamic stability makes the process less appealing. Moreover, the large-scale practical commercialization of electrocatalysts in GL oxidation has been limited by several challenging issues such as high anode overpotential, excessive fuel and water permeability of the polymer electrolyte membrane, and questionable long-term durability of the fuel cells. The issue of high overpotential for anode catalysts is associated with the formation of poisons on the catalyst surface and also with a large amount of catalyst loading. In contrast, the use of waste-derived support could be commendable in the interest of green synthesis. Hence, the utilization of waste for sustainable catalyst processing should be cost-effective, stable over time, facilitate reactions at low temperatures and pressures, have less duration of reaction time, to the desired selectivity of product, and inhibit the formation of undesired by-products.

Thus, to attenuate the rising concerns about environmental and economic sustainability and to address the research gaps identified in Chapter 3, the aims and

objectives of the present work have been decided accordingly and discussed in the next chapter (Chapter 4). Furthermore, to overcome the bottlenecks such as the reaction rate should be enhanced using suitable energy-efficient intensified reactor operation. Additionally, the continuous synthesis of these products should be investigated in an attempt to reduce residence time requirements for improving production capacity. Researchers often need to simulate and predict the performance of the reactor system before the practical application and operation on a large scale to obtain optimal and environmentally sustainable operating conditions. In view of the circular economy, an environmental impact assessment should be a desirable tool to prevent or lower the environmental burden to safeguard human health and mitigate global warming toward a cleaner world.

CHAPTER 4

Aims & Objectives

The proposed research deals with intensifying and optimizing bio-GL conversion into value-added products using an electromagnetically irradiated reactor through novel protocols.

4.1 Biodiesel-Derived Bio-GL Utilization

4.1.1 Esterification using GL with Fatty Acids

In the present work, utilization of surplus bio-GL for the preparation of monostearin and glyceryl monocaprin with their application in energy storage material, and food additive have been investigated through esterification. Moreover, esters have been prepared using fatty acids viz. stearic acid, and capric acid for the preparation of esters.

4.1.2 Transesterification using GL with DMC

Transesterification has been done employing DMC to produce GC. Besides, in the formation of GC huge amount of methanol has been produced as a by-product.

4.1.3 Biodiesel-Derived Bio-GL Utilization and Production of Fuel Additive from By-Product Monohydric Alcohol-Based Product Synthesis

In the transesterification of GL with DMC, methanol has been produced as a by-product along with the product GC. This by-product methanol has been employed in the esterification of oleic acid to prepare methyl oleate.

4.1.4 GL Electrolysis

To valorize GL electrochemically, GL electrolysis has been obtained for the simultaneous production of glyceric acid with hydrogen evolution at the anode and cathode, respectively.

Activities Involved:

- Production of thermal-storage or phase change material possesses promising solid-liquid phase change characteristics and portrays non-corrosive nature.
- Exhibited good food preservation properties when compared to pure substance.
- Production of an efficient electrolyte for energy storage device.

4.2 Mode of Reactor Operation

Employment of various reactor configurations to achieve higher selectivity of the desired products.

- Studying the superiority of the rotating batch reactor over the conventional stirred batch reactor under far infrared radiation.
- Studying the synergistic effect of electromagnetic energy and ultrasonication-assisted rotating reactor over the individual one.
- Studying the superiority of solar-simulated quartz halogen lamp radiated batch reactor in comparison with the thermally heated stirred batch reactor.
- Intensification of the autocatalytic esterification using a continuous flow rotating reactor under recycle mode employing highly efficient hybrid electromagnetic radiation (near-infrared and microwave irradiation).
- Studying the electrooxidation and H_2 evolution in electrochemical cells.

4.3 Minimization of Energy Consumption

Activities involved

- Successful implementation of electromagnetic energy sources (far, near-infrared and microwave, quartz halogen radiation) along with ultrasonic energy to intensify the reaction process by enhancing the reaction rate, and reducing the reaction temperature, reaction time, catalyst concentration, and feedstock requirements.
- Minimizing the energy consumption toward sustainable green process

4.4 Preparation of Cost-Effective Green Heterogeneous Catalyst

Employment of cost-effective solid acid/basic catalyst support derived from e-waste and sea waste

Activities Involved:

- E-waste and cartesian sea waste are the resources for the synthesis of catalyst support that emphasizes the waste-to-wealth concept.
- Solid acid/basic catalysts are prepared via the wet impregnation method.
- Bimetallic catalysts with various compositions of precursors

4.5 Catalytic Activity in Various Reactions

Activities Involved

- Commercial ion exchange resin catalyst has been employed to estimate the higher monoester yield in comparison with no catalyst.
- Comparative study of bulk ion exchange Brønsted acid catalyst and combination of photoactive Lewis and Brønsted acid catalyst in esterification

to establish the plausible improvement on the incorporation of photocatalytic metal in the geometry of the catalyst.

- Waste-derived inexpensive support material-based photo and electrocatalyst synthesis and compared with the commercially available support to verify the superiority of the counterpart.
- Validating the strength of the catalytic, after several consecutive reaction cycles.
- Characterization of the spent catalyst to evaluate the insignificant changes in the spent catalyst compared to the fresh catalyst.

4.6 Design of Experiment

Statistical design of experiments involves analysis of experiments considering several process factors with the smallest number of experiments for assessing parametric effects on process response and optimization of process conditions. Taguchi orthogonal array lies in the fact of a much lower number of experimental runs whereas, response surface methodology encompasses several process factors at a time. These optimization tools reveal the interactive effects among the process factors in governing the process response referred to as maximization of preferred product yield/selectivity.

4.7 Optimal Operating Parameters or Factors

Effects of various operating parameters such as reactant mole ratio, catalyst concentration, temperature, reaction time (residence time), molecular sieves concentration (in-situ water removal) conventional heating, and electromagnetic radiation have been wisely analyzed since these factors intensely influence the

selectivity/yield of the desired product. The selection of a non-conventional energy source aided lower reaction time and temperature with atmospheric pressure concerning the maximization of yield/selectivity of product, leading to less energy consumption as well as low cost vis-à-vis conforming ecological sustainability.

4.8 Reaction Kinetic Study

To interpret plausible reaction pathways for heterogeneous esterification reactions and to evaluate kinetic parameters, Langmuir-Hinshelwood, Eley Rideal, and pseudo-homogeneous kinetic models were fitted with the experimental fatty acid conversion data collected at specific time intervals for finding the best representative kinetic model.

4.9 Evaluation of Environmental and Economical Sustainability

LCA and LCC consider the cradle-to-gate study. LCA consists of four stages i.e., goal and scope definition, life cycle inventory, life cycle impact assessment, and interpretation. LCC was chosen as an indicator to determine economic performance.

Activities Involved:

- LCA analyzes the environmental and economic aspects related to the end-of-life disposal of e-waste with the recovery of both silica and alumina from e-waste (WPCB) for MATLS$_W$ photocatalyst preparation towards sustainable GC production for application as an electrolyte for ESD (energy storage device).
- Comparative environmental impact assessments for the GC synthesis process: in thermally heated stirred batch reactor and solar simulated quartz halogen lamp radiated batch reactor using as-synthesized (MATLS$_W$-5) and commercial support based (MATLS$_C$-5) catalyst + MATLS$_W$-5 and MATLS$_C$-5 catalyst preparation under SSQHLBR + ‘cradle to gate’

worldwide scenario, + total GWP incorporating the involvement of product, raw materials, catalyst, reactor, electricity, transport.

- LCA of recovery of waste + catalyst support preparation + catalyst preparation + waste-pork lard-derived GL electrolysis and compared with the commercial GL electrolysis
- Estimation of the raw material cost, operating cost, revenue, added value of the waste-pork lard-derived GL, and commercial GL electrolysis.

4.10 Scale-Up Study

Process simulators have been proven to be successful in modeling, simulating, and optimizing various industrial processes.

Activity Involved:

- A geometric-based COMSOL model was simulated which confirmed uniformity of hybrid irradiation and temperature distribution within the rotating catalytic packed bed; which was applied for the development of a parallel-autocatalytic reaction kinetic model.
- For larger-scale production of the methyl oleate, the ASPEN PLUS simulator has been deployed for a throughput scale-up factor of 1000 (geometric similarity), which corroborates well with lab-scale yield/reactor performance.

CHAPTER 5

Experimental

5.1 ACTIVITY I

Intensification of MSN (phase change material) synthesis in IR rotating reactor: Optimization and heterogeneous kinetics

Preceding literature revealed the applications of solid acid catalysts viz., Amberlyst-type ion-exchange resin catalysts for heterogeneous esterification. The rotating reactor has been applied previously for fatty acid conversion purposes; wherein instead of using a mechanical impeller, rotating action has been employed to overcome the mass transfer resistance in heterogeneously catalyzed reaction. In the present study, electromagnetic radiation viz., far infrared radiation (FIRR) has been applied for intensification of catalytic esterification of GL with SA for the maximization of MSN yield for application as phase change material. A rotating reactor under FIRR has been employed to compare MSN yield with that obtainable using a reactor fitted with a mechanical impeller under optimal conditions, which have been determined through TED of the variables (viz. mole ratio, time, catalyst concentration and rotating speed). Besides, it reveals the interactive effects among the process parameters in governing the process response. Amberlyst 36 catalyzed heterogeneous esterification kinetics has been evaluated under both mass transfer and surface reaction-controlled regimes. Esterification activation energies under both reactor configurations have been calculated to evaluate the advantage of rotating action over conventional stirring under FIRR.

5.1.1 Materials

AR grade chemicals viz. GL (99.5%), SA (Loba India 99%), KOH (pellets), oxalic acid, toluene and isopropanol (MERCK) were purchased. Amberlyst-36 (wet) catalyst was procured from Sigma Aldrich while molecular sieves were supplied by SRL (India). The physical and chemical properties of the catalyst are tabulated in Table

5.1.a

Table 5.1.a. Physical and chemical properties of Amberlyst 36 (wet) [1]

Categories	Properties
Physical form	Spherical beads
Moisture Content	51-57% (H^+ content)
Acidity	≥ 5.45 eq/kg
Surface Area	33 m^2/g
Average Pore Diameter	24 nm
Pore Volume	0.20 cc/g
Particle Porosity	25-50µm
Particle Size	0.660-0.843 mm
Maximum Operating Temperature	423 K

5.1.2. Experimental Procedure and Design of Experiment

GL-SA esterification was carried out in both far IR rotating batch reactor (FIRR-RBR) and far IR stirred batch reactor (FIRR-SBR). The SBR was equipped with a turbine-type mechanical stirrer (material of construction: 318 stainless steel) comprising of six blades (each length: 14 mm and width: 2 mm) attached to a central shaft (length: 310 mm and diameter: 7 mm). Primarily, the reaction was performed in FIRR-RBR (150 W) which consisted of a one-necked flask with a condenser holding the specific amount of molecular sieves (30 wt.% of SA) for removal of water produced during the reaction. At first, GL was added to the FIRR-RBR; as the temperature attained the preset value (353–373 K), pre-heated SA along with Amberlyst-36 catalyst was added to the FIRR-RBR operated over the rotational speed range of 50–300 rpm. The GL to SA molar ratios were maintained at 20:1, 15:1, and 10:1. The efficacy of RBR was compared with SBR over a speed range from 50 to 300 rpm. Additionally, to evaluate the advantage of using the FIRR system, the optimal esterification run was also conducted in RBR equipped with a CH system (CH-RBR) of the same power input (150 W). The independent factors and their corresponding levels were examined in an L9 orthogonal array using standard TED

[2]. Accordingly, the experiments were conducted in triplicates using three levels of the selected four operating factors viz., GL to SA mole ratio ($\theta_{GL:SA}$), reaction temperature (θ_{RT}), reactor rotational speed (θ_{RPM}), and catalyst concentration (θ_C) in GL-SA esterification. A customized set of nine experimental runs were presented in Table 5.1 with corresponding yields and SN ratios. After each experimental run of specified duration (25 min), the reaction mix was collected and the upper layer containing ester and unreacted SA (with traces of GL) was separated from GL-catalyst containing lower-layer by centrifugation. Subsequently, the upper layer was cooled for separation of ester through crystallization (solidification). The ester so collected was used for GC–MS analyses for quantification of product components.

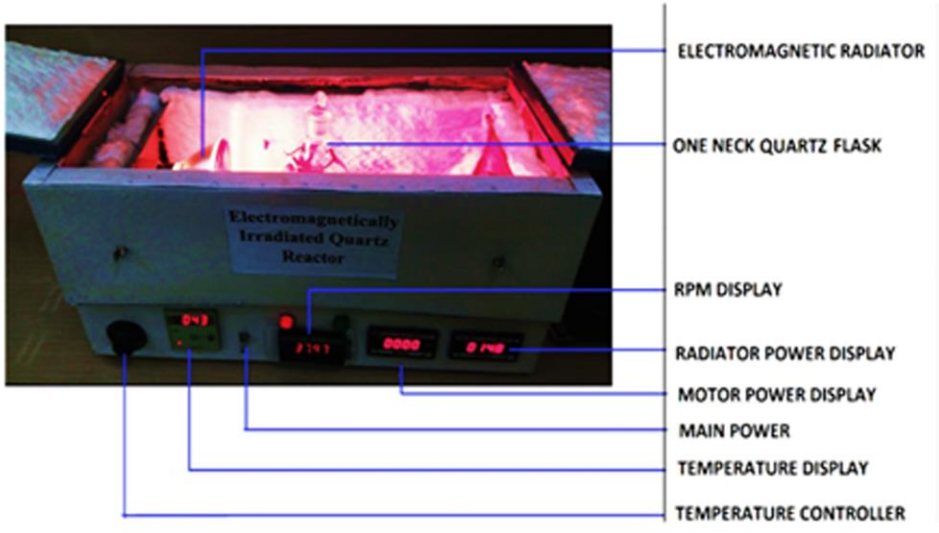

Figure 5.1. Experimental set up for monostearin synthesis

Acid number (A_{SA}) of ester layer and corresponding SA conversion (γ_{SA}) were calculated through direct titration method using Eqs. (5.1) and (5.2):

$$A_{SA} = \frac{56.11 \times M_{KOH} \times V_{KOH}}{m_{MSN}} \tag{5.1}$$

$$\gamma_{SA} = \left[\frac{A_{SA,\,final} - A_{SA,initial}}{A_{SA,initial}} \times 100 \right] \tag{5.2}$$

TED computed the optimal factorial combinations pertaining to maximum MSN yield (ϕ_{MSN}) (Eq. (5.3)) through SN ratios (Eq. (5.4)) and analysis of variance (ANOVA) using MINITAB-17 (Minitab Inc. USA for Windows7) software.

$$\phi_{MSN} = \frac{moles of\ (Monostearin)\ formed}{moles of\ stearic acid\ consumed} \times 100 \tag{5.3}$$

$$SN = -10\log\left(\frac{1}{n}\sum_{i=1}^{n}\frac{1}{\phi_{MSN,i}^{2}}\right) \tag{5.4}$$

Here, i denoted number of replications and n implied number of trial experiments executed in a particular factorial set values as elaborated in Table 5.1.b.

Table 5.1.b Process factorial combinations as per TED with corresponding MSN yield and SN ratio in FIRR-RBR.

Run no.	$\theta_{GL:SA}$	θ_{RT} **(K)**	θ_{RPM} **(rpm)**	θ_{C} **(g/L)**	ϕ_{MSN} **(%)**	***SN* Ratio**
1	10	353	150	4	52.57	34.37
2	10	363	200	6	78.47	37.89
3	10	373	250	8	70.00	36.90
4	15	353	200	8	77.96	37.84
5	15	363	250	4	78.38	37.88
6	15	373	150	6	63.13	35.58
7	20	353	250	6	79.93	38.05
8	20	363	150	8	67.17	36.54
9	20	373	200	4	82.19	38.08

5.1.3 Kinetic Analysis

For evaluation of heterogeneous esterification kinetic parameters, separate runs were conducted using TED derived optimal condition with varying batch-time; and the corresponding ϕ_{MSN} was evaluated. Furthermore, the amount of MSN formed coupled with other products viz., distearin (DSN) and tristearin (TSN) were quantified by gas chromatograph equipped with DB-wax column (30 m × 0.25 mm × 0.25 mm). The column temperature was preset at 343 K and subsequently increased at a ramping rate

of 283 K/min and finally raised to 543 K [3].The sample injection was split less type with 99.99% Helium gas as a carrier (1 mL min^{-1}). The MS detector was operated in the EI mode at 70 eV and 40–900 amu.

5.1.4 Mathematical Interpretation

5.1.4.1 Reaction Mechanism

According to the reaction scheme (Eq. (5.5)), initially, one SA molecule has reacted with one GL molecule to form MSN; which in turn further reacted with another SA molecule to form DSN and the latter subsequently reacts with one more SA molecule to yield TSN. Notably, in Eq. (5.5) $C_{17}H_{35}$ group was denoted by 'S'. Kinetic analysis was performed with respect to the desired product (MSN) considering irreversible GL-SA esterification owing to in-situ removal of byproduct water by molecular sieves (adsorbents) during the reaction. However, as SA was the limiting reactant, the formations of DSN and TSN were likely to be much lower compared to MSN (Eq. (5.5)).

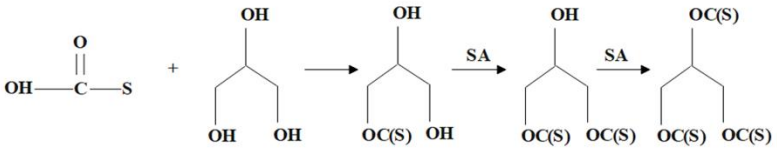

(5.5)

5.1.4.2 Analyses of the Bulk and Internal Diffusion-Controlled Kinetics

In order to identify the regimes of external mass transfer (bulk diffusion of limiting reactant, SA) limitation and subsequent surface reaction controlled in the FIRR-RBR set-up; kinetic analysis was performed using Mears criterion (M_C) (Eq. (5.6)) [4] through variation of θ_{RPM} between 50 and 300 rpm with a ramp of 25 rpm. Accordingly, if M_C < 0:15, the resistance to external mass transfer diffusion was significantly lower, whereas, values of M_C higher than 0.15 implied the external

mass transfer limiting esterification reaction.

$$M_C = \frac{\eta\, r_{SA,obs}\, \rho_C\, R_P}{k_{MTC}\, C_{SA,bulk}} \prec 0.15 \tag{5.6}$$

where η : order of the reaction; R_P (m): catalyst particle radius; $r_{SA,obs}$ (mole/gcat.min): observed reaction rate of limiting reactant (SA); k_{MTC} (m/min): mass transfer coefficient; ρ_C (g/L): catalyst bulk density; $C_{SA,bulk}$ (mol/L): limiting reactant bulk concentration. In order to estimate k_{MTC}, forced convection around a sphere [5] was employed (Eq. (5.7)):

$$\frac{k_{MTC} d_P}{D_{SA:GL}} = 2.0 + 0.6\left(\frac{d_P \upsilon}{\nu}\right)^{1/2}\left(\frac{\nu}{D_{SA:GL}}\right)^{1/3} \tag{5.7}$$

where d_P (m): particle diameter; $D_{SA:GL}$ (m^2 /s): diffusion coefficient of SA through GL; υ (m/min): velocity of GL-SA mixture approaching catalyst; ν (m^2 /s): kinematic viscosity of GL-SA mixture. The diffusivity ($D_{SA:GL}$) of reactant mixture was calculated using Wilke Chang equation [6] as per Eq. (5.8):

$$D_{SA:GL} = 1.173\times10^{-16}\left(\psi M_{GL}\right)^{1/2}\frac{T}{\mu_{bulk}\left(V_{SA}\right)^{0.6}} \tag{5.8}$$

where ψ : the association parameter (=1 for unassociated solvents, i.e., GL); M_{GL} (kg/mol): molecular weight of GL; μ_{bulk} (kg/m s): bulk viscosity of liquid mixture; V_{SA} (m^3/kg mol): molar volume of SA at the boiling point. After evaluation of negligible bulk diffusion-controlled regime, the influence of internal diffusion on GL-SA esterification was also assessed through determination of the effect of catalyst particle size on SA conversion. Accordingly, catalyst beads were disintegrated into three different fractions i.e., $d_P \prec 0.66$, $0.66 \prec d_P \prec 0.84$ and $d_P \succ 0.66$ from 25 to 30

mesh sizes; and corresponding SA conversions were measured using these catalyst particles.

5.1.4.3 Analysis of the Surface Kinetics Controlled Regime

Beyond the external and internal diffusion-controlled regimes, the surface kinetics-controlled regime (SKCR) was determined by keeping θ_{RPM} at such a level which could ensure negligible diffusion resistances. The heterogeneous kinetic parameters under SKCR were evaluated by Langmuir Hinshelwood (LH) and Eley Rideal (ER) mechanisms (Table 5.2) through non-linear fitting of experimental data using LM (Levenberg–Marquardt) method employing POLYMATH 6.10 software. General assumptions (Table 5.2) are: negligible external and internal diffusional resistance; DSN and TSN were formed in negligible amount; MSN being the main product; irreversible reaction, water removal by molecular sieves. Pseudo-homogeneous kinetic analysis was conducted to confirm the appropriateness of heterogeneous kinetics in the present study. After identifying the best-suited model for FIRR-RBR, similar analysis had also been conducted for FIRR-SBR in order to evaluate the superiority of RBR over SBR.

The, reaction rate, $-r_{SA}$ (mole/gcat.min) was evaluated using Eq. (5.9):

$$-r_{SA} = -\frac{1}{\rho_C}\frac{dC_{SA}}{dt} \tag{5.9}$$

Here, ρ_C: catalyst bulk density (g/L)

The reaction activation energy was computed by Arrhenius equation Eq. (5.10):

$$k_{obs} = k_{obs}^{0} \exp\left(\frac{-E_A}{RT}\right) \tag{5.10}$$

Where k_{obs}^{0}: the pre-exponential factor; E_A (kJ/mol): activation energy; R (8.314 J/mol K): universal gas constant; T (K): reaction temperature.

Table 5.2. Reaction kinetic models for GL-SA esterification

Model	Condition	Equation	Eq. no.
LH	Both GL and SA adsorbed on catalyst surface	$-r_{SA} = k_{obs}\left[\frac{K_{SA}C_{SA}K_{GL}C_{GL}}{\left(1+K_{SA}C_{SA}+K_{GL}C_{GL}+\frac{C_{MSN}}{K_{MSN}}\right)^2}\right]$	(5.11)
ERSA	SA adsorbed on catalyst surface	$-r_{SA} = k_{obs}\left[\frac{K_{SA}C_{SA}C_{GL}}{\left(1+K_{SA}C_{SA}+\frac{C_{MSN}}{K_{MSN}}\right)}\right]$	(5.12)
ERGL	Only GL adsorbed on catalyst surface	$-r_{SA} = k_{obs}\left[\frac{C_{SA}K_{GL}C_{GL}}{\left(1+K_{GL}C_{GL}+\frac{C_{MSN}}{K_{MSN}}\right)}\right]$	(5.13)
PH	No adsorption of reactants	$-r_{SA} = k_{obs}C_{SA}C_{GL}$	(5.14)

where, C_{SA} *[mol/L]: SA concentration;* C_{GL} *[mol/L]: GL concentration;* C_{MSN} *[mol/L]: MSN concentration, determined by GC–MS;* k_{obs} *(mole/gcat.min): reaction rate constant*

5.1.5 Product Characterization

The esterification product was characterized by FTIR spectroscopy using Shimadzu (alpha) spectrometer from 400 to 4000 cm^{-1}. Phase change temperature and latent heat of the synthesized product, standard MSN and SA were evaluated using DSC instrument (Perkin Elmer Diamond DSC) at a constant heating rate of 2 °C/min from 10 to 100°C under a constant N_2 flow at the rate of 20 mL/min. Perkin–Elmer TGA analyzer (Pyris Diamond TG/DTA) was used to assess the thermal stability of the prepared ester, where 7.759 mg sample was taken in a platinum crucible and heated under N_2 environment (20 mL/min) from 30 to 500°C.

5.2 ACTIVITY II:

Quartz halogen-ultrasonication integrated rotating reactor for efficient photocatalytic-thermocatalytic synthesis of GMC: Kinetics of heterogeneous

esterification

5.2.1 Materials

Analytical reagent grade chemicals, namely, GL (99.5%), KOH (pellets), and oxalic acid, were purchased from Merck, India. A15 (dry) and NT-P25 of size <100 nm (P25) were procured from Sigma Aldrich, while molecular sieves (size: 3Å), Capric Acid (99%) were supplied by SRL (India), HPLC-grade Ethanol and diethyl ether supplied by Merck (India) were used for determination of acid number by titration method.

5.2.2 Optimization of Esterification

Four independent operating factors viz., A15:NT-P25wt. ratio (f_{ATO}) (from 0.67:1 to 1.5:1); rotating speed (f_{RS}) (from 100 to 200 rpm), CA:G mole ratio (f_{MR}) and reaction temperature (f_{RT}) over the range of 0.25-0.5 and 333-353K respectively along with the dependent factor GMC yield (θ_{GMC}) as the response variable were considered for optimization of the esterification process.

An experimental matrix involving the independent factorial combinations was employed according to L9 orthogonal array of standard TED (Table 5.3). Accordingly, the experiments were conducted in triplicates in concurrence with the generated design matrix (Table 5.3). The response variable (θ_{GMC}) was maximized [2] through signal-noise (θ_{SN}) ratio (Eq. (5.15)) and the factorial effects were assessed by delta-ranks and θ_{SN} values (Table 5.4) using MINITAB-17 (Minitab Inc. USA for Windows7) software.

$$\theta_{SN} = -10\log\left(\frac{1}{n}\sum_{i=1}^{n}\frac{1}{\theta_{GMC,i}^{2}}\right) \tag{5.15}$$

Table 5.3. Factorial array for TED analysis with corresponding GMC yield and SN ratios

f_{ATO} (wt./wt.)	f_{MR}	f_{RT} (K)	f_{RS} (rpm)	θ_{GMC} (%)	θ_{SN}
0.67	0.25	333	100	70.00	36.90
0.67	0.35	343	150	87.50	38.84
0.67	0.50	353	200	80.00	38.06
1.00	0.25	343	200	76.89	37.71
1.00	0.35	353	100	72.00	37.14
1.00	0.50	333	150	74.35	37.42
1.50	0.25	353	150	72.98	37.26
1.50	0.35	333	200	69.00	36.77
1.50	0.50	343	100	72.00	37.14

Table 5.4. Delta-Ranks and SN ratio values

Level	f_{ATO} (wt./wt.)	f_{MR}	f_{RT} (K)	f_{RS} (rpm)
1	37.93#	37.29	37.03	37.07
2	37.43	37.59#	37.90#	37.84#
3	37.06	37.54	37.49	37.52
Delta	0.87	0.29	0.87	0.78
Rank	1	4	2	3

 # SN ratio values of the opearting factors rendering maximum GMC yield

5.2.3 Reactor Configurations and Reaction Procedure

Esterification of GL with CA was performed in a rotating 250 mL round bottom three-neck quartz glass flask under different electromagnetic energies viz., quartz halogen radiation (QHR; which represents near-infrared spectra), ultrasonication (US) and a combination of QHR and US. The integrated quartz halogen radiator-US energized rotating reactor (QHRUERR) (200W, 340-850 nm, 50% UV, 14% visible, 26% NIR) [7] and US energized bath arrangement (20 kHz, power 100 W), as given in Figure 5.2; wherein, the reaction mass was under the continuous exposure to ultrasonic wave and QH light wave. For a representative experimental run, mix of A15 and NT-P25 i.e., ATO was used as a heterogeneous catalyst due to their similar surface area (42-45 m^2/g) and required acidic and photochemical properties. Necessary amount of GL and CA were preheated at pre-set temperature and added to the reactor along with catalyst mixture (ATO). Furthermore, to eliminate the residual water generated during CA-GL

esterification, vacuum dried molecular sieves (as desiccants) were used as an adsorbent media.

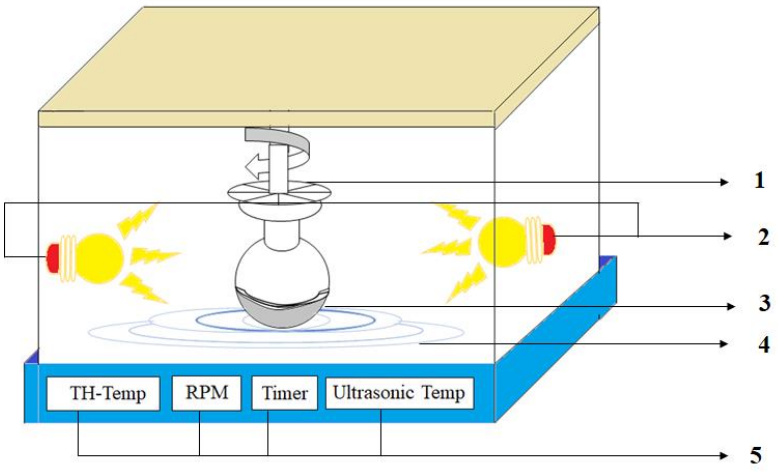

Figure 5.2. Schematic diagram of the quartz-halogen radiator-ultrasound energized rotating reactor; 1-rotating arrangement, 2-quartz halogen radiator, 3-one neck round bottom flask, 4-ultrasonic cavitation, 5-controller.

As benchmark, experiments were also conducted in CEMR (conventionally energized mechanically stirred reactor) and compared with ultrasound energized rotating reactor (USERR), quartz halogen energized rotating reactor (QHERR) and QHRUERR to identify the superiority in reactor efficacy for CA-GL esterification. After the reaction, the reaction mix was separated from the ATO catalyst through membrane filtration and subjected to GMC purification through crystallization method due to high melting point differences between reactants (CA: 304.6K and GL: 290.8K) and the products (GMC: 326K).The purified product composition was subsequently quantified by reported HPLC (make: Waters, model: Perkin Elmer 200 series) method [8].

5.2.4 Product Analysis

The acid number of product ester layer and corresponding CA conversion were calculated through standard titration method using 1:1 (v/v) ethanol: diethyl ether as solvent and titrated against 0.1N alcoholic KOH solution. The endpoint of titration

was detected by pH meter (EUTECH INSTRUMENTS: pH Tutor) and the acid number was determined by Eq. (5.16) and Eq. (5.17) [9].

$$A_{CA} = \frac{56.11 \times M_{KOH} \times V_{KOH}}{m_{GMC}} \tag{5.16}$$

$$\theta_{CA} = \left[\frac{A_{CA,t=t_i} - A_{CA,t=0}}{A_{CA,t=0}} \right] \times 100 \tag{5.17}$$

UV-Vis diffuse reflectance spectra (DRS) was obtained for the dry-pressed disk samples of NT-P25 and $ATO^{0.67}$ by using a Shimadzu UV 2550 spectrophotometer, (equipped with an integrating sphere) and PL spectra (PerkinElmer: LS55 model) was also obtained for the dry powder samples of NT-P25 and $ATO^{0.67}$. Furthermore, to obtain the direct band gap, Tauc plot of Kubelka-Munk function was employed. Kubelka-Munk relation was represented by the Eq. (5.18)

$$F(h\upsilon) = \frac{(1 - Rh\upsilon)^2}{2Rh\upsilon} \tag{5.18}$$

5.2.5 Evaluation of Esterification Kinetics

Reaction mix samples were collected at 5 min interval till maximum CA conversion had been reached and for evaluation of concentration of reaction species, the purified samples were then subjected to HPLC analyses. Since the appreciable quantity of desiccants were used for water removal; hence, the CA-GL esterification reaction was considered irreversible. Accordingly, heterogeneous esterification rate equations considering surface kinetics as the limiting step were expressed by Eq. (5.20), Eq. (5.21) and Eq. (5.22) respectively; while, pseudo homogeneous rate law was represented by Eq. (5.19).

The rate expression of consumption of CA in the batch reactor was given by equation (9). Also, the surface reaction limiting condition was considered only after confirming negligible bulk and internal diffusional resistances.

$$-r_{CA} = k_{forward}\left(C_{CA} \times C_G\right) \tag{5.19}$$

$$-r_{CA} = \frac{k_{forward}\left(K_{ads,CA}C_{CA} \times K_{ads,G}C_G\right)}{\left(1 + K_{ads,CA} + K_{ads,G}C_G + \frac{C_{GMC}}{K_{des,GMC}}\right)^2} \tag{5.20}$$

$$-r_{CA} = \frac{k_{forward}\left(K_{ads,CA}C_{CA} \times C_G\right)}{\left(1 + K_{ads,CA}C_{CA} + \frac{C_{GMC}}{K_{des,GMC}}\right)} \tag{5.21}$$

$$-r_{CA} = \frac{k_{forward}\left(C_{CA} \times K_{ads,G}C_G\right)}{\left(1 + K_{ads,G}C_G + \frac{C_{GMC}}{K_{des,GMC}}\right)} \tag{5.22}$$

where, $-r_{CA}$ was calculated from Eq. (9)

$$-r_{CA} = -\frac{d\left(C_{CA}\right)}{dt} = -\frac{1}{W} \times \frac{d\left(N_{CA}\right)}{dt} \tag{5.23}$$

All the kinetic constants were evaluted by non linear regression using Levenberg Marquardt algorithm (Polymath 7.0®).

5.2.6 Catalyst Reusability

To evaluate the reusability of ATO catalyst in CA-GL esterification under QHRUERR and CERR, after each experimental trial, the catalyst was separated from the reaction mix by membrane filtration and was thoroughly washed with dichloromethane in order to remove residual reaction species. The catalyst was finally regenerated by vacuum drying at 338 K to completely dryness (≤1.6% moisture content) and reused in the next batch.

5.2.7 Antifungal Activity of the Product

To determine the antifungal activity of GMC, potato dextrose broth (PDB) was prepared. Briefly, the antifungal property test was done to determine the zone of inhibition against the pathogen *A. Niger*. Initially, 1 mL of spores was added to 99 mL

PDB with minimum inhibition concentration of GMC. Sodium Benzoate and pure GMC were used as a reference in establishing the effect of prepared GMC against the food pathogen. The growth inhibition study of *A. Niger* was performed for 144 h at 35°C temperature. The media were cultured in an incubator at 35 °C and 120 rpm. Every 24 h, the growth was assessed by determining the increase of dry weight of mycelium.

5.3 ACTIVITY III

E-waste derived silica-alumina for eco-friendly and inexpensive Mg-Al-Ti photocatalyst towards GC (electrolyte) synthesis: Process optimization and LCA

5.3.1 Materials

A multi-layered waste PCB of FR-4 type was collected from waste dumping site. Animal biochar was purchased from local market. GL (99.5%), DMC (99%), $Mg(NO_3)_2$. $6H_2O$ (99.99% pure), titanium tetra isopropoxide ($C_{12}H_{28}O_4Ti$, 99% pure), SiO_2 and $Al(NO_3)_3$. $6H_2O$ (99% pure) were procured from Sigma Aldrich. N-N dimethylformamide (DMF), nitric acid (HNO_3, 65 wt.%), hydrochloric acid (HCl, 37 wt.%), ethanol (≥ 99.9% purity), ammonium hydroxide aqueous solution (NH_4OH, 25%), and ammonium carbonate ($(NH_4)_2CO_3$) were procured from Merck chemicals, India. All chemicals were of AR grade.

5.3.2 Catalyst Preparation

5.3.2.1 Extraction of Mesoporous Silica from WPCB

All the unnecessary electronic parts of WPCB were dismantled mechanically using cutting mill. Subsequently, WPCB integrated with metal components like Au, Pt, Cu, Zn, etc. were leached in aqua-regia [10]. Next, BER, mixed with glass fiber (mesoporous silica and alumina) was swollen in DMF solution maintaining WPCB to liquid ratio of 300 g/L. Ultrasonic cavitation (20 kHz, power 100 W) was carried out

to perform separation of silica and alumina from the constituents as resins were very difficult to get dissolved in solvent following the literature-reported method [11]. Afterward, the obtained sample was grinded again, this time using drum sander into fine powder and screened by (240 BSS/ 300 BSS) and was subsequently pre-treated thoroughly using 1 N HCl aqueous solution at stirring speed 800 rpm and 90 °C. To leach out the undesired substances (i.e., Zn, Cu, Pb, Cd, Ni, Cr, Hg), water washing was done followed by oven drying at 60 °C for 2 h. Finally, the dried $SA_{(WPCB)}$ powder was grinded using a mortar and pestle to obtain 0.049 mm average particle size for subsequent use in catalyst preparation. Inductively coupled plasma optical emission spectrometry (ICP-OES) (PerkinElmer, Optima8000) was used to identify the compositions (70.96% silica, 29% alumina, and trace amount of calcium) of the $SA_{(WPCB)}$ powder. Nevertheless, the smaller amount of aforementioned dissolved metals (Table 5.5) was discharged to the soil through the mechanism of electrostatic absorption technique [12, 13] in the form of animal biochar, which is more effective in plant cultivation and mostly in reducing CO_2 emission from soil [14]. However, the inferior amount of off-gases (Table 5.5) traveled through the gas collector tunnel owing to lack of suitable recovery infrastructure. The employment of off-gas treatment has not been estimated. After the reaction, all the process wastes specifically,

Table 5.5. Life cycle inventory of 2.0 kg e-waste disassembling processes.

Flow	Amount	Unit
Input		
WPCB	2	kg
Acetic Acid	0.1	kg
Ethanol	0.5	kg
Hydrochloric Acid	0.25	kg
N,N-Dimethylformamide	0.05	kg
Nitric Acid	0.1	kg
Deionised water	1	kg
Energy		
Electricity	0.6648	kWh
Transport		

Lorry	24	kg*km
Output flow		
Product		
Extracted silica-alumina	1.5	kg
Emission to air	0.002	kg
Waste treatment & disposal	0.02	kg
Shredded fraction, Materials recovery	0.2	kg
Wastewater treatment	0.5	L
Direct air emissions		
Acetic acid	$1.51307E^{-06}$	kg
Cadmium	$-2.61745E^{-08}$	kg
Chromium	$-5.84167E^{-08}$	kg
Copper	$-7.45168E^{-07}$	kg
Particulates	$8.46284E^{-05}$	kg
Ammonia	0.000282559	kg
Nitrogen oxides	0.001767954	kg
Hydrogen chloride	$5.99943E^{-05}$	kg
Emission to soil, in the form of Biochar		
Cadmium	$1.45272E^{-09}$	kg
Copper	$3.95551E^{-08}$	kg
Mercury	$5.62979E^{-11}$	kg
Zinc	$8.18602E^{-08}$	kg
Chromium	$1.03608E^{-08}$	kg
Lead	$6.53349E^{-09}$	kg
Sodium salt	$3.58021E^{-15}$	kg
Emission to water		
Copper, ion	$4.24414E^{-08}$	kg
Chromium, ion	$1.53934E^{-09}$	kg
Magnesium	$8.18563E^{-05}$	kg
Nitrate	$2.14198E^{-05}$	kg
Zinc, ion	$6.48818E^{-07}$	kg
Aluminium	0.003787715	kg
Ethanol	$2.90855E^{-06}$	kg
Suspended matters	$3.16251E^{-11}$	kg

spent catalyst, catalyst support, and wastewater, which were measured to be settled via waste treatment, disposal, and wastewater treatment respectively, were considered in the LCA for potential environmental impacts.

5.3.2.2 Preparation of SiO_2@Mg-Al-Ti LDO

A prerequisite amount of extracted $SA_{(WPCB)}$ was added to a measured amount of ethanolic solution of magnesium nitrate hexahydrate and titanium tetraisopropoxide. The wet-impregnation was performed at a temperature of 70 °C for 1 h with reflux

condition in a solar simulated quartz halogen lamp radiated batch reactor (SSQHLBR); 100 W, wavelength: 300–1100 nm) consisting of a three-necked 0.5 L glass flask fitted with a mechanical agitator (1000 rpm) [15]. Co-precipitation was conducted by adding NH_4OH and $(NH_4)_2CO_3$ dropwise to maintain the pH at 9 ± 0.5 and the mix was kept for aging over 24 h. Later, it was vacuum-filtered and washing was carried out with deionized water and ethanol rigorously, then the suspension was oven-dried at 70 °C for 2 h. To obtain the activated $SiO_{2(WPCB)}$@Mg-Al-Ti-LDO catalyst (MATLSW), the dried mass was air calcined at 600 °C for 2.5 h which removed the adsorbed interlayer –OH ion, water molecule, and CO_3^{2-} anion. Eventually, the prepared catalyst was ground by maintaining the particle size 250–300 BSS. For comparison purposes, commercially available $SiO_{2(C)}$ and aluminum precursors were also used as catalyst support and catalyst precursor to prepare $SiO_{2(C)}$ supported Mg-Al-Ti LDO catalyst i.e., $SiO_{2(C)}$@Mg-Al-TiLDO ($MATLS_C$) in a similar manner. To explore the photochemical activity of the synthesized catalyst, the catalytic performance was studied under photon excitation, thermal excitation, and in dark condition. Several $MATLS_W$ catalysts were prepared by varying the concentrations of $SA_{(WPCB)}$, magnesium precursor, titanium precursor in various mole ratios of SA:Mg:Ti.

5.3.3 Experimental Set Up

The transesterification reaction of 3 mol GL with 5 mol DMC was performed in a three-neck flask (250 mL) using a solar simulated quartz halogen lamp radiated batch reactor (SSQHLBR; 100 W, wavelength: 300–1100 nm) with an impeller stirring speed of 800 rpm equipped with condensers to maintain reflux condition at set temperature. A required amount of preheated prepared catalyst was fed to the reaction mix and the reaction was executed at 70 ˚C temperature for 25 min. Afterward, the

solid photo-active catalyst MATLSW was separated from the reaction mix through filtration. Additionally, the filtrate was further centrifuged (5000 rpm, 7 min) to separate the product from the heterogeneous mixture. Subsequently, the by-product methanol and water were separated through rotary evaporation.

5.3.4 Box-Behnken Optimization

The optimization of transesterification reaction in the SSQHLBR was performed to obtain the maximum GC yield considering the effects of important process parameters at three levels according to Box-Behnken design (BBD) [16] employing Design Expert 7.0 software (Table 5.6). Three prominent process parameters for the experimental design were: A: catalyst concentration (2–8 wt%), B: reaction temperature (50–70 °C), and C: reaction time (15–35 min). Using BBD, the experimental runs (each repeated 4 times) were carried out in 17 different combinations of the coded parameters (Table 5.7) to predict the optimal conditions for achieving maximum GC yield.

Table 5.6. Experimental process parameters and levels used in Box Behnken

Factors	Name	Units	-1 level	0 level	+1 level
R_{CC}	Catalyst concentration	wt.%	2	5	8
R_T	Reaction temperature	°C	50	60	70
R_t	Reaction time	min	15	25	35

Coded parameters: $\gamma_{CC} = \frac{R_{CC} - 5}{3}$, $\gamma_T = \frac{R_T - 60}{10}$, $\gamma_t = \frac{R_t - 25}{1}$

Table 5.7. Box Behnken layouts for different parametric combinations of transesterification of GL and DMC

Runs	Parameter (γ_{CC}) Catalyst Concentration	Parameter (γ_T) Reaction temperature	Parameter (γ_t) Reaction time	Response (γ_{GC}) GC Yield (%)
1	1	0	-1	94.23
2	0	0	0	95.67
3	1	1	0	98.68
4	0	1	-1	92.11
5	0	1	1	97.53
6	1	-1	0	96.28
7	-1	-1	0	90.08
8	-1	1	0	94.99
9	-1	0	1	94.01
10	0	-1	-1	89.78
11	0	0	0	95.67
12	1	0	1	98
13	0	0	0	95.67
14	0	-1	1	93.89
15	0	0	0	95.67
16	-1	0	-1	87.56
17	0	0	0	95.67

To estimate the omnipotence of SSQHLBR over thermally (conductively and convectively) heated stirred batch reactor (THBR) (650 W), transesterification reaction was further carried out using MATLSW catalyst at the optimal parametric combinations. Besides, the transesterification for GC synthesis was also assessed by using commercial $SiO_{2(C)}$ supported catalyst $MATLS_C$ at the derived optimum condition.

5.3.5 Catalyst Characterization and Product Analysis

The crystal structure and the phase composition of the optimum $MATLS_W$ have been identified by X–ray diffraction (XRD) analysis over Bragg's angle range from 10 to 70° with a scan rate of 2° per min using Bruker D8 (Cu Kα λ = 0.15406 nm). The chemical structural features of the manufactured catalyst have been recognized by

Fourier Transform Infrared Spectroscopy (FTIR) analysis (Shimadzu (alpha)) from 4000 to 400 cm^{-1}. The morphology of the $MATLS_W$ catalyst at optimal composition was analyzed by FESEM at 17 kV (JEOL Ltd., Japan, model JSM 6700F) coupled to an EDS detector that provided the sample micrographs (70 μm) and the corresponding elemental composition. Furthermore, thermogravimetric analyses (TGA) (Perkin Elmer STA 6000) have been performed for both uncalcined and calcined catalyst at a heating rate of 10 °C/min (nitrogen gas flow rate: 20 ml/min) from 30 °C to 1000 °C. Thereafter, the basicity of the synthesized catalyst was confirmed by CO_2-TPD (Micromeritics) analysis. The textural property of the catalysts has been revealed by Brunauer-Emmett-Teller (BET) (Quanta chrome Instruments, Nova 4000e). The electronic structural composition of the optimal catalyst has been identified by X-ray photoelectron spectroscopy (XPS) analysis with the binding energies for the optimum catalyst compositions calibrated using C1s at 284.6 eV. The photocatalytic characteristic has been determined by UV–visible diffuse reflectance spectra (UV–Vis DRS) on a UV–vis 2600 spectrophotometer (Perkin Elmer LAMBDA) and identified by Kubelka–Munk function. Nonetheless, in order to detect the interaction of light with the molecular vibration and other excitations in the catalyst, Raman spectra was obtained. The product GC was confirmed by gas chromatography-mass spectroscopy (Thermo fisher) equipped with a capillary column TG-5MS (30 m × 0.25 mm × 0.5 μm). Eq. (5.24) was used for calculation of the GC yield:

$$Yield\,(\gamma_{GC}) = \frac{moles of\ glycerolcarbonate formaed}{moles of\ glycerolconsumed} \times 100 \qquad (5.24)$$

Electrochemical property and cyclic voltammetry of GC were performed by using Biologic SP-150 electrochemical workstation.

5.3.6 LCA Methodology

The LCA considering the 'cradle-to-gate' study i.e., starting with the e-waste (i.e., WPCB) collection, extraction of $SA_{(WPCB)}$ from WPCB, preparation of MATLSW-5 towards GC synthesis was performed employing the Open LCA 1.10.2 software. The aim of the process has been mainly to compare the environmental impacts pertaining to the preparation of $MATLS_W$ catalyst over the MATLSC catalyst; and secondly, to assess the relative environmental impacts concerning the GC production deploying the synthesized catalyst in the SSQHLBR and THBR. Thirdly, the LCA results of the overall process (conducted in India) have been analyzed and compared with other countries. In order to evaluate the effect of inputs as transportation of chemicals, materials production, depending on the availability and reliability, the data were taken from a global database, reported in Ecoinvent database 3.5 (life cycle inventory). Notably, the electricity grid mix database for energy input could be obtained for the experimental location (West Bengal, India). To evaluate both the potential environmental and economic impacts of the catalyst and process, the LCIA methodology "ReCiPe Midpoint (H)" has been implemented. The system boundaries mainly involved upstream and downstream processes in the LCA (Figure 5.3). The 1st system boundary contains the upstream process [17] i.e., WPCB treatment, recovery of $SA_{(WPCB)}$, assuming 100% pure acid used for the treatment, embedded in the Ecoinvent database of LCI, primarily the LCIA result has been calculated based on the functional unit of 1.5 kg extracted $SA_{(WPCB)}$. The 2nd system boundary covers the preparation of 1 kg $MATLS_W$-5 catalyst. Owing to the absence of suitable global data in the LCI datasets for nanomaterial feedstocks, the analysis could depend on some reasonable approximations. All materials were collected through BS6 compliant lorry > 32 metric tons, EURO6|APOS, U-ROW. To reduce the influence of the

environmental impacts due to transportation distance, the same has been assumed to be inside the city. 3rd boundary encompasses the production of 1 kg of GC along with the WPCB treatment and MATLS$_W$-5 preparation. In the output processes of the boundary system, an approximate amount of water waste, heat loss, acid water, shredded fraction of materials, suspended matters, spent catalyst, salt impurities, etc. have been considered for wastewater treatment, treatment of gaseous emission are discussed in Table 5.5, (see Table 5.8-5.11). The overall LCA analysis provides estimations of the probable impact of energy consumption and emissions in terms of global warming potential, human health, fossil depletion, ecotoxicity, etc. according to specific functional units have been stated in Table 5.12.

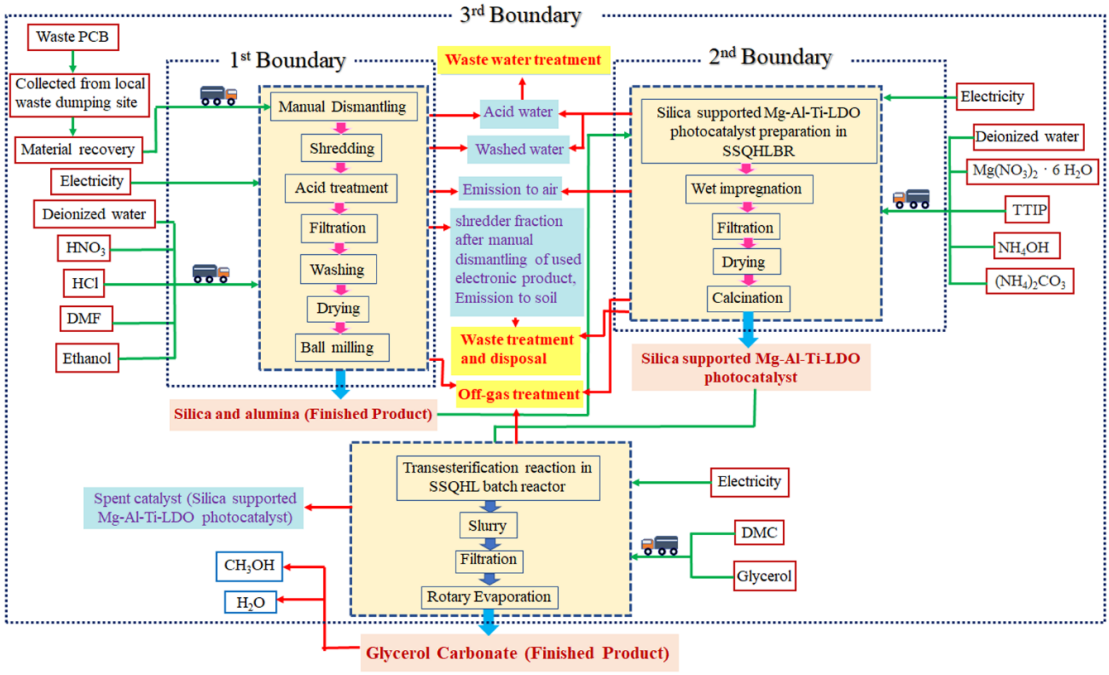

Figure 5.3. Schematic diagram of the process and system boundary in LCA

Table 5.8. Life cycle inventory of 1kg $MATLS_W$-5 catalyst.

Flow	Amount	Unit
Input		
Activated silica-alumina	1.5	kg
Ammonia	0.05	kg
Ethanol	0. 5	kg
Hydrochloric acid	0.25	kg
Magnesium nitrate	0.5	kg
hexahydrate	0.5	kg
Titanium isopropoxide		
Deionised water	1	kg
Energy		
Electricity	2.7233	kWh
Transport		
Lorry	0.93750	kg*km
Output flow		
Product		
$MATLS_W$-5	1	kg
By-product		
Silica-alumina	0.2	kg
Emission to air	0.002	kg
Raw sewage sludge	0.01	kg
Waste water treatment	0.489	L

Table 5.9. Life cycle inventory of 1kg $MATLS_C$ catalyst.

Flow	Amount	Unit
Input		
Commercial silica	1.5	kg
Aluminium nitrate	1	kg
Ammonia	0.05	kg
Ethanol	0. 5	kg
Hydrochloric acid	0.25	kg
Magnesium nitrate	0.5	kg
hexahydrate	0.5	kg
Titanium isopropoxide		
Deionised water	1	kg
Energy		
Electricity	2.7233	kWh
Transport		
Lorry	0.93750	kg*km
Output flow		
Product		
$MATLS_C$	1	kg
By-product		
silica	0.2	kg
Emission to air	0.002	kg
Ammonium nitrate	0.09	kg
Raw sewage sludge	0.01	kg
Waste water treatment	0.6	L

Table 5.10. Life cycle inventory of 1kg GC production in THBR.

Flow	Amount	Unit
Input		
GL	0.5	kg
DMC	1	kg
MATLS$_W$-5	0.3	kg
Energy		
Electricity	1.074	kWh
Transport		
Lorry	3	kg*km
Output flow		
Product		
GC	1	kg
By-product		
DMC	0.08	kg
Emission to air, Methanol	0.001	kg
Spent catalyst	0.01	kg
Waste water	0.002	kg

Table 5.11. Life cycle inventory of 1kg GC production in SSQHLBR.

Flow	Amount	Unit
Input		
GL	0.5	kg
DMC	1	kg
MATLS$_W$-5	0.3	kg
Energy		
Electricity	0.4656	kWh
Transport		
Lorry	3	kg*km
Output flow		
Product		
GC	1	kg
By-product		
DMC	0.068	kg
Emission to air, Methanol	0.001	kg
Spent catalyst	0.01	kg
Waste water	0.002	kg

Table 5.12. Impact Analysis for GC production

Impact Category	Results		Scaling Up SSQHLBR (1MT GC)	References
	THBR (1kg GC)	SSQHLBR (1kg GC)		
climate change (GWP100)	4.84	4.56	4559.31	kg CO_2-Eq
fossil depletion (FDP)	2.22	2.14	2136.80	kg oil-Eq
freshwater ecotoxicity (FETPinf)	0.06	0.06	59.92	kg 1,4-DCB-Eq
human toxicity (HTPinf)	1.92	1.81	1809.20	kg 1,4-DCB-Eq
ionising radiation (IRP_HE)	0.29	0.25	288.43	kg U235-Eq
marine ecotoxicity (METPinf)	0.05	0.04	45.23	kg 1,4-DCB-Eq
metal depletion (MDP)	0.25	0.21	248.47	kg Fe-Eq
ozone depletion (ODPinf)	$3.96E^{-07}$	$3.94E^{-07}$	0.00	kg CFC-11-Eq
photochemical oxidant formation (POFP)	0.02	0.01	17.92	kg NMVOC
terrestrial acidification (TAP100)	0.02	0.02	21.33	kg SO_2-Eq
water depletion (WDP)	0.07	0.06	58.36	m^3

5.4 ACTIVITY IV

Intensification of autocatalytic MO synthesis in continuous flow rotating recycle reactor under hybrid radiation: Process optimization and Scale-up

5.4.1 Materials

Methanol (CH_3OH, 99.5 %), OA (R1COOH, 99 %), potassium hydroxide (pellets), oxalic acid, toluene, isopropyl alcohol, hydrofluoric acid (HF), and phenolphthalein were purchased from Merck chemicals, India. Titanium dioxide (TiO_2 P-25), zinc oxide (ZnO) and borosilicate glass beads (3.5 × 4.5 mm^2) were procured from Sigma Aldrich; while SRL, India, supplied molecular sieves (3Å). All chemicals were of AR grade and for further experimentation as received.

5.4.2 Reactor Design and Catalytic Performance Evaluation for Esterification

The MRPBR reactor consisted of a cylindrical quartz tube reactor with an inner diameter, outer diameter, and axial height of 21, 24.1 and 285 mm, respectively, and two separate reservoirs for storing the reactants, viz. methanol and OA. The mixture of 32.2 mL OA and 44.5 mL methanol (to achieve 11 % molar excess of methanol) for injection into the packed bed was executed by using a mixture and/or T-connector before the entrance of the reactor as shown in Figure 5.4.

The reactor was operated in a rotating electromagnetic irradiation field. The rotation of the packed bed was regulated with a digital speed controller. The peristaltic pump (Rivotek, India) controlled the reaction mixture flow through the system. The exterior of the whole quartz reactor tube and radiator assembly (NIR and MW) were insulated by means of quartz wool layer. The quartz tube reactor was transparent to NIR and MW. Thus, the hybrid electromagnetic waves could heat up the catalytic bed effectively. This irradiation induced the esterification via shifting the reaction equilibrium to improve the reaction rate. The esterification study of methanol with OA was performed in MRPBR equipped with non-ionizing radiation, namely MW and NIR irradiation. The reactor system comprised a continuous custom-made NIR irradiation (100 W, 200–3000 nm) and MW (750 W, 30 cm to 1 mm) power operating system fitted with a digital temperature and power control relay. The source of light was located at a 2.5 cm penetration depth from the reactor. In order to increase the amount of product yield, recycle facility was incorporated into the reactor system. The reactor outlet at the bottom is bifurcated so that one of the streams can be recycled and the other stream can be extracted as the net product. The recycle flow was governed using another peristaltic pump, and the rotameter was used to control the flow rate.

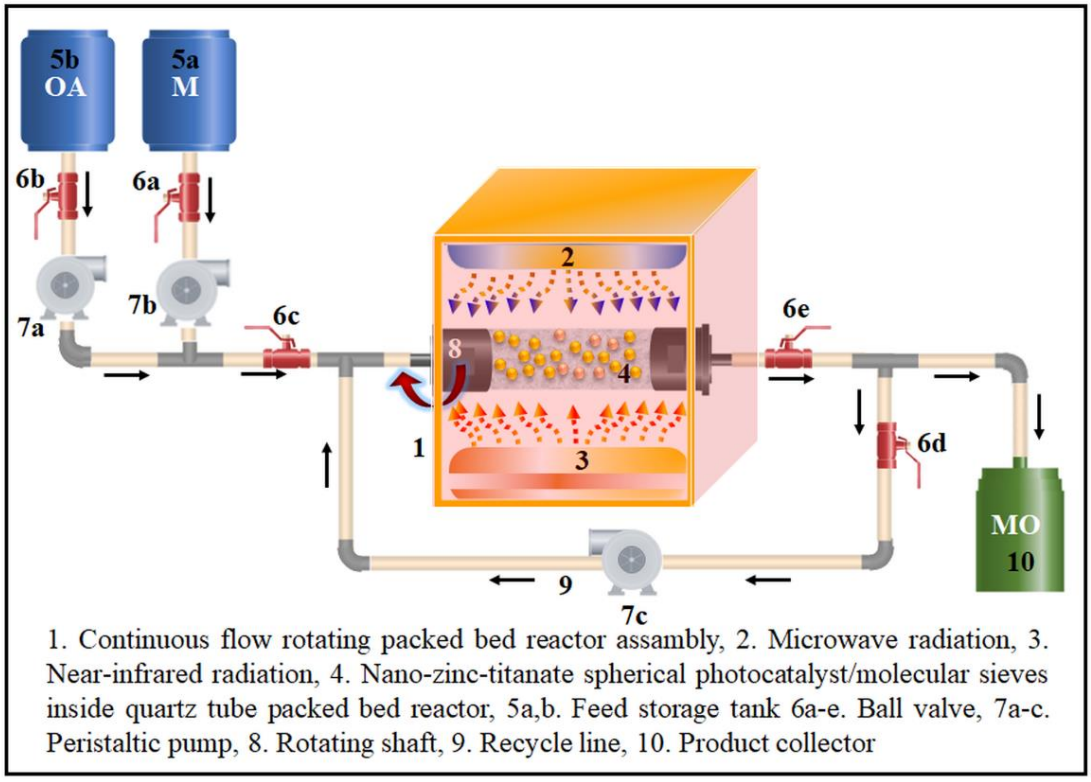

Figure 5.4. Schematic diagram of MRPBR.

The reactor was packed with $ZnTiO_3$ photocatalysts coated over equally sized borosilicate glass beads (4.5 mm diameter) and molecular sieves (water/moisture adsorbent). To increase the available surface area of the catalyst, the potential catalyst load increases per unit volume of the rotating reactor. The esterification process is performed under atmospheric pressure with a rotating speed varying from 20 to 300 rpm, and the reactant flow rate viz., limiting reactant OA flow rate is within 0.75–11.8 mL/min and excess methanol follows the flow rate of 2.52–27.66 mL/min. The reaction was carried out for 24 h. The yields reached a steady state of about 0.21–0.17 min^{-1} of LHSV. The water generated during the esterification was removed by a molecular sieve adsorbent, partially packed in the reactor bed. The surface reaction kinetics has been developed based on the species adsorbed on the surface of the photocatalyst. Therefore, water has not been considered in the reaction mechanism and as per LH kinetics, no water molecules are considered to adsorb on the surface of

the active site of the catalyst [18]. Next, the products formed in the reactor were collected from the outer part of the reactor in a receiver, where the valve in the outlet was kept closed. Accordingly, the products were pumped back by varying the recycling flow rate (6.08–30.83 mL/min) through a peristaltic pump into the reactor continuously to achieve the recycle action by keeping the recycle line valve open. The recycling of the product mix was carried out either to increase the amount of OA conversion/ MO yield. The steady-state flow in the reactor operation is reached within 4.87–5.92 min of space–time for a given flow condition. For every run, the sufficient time to get the uniform temperature distribution was very low compared to the space–time. The reactor effluent was collected for the sample analysis after 1.5 times the space-time (7.30 min), which is much greater than the time (2.24 min) required to reach the steady state temperature distribution. Then, the product was shifted to the separating vessel and centrifuged to purify the product layer. After centrifugation, the product was diluted 15–20 times before GC-MS analysis.

5.4.3 Preparation of Glass Bead Supported Photocatalyst

The glass beads, nano ZnO and TiO_2 P-25 based photocatalysts, as obtained from the supplier, were dried in hot air oven at 343 K for 2 h to remove the moisture at the beginning. Next, glass beads were pretreated with diluted HF (7 %, v/v) for 24 h and washed thoroughly with DI water to achieve a pH of 7. It is worthwhile to mention that HF was used to make a rough surface [19] for better contact with photocatalysts on it. Afterward, pre-treated glass beads were dried at 353 K for 1.5 h. Then, ball-milled $ZnTiO_3$ (BMZTO) powders were fabricated using a planetary ball milling instrument operating at 1000 rpm with some modifications [20]. In detail, 0.5 g of ZnO and 0.7 g of TiO_2 P-25 were mixed thoroughly and then placed in a ball mill with spherical zirconia balls for 10, 20, 40, and 60 min. After grinding, screening was

carried out to separate the mixture from the zirconia ball using a metallic sieve by maintaining the particle size of 275 BSS. To synthesize the supported BMZTO/glass bead catalyst, pre-treated glass beads (4 g), ball-milled ZnO/TiO_2, and ethanol/water aqueous suspension were mixed in a one-neck flask using a mechanical impeller for 30 min at a rotating speed of 400 rpm. The coated beads were then put in the muffle furnace, pre-heated at 553 K for 5 min, and then post-heated at 723 K for 2 h with a heating rate of 275 K/min. To ensure the penetration depth and absorptivity of the radiators, the deposition of the catalyst was repeated 3 times to obtain the desired thickness (0.045-0.079 μm). The penetration depth of MW and NIR have been found to be in the range of 22.07-29.79 mm, and 577.02-778.99 mm, respectively in the visible range while the dielectric constant value is set to 22.13-23.69. Nevertheless, during scale-up, the penetration depth of MW and NIR would be 1.418 m and 37.094 m, respectively; for uniform heating of the reaction medium throughout the reactor. The average weight of the catalyst-coated beads was measured by weighing the glass beads before and after coating. Lastly, the coated glass beads were rinsed with distilled water to remove the uninvolved powder mixture.

5.4.4 Statistical Design of Experiments

In the present study, the continuous production of MO was optimized by using the Box-Behnken statistical design of experiments (DoE). Response surface methodology (RSM) encompasses mathematical and statistical techniques [21]. Box-Behnken is one of the popular types of RSM and was used as an effective tool to estimate optimization. This statistical optimization technique was performed using Design Expert 7.0 software. The regression analysis, graphical analysis, and numerical optimization were carried out in MPBR. To determine the optimal conditions and to investigate the impacts of independent variables, viz. catalyst concentration from 20

to 40 wt%, reaction temperature from 323 to 333 K, the molar ratio of methanol to OA from 7:1 to 15:1, LHSV from 0.45 to 0.13 min^{-1} were selected whereas, the maximum yield of MO has been defined as the response variable in the experimental design. The range and the coded levels are summarized in Table 5.13. The response pattern of esterification experiments consisting of 4 process variables and 3 coded levels (-1, 0, +1) for each variable with a total of 29 experimental results (4 replicas on the center point) are shown in Table 5.14. In each set, experimental runs were performed in triplicate to assess the repeatability of the results. The response variable (yield % of MO) was fitted with a quadratic model equation (Eq. (5.25)) to estimate the optimum value and, consequently, to describe the interaction between the factors. A detailed discussion has been reported in the result section.

$$Y = \alpha_0 + \sum \alpha_{ii} x_i^2 + \sum \alpha_{ij} x_i x_j \qquad (5.25)$$

where, Y is the response for the yield of MO, x_i and x_j are independent variable, α_0 is a constant term, α_i, α_{ii} and α_{ij} are the regression coefficient of the linear effect term, quadratic effect term, and product term for the interaction between i and j, respectively.

Table 5.13. Experimental process parameters and levels used in Box Behnken.

Process variables	Name	Units	-1	0	+1
R_{CC}	Catalyst concentration	wt.%	20	30	40
R_T	Reaction temperature	K	323	328	333
R_{MR}	Methanol: OA		7	11	15
R_{LHSV}	LHSV	min^{-1}	0.45	0.2	0.13

5.4.5 Analytical Methods

The product of MO has been collected and analyzed by gas chromatography-mass spectroscopy (GC-MS) equipped with a DB-23 column (60 m × 0.25 mm ID × 0.15 μm). Helium gas has been used as the carrier gas with a flow rate of 1 mL/min. The injector and the detector temperature have been maintained at 503 K and 553 K, respectively. The acid number of the ester layer and conversion of OA were determined by standard titration method with KOH standard solution, adding phenolphthalein as an indicator. The reactor effluent was collected for the sample analysis after 1.5 times of the space time (7.30 min), which is much greater than the time (2.24 min) required to reach the steady state temperature distribution. Since experimental observations revealed steady-state concentration values of all the species (reacted, and unreacted) at a given operating condition for each experimental run, samples were collected after 1-2.5 times of the space-time value and there has been no change in the concentration values. Thus, it ensures the attainment of adsorption equilibrium. The titration was repeated in triplicates and the results were considered from the average of three independents.

Table 5.14. Box Behnken layout showing different parametric combinations for concurrent esterification of OA and methanol

Runs	Parameters (ψ_{CC}) Catalyst concentration (wt.%)	Parameters (ψ_T) Reaction temp (K)	Parameters (ψ_{MR}) Methanol: OA mole ratio	Parameters (ψ_{LHSV}) LHSV (min^{-1})	experimental MO yield (ψ_{MO}) (%)	Model MO yield (%)
1	0	0	1	-1	70.25	70.25
2	1	1	0	0	76.23	76.5
3	1	0	0	1	70.12	70.12
4	0	-1	1	0	61.18	61
5	0	0	0	0	75.85	75
6	0	-1	-1	0	60.45	60.01
7	0	0	0	0	75.85	75

8	0	0	1	1	59.88	59.23
9	-1	-1	0	0	59.45	59.4
10	0	1	1	0	72.8	72
11	-1	0	1	0	64.85	64
12	0	1	0	-1	74.47	74.47
13	0	-1	0	-1	69	68.8
14	1	0	-1	0	64.9	63.12
15	0	0	0	0	75.85	75
16	1	-1	0	0	60	59.88
17	0	1	0	1	79.04	80.36
18	1	0	0	-1	64.12	64.12
19	1	0	1	0	65	64.23
20	-1	0	0	-1	73.4	72.56
21	0	0	-1	-1	65.8	65.25
22	0	1	-1	0	75.14	75.6
23	-1	0	-1	0	72	71.23
24	0	0	0	0	75.85	75
25	-1	1	0	0	76.82	76.23
26	0	0	-1	1	70.3	70.69
27	0	-1	0	1	55	54
28	0	0	0	0	75.85	75
29	-1	0	0	1	61.65	61.22

The acid number $A_{oleic\,acid}$, OA conversion $\theta_{oleic\,acid}$, and MO yield $\psi_{methyl\,oleate}$, LHSV R_{LHSV} were calculated using Eq. (5.26), (5.27), (5.28), and (5.29); respectively.

$$A_{oleic\,acid} = \frac{56.11 \times M_{KOH} \times V_{KOH}}{m_{methyl\,oleate}} \tag{5.26}$$

$$\theta_{oleic\,acid} = \frac{A_{oleic\,acid,t=t_i} - A_{oleic\,acid,t=t_0}}{A_{oleic\,acid,t=t_0}} \times 100 \tag{5.27}$$

$$\psi_{methyl\,oleate} = \frac{moles\,of\,methyl\,oleate\,formed}{moles\,of\,oleic\,acid\,converted} \times 100 \tag{5.28}$$

$$R_{LHSV} = \frac{void\,volume(cm^3)}{volumetric\,flowrate(cm^3)} \tag{5.29}$$

5.4.6 Characterization of Catalyst

The characterizations were reported for supported BMZTO/glass bead photocatalysts that rendered maximum OA conversion at optimal reaction conditions. High-resolution X-ray diffraction (HR-XRD) was conducted to identify the active phase composition in the catalyst using Bruker D8 (Cu Kα λ = 0.15406 nm). Fourier Transform Infrared Spectrometer (FT/IR-4100, JASCO, Easton, MD) was employed to investigate the chemical structural features of the manufactured catalyst in the range of 4000-400 cm^{-1}. The morphology of the catalyst at optimal composition was observed by FESEM at 17 kV (Supra 40 VP instrument Zeiss Co., Germany) coupled to an EDS detector (Oxford Instruments, UK) that provided the sample micrographs (70 µm) and the corresponding elemental composition. Transmission electron microscopy (JEM-2200FS instrument JEOL Co., USA) analysis was carried out for the requisite catalyst, and the HR-TEM was applied to study the d-spacing between the lattice planes existing in the prepared optimum catalyst. The optical properties and recombination properties of the optimum sample were recognized by using UV/VIS/NIR spectrometer (JASCO V-670, Japan) and luminescence meter (JASCO FP-6500).

5.4.7 Recycle Reactor Study

A section of MRPBR where fresh methanol and OA are mixed with a portion of MO (consists of MO, unreacted OA, and methanol) releases from a packed bed reactor outlet is known as recycle flow. If the recycle flow rate is relatively higher than the inlet flow rate, at that point, the reaction system is identified as a "Recycle reactor." In order to make the process energy-efficient, recycling is often used in industrial operations. The recycle reactor has some advantages; for example, the temperature of the reaction system could be precisely controlled, and due to high recirculation rates,

mass transfer resistances could be reduced significantly [22]. The recirculation is defined as recycle ratio $RR = \frac{F_{V_R}}{F_V}$, where F_{V_R} : the volumetric flow rate of fluid returning to the reaction chamber entrance and F_V : the volumetric flow rate of fluid leaving the system. The reactor model corresponded to a lab-scale experiment developed in a simplified way with the aid of negligible pressure drop with respect to the system pressure. Consequently, the temperature of the recycle stream remained constant throughout the system [23].

5.4.8 Mass Transfer in Packed Bed

In heterogeneous catalytic reactions, liquid-solid mass transfer plays a significant role. The external and internal diffusion from bulk to catalyst surface area and from surface to interior of catalyst, respectively, act as resistances in the packed bed reactor system. In order to evaluate the surface kinetics, the effect of mass transfer elimination played a crucial role. To identify the external mass transfer coefficients under the steady-state conditions in MRPBR, Mears criterion (C_m) (Eq. 5.30) [24] is used by varying the feed flow rate in the range of 3.28 to 39.46 mL/min. To check the relationship between the reaction rate and the diffusion rate of the reactant molecules within the catalyst and the surface of heterogeneous catalyst from the bulk of fluid is given below:

$$C_m = \frac{-r_A \rho_b Rn}{k_C C_{oleic\,acid}} \prec 0.15 \qquad (5.30)$$

The mass transfer coefficient (k_C) could be evaluated from the correlation of Sherwood number (Sh) (Eq. 5.31).

$$k_C = \frac{1-\phi}{\phi}\left(\frac{D_{oleic\,acid\_methanol}}{d_P}\right)Sh \qquad (5.31)$$

The relationship of k_C with Sh has been described by molecular diffusion co-efficient $D_{oleic\,acid\_methanol}$ (Eq. 5.32, 5.33) for OA in methanol using Wilke-Chang correlation [25] where φ is the porosity, Sh is a function of Reynolds number (Re) and Schmidt number (Sc). Re was estimated with respect to superficial velocity (U).

$$D_{oleic\,acid\_methanol} = \frac{7.4\times10^{-8}\left(\psi_{methanol} M_{methanol}\right)^{1/2} T}{\mu_{methanol} V_{oleic\,acid}^{0.6}} \tag{5.32}$$

$$Sh = (\mathrm{Re})^{\frac{1}{2}} (Sc)^{\frac{1}{3}} \tag{5.33}$$

$$\mathrm{Re} = \frac{U d_P}{(1-\varphi)\upsilon} \tag{5.34}$$

$$Sc = \frac{\upsilon}{D_{oleic\,acid\_methanol}} \tag{5.35}$$

Thoenes-Kramers correlation [26] for flow through packed bed had proposed the above Eq. (5.33) for $0.25 \prec \varphi \prec 0.5$, $40 \prec \mathrm{Re} \prec 4000$, and $1 \prec Sc \prec 4000$.

Similarly, according to the evaluation of the internal mass transfer limitation, the Weisz-Prater parameter (C_{WP}) [27, 28] has been calculated using Eq. 5.36. The effective diffusion coefficient (D_{eff}) and particle tortuosity (τ) have been evaluated through Eq. 5.37 and 5.38, respectively.

$$C_{WP} = \frac{-r_A \rho_b R^2}{D_{eff} C_{oleic\,acid}} \prec 1 \tag{5.36}$$

$$D_{eff} = \frac{D_{oleic\,acid\_methanol}\phi\sigma_C}{\tau} \tag{5.37}$$

$$\tau = 1 - 0.5\ln\varphi \tag{5.38}$$

For internal diffusion within the catalyst pores in packed bed reactor, the effectiveness

factor (η) is used to check whether internal diffusion is the rate-limiting step. It depends on the reaction order and catalyst shape. The relation between the effectiveness factor (η) and Thiele modulus (ϕ_{TM}) for spherical catalysts has been described in Eq. 5.39 and 5.40, respectively [29].

$$\eta = \frac{3}{\phi_{TM}^2}\left(\phi_{TM} Coth\phi_{TM} - 1\right) \tag{5.39}$$

$$\phi_{TM} = R\sqrt{\frac{k_1^{'}\rho_b S_a}{D_{eff}}} \tag{5.40}$$

5.4.9 Simulation of the Heat Transfer

In order to validate the experimental studies under the hybrid (MW-NIR) electromagnetic irradiation in observing the temperature profile theoretically in all domains, namely methanol-OA reactants flow, BMZTO solid catalysts, quartz tube, COMSOL Multiphysics software (version 5.5, COMSOL Inc.) has been selected for the simulation study. To determine the combined electromagnetic radiation heat transfer, heat transfer module has been chosen. The added physics interfaces are heat transfer in surface-to-surface radiation (htrad), heat transfer in solids and fluids, laminar flow, electromagnetic waves, frequency domain (emw). The following Multiphysics are heat transfer with surface-to-surface radiation (rad), nonisothermal flow, and electromagnetic heating (emh1). The frequency was set to 915 MHz and 35 MHz which are the operating frequency of the MW and near-infrared, respectively. Frequency-transient study has been used as a solver scheme to obtain the temperature profiles. The complete mesh of the model consists of 44 vertex elements, 1230 edge elements, 29644 boundary elements, 321726 total elements. To calculate the heat transfer in the porous matrix (packed bed filled with the solid-liquid system) as a function of time, the following transient equation (Eq. 5.41) and thermal radiation (Eq.

5.42) are calculated simultaneously in the simulation module.

$$\rho C_P \frac{\partial T}{\partial t} + \rho C_P u.\nabla T + \nabla.q = Q_{MW} + Q_{NIR}$$

$$q = -k\nabla T(\Delta H = +ve) \quad (5.41)$$

$$-n.q = \varepsilon_M \sigma\left(T_{amb}^4 - T^4\right) \quad (5.42)$$

where, ρ, C_P, k, q, ε_M, σ, T_{amb}, and T are density, heat capacity, thermal conductivity, the total heat flux, emissivity, Stefan-Boltzmann constant, ambient temperature, and temperature of the catalyst bed; respectively. The symbol u stands for the flow velocity vector field for 3-D modeling. The simulation model reflects the geometry of the experimental MRPBR. The minimum percentage of the reactor volume has been considered to reduce the computational load.

5.4.10 Evaluation of Esterification Kinetics

Under the optimal operating condition of MRPBR, considering negligible mass transfer resistances, the esterification of methanol and OA with BMZTO can be regarded as a surface reaction limited under uniform temperature distribution. The heterogeneous kinetics of two parallel reactions representing a very useful autocatalytic parallel esterification as depicted in Eq. 5.43 and 5.44 was modelled using LH duel site mechanism, and ER model, PH mechanism on the active site of the catalyst surface as follows:

$$C_{18}H_{34}O_2 + CH_3OH \xrightarrow{k_1 / BMZTO(as\,catalyst)} C_{19}H_{36}O_2 + H_2O(in-situ\,adsorption)$$

(non-recycle) (5.43)

$$C_{18}H_{34}O2 + CH_3OH + C_{19}H_{36}O_2 \xrightarrow{k_2 / C_{19}H_{36}O_2(as\,catalyst)} 2C_{19}H_{36}O_2 + H_2O(in-situ\,adsorption)$$

(recycle) (5.44)

In non-recycle stream, the esterification was considered to be irreversible (as water

was adsorbed on molecular sieves), whereas under recycling conditions the autocatalytic behavior was pronounced through augmented yield of MO. In such a process, reaction proceeds in parallel involving simultaneous reactions as per Eq. 5.43, 5.44. A careful inspection of the stream compositions under optimal recycle indicates that the mole fraction of methanol and OA are in excess in comparison with MO in MIXFEED1. Thus, the reactants were not in a stoichiometric ratio (Eq. 5.44) as per the autocatalytic reaction stoichiometry. Since the methanol and OA are in large excess in the combined reactor feed (MIXFEED1), it is imperative to consider the practical occurrence of MO formation through Eq. 5.43 in addition to Eq. 5.44.

Justification of the kinetic model is of crucial importance. The kinetic model was developed on the following assumptions: isothermal reactor, negligible external and internal mass transfer resistances, and the surface of the catalyst is considered to have a uniform distribution of active sites. Heterogeneous esterification rate equations considering the surface reaction as a rate-limiting step might follow the LH (Eq. 5.47, 5.51) or ER mechanism (Eq. 5.48, 5.52, 5.49, 5.53, 5.54) with respect to the reactive species involved; whereas PH model was expressed by Eq. 5.50, 5.55. Notably, the adsorption equilibrium is related to the bulk phase concentrations vis-à-vis the corresponding activity coefficients of the species involved. In the present study, the non-random two liquids (NRTL) model has been used to determine the activity coefficient (γ_i) of the components present in the reaction mix. Binary interaction parameters in the NRTL model were obtained from the ASPEN plus database. A detailed calculation of γ_i has been provided. To estimate the behavior of the reaction mixture, the activity coefficient (γ_i) has been measured. A non-random two liquids (NRTL) activity co-efficient model was employed to calculate the γ_i using Eq. 5.56

[30]. The binary interaction parameters were determined from the LLE data correlation estimated from the NRTL model by the ASPEN plus simulation. The binary interaction parameters of the NRTL model as obtained from the ASPEN plus database are listed in Table 5.15.

Table 5.15. NRTL model parameters

Component i	**Component j**	**Source**	a_{ij}	a_{ji}	b_{ij}	b_{ji}	α_{ij}
Methanol (1)	OA (2)	R-PCES	0	0	662.83	-182.31	0.3
Methanol (1)	MO (3)	R-PCES	0	0	997.38	66.97	0.3
OA (2)	MO (3)	R-PCES	0	0	-132.52	255.54	0.3
MO (3)	Water (4)	R-PCES	0	0	930.14	5916.04	0.3

Activity coefficient of each component present in the reaction system was measured. The activity coefficient of methanol, OA, and MO are 1.000563, 1.000202, and 1.00162, respectively. In this regard, γ_i shows an ideal behavior of the reaction mixture, and its value is considered to be approximately 1. Remarkably, the value of γ_i for each component present in the reaction mix was found to be approximately 1 (computed using Eq. 5.56). Consequently, the activity coefficient was not mentioned in the kinetic rate equations. The fitting of the experimental data using the Levenberg-Marquardt (L-M) algorithm was employed through non-linear fitting in Polymath 5.1 software. Intensively used squared regression coefficient (R^2) or residual sum of squares (RSSQ) could provide a reliable indication of the fitness of the model. The design equations of MPBR and MRPBR are expressed in Eq. 5.45 and Eq. 5.46, respectively, as follows:

$$F_{OA0}\frac{dX_{OA}}{dW} = -r^{'} \tag{5.45}$$

$$(1+RR)F_{OA0}\frac{dX_{OA}}{dW} = -r^{''} \tag{5.46}$$

$$-r_{LH}^{'} = \frac{k_1\left[K_{OA}C_{OA}K_M C_M\right]}{\left[1+K_{OA}C_{OA}+K_M C_M+{C_{MO^{'}}}/{K_{MO^{'}}}\right]^2} \tag{5.47}$$

$$-r_{EROA}^{'} = \frac{k_1\left[K_{OA}C_{OA}C_M\right]}{\left[1+K_{OA}C_{OA}+{C_{MO^{'}}}/{K_{MO^{'}}}\right]} \tag{5.48}$$

$$-r_{ERM} = \frac{k_1\left[K_M C_M C_{OA}\right]}{\left[1+K_M C_M+{C_{MO^{'}}}/{K_{MO^{'}}}\right]} \tag{5.49}$$

$$-r_{PH} = k_1 C_M^a C_{OA}^b \tag{5.50}$$

$$-r_{LH}^{''} = \frac{k_1\left[K_{OA}C_{OA}K_M C_M\right]}{\left[1+K_{OA}C_{OA}+K_M C_M+{C_{MO^{'}}}/{K_{MO^{'}}}\right]^2} + \frac{k_2\left[K_{OA}C_{OA}K_M C_M K_{MO^{'}}C_{MO^{'}}\right]}{\left[1+K_{OA}C_{OA}+K_M C_M+K_{MO^{'}}C_{MO^{'}}+{C_{MO}}/{K_{MO}}\right]^2} \tag{5.51}$$

$$-r_{EROA}^{''} = \frac{k_1\left[K_{OA}C_{OA}C_M\right]}{\left[1+K_{OA}C_{OA}+{C_{MO^{'}}}/{K_{MO^{'}}}\right]} + \frac{k_2\left[K_{OA}C_{OA}C_M C_{MO^{'}}\right]}{\left[1+K_{OA}C_{OA}+{C_{MO}}/{K_{MO}}\right]} \tag{5.52}$$

$$-r_{ERM}^{''} = \frac{k_1\left[K_M C_M C_{OA}\right]}{\left[1+K_M C_M+{C_{MO^{'}}}/{K_{MO^{'}}}\right]} + \frac{k_2\left[K_M C_M C_{OA}C_{MO^{'}}\right]}{\left[1+K_M C_M+{C_{MO}}/{K_{MO}}\right]} \tag{5.53}$$

$$-r_{ERMO^{'}}^{''} = \frac{k_1\left[K_M C_M K_{OA}C_{OA}\right]}{\left[1+K_{OA}C_{OA}+K_M C_M+{C_{MO^{'}}}/{K_{MO^{'}}}\right]} + \frac{k_2\left[K_{MO^{'}}C_{MO^{'}}C_{OA}C_M\right]}{\left[1+K_{MO^{'}}C_{MO^{'}}+{C_{MO}}/{K_{MO}}\right]} \tag{5.54}$$

$$-r_{PH}^{''} = k_1 C_M^a C_{OA}^b + k_2 C_M^{a1} C_{OA}^{b1} C_{MO^{'}}^{c1} \tag{5.55}$$

$$\ln \gamma_i = \frac{\sum_{j=1}^{C} \tau_{ji} G_{ji} x_j}{\sum_{k=1}^{C} G_{ki} x_k} + \sum_{j=1}^{C} \frac{x_j G_{ij}}{\sum_{k=1}^{C} G_{ki} x_k} \left(\tau_{ij} - \left(\frac{\sum_{r=1}^{C} x_r \tau_{rj} G_{rj}}{\sum_{k=1}^{C} G_{ki} x_k} \right) \right)_{T_{lower} < T < T_{upper}} \quad (5.56)$$

Where, $G_{ij} = \exp\left(-\alpha_{ij}\tau_{ij}\right)$, $\tau_{ij} = a_{ij} + \left(b_{ij}/T\right)$, $G_{ji} = \exp\left(-\alpha_{ij}\tau_{ji}\right)$, $\tau_{ji} = a_{ji} + \left(b_{ji}/T\right)$.

a_{ij} : interaction parameters of the NRTL model for i-j pair (K), b_{ij} : interaction parameters of the NRTL model for i-j pair (K), C: number of components, τ_{ij} : interaction parameters of the NRTL model for i-j pair, G_{ij} : variable in the NRTL model for i-j pair, α_{ij} : non-randomness parameter in the NRTL model, γ_i : activity co-efficient for component i.

Table 5.16. Model summary of the heater

Heater	
Name	HEATER
Property method	NRTL
Use true species approach for electrolytes	YES
Free-water phase properties method	STEAM-TA
Water solubility method	3
Specified pressure [bar]	1.0132
Specified temperature [C]	60
Calculated pressure [bar]	1.0132
Calculated temperature [C]	60
Calculated vapor fraction	0
Calculated heat duty [cal/sec]	1412.96163
Net duty [cal/sec]	1412.96163
First liquid / total liquid	1

5.4.11 Process Simulation Methodology

To assess the viability of the scale-up of the developed reaction kinetic model (at optimal conditions) in the MRPBR; modeling of the esterification process has been performed both at lab-scale and large-scale reactors. In this study, ASPEN PLUS (V.11.1) process simulator was used to conduct the modeling. The model was developed using a throughput scale-up factor of 1000 considering geometric similarity. The developed appropriate kinetic model (LH kinetics) was employed for the

simulation. Since the esterification has a strong impact on the liquid-liquid equilibrium (LLE) and as the reaction was conducted at 1atm, a NRTL activity coefficient model has been recommended [31]. The detailed procedure and the realistic approximations considered for the ASPEN simulation are outlined in Table 5.16-5.22.

Table 5.17. Model summary of separator

Separator	
Name	SEPARATE
Property method	NRTL
Use true species approach for electrolytes	YES
Free-water phase properties method	STEAM-TA
Water solubility method	3
Inlet flash pressure [bar]	1.0132
First outlet flash temperature [C]	60
First outlet flash pressure [bar]	1.0132
Second outlet flash temperature [C]	60
Second outlet flash pressure [bar]	1.0132
Heat duty [cal/sec]	15260.1606

Table 5.18. Model summary of pumps

Pump			
Name	PUMP1	PUMP2	PUMP3
Property method	NRTL	NRTL	NRTL
Use true species approach for electrolytes	YES	YES	YES
Free-water phase properties method	STEAM-TA	STEAM-TA	STEAM-TA
Water solubility method	3	3	3
Model Type			
Specified discharge pressure [bar]	1.0132	1.0132	1.0132
Pump efficiencies	0.75	0.75	0.75
Driver efficiencies	0.9	0.9	0.9
Volumetric flow rate [l/min]	3.17684003	4.30935669	11.1333523
Calculated discharge pressure [bar]	1.0132	1.0132	1.0132
Calculated pressure change [bar]	0	0	0
NPSH available [m-kgf/kg]	11.8222907	8.68043326	3.19431344
Pump efficiency used	0.75	0.75	0.75

Table 5.19. Model summary of valves

	Valve				
Name	VALVE1	VALVE2	VALVE3	VALVE4	VALVE5
Property method	NRTL	NRTL	NRTL	NRTL	NRTL
Use true species approach for electrolytes	YES	YES	YES	YES	YES
Free-water phase properties method	STEAM-TA	STEAM-TA	STEAM-TA	STEAM-TA	STEAM-TA
Water solubility method	3	3	3	3	3
Specified outlet pressure [bar]	1.0132	1.0132	1.0132	1.0132	1.0132
Calculation type	ADIAB-FLASH	ADIAB-FLASH	ADIAB-FLASH	ADIAB-FLASH	ADIAB-FLASH
Valve pressure specification (design mode)	P-OUT	P-OUT	P-OUT	P-OUT	P-OUT
Valve pressure specification (rating mode)	VAL-POSN	VAL-POSN	VAL-POSN	VAL-POSN	VAL-POSN
Calculated outlet pressure [bar]	1.0132	1.0132	1.0132	1.0132	1.0132
Calculated pressure drop [bar]	0	0	0	0	0
Piping geometry factor	1	1	1	1	1

Table 5.20. Model summary of MRPBR

RPlug	
Name	CFHMRPBRR
Process stream property method	NRTL
Process stream use true species approach for electrolytes	YES
Process stream free-water phase properties method	STEAM-TA
Process stream water solubility method	3
Thermal fluid property method	NRTL
Thermal fluid use true species approach for electrolytes	YES
Thermal fluid free-water phase properties method	STEAM-TA
Thermal fluid water solubility method	3
Reactor dimensions length [meter]	13.57
Reactor dimensions diameter [meter]	1
Pressure at reactor inlet: process stream [bar]	0
Heat duty [cal/sec]	1484.36391
Minimum reactor temperature [C]	60
Maximum reactor temperature [C]	60
Residence time [hr]	3.09784074

Table 5.21. Model summary of mixers

Mixer		
Name	MIXER1	MIXER2
Property method	NRTL	NRTL
Use true species approach for electrolytes	YES	YES
Free-water phase properties method	STEAM-TA	STEAM-TA
Water solubility method	3	3
Specified pressure [bar]	0	0
Outlet temperature [C]	38.5477656	51.4573916
Calculated outlet pressure [bar]	1.0132	1.0132
Vapor fraction	0	0
First liquid /Total liquid	1	1

Table 5.22. Model summary of the splitter

Splitter	
Name	SPLITTER
Property method	NRTL
Henry's component list ID	
Electrolyte chemistry ID	
Use true species approach for electrolytes	YES
Free-water phase properties method	STEAM-TA
Water solubility method	3
First outlet stream	
First specified split fraction	
First flow [kmol/hr]	
First calculated split fraction	0.411628336
Second outlet stream	
Second specified split fraction	
Second flow [kmol/hr]	9.78
Second calculated split fraction	0.588371664

5.5 ACTIVITY V

Barnacle carapace-chitosan supported highly-efficient nano Al-W alloy electrocatalyst for sustainable bio-GL valorization: Environmental impact and cost analyses

5.5.1 Materials

Rock barnacles (*Balanus balanoides*) with carapace were collected from the rocks alon g the seashore, and pork lard was collected from a slaughterhouse. CH (low molecular weight), ammonium metatungstate hydrate (99.99%), aluminum chloride hexahydrate (

99%), sodium hydroxide (97%), a Nafion solution (5%), glyceraldehyde, L-glyceric aci d sodium salt, formic acid, and D_2O were purchased from Sigma-Aldrich Co., USA. Ni ckel foam (Ni-foam) (pore size of 0.2-0.5 mm and thickness of ~1.5 mm) was obtained from Taiyuan Liyuan Technology Co. Ltd., China. Pristine multiwalled carbon nanotub es (MWNTs, 3 wt.% in water, purity >95%, diameter = 20-30 nm, length = 10-30 μm) were procured from Nanostructured & Amorphous Materials, Inc. All other chemicals were obtained from Samchun Chemicals, Republic of Korea. All the electrolytes were prepared using deionized (DI) water. All chemicals were of AR grade and were used as received.

5.5.2 Preparation of Functionalized Chitosan

The rock barnacles were obtained from the seashore. Chitin and deacetylated chitin samples were prepared using a previously reported established method with slight modifications (Figure 5.5a) [32]. Initially, 25 g of barnacle was intensely and repeatedly washed with running tap water for 15-20 min to remove the flesh and fats. Then the wet sample was oven dried at 60 °C overnight. Subsequently, the dry substance was grinder-ground to a fine powder. To remove the impurities, mainly calcium phosphate and calcite, 10 g of powder sample was demineralized with 1M HCl solution at a substrate/solution ratio of 1:15 (w/v) at room temperature for 10 min. Next, the treated material was washed and filtered with DI water/EtOH until neutral pH. After that, the deproteinization process was applied to remove proteins by treating them with 2 M NaOH solution at room temperature for 20 min. Subsequently, the decolorization was executed using acetone, the precipitate was thoroughly washed with DI water and filtered through filter paper. Lastly, the deacetylation process was implemented to convert chitin to CH. The dried chitin (290 mg) was processed with 50% NaOH solution (1:10 w/v) at 100 °C for 6 h. To get CH, NaOH-treated chitin was neutralized

with DI water washing, and filtration was carried out through filter paper. After each treatment process, the sample was oven-dried at 70 °C for 2 h.

5.5.3 Preparation of Al/W@functionalized MWNT-chitosan Nanocomposites

A chemical reduction method has been proposed to prepare Al_1/W_2@FMWNT-CH nanocomposites (Figure 5.5b). Primarily, functionalized CH has been developed by dissolving a prerequisite amount of preheated lab-prepared water-insoluble deacetylated chitin (rock barnacles) powder of 0.2 g in 50 mL of 1% (v/v) acetic acid solution [33]. The dissolution process was carried out with a continuous magnetic stirring speed of 700 rpm at 25 °C for a minimum of 24 h until the crystal-clear solution appeared. As a result, the amino group of CH is readily protonated to form NH^{3+}. After getting a transparent solution of CH, 0.04 g of MWNT was added to the CH solution under ultrasonication for 2 h to obtain a homogeneously dispersed black suspension of FMWNT-CH. To prepare Al/W@FMWNT-CH alloy composite, 0.1 mmol of ammonium meta-tungstate hydrate and 0.05 mmol of aluminum chloride hexahydrate, were added to the FMWNT-CH solution one after another and were stirred for 20 min. After that, 90 mg of ascorbic acid was poured into the solution to reduce the salt to its zero valence. In forming the nanocomposite alloy, ascorbic acid was used as a reducing agent. Then, the solution was stirred for 5 h at 80 °C. Afterward, co-precipitation took place by adding NH_4OH drop-wise to keep the pH at 9 ± 0.5, and the mixture was retained for aging overnight. After a while, the reactor effluent was centrifuged and washed rigorously with DI water/acetone to eliminate all excess reducing agents from the solution. To obtain the Al/W alloy supported on FMWNT-CH, the suspension was transferred to the suitably sized container (polytetrafluoroethylene) and oven-dried at 70 °C for 3 h. For comparison, Al/W, Al@MWNT, W@MWNT, Al@CH, W@CH, Al@FMWNT-CH, and W@FMWNT-CH composites were also prepared. Similarly,

Al/W@FMWNT-CH was prepared with various Al:W mole ratios of 3:1, 2:1,1:2 to optimize the efficiency of the catalyst.

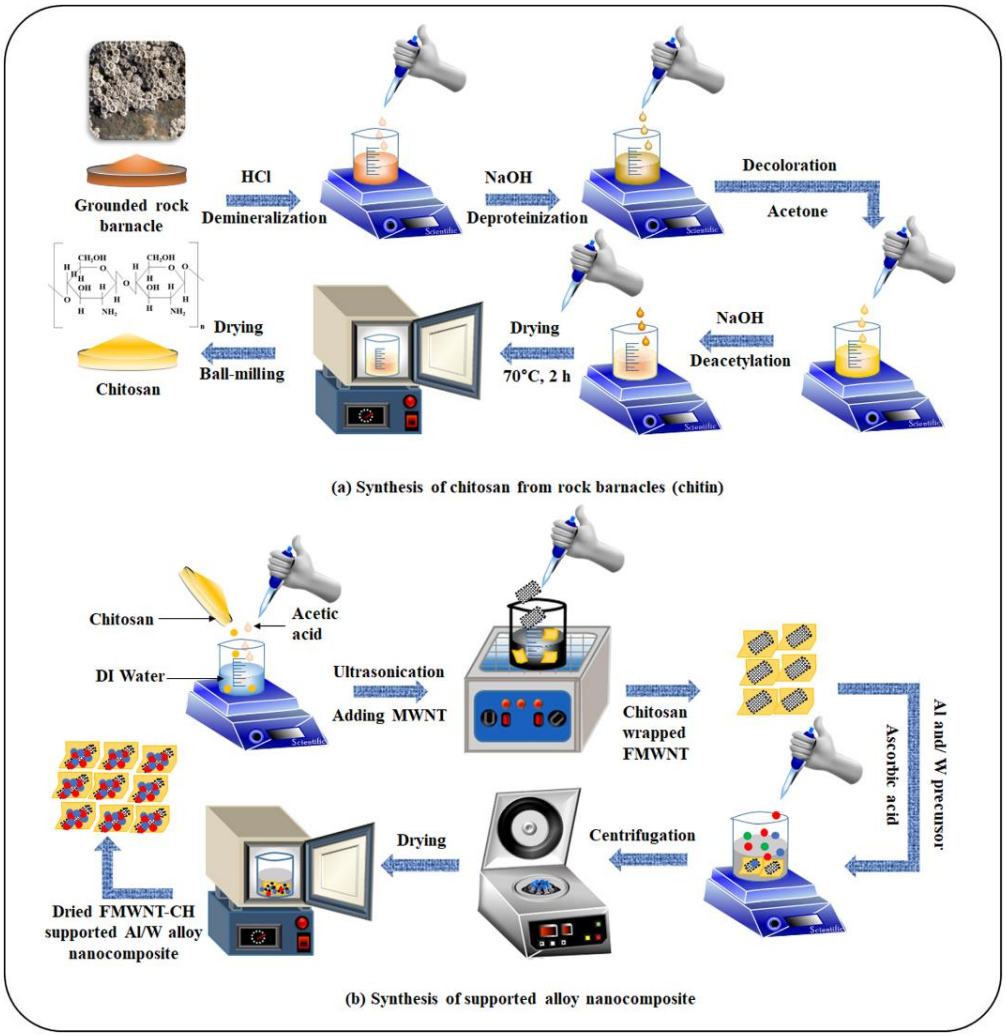

Figure 5.5. Schematic of (a) chitosan synthesis from barnacle carapace and (b) nanocomposite synthesis

5.5.4 Cleaning of Ni-Foam

Ni-foam (1 cm × 1 cm) was treated with 1 M HCl solution under ultrasonication for 20 min to eliminate the NiO_X layer and contaminants. Next, it was again ultrasonicated using acetone, and absolute EtOH (each for 15 min) and was dried in a hot air-oven to ensure a clean surface.

5.5.5 Electrode Preparation

The working electrodes were prepared by coating the catalyst ink onto Ni-foam. Prior to uniform dispersion, 7 mg of catalyst powder was added to 20 µL of a Nafion (5 wt.%) solution, 0.25 mL of DI water, and 0.75 mL of isopropyl alcohol, followed by ultrasonication for 2 h. Following, the homogeneous ink (90 mg cm^{-2}) was drop-casted onto the pre-cleaned Ni-foam, which was then dried in a hot air-oven overnight at 50°C.

5.5.6 Electrocatalytic Reaction

The present work involves bio-GL as a by-product of synthesizing pork lard methyl esters (biodiesel). The transesterification was done with pork lard and methanol, where KOH was used as an alkali catalyst. However, the procedure for preparing pork lard methyl esters and separating bio-GL has been explained elsewhere [34]. A three-electrode system was employed for all electrocatalysis studies consisting of as-prepared electrocatalysts as a working electrode, Pt wire as a counter electrode, and Ag/AgCl as a reference electrode. A VersaSTAT3 potentiostat was employed for electrochemical measurements. All electrochemical measurements for oxygen evolution reaction (OER), bio-GL oxidation reaction (GOR), and hydrogen evolution reaction (HER) were performed in N_2-saturated 1 M NaOH electrolytes without and with 0.5 M bio-GL electrolyte solution. All electrochemical experiments were conducted at 25 °C and 1 atm pressure. In the electrocatalytic reaction, bio-GL is converted through the intermediate glyceraldehyde to produce glyceric acid, H^+, and e^- at the anode. Concurrently, H^+ is transported to the cathode from the anode via the electrolyte medium and combined with the e^- to form renewable H_2 gas. Therefore, combining glyceric acid from GOR at the anode and HER at the cathode took place to

achieve overall bio-GL electrolysis. It is worth mentioning that among the all-prepared catalysts, the catalyst, Al_1/W_2@FMWNT-CH, showed the best electrocatalytic performance toward bio-GL electrolysis. Thus, further characterizations have been carried out with the aforementioned catalyst.

5.5.7 Electrochemical Studies

The polarization curves were recorded by performing linear sweep voltammetry (LSV) at a scan rate of 1 mV s^{-1} in the potential window -0.6 to 2 V vs. RHE. All potentials reported were calibrated against a reversible hydrogen electrode potential ($E_{(vs.RHE)}$) at pH 11 using Eq. 5.57. To evaluate the electrodes' anodic and cathodic catalytic activity, Tafel slopes were drawn. The LSV and cyclic voltammograms (CV) curves were plotted after iR correction. CVs were recorded at various scan rates ranging from 1 to 80 mV s^{-1}.

$$E_{(vs.RHE)} = E_{(vs.Ag/AgCl)} + 0.059\,pH + E^{\circ}_{Ag/AgCl} \tag{5.57}$$

Further, the iR-corrected potential ($E_{iR-corrected}$) was calculated using Eq. 5.58 as follows:

$$E_{iR-corrected} = E_{(vs.RHE)} - i \times R_{ES} \tag{5.58}$$

where $E^{\circ}_{Ag/AgCl} = 0.197V$ at 25°C, $E_{Ag/AgCl}$ is measured potential vs. the Ag/AgCl electrode, i is current, and R_{ES} represents equivalent series resistance. The anti-corrosion proficiency of the prepared catalysts with and without support has been assessed by electrochemical impedance spectroscopy (EIS) measurements. Bio-GL conversion $(\theta_{glycerol})$ was calculated using Eq. 5.59.

$$\theta_{glycerol} = \frac{C_{glycerol,t=t_i} - C_{glycerol,t=t_0}}{C_{glycerol,t=t_0}} \times 100 \quad (5.59)$$

The electricity consumption per m^3 of H_2 produced (W, kWh per m^3 H_2) was calculated based on the following Eq. 5.60 [35]

$$W_{H_2} = \frac{n \times F \times U \times 1000}{3600 \times V_m} \quad (5.60)$$

where, W_{H_2} is the electricity consumption per unit of H_2 production (W, kWh per m^3 H_2), n is the number of electrons transferred for each product molecule ($n = 2$), U is the applied voltage, and V_m is the molar volume of the gas at normal temperature and pressure (22.4 L mol^{-1})

5.5.8 Materials Characterization

Structural analyses of different composites were conducted using wide-angle X-ray diffraction analysis (D/Max 2500 V/PC; Rigaku Co., Japan) with a 2θ range from 10 to 80° at a scan rate of 2°/min using Cu-Kα radiation (λ = 0.154 nm). Field emission scanning electron microscopy (FESEM, Supra 40 VP instrument Zeiss Co., Germany) equipped with an energy dispersive X-ray (EDX) system (Oxford Instruments, UK), transmission electron microscopy (TEM, JEM-2200FS instrument JEOL Co., USA), high-resolution transmission electron microscopy (HRTEM) were used for the morphological and micro and/or nanostructural characterization. In tapping mode, the surface topological properties of fabricated samples were analyzed using atomic force microscopy (AFM, NX10 Park System). A Fourier Transform Infrared Spectrometer (FT-IR-4100, JASCO, Easton, MD) was used to explore the chemical structural and functional information of the product catalyst in the range of 4000-400 cm^{-1}. The electronic state of the elements present in the catalyst was obtained by X-ray

photoelectron spectrometry (XPS, VG ESCALAB 220i, Thermo Fisher, UK) analysis with the binding energies for the catalyst compositions calibrated using C1s at 284.6 eV. Raman spectrometry (Nanofinder 30, Tokyo Instruments, INC., Japan) was used at 532.06 nm laser excitation with a laser power of 0.65 mW to detect the interfacial interaction with the molecular vibration among CH, FMWNT, and Al/W metal-alloy present in the catalyst. Pore structures were analyzed based on N_2-adsorption/desorption isotherms, and the Brunauer-Emmett-Teller (BET) algorithm and Barrett–Joyner–Halenda (BJH) theory were obtained to measure the specific surface area and pore size distribution, respectively. Degassing of all samples was carried out at 250 °C for 4 h before the adsorption experiment.

5.5.9 Product Quantification

Nuclear magnetic resonance (^{13}C NMR) measurements were conducted using JNM-ECZ600R (JEOL Ltd., solution-state NMR 500 MHz Spectrometer). To identify the oxidized products of bio-GL, the electrolyte medium was collected. The distinctiveness of glyceraldehyde, glyceric acid, and byproduct formic acid, developed in the bio-GL electro-oxidation in the alkali electrolyte medium, was confirmed by ^{13}C NMR analyses. ^{13}C NMR was recorded by analyzing the reaction mixture obtained after chronoamperometric measurements. The sample mix was prepared by diluting known amounts of compounds (50 mg) in 0.65 mL D_2O. Then, the sample was taken in the NMR tube for ^{13}C NMR. ^{13}C NMR spectra was recorded before and after the reaction. During electrolysis, the gaseous products produced from the cathode were collected and analyzed by gas chromatography (GC-2014C, SHIMADZU) coupled with a thermal conductivity detector where argon was used as the carrier gas.

5.5.10 Life Cycle Methodology

The LCA methodologies have been performed through two alternative scenarios: WPLG and commercial GL electrolysis system. This study aimed to compare the environmental impacts encompassing the production scale-up of 1 kg of glyceric acid and 0.5 kg of H_2 through the electrolysis of WPLG over commercial GL. The results obtained from the two resources have been compared by evaluating the environmental impact categories and economic cost. The LCA and the LCC studies have been performed using the *OpenLCA 1.11.0* open-access LCA software (GreenDelta Berlin) [36] by ISO-14044 international standards [37]. LCA consists of four stages: goal and scope definition, life cycle inventory (LCI), life cycle impact assessment (LCIA), and interpretation [38]. LCC was chosen as an indicator to determine economic performance. The goal was to perform a detailed LCI and LCIA study of the laboratory-scale synthesis process and quantify the environmental benefits of producing glyceric acid and H_2 energy from WPLG and commercial GL electrolysis. The Ecoinvent 3.5 database was used to attain "cradle-to-gate" inventories. To illustrate the effect of inputs as transportation of raw materials, depending on the availability of the data in the database, most data were taken from a global database. Some data used in the boundaries unavailable in the LCI database were generated with reasonable approximations. Electricity at high voltage (Republic of Korea) was used as an electricity source. Notably, the LCA results of the whole process have been determined based on the geographical location of Republic of Korea. The ReCiPe Midpoint (H) [39] impact assessment method was carried out to calculate the environmental impact category indicators, including climate change (GWP 100), fossil depletion (FDP), human toxicity (HTPinf), and particulate matter formation (PMFP), terrestrial ecotoxicity (TETPinf), agricultural land occupation (ALOP), and

water depletion (WDP) for the whole system boundary. The system's boundary is represented in Figure 5.6, including upstream, laboratory, and downstream processes. The upstream process includes chitin extraction from rock barnacle-carapace, transportation of metal precursors, and other chemicals used directly or indirectly to prepare the Al_1/W_2@FMWNT-CH electrode and the electrolyte for WPLG and commercial GL electrolysis. No transportation and purification costs have been comprised of chitin and laboratory made WPLG. The laboratory processes include synthesizing support material, anode/cathode electrode, and the electrolysis system assembly. Lastly, the downstream processes contain other waste flows toward waste treatment from upstream and laboratory techniques.

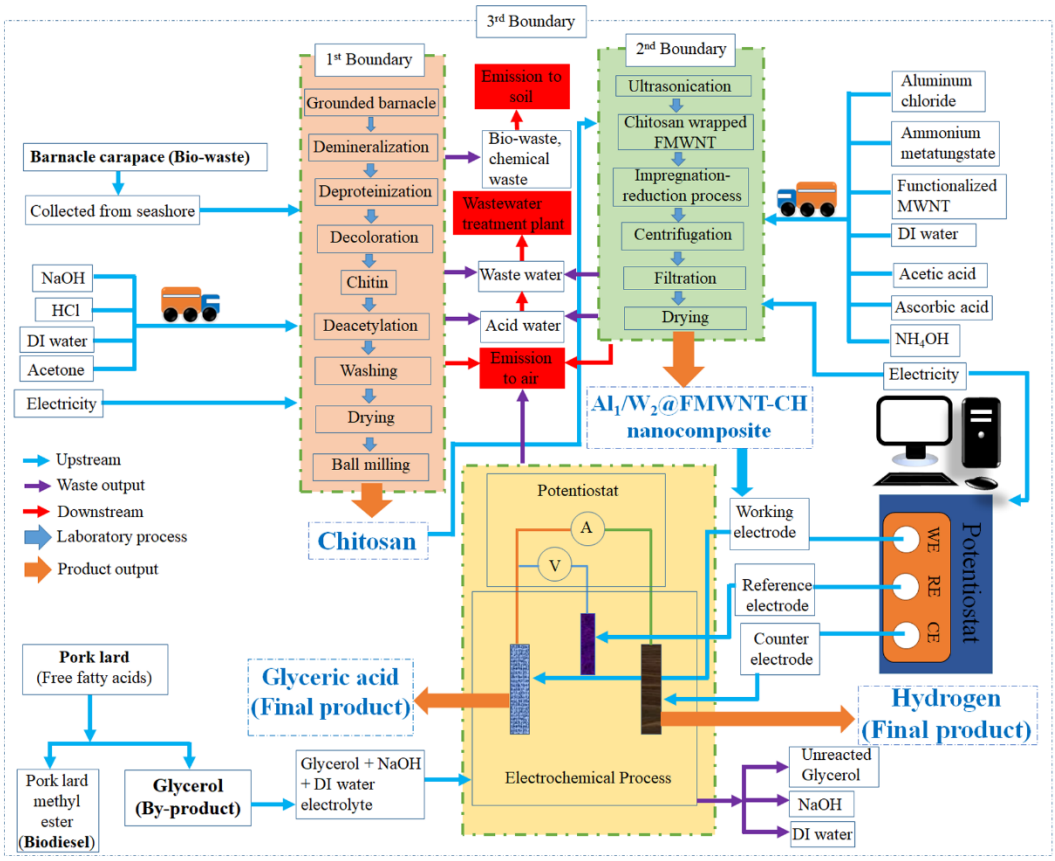

Figure 5.6. Flow diagram of the system boundaries in LCA

The ReCiPe Endpoint (H, A) impact assessment method was also followed to interpret the effect of waste emission on ecosystem quality, human health, and

resources. All input and output amounts and costs of each stage of WPLG and commercial GL electrolysis have been mentioned in Table 5.23-5.26. The quantity and price of different emissive substances (CO_2, CO, N_2O, CH_4, SO_2, NO_X) [40] in the air are shown in Table 5.27.

Table 5.23. LCI for 1 kg of CH preparation

Flow	Amount	Unit	Costs	Provider
Input				
acetone, liquid	0.25	kg	1.73 USD	market for acetone, liquid | acetone, liquid | APOS, S - RoW
chitin	0.25	kg		
electricity, high voltage	0.25	kWh	17.48 USD	electricity production, photovoltaic, 570kWp open ground installation, multi-Si | electricity, high voltage | APOS, S - KR
ethanol, without water, in 99.7% solution state, from ethylene	0.25	kg	1.91 USD	market for ethanol, without water, in 99.7% solution state, from ethylene | ethanol, without water, in 99.7% solution state, from ethylene | APOS, S - RoW
hydrochloric acid, without water, in 30% solution state	0.5	kg	1.4 USD	market for hydrochloric acid, without water, in 30% solution state | hydrochloric acid, without water, in 30% solution state | APOS, S - RoW
sodium hydroxide, without water, in 50% solution state	1	kg	38.91 USD	market for sodium hydroxide, without water, in 50% solution state | sodium hydroxide, without water, in 50% solution state | APOS, S - GLO
transport, freight, lorry 3.5-7.5 metric ton, EURO5	11.4	kg*km	15.66 USD	transport, freight, lorry 3.5-7.5 metric ton, EURO5 | transport, freight, lorry 3.5-7.5 metric ton, EURO5 | APOS, S - RoW
water, deionised	194	kg	1.42 USD	water production, deionised | water, deionised | APOS, S - RoW
Output			**Revenue**	
Chitosan	1	kg	337.69 USD	
Inert waste, for final disposal	1.58	kg		treatment of inert waste, inert material landfill | inert waste, for final disposal | APOS, S - RoW
Waste water treatment	2	l		treatment of wastewater, unpolluted, capacity 5E9l/year | wastewater, unpolluted | APOS, S - RoW

Table 5.24. LCI for 1 kg of Al_1/W_2@FMWNT-CH catalyst production

Flow	Amount	Unit	Costs	Provider
Input				
acetic acid, without water, in 98% solution state	0.1	kg	4.89 USD	acetic acid production, product in 98% solution state | acetic acid, without water, in 98% solution state | APOS, S - RoW
aluminium chloride	0.055	kg	84.93 USD	aluminium chloride production | aluminium chloride | APOS, S - GLO
Ammonium metatungstate hydrate	0.5	kg	107.94 USD	
ascorbic acid	5.00E-04	kg	3059.7 USD	ascorbic acid production | ascorbic acid | APOS, S - RoW
carbon black	0.1	kg	105.0 USD	carbon black production | carbon black | APOS, S - GLO
Chitosan	0.5	kg	168.875 USD	chitosan production - KR
electricity, high voltage	20.85	kWh	17.48 USD	electricity production, photovoltaic, 3kWp slanted-roof installation, single-Si, panel, mounted | electricity, high voltage | APOS, S - KR
nickel, 99.5%	0.11	kg	60.0 USD	market for nickel, 99.5% | nickel, 99.5% | APOS, S - GLO
transport, freight, lorry 3.5-7.5 metric ton, EURO5	194	kg*km	15.66 USD	market for transport, freight, lorry 3.5-7.5 metric ton, EURO5 | transport, freight, lorry 3.5-7.5 metric ton, EURO5 | APOS, S - RoW
water, deionised	1	kg	2.13 USD	water production, deionised | water, deionised | APOS, S - RoW
Output			**Revenue**	
Al/W@FMWNT-CH	1	kg	3626.50 USD	
inert waste, for final disposal	0.028	kg		treatment of inert waste, inert material landfill | inert waste, for final disposal | APOS, S - RoW
used outside air intake stainless steel, DN 370	0.18	items		treatment of used outside air intake, stainless steel, DN 370 | used outside air intake stainless steel, DN 370 | APOS, S - RoW
wastewater, average	0.54	l		treatment of wastewater, average, capacity 1E9l/year | wastewater, average | APOS, S - RoW

Table 5.25. LCI for 1 kg of glyceric acid and 0.5 kg of hydrogen production from WPLG electrolysis

Flow	Amount	Unit	Costs	Provider
Input				
Al/W@FMWNT-CH	0.005	kg	3626.515 USD	Al/W@FMWNT-CH production - KR
Ag/AgCl, reference electrode	0.2	kg	45.0 USD	anode slime, silver and tellurium containing stockpiling | anode slime, silver and tellurium containing stockpiling | APOS, S - RoW
Platinum wire, counter electrode	0.2	kg	128.5 USD	market for platinum | platinum | APOS, S - GLO
electricity, high voltage	20.85	kWh	17.48 USD	electricity production, photovoltaic, 3kWp slanted-roof installation, single-Si, panel, mounted | electricity, high voltage | APOS, S - KR
electrolyte, NaOH,	1	kg	56.52 USD	electrolyte production, NaOH | electrolyte, NaOH | APOS, S - GLO
WPLG	0.5	kg		
nickel, 99.5%	0.11	kg	60.0 USD	smelting and refining of nickel ore | nickel, 99.5% | APOS, S - GLO
transport, freight, lorry 3.5-7.5 metric ton, EURO5	194	kg*km	15.66 USD	transport, freight, lorry 3.5-7.5 metric ton, EURO5 | transport, freight, lorry 3.5-7.5 metric ton, EURO5 | APOS, S - RoW
water, deionised	0.5	kg		water production, deionised | water, deionised | APOS, S - RoW
Output			**Revenue**	
Glyceric acid	1	kg	10084.07 USD	
Hydrogen	0.5	kg	3.29 USD	
wastewater from fuel cell	0.0985	l		treatment of wastewater from PV cell production, capacity 5E9l/year | wastewater from PV cell production | APOS, S - RoW
Water vapor	0.1515	kg		

Table 5.26. LCI for 1 kg of glyceric acid and 0.5 kg of hydrogen production from commercial GL electrolysis

Flow	Amount	Unit	Costs	Provider
Input				
Al/W@FMWNT-CH	0.005	kg	3626.515 USD	Al/W@FMWNT-CH production - KR
Ag/AgCl, reference electrode	0.2	kg	128.5 USD	market for anode slime, silver and tellurium containing stockpiling | anode slime, silver and tellurium containing stockpiling | APOS, S - GLO
Platinum wire, counter electrode	0.2	kg	45.0 USD	market for platinum | platinum | APOS, S - GLO
electricity, high voltage	10.425	kWh	17.48 USD	electricity production, photovoltaic, 3kWp slanted-roof installation, multi-Si, panel, mounted | electricity, high voltage | APOS, S - KR
electrolyte, NaOH	1	kg	56.52 USD	market for electrolyte, NaOH | electrolyte, NaOH | APOS, S - GLO
glycerine	0.5	kg	315.59 USD	market for glycerine | glycerine | APOS, S - RoW
nickel, 99.5%	0.11	kg	60.0 USD	market for nickel, 99.5% | nickel, 99.5% | APOS, S - GLO
transport, freight, lorry 3.5-7.5 metric ton, EURO5	97	kg*km	15.66 USD	transport, freight, lorry 3.5-7.5 metric ton, EURO5 | transport, freight, lorry 3.5-7.5 metric ton, EURO5 | APOS, S - RoW
water, deionised	0.5	kg	2.13 USD	market for water, deionised | water, deionised | APOS, S - RoW
Output			**Revenue**	
Glyceric acid	1	kg	10084.07 USD	
Hydrogen	0.5	kg	3.29 USD	
wastewater from fuel cell	0.0985	l		treatment of wastewater from PV cell production, capacity 5E9l/year | wastewater from PV cell production | APOS, S - RoW
Water vapor	0.1515	kg		

Table 5.27. The amount and cost of different emission substances in air

Emissions	CO_2	CO	N_2O	CH_4	VOC	SO_2	NOx
$/kg	0.032	0.68	4.5	0.24	3.58	4.01	5.23
Chitosan	1.28	0.00094	0.00325	5.04E-9	0.00011	0.00484	5.49E-11
Al_1/W_2@FMWNT-CH	2.94	0.00198	0.00771	0.01212	6.09E-5	0.29	0.00771
WPLG electrolysis	1.59	0.0021	0.0042	2.56E-8	1.11E-5	0.0075	1.15E-10
Commercial GL electrolysis	3.77	0.0026	0.01061	0.1316	1.38E-5	0.39	1.27E-10

References

[1] E.Ö. Akbay, M.R. Altıokka, Kinetics of esterification of acetic acid with n-amyl alcohol in the presence of Amberlyst-36, Applied Catalysis A: General 396(1-2) (2011) 14-19.

[2] R. Chakraborty, P. Mukhopadhyay, B. Kumar, Optimal biodiesel-additive synthesis under infrared excitation using pork bone supported-Sb catalyst: Engine performance and emission analyses, Energy Conversion and Management 126 (2016) 32-41.

[3] M. Martínez, R. Oliveros, J. Aracil, Synthesis of biosurfactants: enzymatic esterification of diglycerol and oleic acid. 1. Kinetic modeling, Industrial & engineering chemistry research 50(11) (2011) 6609-6614.

[4] Z. Ziyang, K. Hidajat, A.K. Ray, Determination of adsorption and kinetic parameters for methyl tert-butyl ether synthesis from tert-butyl alcohol and methanol, Journal of Catalysis 200(2) (2001) 209-221.

[5] A. Asfour, Diffusion: Mass transfer in fluid systems By EL Cussler, Cambridge University Press, 1984, 525 $49.50, Wiley Online Library, 1985.

[6] M. Mekala, S.K. Thamida, V.R. Goli, Pore diffusion model to predict the kinetics of heterogeneous catalytic esterification of acetic acid and methanol, Chemical Engineering Science 104 (2013) 565-573.

[7] Y.-K. Kim, L. Quadro, Reverse-phase high-performance liquid chromatography (HPLC) analysis of retinol and retinyl esters in mouse serum and tissues, Retinoids: Methods and Protocols (2010) 263-275.

[8] C. Paquot, Standard methods for the analysis of oils, fats and derivatives, Elsevier2013.

[9] R. Chakraborty, D. RoyChowdhury, Optimization of biological-hydroxyapatite supported iron catalyzed methyl oleate synthesis using response surface methodology, Journal of the Taiwan Institute of Chemical Engineers 45(1) (2014) 92-100.

[10] A. Hubau, A. Chagnes, M. Minier, S. Touzé, S. Chapron, A.-G. Guezennec, Recycling-oriented methodology to sample and characterize the metal composition of waste Printed Circuit Boards, Waste Management 91 (2019) 62-71.

[11] M. Tatariants, S. Yousef, R. Sidaraviciute, G. Denafas, R. Bendikiene, Characterization of waste printed circuit boards recycled using a dissolution approach and ultrasonic treatment at low temperatures, RSC advances 7(60) (2017) 37729-37738.

[12] S. Wang, Y. Xu, N. Norbu, Z. Wang, Remediation of biochar on heavy metal polluted soils, IOP Conference Series: Earth and Environmental Science, IOP Publishing, 2018, p. 042113.

[13] D. Chu, Z.-L. Ye, S. Chen, Interactions among low-molecular-weight organics, heavy metals, and Fe (III) during coagulation of landfill leachate nanofiltration concentrate, Waste Management 104 (2020) 51-59.

[14] X. Song, X. Xue, D. Chen, P. He, X. Dai, Application of biochar from sewage sludge to plant cultivation: Influence of pyrolysis temperature and biochar-to-soil ratio on yield and heavy metal accumulation, Chemosphere 109 (2014) 213-220.

[15] P. Pradhan, R. Chakraborty, Optimal efficient biodiesel synthesis from used oil employing low-cost ram bone supported Cr catalyst: Engine performance and exhaust assessment, Energy 164 (2018) 35-45.

[16] S. Sahani, T. Roy, Y.C. Sharma, Smart waste management of waste cooking oil for large scale high quality biodiesel production using Sr-Ti mixed metal oxide as solid catalyst: Optimization and E-metrics studies, Waste management 108 (2020) 189-201.
[17] E.M. Iannicelli-Zubiani, M.I. Giani, F. Recanati, G. Dotelli, S. Puricelli, C. Cristiani, Environmental impacts of a hydrometallurgical process for electronic waste treatment: A life cycle assessment case study, Journal of Cleaner Production 140 (2017) 1204-1216.
[18] P. Karan, P. Mukhopadhyay, R. Chakraborty, Quartz halogen-ultrasonication integrated rotating reactor for efficient photocatalytic-thermocatalytic synthesis of glyceryl monocaprin: Kinetics of heterogeneous esterification, Asia-Pacific Journal of Chemical Engineering 15(1) (2020) e2379.
[19] B.V. Hassas, H. Caliskan, O. Guven, F. Karakas, M. Cinar, M.S. Celik, Effect of roughness and shape factor on flotation characteristics of glass beads, Colloids and Surfaces A: Physicochemical and Engineering Aspects 492 (2016) 88-99.
[20] P. Van Viet, T.H.T. Vinh, N.T.N. Dung, C.M. Thi, Facile ball-milling synthesis of TiO_2 modified ZnO for efficient photocatalytic removal of atmospheric nitric oxide gas under solar light irradiation, Chemical Physics Letters 775 (2021) 138642.
[21] C.S. Latchubugata, R.V. Kondapaneni, K.K. Patluri, U. Virendra, S. Vedantam, Kinetics and optimization studies using Response Surface Methodology in biodiesel production using heterogeneous catalyst, Chemical Engineering Research and Design 135 (2018) 129-139.
[22] T. Ido, M. Goto, S. Goto, H. Teshima, Transient behavior of recycle reactor with consecutive reaction, The Canadian Journal of Chemical Engineering 60(3) (1982) 407-410.
[23] S. Theurich, S. Rönsch, R. Güttel, Transient flow rate ramps for methanation of carbon dioxide in an adiabatic fixed-bed recycle reactor, Energy Technology 8(3) (2020) 1901116.
[24] N. Gholipour Zanjani, A. Kamran Pirzaman, E. Yazdanian, Biodiesel production in the presence of heterogeneous catalyst of alumina: Study of kinetics and thermodynamics, International Journal of Chemical Kinetics 52(7) (2020) 472-484.
[25] L. Perkins, C. Geankoplis, Molecular diffusion in a ternary liquid system with the diffusing component dilute, Chemical Engineering Science 24(7) (1969) 1035-1042.
[26] D. Thoenes Jr, H. Kramers, Mass transfer from spheres in various regular packings to a flowing fluid, Chemical Engineering Science 8(3-4) (1958) 271-283.
[27] H. Fogler, Elements of Chemical Reaction, (2020).
[28] G. Wu, E. Cao, P. Ellis, A. Constantinou, S. Kuhn, A. Gavriilidis, Development of a flat membrane microchannel packed-bed reactor for scalable aerobic oxidation of benzyl alcohol in flow, Chemical Engineering Journal 377 (2019) 120086.
[29] A.M. Lattanzi, M.B. Pecha, V.S. Bharadwaj, P.N. Ciesielski, Beyond the effectiveness factor: Multi-step reactions with intraparticle diffusion limitations, Chemical Engineering Journal 380 (2020) 122507.
[30] Y.-T. Tsai, H.-m. Lin, M.-J. Lee, Kinetics behavior of esterification of acetic acid with methanol over Amberlyst 36, Chemical Engineering Journal 171(3)

(2011) 1367-1372.
[31] O. Aboelazayem, M. Gadalla, B. Saha, Biodiesel production from waste cooking oil via supercritical methanol: Optimisation and reactor simulation, Renewable Energy 124 (2018) 144-154.
[32] M. Kaya, M. Karaarslan, T. Baran, E. Can, G. Ekemen, B. Bitim, F. Duman, The quick extraction of chitin from an epizoic crustacean species (Chelonibia patula), Natural product research 28(23) (2014) 2186-2190.
[33] N.L.L. Hekiem, A.A.M. Ralib, M.A.M. Hatta, F.B. Ahmad, A.N. Nordin, R. Ab Rahim, N.F. Za'bah, Effect of chitosan dissolved in different acetic acid concentration towards VOC sensing performance of quartz crystal microbalance overlay with chitosan, Materials Letters 291 (2021) 129524.
[34] T.M. Mata, N. Cardoso, M. Ornelas, S. Neves, N.S. Caetano, Evaluation of two purification methods of biodiesel from beef tallow, pork lard, and chicken fat, Energy & Fuels 25(10) (2011) 4756-4762.
[35] T. Wang, L. Tao, X. Zhu, C. Chen, W. Chen, S. Du, Y. Zhou, B. Zhou, D. Wang, C. Xie, Combined anodic and cathodic hydrogen production from aldehyde oxidation and hydrogen evolution reaction, Nature catalysis 5(1) (2022) 66-73.
[36] B. Young, T. Hottle, T. Hawkins, M. Jamieson, G. Cooney, K. Motazedi, J. Bergerson, Expansion of the petroleum refinery life cycle inventory model to support characterization of a full suite of commonly tracked impact potentials, Environmental science & technology 53(4) (2019) 2238-2248.
[37] I. ISO, 14040, Environmental management—life cycle assessment—principles and framework (2006) 235-248.
[38] L.J. Dahlben, M.J. Eckelman, A. Hakimian, S. Somu, J.A. Isaacs, Environmental life cycle assessment of a carbon nanotube-enabled semiconductor device, Environmental science & technology 47(15) (2013) 8471-8478.
[39] Q. Tu, A. Parvatker, M. Garedew, C. Harris, M. Eckelman, J.B. Zimmerman, P.T. Anastas, C.H. Lam, Electrocatalysis for chemical and fuel production: investigating climate change mitigation potential and economic feasibility, Environmental Science & Technology 55(5) (2021) 3240-3249.
[40] S. Xu, Z. Li, Q. Yang, G. Chu, J. Zhang, D. Zhang, H. Zhou, M. Gao, Comparative life cycle assessment of energy consumption, pollutant emission, and cost analysis of coal/oil/biomass to ethylene glycol, ACS Sustainable Chemistry & Engineering 9(47) (2021) 15849-15860.

———————————

CHAPTER 6

Results and Discussion

6.1 ACTIVITY I

The present study offers an intensification effort for the synthesis of glycerol monostearate (MSN, a phase change material) using Amberlyst 36 (wet) catalyst. This work demonstrates the superiority of rotating batch reactor (RBR) over the stirred batch reactor (SBR) in glycerol (GL) stearic acid (SA) esterification under far infrared radiation (FIRR). RBR depicted 92 ± 1% MSN yield, which is 40% higher than the yield obtained in SBR under optimal process conditions viz., 20:1 GL: SA mole ratio, 363 K reaction temperature, and 6.0 wt.% catalyst concentration in only 25 min. The speed regimes for mass transfer limitation and surface kinetics controlled were determined using the Mears criterion. The heterogeneous surface reaction kinetics in RBR followed Langmuir Hinshelwood (LH) mechanism (R^2 = 0.98) under the resultant optimal condition. The reaction activation energy for the two different reactor configurations indicated that under identical operating conditions, SBR consumed almost double the energy required for RBR; thus, representing superior energy efficiency of RBR. Notably, the optimally synthesized MSN demonstrated desirable properties of phase change material as confirmed by FTIR, TGA and DSC analyses.

6.1.1 ANOVA Analysis of Process Factors

To evaluate the influence of process factors affecting, analysis of variance (ANOVA) had been executed (Table 6.1); wherein F-value and p-value implied the prominences of different process factors. Accordingly, θ_{RPM} was the most significant factor that affected ϕ_{MSN} followed by $\theta_{GL:SA}$. On the other hand, θ_{RT} and θ_{C} (wt.%) exhibited insignificant effects on ϕ_{MSN}.

Table 6.1. ANOVA results for MSN Yield.

Source	DF Ratio	Seq SS	Adj SS	Adj MS	F-value	p-value	Value
$\theta_{Gly:SA}$	1	133.01	133.01	133.01	1.72	0.089	
θ_{RT}, K	1	0.58	0.58	0.58	0.01	0.935	
θ_{RPM}, rpm	1	424.03	424.03	424.03	5.49	0.051	
θ_C, g/L	1	5.98	5.98	5.98	0.08	0.795	
Error	4	308.91	308.91	77.23			
Total	8	872.51					
R^2							80.32 %

Table 6.2 depicts factorial ranks based on relative effects on the output variable (ϕ_{MSN}) using 'higher the better' criterion for SN ratios [1]. Notably, the reactor rotational speed ranked 1st as it represented highest Δ-values followed by those of $\theta_{GL:SA}$, θ_{RT} and θ_C. Additionally, GL to SA molar ratio had a synergistic effect (Figure 6.1) on ϕ_{MSN}, while θ_{RT} and θ_{RPM} had antagonistic effects after 363 K and 200 rpm respectively. Notably, θ_C had trivial influence on ϕ_{MSN} above 6.0 wt.%. This illuminated the fact that an increase in catalyst concentration above a certain limit could cause no further change in ϕ_{MSN} which corroborated well with the findings of Veillette et al. [2].

Table 6.2. Relative ranks of process factors in maximizing MSN Yield in FIRR-RBR

Level	$\theta_{GL:SA}$	θ_{RT}	θ_{RPM}	θ_C
1	36.4	36.77	35.51	36.79
2	37.1	37.44*	37.94*	37.18*
3	37.56*	36.86	37.61	37.09
Delta (Δ)	1.16	0.67	2.42	0.38
Rank	2	3	1	4

* Represents the optimum levels of process factors corresponding to maximum MSN yield

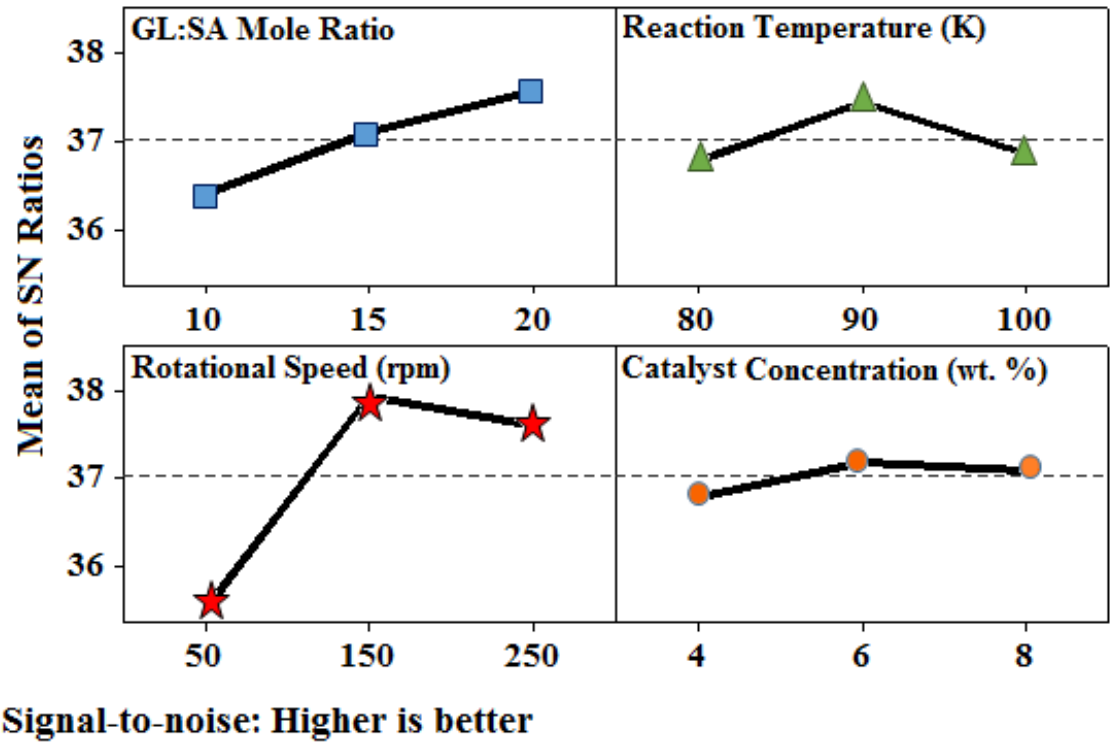

Figure 6.1. Individual factorial effect on SN ratios (corresponding to MSN yield) in FIRR-RBR.

6.1.2 Interactive Factorial Effects on MSN Yield

Contour plot (Figure 6.2) demonstrated the interactive effects of θ_{RPM} with other operating factors on ϕ_{MSN}. Regions showing maxima and minima of ϕ_{MSN} were highlighted with different colors. The dark blue area depicted the region for maximum ϕ_{MSN}. Figure 6.2a demonstrates maximum ϕ_{MSN} in the region encircled by $\theta_{GL:SA}$ from 16 to 20 mol ratio and θ_{RPM} from 200 to 250 rpm. Furthermore, Figure 6.2b illustrates that for the same speed range (200–250 rpm), maximum ϕ_{MSN} was achieved up to 6.0 wt.% θ_C owing to the mass transfer hindrance created by the higher amount of θ_C (above 6.0 wt.%). Besides, the region (Figure 6.2c) encompassing 363 K and 200–250 rpm resulted maximum ϕ_{MSN}. Figure 6.2c also implies that increase in temperature up to 363 K could escalate ϕ_{MSN}, while a further increase in θ_{RT} renders a diminished

ϕ_{MSN} . However, a classical study on the individual factorial effect on ϕ_{MSN} along with the deterministic approach for consideration of mass transfer resistance could give better insight regarding an optimum selection of θ_{RPM} .

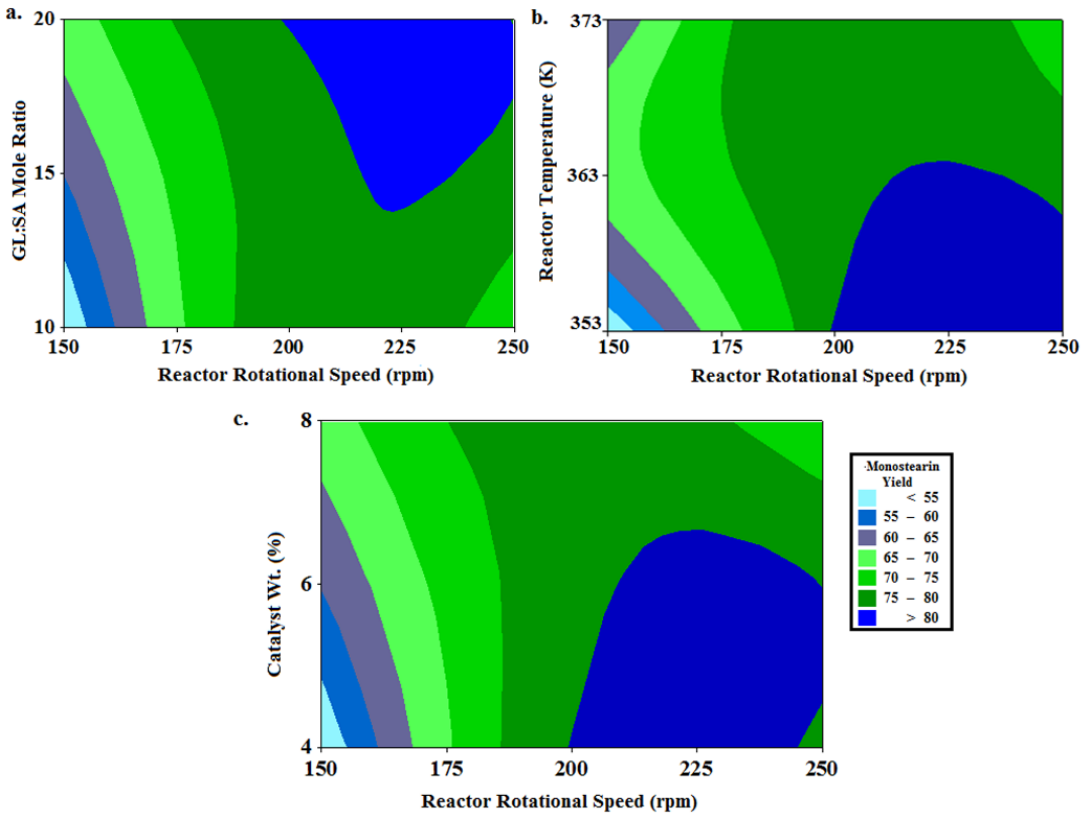

Figure 6.2. Contour plots showing interactive effects of rotational speed with other variables on MSN yield in FIRR-RBR

6.1.3 Individual Influence of Process Factors on MSN Yield

Figure 6.3a demonstrates that increase in $\theta_{GL:SA}$ from 10 to 20 renders the corresponding increments in ϕ_{MSN} from 80 ± 0.05% to 92 ± 1%. This might be due to the fact that presence of excess alcohol in the system facilitated forward reaction [3] and reduced the chance of formation of 2° (distearin) and 3° (tristearin) esters [4]. However, further increase in $\theta_{GL:SA}$ above 20:1 rendered no significant change in ϕ_{MSN} .

Likewise, Figure 6.3b demonstrates that 363 K was the most favorable θ_{RT} for formation of MSN while further rise in θ_{RT}, a reduction in ϕ_{MSN} from 91 ± 1% to 85 ± 2% is observed due to enhanced formation of DSN and TSN; thus, reducing the overall selectivity to MSN [5, 6]. Figure 6.3c displays that above 6.0 wt.% θ_C no significant enhancement in γ_{SA} is observed while ϕ_{MSN} diminished slightly. This could be explained by enhanced mass transfer resistance created by the additional amount of catalyst for a fixed reactor volume while keeping other factors at optimum condition [7]. Nevertheless, augmentations in ϕ_{MSN} and γ_{SA} with an increase in catalyst concentration also ascertained that GL-SA esterification was surface kinetic controlled [8, 9] at the derived optimal condition. Additionally, Figure 6.3d illustrates that for the longer θ_{RT}, ϕ_{MSN} decreases with time as MSN is getting converted to DSN and TSN (Eq. (5.5)) to a greater extent; whereas, γ_{SA} attained its equilibrium point, within 25 min. Moreover, in order to estimate the influence of Amberlyst 36 (wet) catalyst on GL-SA esterification, reactions under optimal process condition were performed with another commercial catalyst i.e., Amberlyst 15 (dry) and also in the absence of catalyst (Table 6.3). It was observed that the product yield and γ_{SA} were much lower due to absence of any catalyst which immensely increased after addition of catalyst. Furthermore, Amberlyst 36 (wet) outperformed in ϕ_{MSN} showing 15 ± 1% more ϕ_{MSN} and 5 ± 1% higher γ_{SA} in comparison with Amberlyst 15 (dry).

Table 6.3. Catalytic effects on MSN yield under FIRR-RBR.

Catalyst applied	γ_{SA} **%**	**Yield %**		
		MSN	**DSN**	**TSN**
No catalyst	32	28.9	2.3	0.06
Amberlyst 15 (dry)	93	78.9	10.2	3.9
Amberlyst 36 (wet)	98.27	92.0	5.1	0.09

This could be attributed to the higher cationic exchange capacity of Amberlyst 36 [10]. Accordingly, all esterification runs were performed with Amberlyst 36 (wet) as the catalyst for further analyses.

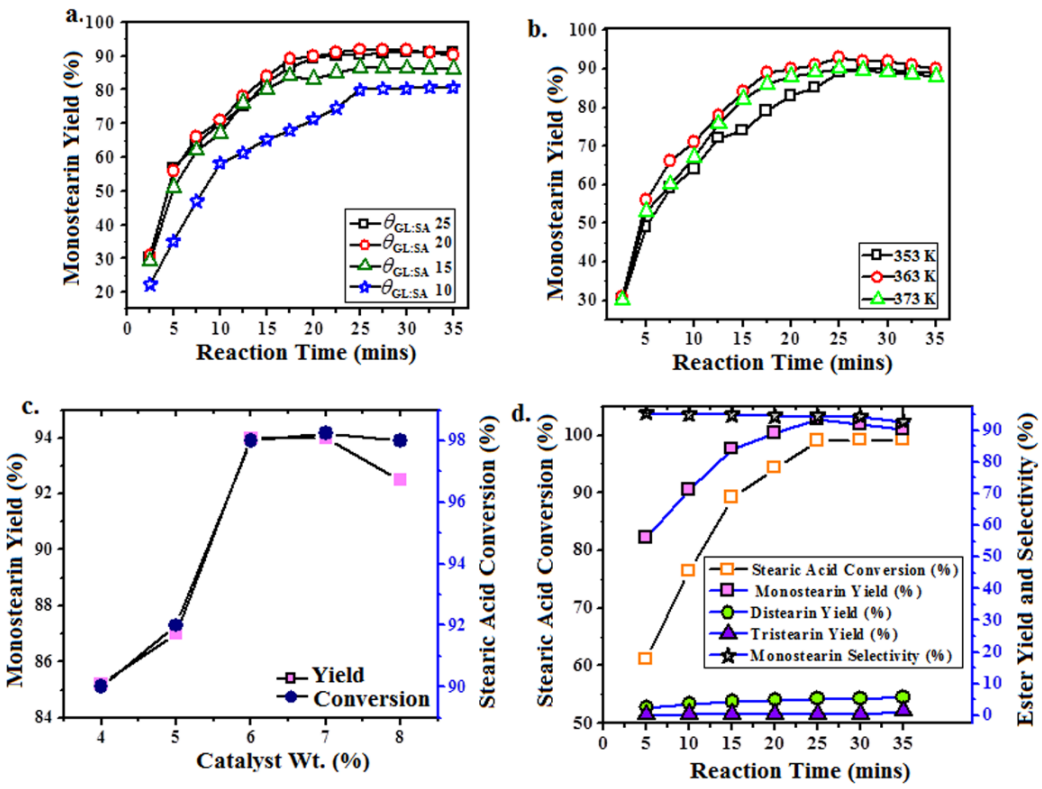

Figure 6.3. Effects of (a) GL to SA mole ratio; (b) reaction temperature; (c) reaction time; and (d) catalyst concentration (wt.%) on MSN yield and SA conversion in FIRR-RBR.

6.1.3.1 Influence of Rotary Action on MSN Yield

To explore the positive effect of rotating action on ϕ_{MSN}, experimental trial was also conducted in SBR at the derived optimal condition over a speed range from 50 to 300 rpm. It could be observed from Figure 6.4 that in the case of SBR (at 225 rpm mechanical stirrer speed), ϕ_{MSN} and γ_{SA} are 40 ± 1% and 44 ± 0.8% lowered respectively compared to the RBR operated at same speed. However, a further increase in θ_{RPM} above 225 rpm, resulted deterioration in γ_{SA}, which was in contrast

with the SBR. This could be ascribed to the fact that at higher speed, central vortex [11] was created that resulted in inefficient mixing of reactants, therefore, lowering the overall conversion (γ_{SA}) and ϕ_{MSN} [12] in RBR. Thus, from the classical study of individual parameters, 225 rpm was considered as the optimum rotational speed instead of 200 rpm obtained from TED analysis.

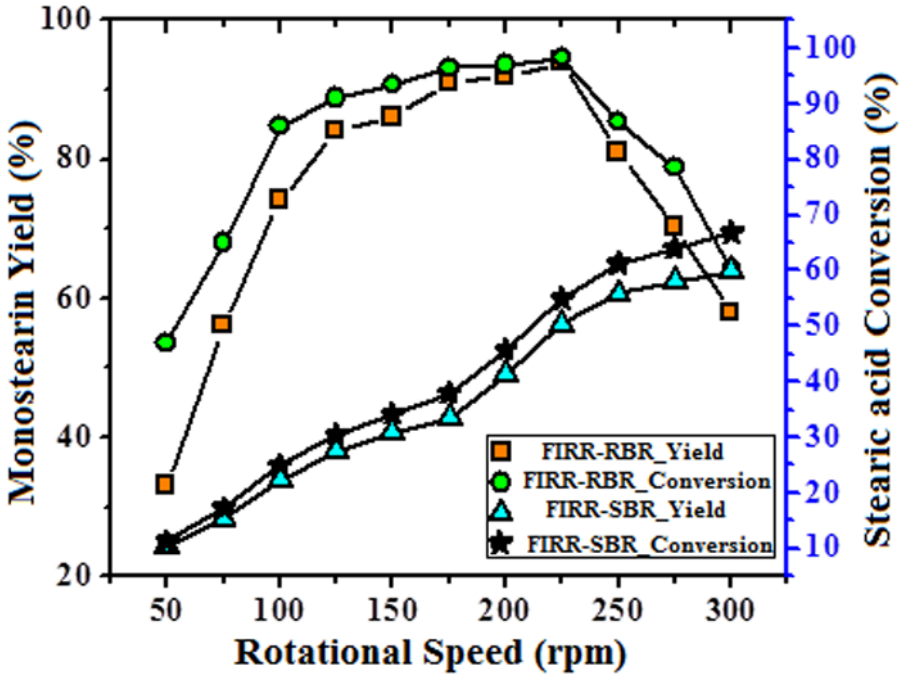

Figure 6.4. Effects of rotating speed (FIRR-RBR) and stirrer speed (FIRR-SBR) on MSN yield and SA conversion.

6.1.3.2 Comparison of Conventional Heating and Infrared Radiation on MSN Yield

At the derived optimal condition, a comparative assessment was conducted between FIRR-RBR and RBR equipped with a conventional heating (CH) system (150 W) as depicted in Figure 6.5. The results revealed the superiority of FIRR over conventional thermal sources in synthesis of MSN.

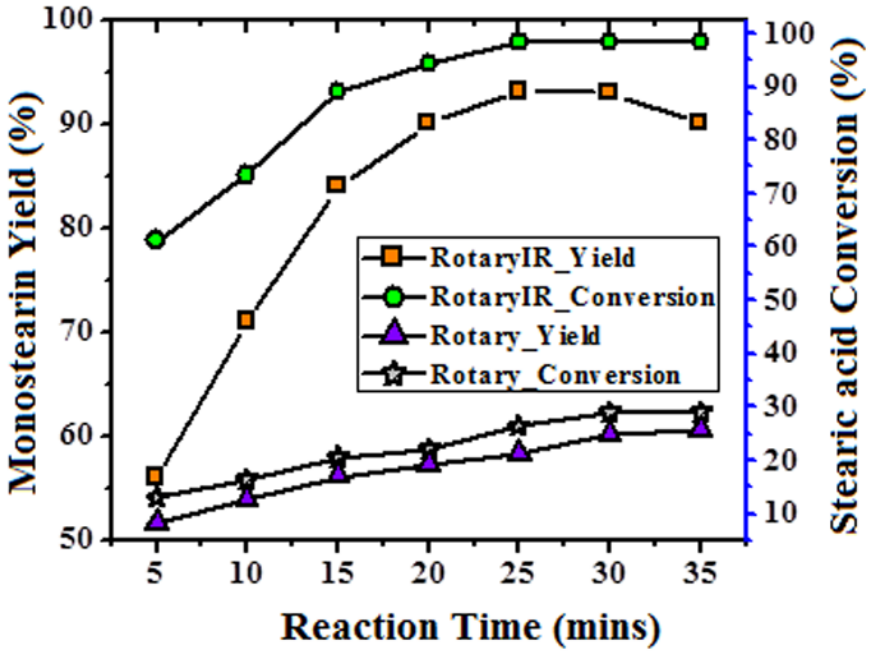

Figure 6.5. Effects of FIRR on MSN yield and SA Conversion.

Far infrared activation had intensely promoted the ϕ_{MSN} compared to CH. This phenomenon could be explained by the better propagation capacity of FIRR through the reaction mixture compared to CH [13]. Application of FIRR had resulted in strong molecular stretching and bending vibrations that rendered faster reaction rate and higher ϕ_{MSN} at a considerably shorter time (25 min), as depicted in Figure 6.5. A comparative assessment with previous reports (Table 6.4) elucidated that the application of RBR coupled with FIRR could immensely improve MSN synthesis while requiring shorter reaction time and lower energy consumption in comparison with conventional reaction systems.

Table 6.4. Comparative analyses between previous and present studies on MSN synthesis.

Catalyst	Reactor Type	Heating	Solvent	Temperature (°C)	Time (h)	SA Conversion (%)	MSN Yield (%)	Ref.
Novozyme 435	SBR	Conventional	-	75	8	-	28.73	[14]
Basic Oxide (ZnO)	SBR		Diglyme	110	16	63	52	[15]
Novozyme 435	SBR		Dioxane	40	6	90	-	[16]
Amberlyst 36(wet)	RBR	Conventional	-	90	0.41	28	20	Present Work
	RBR	FIR Radiation	-	90	0.41	97	92	
	SBR	FIR Radiation	-	90	0.41	55	52	

6.1.4 Assessment of Heterogeneous Reaction Kinetics

6.1.4.1 Effects of External and Internal Diffusion

It is observed from Figure 6.6a that increment in θ_{RPM} of FIRRRBR resulted in augmented k_{MTC} up to 225 rpm and subsequently declined due to vortex formation and improper mixing at higher θ_{RPM} . The point of minimum bulk diffusional resistance Eqs. (5.6, 5.8) were evaluated using the kinetic data obtained at different θ_{RPM} (50–300 rpm). From Figure 6.6b, it is clearly observed that the regime between 125 and 250 rpm depicted insignificant bulk diffusional resistance, with a minimum $M_C = 3.9\times10^{-2}$ ($M_C \prec 0.15$) at 225 rpm, implying negligible external diffusional hindrance [17] in Amberlyst 36 catalyzed GL-SA esterification. It was also noted that between 225 and 250 rpm rotational speed, $M_C \prec 0.15$. However, θ_{RPM} beyond 250 rpm enunciated external mass transfer-controlled regime ($M_C \succ 0.15$); which could

be attributed to the vortex formation resulting in poor reactant mixing. Therefore, the optimal condition of esterification was 20:1 $\theta_{GL:SA}$, 363 K θ_{RT}, 225 rpm θ_{RPM} and 6.0 wt.% θ_C corresponding to maximum ϕ_{MSN}.

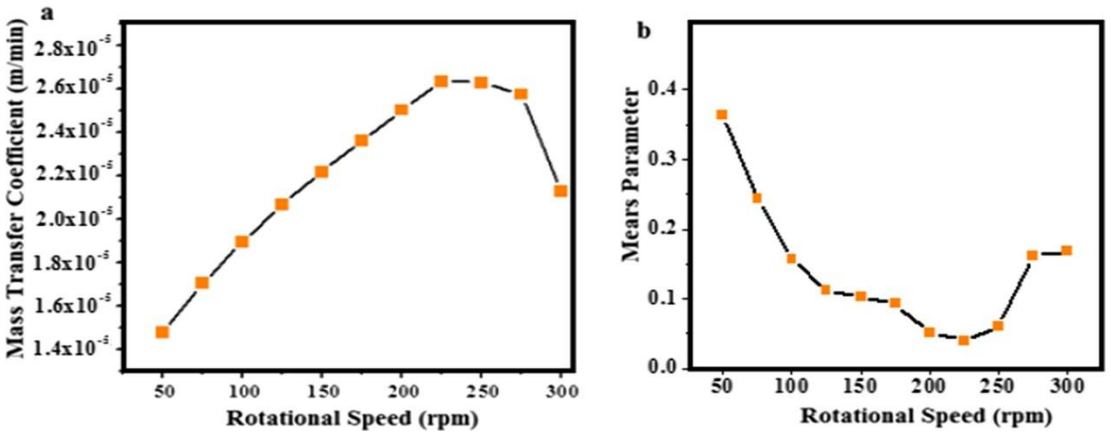

Figure 6.6. Effects of rotational speed on (a) mass transfer coefficient and (b) Mears factor in FIRR-RBR.

Possibility of existence of internal pore diffusional resistance-controlled regime was also assessed using catalyst particles of different sizes under optimal condition (Figure 6.7). Insignificant influence of catalyst size was observed on γ_{SA} confirming negligible internal pore diffusional resistance. These observations enumerated the fact that at the optimal θ_{RPM} (225 rpm), the reaction mechanism was surface kinetic controlled; since both external and internal (pore) diffusional resistances were negligible [18].

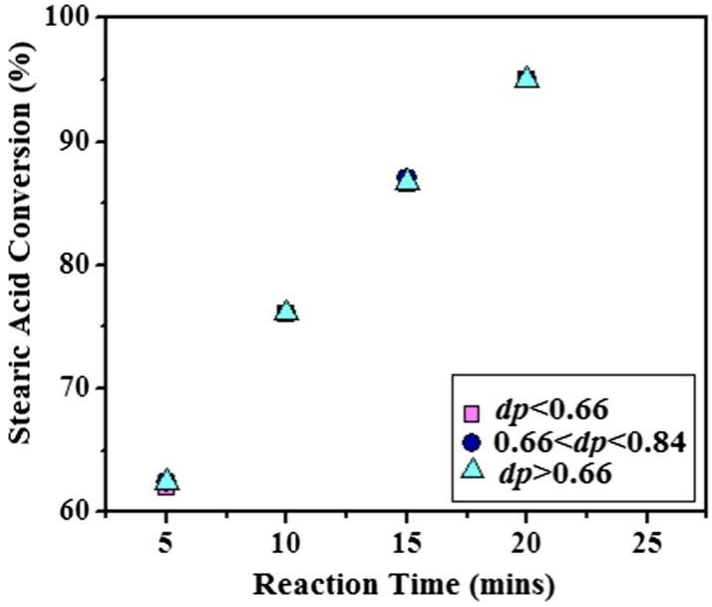

Figure 6.7. Effects of variation of catalyst particle size on SA conversion with time in FIRR-RBR.

6.1.4.2 Surface Reaction Study

LH, ERSA, ERGL and PH models were tested using the GL-SA esterification kinetic data recorded at optimal condition in FIRR-RBR in the diffusion resistance free regime. From Table 5, it is perceived that the R^2 and the adj. R^2 values of LH model were higher than other three models. It was also noted that LH model at 363 K possessed maximum R^2 value (0.98) in comparison with LH models at other two θ_{RT}. This could be attributed to the fact that, lower θ_{RT} (353 K) caused lower desorption rate of desired product; thus, lowering product yield; while, higher θ_{RT} (373 K) had adverse effect on the adsorption of reactants; thus providing lower model fit at two extreme θ_{RT}.

Furthermore, after evaluation of best kinetic model for FIRRRBR, the LH model was also fitted with the data of FIRR-SBR in order to evaluate the kinetic parameters of FIRR-SBR. Significantly, the energy-efficient behavior of FIRR-RBR was evident

from the computed reaction activation energy (Table 6.5) of FIRR-SBR (E_A = 40.2 kJ/mol) and FIRR-RBR (E_A = 21.84 kJ/mol); thus, indicating almost double energy consumption in SBR in comparison with RBR. Again, from the parity plot (Figure 6.8a) for FIRR-RBR, it could be observed that under optimal factorial combinations, LH model for FIRR-RBR had demonstrated close proximity to experimental data giving Adj. R^2 = 0.87 with slope close to unity (0.987); whereas, Figure 6b depicted lower Adj. R^2 = 0.81 with slope much less than unity (0.79) for FIRR-SBR. Also, it would be worthy to mention here, that the activation energy obtained in present case of FIRR-RBR (21.84 kJ/mol) was lower than previously reported esterification studies carried out with Amberlyst 36 (wet) catalyst [19]. The LH mechanism indicated strong adsorption of GL and SA on the surface of Amberlyst 36 catalyst. Thus, SA was activated by the active site of Amberlyst 36 and had undergone surface reaction with the 1° alcohol group of GL resulting in the formation of MSN (MSN) [9]. Consequently, the products water and MSN diffused out into the bulk and subsequently water molecules were removed in situ from the bulk with the aid of desiccant (molecular sieves); thus, preventing backward reaction.

Table 6.5. Kinetic parameters for GL-SA esterification in FIRR-RBR.

Reactor Type	**Model Type**	**Temperature, [K]**	$k_{obs}\times10^{-4}$ **[L²/molgmin]**	$K_1\times10^{-3}$ **[L/mol]**	$K_2\times10^{-3}$ **[L/mol]**	$K_3\times10^{-3}$ **[mol/L]**	R^2	R^2_{adj}	k^0_{obs} **[L²/mol.g.min]**	E_A **[kJ/mol]**
RBR	ERSA	353	6.80	51.49 ± 3.82	1.92 ± 0.14	8.82×10^{-3} ± 0.014	0.87	0.80	3.225	31.72
		363	8.83	36.11 ± 3.7×10^{-3}	1.51 ± 1.59×10^{-4}	1.0 ± 0.31	0.98	0.94		
		373	10.83	19.64 ± 1.29×10^{-3}	0.76 ± 5.07×10^{-5}	1.01 ± 0.18	0.90	0.85		
		353	5.07	26.45 ± 2.65×10^{-3}		1.01 ± 0.47	0.80	0.70		
		363	6.80	26.11 ± 2.14×10^{-3}	-	1.011 ± 0.38	0.87	0.83		
		373	6.93	16.45 ± 1.37×10^{-3}		1.013 ± 0.46	0.86	0.82		
	ERGL	353	6.49		26.88 ± 3.9×10^{-3}	1.092 ± 0.69	0.74	0.70	1.147	24.825
		363	8.90	-	25.65 ± 2.8×10^{-3}	1.0098 ± 0.51	0.85	0.81		
		373	10.2		23.68 ± 1.8×10^{-3}	1.0099 ± 0.44	0.90	0.87		
	PH	353	4.95				0.75	0.75	0.140	22.622
		363	6.97		-		0.88	0.88		
		373	7.15				0.87	0.87		
SBR	LH	353	1.51	15.44 ± 2.03×10^{-2}	1.01 ± 1.59×10^{-3}	3.76×10^{-4} ± 1.91×10^{-6}	0.76	0.70	4.835	40.198
		363	1.608	12.64 ± 3.81×10^{-3}	0.96 ± 2.94×10^{-4}	1.0 ± 0.012	0.93	0.82		
		373	2.61	11.09 ± 6.1	0.72 ± 0.40	7.75×10^{-4} ± 1.29×10^{-4}	0.91	0.80		

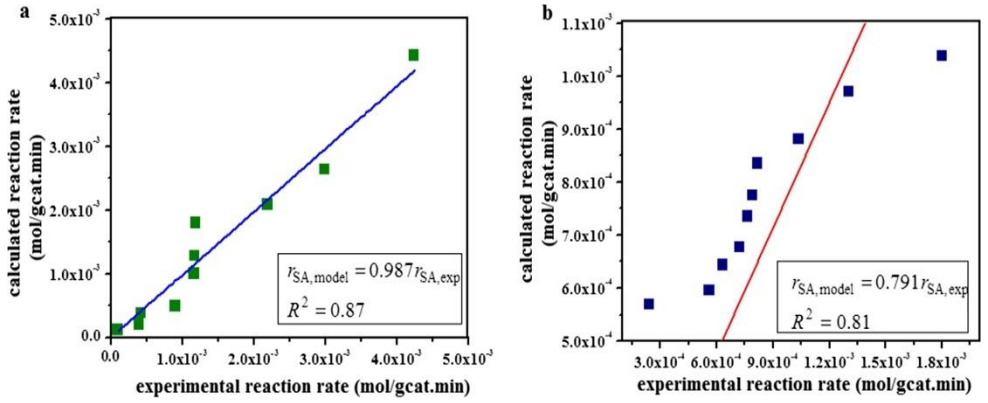

Figure 6.8. Parity plots for LH model at optimal condition (a) FIRR-RBR and (b) FIRR-SBR.

6.1.5 Characterization of the Optimally Synthesized Product

FTIR (Figure 6.9a) analyses were performed for the optimal product MSN, SA and standard MSN samples. Absence of any prominent peak in product MSN over the range 3200–3650 cm^{-1} was in contrast with that observed for pure SA at 3490 cm^{-1}; this clarified the insignificant presence of carboxylic groups in the prepared ester. This observation further indicated that most of the SA was converted to the product MSN [20] and its spectra corroborated well with the FTIR pictogram of standard MSN. Moreover, vibrations at 2918 and 2842 cm^{-1} represented asymmetric and symmetric vibrations of the CH_2 group [21]. Sharp peak located at 1467 cm^{-1} signified OH stretching vibration while peak at 716 cm^{-1} corresponded to stretching vibration of $(-CH_2-)_n$ ($n \geq 4$) groups [22]. All these peaks were spotted in SA, product MSN and standard MSN samples; thus, elaborating the carboxylic structure of the samples. Further, FTIR spectra of both product and standard MSN showed two characteristic peaks at 1730 cm^{-1} and 1169 cm^{-1} illustrating the stretching vibrations of C=O and C-O groups of the ester. Notably, these two peaks were absent in SA; thus, confirming the presence of MSN in the synthesized product; however, slight shift and broadening

in FTIR peaks were observed in product MSN compared to standard MSN sample, which could be due to the presence of DSN and TSN in the product MSN.

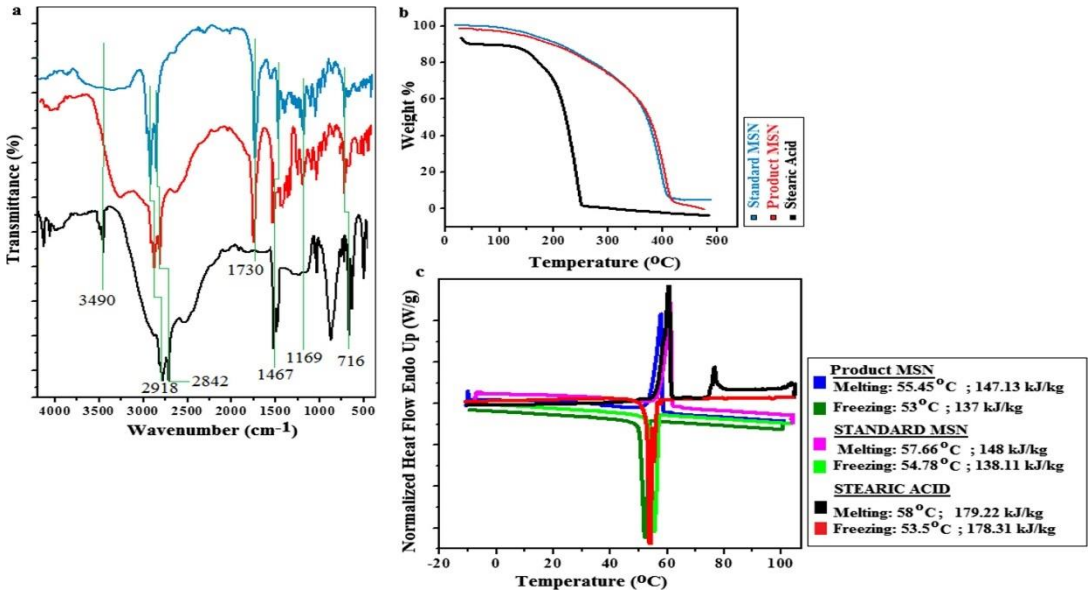

Figure 6.9. (a) FTIR spectra (b) TGA, (c) DSC of the optimal product MSN and standard samples.

Thermogravimetric (TG) curves depicted the thermal stability of the prepared MSN. From Figure 6.9b, it is observed that 5% weight loss occurred for standard SA sample at 120 °C, followed by complete decomposition before 200 °C. Whereas, product MSN depicted 5% weight loss at 180 °C, which was just 5 °C lower than standard MSN sample. While the maximum decomposition temperature for both product MSN and standard MSN was identical (240 °C); these observations signify the purity of the prepared MSN and its thermal endurance towards exothermic cycles [20]. The DSC curves (Figure 6.9c) illustrated the thermal storage capability of product MSN implying promising thermal behavior. Comparative DSC analyses (Figure 6.9c) indicated that the characteristic curve of product MSN matched well with the standard MSN sample. The melting and freezing enthalpies of the prepared MSN were 147.13 kJ/kg and 137 kJ/kg respectively. Moreover, the difference between melting and

freezing temperatures of the synthesized product was 2.45 °C (< 3 °C); thus, displaying the characteristic of a promising PCM for thermal storage [23, 24]. Additionally, DSC analysis of SA (melting point: 58 °C, fusion enthalpy: 179 kJ/kg) validated the fact that the quantity of SA in the prepared MSN was quite insignificant; thus, further reinforcing suitable attributes of the synthesized MSN.

6.2 ACTIVITY II

6.2.1 Factorial Effects on GMC Selectivity and CA Conversion

The results of CA-G esterification has been displayed in Table 6.6.

6.2.1.1. Radiation Temperature

Optimum factorial combination determined using TOD (Table 6.7), disclosed that $ATO^{0.67}$ i.e. A15:NT-P25 of 0.67:1 (w/w), 0.35:1 CA:G mole ratio, 343K reaction temperature and 150 rpm rotating speed as the optimum factorial combination resulted in maximum GMC production. Yet again, to probe the individual factorials effects on CA:GL esterification over a wider factorial range, additional runs were taken keeping other factors at the optimum condition.

Figure 6.10 indicated the effect of radiation temperature on ATO performance during CA-G esterification in QHRUERR. Reaction temperature (f_{RT}) has been varied between 303K and 353K to assess the effects of ATO on CA conversion.

It was apparent from Figure 6.10a that at lower reaction temperatures (viz. 303K and 313K), although the initial reaction rates were substantially high, yet the corresponding curve reached a plateau around 15 mins and 25 mins. This was because of the higher melting points of the monoester (326K) formed during the reaction course that hindered further interaction of the catalysts with the liquid reactants; thereby,retarding the reaction rate before attaining maximum conversion. Evidently, higher initial rates at a lower temperature also indicated appreciable photo-activity of

NT-P25 catalyst owing to its excitation under UV-visible spectral radiance emitted by quartz-halogen radiator [25]. Conversely, the thermocatalytic contribution of A15 catalyst became prominent at higher temperatures (343 K, 353 K) and the reaction proceeded to maximum CA conversion (97±0.5%) in 1h. Although, further increase in f_{RT} above 343 K (Figure 6.10b) escalated the CA conversion; nevertheless, it also promoted GDC (glyceryl dicaprin) and GTC (glyceryl tricaprin) formation successively (Figure 6.11); thus, reducing GMC selectivity.

Table 6.6. Factorial array for TOD analysis with corresponding GMC yield and SN ratios

f_{ATO} **(wt./wt.)**	f_{MR}	f_{RT} **(K)**	f_{RS} **(rpm)**	θ_{GMC} **(%)**	θ_{SN}
0.67	0.25	333	100	70.00	36.90
0.67	0.35	343	150	87.50	38.84
0.67	0.50	353	200	80.00	38.06
1.00	0.25	343	200	76.89	37.71
1.00	0.35	353	100	72.00	37.14
1.00	0.50	333	150	74.35	37.42
1.50	0.25	353	150	72.98	37.26
1.50	0.35	333	200	69.00	36.77
1.50	0.50	343	100	72.00	37.14

Table 6.7. Delta-Ranks and SN ratio values

Level	f_{ATO} **(wt./wt.)**	f_{MR}	f_{RT} **(K)**	f_{RS} **(rpm)**
1	37.93$^{\#}$	37.29	37.03	37.07
2	37.43	37.59$^{\#}$	37.90$^{\#}$	37.84$^{\#}$
3	37.06	37.54	37.49	37.52
Delta	0.87	0.29	0.87	0.78
Rank	1	4	2	3

 # SN ratio values of the opearting factors rendering maximum GMC yield

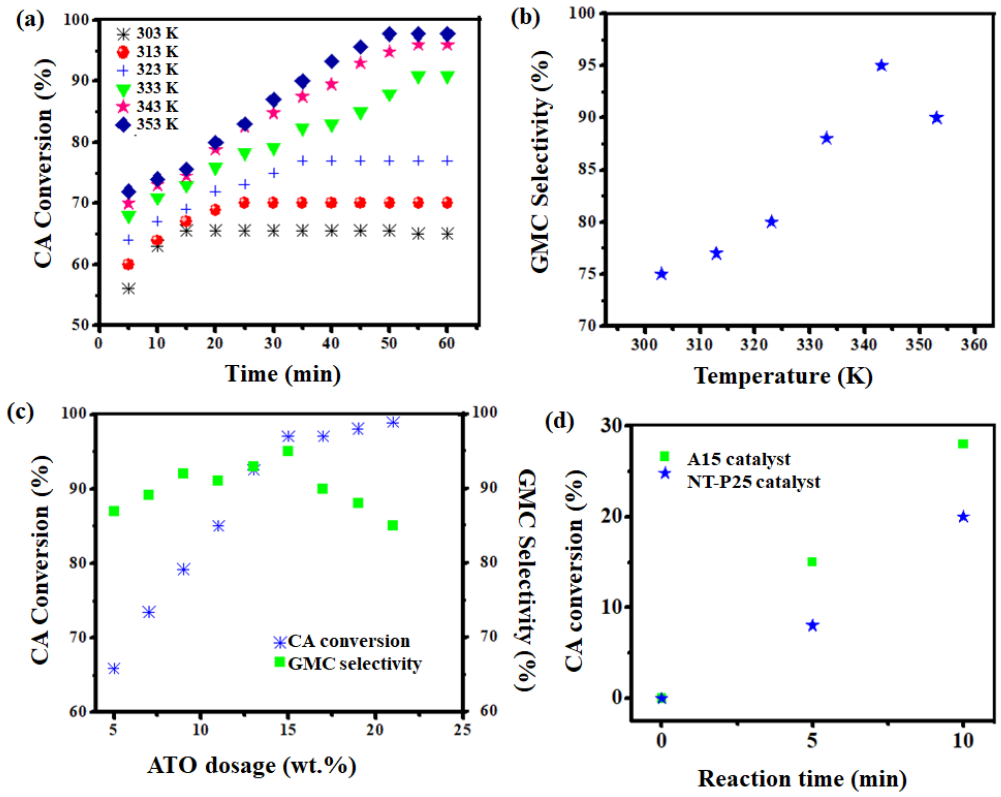

Figure 6.10 (a), (b) Effect of radiation temperature on ATO performance; (c) Effect of ATO dose; (d) Effect of A15 and NT-P25 dose in QHRUERR.

6.2.1.2 Effect of Catalyst

Influences of catalyst dosages and catalyst types on CA-GL esterification were meticulously scrutinized under TOD-derived optimal condition. Table 6.8 describes the effect of ATO addition on GMC selectivity and CA conversion under QHR-US energy exposure. It is perceived from Table 6.8 that the catalytic efficacy in CA conversion and GMC selectivity followed the following order, that is, NTO-P25 < A15 < $ATO^{0.67}$ < ATO^{1} < $ATO^{1.5}$ and A15 < $ATO^{1.5}$ < NTO-P25 < ATO^{1} < $ATO^{0.67}$, respectively. This could be explained by the fact that the presence of a higher amount of Brønsted acid sites (A15 catalyst) in reaction mix could augment CA conversion; nevertheless, it has negatively influenced GMC selectivity. This scenario has been altered in the presence of Lewis acid sites (NT-P25), wherein lower CA conversion

and higher GMC selectivity were detected. The individual effect of Ti^{4+} and H^{+} ions

Table 6.8. Esterification of CA with GL using various catalysts

Catalyst	Product Selectivity			CA conversion (%)
	GMC	GDC	GTC	
Blank	0.69	0.2	0.045	56
A15	0.81	0.17	0.04	90±0.3
NT-P25	0.88	0.07	0.002	87.57±0.5
$ATO^{0.67}$	0.95	0.034	0.021	97±0.2
ATO^{1}	0.91	0.089	0.0015	98±0.6
$ATO^{1.5}$	0.89	0.08	0.001	98±0.5

at lower conversion below 20% could be observed from Figure 6.10d. For the same reaction time (5 and 10 min), it is detected that A15 rendered higher conversion compared with NT-P25, whereas the presence of both acidic sites ($ATO^{0.67}$) synergistically improved CA conversion and GMC selectivity. However, it is inferred from Table 6. that increase in Brønsted acidity (H^{+}) in ATO mixture deteriorated GMC selectivity, which indicated that monoester selectivity was predominantly controlled by Lewis acid catalytic sites [26]. Again, electromagnetic energy (UV-visible spectra) contributed by quartz-halogen radiator caused excitation and relocation of electron-hole pairs from the valence band to conduction band in NT-P25, thereby facilitating higher GMC selectivity and CA conversion simultaneously [27]. Moreover, ATO dosage also played an important role in improving GMC selectivity and CA conversion (Figure 6.10c). Noticeably, an additional increase in ATO dosage above 15 wt.% had resulted in deterioration of overall GMC selectivity. This was because of excess catalyst mass that hindered acoustic streaming generated by US wave, thus lowering the interaction of two immiscible reactants and offering additional mass transfer resistances, eventually reducing GMC selectivity [28]. Therefore, 15 wt.% catalyst dose was considered as optimum.

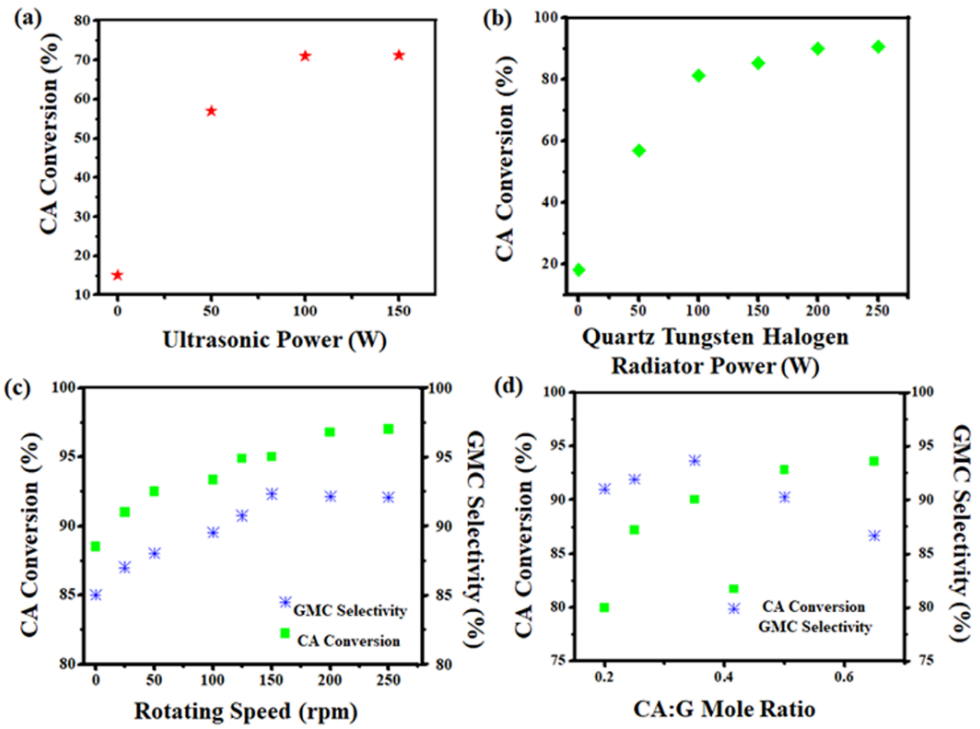

Figure 6.11. Effect of (a) ultrasonic power; (b) quartz halogen radiator power; (c) rotating speed; (d) CA: GL mole ratio in QHRUERR.

6.2.1.3 Effect of Electromagnetic Energy

Another important parameter that had a major impact on CA conversion/GMC selectivity was ultrasonic/quartz halogen electromagnetic energy. To explore the individual effect of electromagnetic energy, experiments were conducted under TOD-derived optimum condition along with variation in input power. Figure 6.11a portrays the experiments executed only under ultrasonic wave energy (USWE). It was observed that without USWE, maximum 15% ± 0.5% CA conversion was attained, which increased up to 70% ± 1% with the addition of 100 W USWE in 1 h. This was because of the fact that USWE created shock waves from the peizo zone due to symmetrical collapse of cavitation bubbles that rendered compression and rarefaction of the reactant media [29]. This physical force disintegrates the reactant molecules into free radicals, which recombine at a faster rate to generate desired GMC. However,

at 150 W USWE, no further significant enhancement was achieved (72.5% ± 0.5%); hence, for this study, US power was fixed at 100 W. Similar esterification experiments were also conducted under individual influence of QHR wave energy (QHRWE), where the QHR power was varied between 100 and 250 W (Figure 6.11b). It could be noticed that CA conversion reached 82% ± 0.3% in 1 h at 100 W QHR power. This considerable improvement was due to the penetrating influence of QHRWE at the molecular level that caused robust molecular collision due to bending and stretching vibration of bonds resulting in 12% more CA conversion compared with USWE under otherwise identical operating conditions [30]. Besides, a further increase in QHR power up to 200 W escalated CA conversion to 88% ± 0.5%. However, at 250 W QHR power input, no further substantial improvement in CA conversion (90% ± 0.5%) was observed; hence, 200 W QHR power was selected for the esterification study concerning the aspect of choosing sustainable energy-efficient reactors.

Moreover, the concurrent application of US and QHR wave energies upsurge the CA conversion to 97% ± 0.5% in 1 h with satisfactory GMC selectivity (94% ± 1%) under otherwise identical reaction conditions. This occurred owing to the intense reactant mixing triggered by USWE and severe molecular vibrations instigated by QHRWE ensuring enhanced mass transport along with photoactivation that rendered 8% additional increment in the product output in expense of minimal energy compared with CERR and conventionally energized mechanically stirred reactor (Table 6.9).

Table 6.9. Energy disbursement of different reactors.

Reactor Types	Power (W)	GMC Selectivity (%)	Energy Consumed (kJ)
CEMR	650	80	2340
CERR	516	86	1393.2
USERR	116	89	174
QHERR	216	91	194.4
QHRUERR	316	95	94.8

6.2.1.4 Effect of Rotational Speed

It might be noted from the Taguchi analyses (Table 5.4) that rotational speed had least influence on CA-G esterification; 150 rpm was the optimum speed facilitating maximum CA conversion. However, the effect of rotational speed of the reactor was clearly understood on comparing with the conventional batch reactor equipped with mechanical impeller operating at the same optimum speed (150 rpm). It could be observed from Table 6.9 that mechanical impeller was less productive with higher power consumption. Figure 6.11c displays that at similar operating condition, reactions performed under nonrotating action resulted in 87% ± 1% CA conversion; this high CA conversion was contributed by the ultrasonic cavitation mixing of reactants. Advantageously, addition of rotating speed contributed 10% more CA conversion in 1 h, which deteriorated on further increase in rotating speed (250 rpm) due to improper mixing of the reactants due to vortex formation.

6.2.1.5 Effect of Reactant Mole Ratio

Figure 6.11d shows the CA:GL mole ratio has a noticeable effect on CA conversion as well as on GMC selectivity. At CA:GL mole ratio 0.25:1, the CA conversion is 94% ± 1%, and at mole ratio 0.35:1, CA conversion could be enhanced by 3% ± 0.5%. However, further increase has attenuated the CA conversion. This fact could be elucidated by the phenomena that at a very low CA concentration, the $ATO^{0.67}$ catalyst sites were mostly covered with G, which could not facilitate surface reaction. On the contrary, at mole ratio of 0.35:1, [31] the surface concentration of CA was adequate to augment CA conversion. Nevertheless, higher CA content resulted pseudo-inhibition of the catalyst sites due to large molecular dimension of CA, [32] which restricted further enhancement in CA conversion.

6.2.2 Esterification Kinetic Assessments

Kinetic study for CA-GL esterification had been executed by considering PH and heterogeneous kinetic models. At the derived optimal reaction condition (f_{ATO} : 0.67:1, f_{MR} : 0.35:1, f_{RT} : 343 K, f_{RS} : 150 rpm); all three reactors, namely, USERR, QHRUERR, and QHERR, had been employed in order to evaluate the reactor efficacy and to determine kinetic parameters. However, prior to the evaluation of the abovementioned kinetic models, CA conversion versus time data acquired for kinetic analyses were used for probable external and internal diffusional interventions.

6.2.2.1 External Mass Transfer Hindrance

Estimations of external mass transfer (bulk diffusion of limiting reactant, CA) limitation for USERR, QHRUERR and QHERR were performed in accordance with Mears criteria (M_T) in accordance with Eq. (6.1). As per Mears test, when $M_T \prec 0.15$, external diffusional resistance was insignificant, [33] whereas, $M_T \succ 0.15$ demonstrated that mass transfer limitation was dominant in CA: G esterification reaction.

$$M_{\mathrm{T}} = \frac{\beta\left(-r_{CA,\exp}\right)\rho_{A15}R_{A15}}{k_{EDC}C_{CA,bulk}} \prec 0.15 \qquad (6.1)$$

where, β : the reaction order; R_{A15} : catalyst pellet radius (m); $-r_{CA,\exp}$ (mole/gcat.min): experimental reaction rate for limiting reactant (CA); K_{EDC} (m/min): external diffusion coefficient; ρ_{A15} (g/L): catalyst bulk density; $C_{CA,bulk}$ (mol/L): limiting reactant bulk concentration.

K_{EDC} could be evaluated through Eq. (6.2) considering forced convection around the catalyst particle [34]

$$\frac{k_{EDC}d_{A15}}{D_{CA:G}} = 2.0 + 0.6\left(\frac{d_{A15}v_{CA:G}}{\nu_{CA:G}}\right)^{1/2}\left(\frac{\nu_{CA:G}}{D_{CA:G}}\right)^{1/3} \quad (6.2)$$

where, d_{A15} (m): catalyst pellet diameter; $D_{CA:G}$ (m^2/s): CA diffusivity through G; $\upsilon_{CA:G}$ (m/s): approaching velocity of CA: G mixture towards catalysts; $\upsilon_{CA:G}$ (m^2/s): kinematic viscosity of CA: G mix. The $D_{CA:G}$ had been calculated by Wilke Chang equation [35] given by Eq. (6.3):

$$D_{CA:G} = 1.173\times10^{-16}(\sigma MW_G)^{1/2}\frac{T}{\mu_{bulk}(V_{CA})^{0.6}} \quad (6.3)$$

where, σ the association parameter (=1 for un-associated solvents, i.e., G); MW_G (kg/mol): molecular weight of G; μ_{bulk}(kg/m sec): bulk viscosity of reaction mixture; V_{CA} (m^3/kg mol): CA molar volume at boiling point.

From Table 6.10, M_T is <0.15 for all reactor systems, thus enunciating the statement that external diffusional resistance can be completely neglected. Additionally, QHRUERR showed highest K_{EDC} and lowest M_T value (Table 6.10); therefore, illuminating the superiority of QHRUERR over other reactors under consideration.

6.2.2.2 Internal Mass Transfer Hindrance

Weisz–Prater criterion was applied to evaluate the existence of internal pore diffusional resistance. The Weisz-Prater factor (C_{WPF}) could be estimated using Eq. (6.4).

$$C_{WPF} = \frac{(-r_{CA,\exp})\rho_{A15}R_{A15}^2}{D_{eff,CA:G}C_{CA}} \quad (6.4)$$

where, $D_{eff,CA:G}$ effective diffusivity (m^2/min) could be calculated using Eq. (6.5). Now, if $C_{WPF} \succ 1$, internal pore diffusional resistance was resilient enough to create concentration gradient from the resinous catalyst surface to catalyst pores.

$$D_{eff,CA:G} = \frac{\xi}{\tau} D_{CA:G} \quad (6.5)$$

Here, ξ was the void fraction and τ was the tortuosity. For $ATO^{0.67}$ catalyst, τ = 3 and ξ = 0.36 [36].

It had been observed that for all the reactor systems (Table 6.10), C_{WPF} was quite less than 1; thus, endorsing negligible internal pore diffusional resistance.

Table 6.10. External and internal diffusion parameters for evaluation of mass transfer resistance.

Reactors	K_{EDC} **(m/min)**	M_T	C_{WPF}
QHRUERR	7.96×10^{-05}	3.66×10^{-05}	0.0072
QHERR	9.71×10^{-07}	6.79×10^{-03}	0.011
USERR	9.71×10^{-07}	7.41×10^{-03}	0.0133

6.2.2.3 Assessment of Surface Kinetics

In analyzing esterification kinetics, it had been assumed that the rate of backward reaction could be neglected because by-product water was efficiently removed in-situ by desiccant. Again the average combined yield of GDC and GTC for all the reactor studies were quite lower than 10% therefore, the formation rate of secondary and tertiary esters had been neglected. Amongst the three models, PH, LH and ER, the best correlated model having the highest R^2 and lowest APE values were accepted to describe the esterification kinetics. Accordingly, LH model (Table 6.11) was found to be the best representative kinetic model in all three reactors viz., QHRUERR, QHERR and USERR. On the other hand, PH model had shown lowest R^2 values; thus, confirming the heterogeneous characteristics of CA:G esterification reaction. Furthermore, highest R^2 values were observed at reaction temperature 343K, thus, 343K was confirmed as the optimum temperature for maximum GMC production. Moreover, the reaction activation energy required in case of QHRUERR was 9.63

kJ/mol; whereas, QHERR and USERR corresponded to 27.5 kJ/mol and 32.74 kJ/mol respectively; these data evidenced the superior energy efficiency of QHRUERR over QHERR and USERR.

6.2.3 Characterization of Catalysts

To investigate the photoactive properties of NT-P25 and $ATO^{0.67}$ catalysts, UV-Diffuse reflectance Spectra (DRS) was obtained at room temperature. NT-P25 demonstrated the reflectance spectra (Figure 6.12a) that illustrated high-pitched edge prominent at 360 nm, whereas, $ATO^{0.67}$ showed the prolonged absorption edge at 387nm wavelength. This phenomenon shows the photocatalytic activity of $ATO^{0.67}$ towards the near infrared spectrum or visible light region (>400nm). It could be interpreted from Figure 7 that due to the presence of SO_3H group of A15, the absorption of $ATO^{0.67}$ abruptly shifted towards near visible region. The direct band gap energy of $ATO^{0.67}$ was evaluated using Tauc plot [37] between $\left[\frac{h\nu\left(R_{\max}-R_{\min}\right)}{\left(R-R_{\min}\right)}\right]^2$ (y-axis) and hν (x-axis) using Kubelka-Munk function. Therefore, $ATO^{0.67}$ could successfully facilitate the photocatalytic effect (by lowering the band gap energy 2.98 eV compared with the band gap energy of NT-P25 of 3.2-3.35eV) in the esterification reaction under QHR radiator. The lower intensity PL spectra of $ATO^{0.67}$ in comparison with NT-P25 (Figure 6.12b) implied that in presence of sulfate group, the recombination of electron and holes are lesser with high separation efficiency, that could mobilize the transition of an electron from the valence band to the conduction band of $ATO^{0.67}$.

Table 6.11. Esterification kinetic parameters for QHRUERR, QHERR and USERR reactor

Reactor Type	Kinetic Model	Temperature, K	$k_{forward,LH}$ [mol/gcat.min]	$k_{ads,CA}$ ×10³ [L/mol]	$k_{ads,G}$ ×10³ [L/mol]	$k_{des,GMC}$ ×10⁻³ [mol/L]	R^2	R_{adj}^2	APE[a] (%)
QHRUERR	L H	333	2.14 ± 0.61	31.29 ± 8.92	1.76 ± 0.59	$1.32\times10^{-4} \pm 2.29\times10^{-5}$	0.97	0.90	
		343	2.33 ± 0.15	29.27 ± 1.87	0.73 ± 0.05	$2.43\times10^{-4} \pm 1.02\times10^{-5}$	0.99	0.98	5.84
		353	2.63 ± 0.02	7.49 ± 0.058	9.07 ± 0.24	$1.94\times10^{-4} \pm 1.37\times10^{-6}$	0.97	0.93	
QHERR		333	0.76 ± 0.01	14.12 ± 0.08	1.41 ± 0.01	$1.49\times10^{-4} \pm 9.21\times10^{-7}$	0.95	0.92	
		343	1.09 ± 0.0293	14.12 ± 0.3837	1.52 ± 0.0688	$2.48\times10^{-4} \pm 7.07\times10^{-6}$	0.98	0.95	10.57
		353	1.33 ± 0.47	13.11 ± 4.72	1.13 ± 0.52	$3.06\times10^{-4} \pm 8.46\times10^{-5}$	0.96	0.85	
USERR		333	2.00 ± 0.01	3.41 ± 0.01	9.88 ± 0.19	$3.89\times10^{-5} \pm 1.64\times10^{-7}$	0.97	0.93	
		343	3.02 ± 0.45	1.76 ± 0.26	1.60 ± 0.56	$3.62\times10^{-4} \pm 7.66\times10^{-5}$	0.99	0.99	5.57
		353	3.98 ± 0.14	4.23 ± 0.15	1.21 ± 0.05	$1.73\times10^{-4} \pm 4.5\times10^{-6}$	0.94	0.86	
			$k_{forward,ER}$ [L/gcat.min]	$k_{ads,CA}$ ×10³ [L/mol]	$k_{ads,G}$ ×10³ [L/mol]	$k_{des,GMC}$ ×10⁻³ [mol/L]	R^2	R_{adj}^2	APE[a] (%)
QHRUERR	ERCA	333	2.01 ± 0.034	1.78 ± 0.03	-	$5.68\times10^{-4} \pm 1.47\times10^{-5}$	0.86	0.72	
		343	1.81 ± 0.036	2.01 ± 0.040		$8.082\times10^{-4} \pm 2.84\times10^{-5}$	0.91	0.86	20.13
		353	1.81 ± 0.03	2.01 ± 0.035		$9.62\times10^{-4} \pm 3.14\times10^{-5}$	0.92	0.89	
	ERG	333	3.02 ± 0.06	-	1.22 ± 0.02	$7.19\times10^{-4} \pm 2.75\times10^{-5}$	0.82	0.64	
		343	9.07 ± 0.13		1.94 ± 0.03	$1.13\times10^{-4} \pm 2.00\times10^{-6}$	0.95	*0.92*	15.64
		353	3.01 ± 0.05		2.69 ± 0.06	$4.1\times10^{-4} \pm 1.26\times10^{-5}$	0.92	*0.89*	
QHERR	ERCA	343	1.90 ± 0.01	1.90 ± 0.01	-	$3.59\times10^{-4} \pm 1.98\times10^{-6}$	0.96	0.94	10.78
	ERG	343	1.99 ± 0.026	-	1.89 ± 0.03	$5.21\times10^{-4} \pm 1.48\times10^{-5}$	0.95	0.92	11.4
USERR	ERCA	343	1.46 ± 0.02	1.70 ± 0.02	-	$2.91\times10^{-4} \pm 7.73\times10^{-6}$	0.92	0.87	7.73
	ERG	343	1.73 ± 0.03	-	1.80 ± 0.04	$2.92\times10^{-4} \pm 1.00\times10^{-5}$	0.90	0.85	14.5
			$k_{forward,PH}$ [L²/gcat.mol.min]	$k_{ads,CA}$ ×10³ [L/mol]	$k_{ads,G}$ ×10³ [L/mol]	$k_{des,GMC}$ ×10⁻³ [mol/L]	R^2	R_{adj}^2	APE[a] (%)
QHRUERR	P H	333	1.22 ± 0.45		-		0.68	0.68	
		343	1.54 ± 0.34		-		0.78	0.78	29.82
		353	1.64 ± 0.27				0.85	0.85	
QHERR	P H	343	1.14 ± 0.19		-		0.83	0.83	17.56
USERR	P H	343	0.754 ± 0.09		-		0.87	0.87	15.68

Bold letters indicate selected model ; a: APE (Average Percentage Error)= $\left(\frac{\sum_{i=1}^{n} \left| \frac{r_{CA,\exp} - r_{CA,pred}}{r_{CA,\exp}} \right| \times 100}{\text{no.of experiments}} \right)$

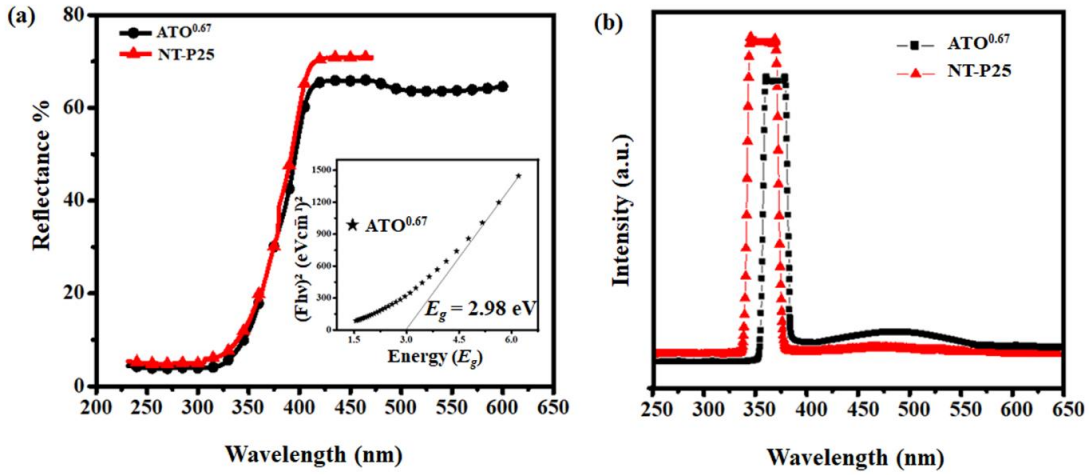

Figure 6.12. Photocatalytic activity of NT-P25 and $ATO^{0.67}$ using (a) UV–Vis diffuse reflectance spectra (b) PL spectra

Thus, NT-P25 showed photocatalytic activity in the UV region; while, $ATO^{0.67}$ displayed the photocatalytic activity in near visible region under QHR radiator.

6.2.4 Reaction Mechanism

The plausible reaction mechanism following LH model narrated simultaneous adsorption of CA and G on acidic sites present in the reaction mix. Figure 6.13 shows that the Lewis acid center (Ti^{4+}) forms an intermediate complex with the carbonyl oxygen of CA. Then deprotonation of hydroxyl groups of G takes place by the Lewis acid sites while oxygen produces nucleophile, that attacks the carbocation and eventually form a tetrahedral complex [38]. Subsequently, the Brønsted acid site (H^{+}) gets linked with the tetrahedral complex followed by the subsequent release of Ti^{4+} ions [39].

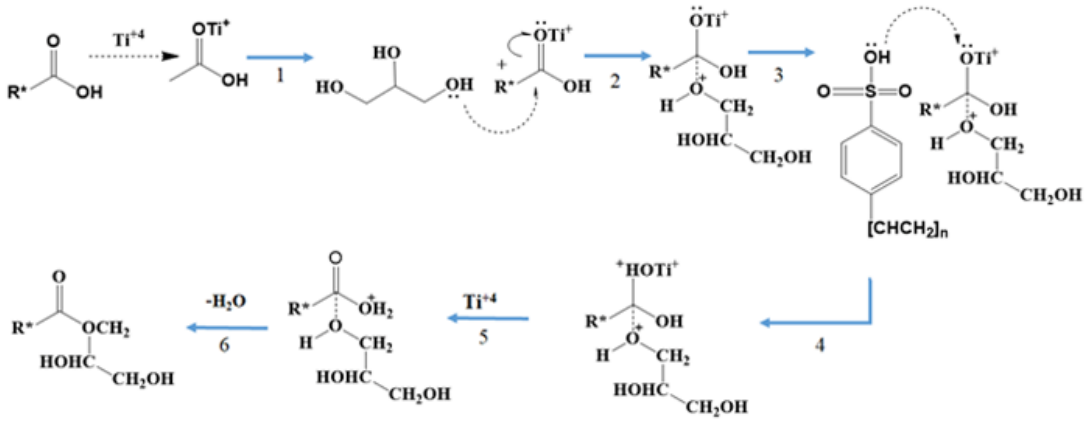

Figure 6.13. Reaction Mechanism for $ATO^{0.67}$ in CA-GL esterification

Consequently, the intermediate complex eliminates the water while forming the desired product (GMC). The ester and the by-product water were desorbed and diffused out of catalyst sites and water was eventually adsorbed by desiccants while GMC stayed in the bulk phase. The quantification of GMC was eventually accomplished by HPLC analysis (Figure 6.14).

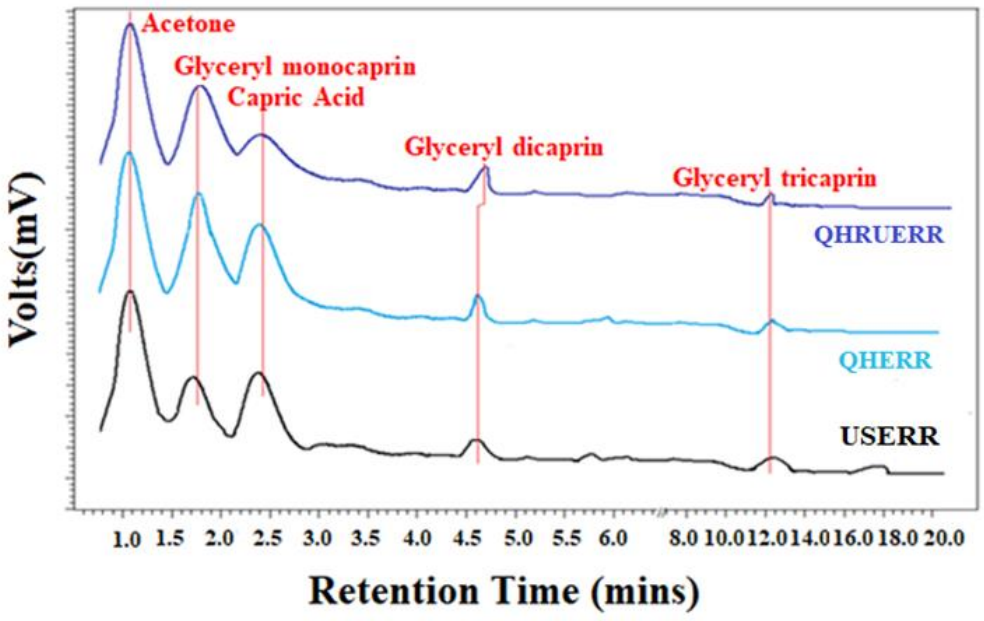

Figure 6.14. HPLC of optimal product of CA-GL esterification in different reactors.

6.2.5 Catalyst Recycle Efficacy

Figure 6.15 shows the activity of $ATO^{0.67}$ catalyst in terms of CA conversion as a function of catalyst age in different reactor configurations. The reuse of catalyst up to

8 batch cycles (480 min) resulted in diminution in CA conversion from 97±0.5% to 86% (QHRUERR),whereas, a larger reduction in CA conversion from 56% to 27% was observed in CERR. The results evidently established the superior efficacy of ultrasonic mixing and molecular excitation caused by QH radiation that could facilitate overcoming the phase boundaries resulting in effortless adsorption and desorption of reaction species in QHRUERR than in CERR.

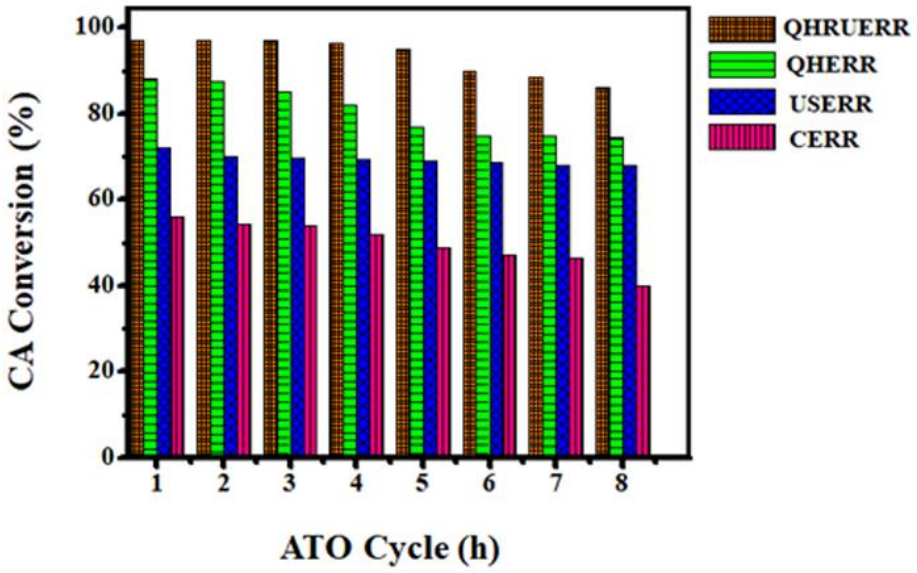

Figure 6.15. Reusability of ATO catalyst

6.2.6 Application of GMC as Food Preservative

From Figure 6.16, it is confirmed that synthesized GMC resulted better inhibition efficacy than sodium benzoate and exhibited comparable performance with respect to pure GMC. The growth of the spores and the inhibition exerted by the synthesized GMC were observed after every 24 h, as shown in Figure 6.16a-e.

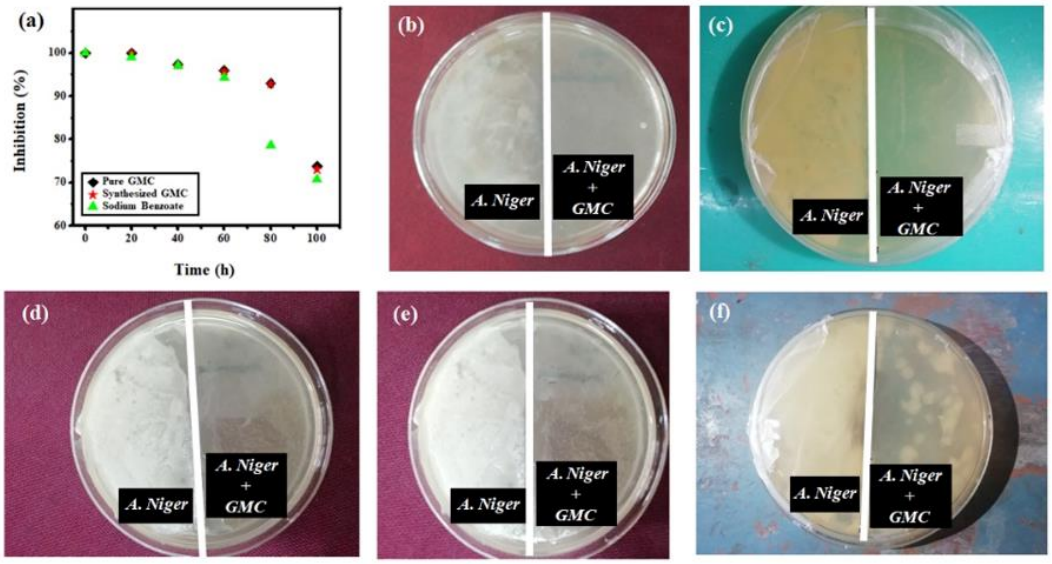

Figure 6.16. Zone of inhibition result of GMC on the growth of *Aspergillus Niger* (a**)** Image of the culture in every 24 h gaping: after (b) 24 h, (c) 48 h, (d) 72 h, (e) 96 h (f) 144 h.

Moreover, *A. Niger* growth was observed after 144 h; thus, implying that the synthesized GMC could provide necessary inhibitory effect towards the growth of *A. Niger* and may be effectively used as an efficient food preservative. The mechanism of antifungal property corroborated well with the previously reported findings [40].

6.3 ACTIVITY III

The details of catalyst characterizations vis-à-vis application thereof in optimal GC synthesis along with the LCA of the overall process have been presented in the following sections.

6.3.1 Catalyst Characterizations

6.3.1.1 XRD Study

Figure 6.17 demonstrates the XRD pattern of WPCB derived $SA_{(WPCB)}$ (i), uncalcined $MATLS_W$-5 (ii), calcined $MATLS_W$-5 (iii), and calcined $MATLS_C$ (iv). The broad

hump in all the diffraction patterns can be ascribed to the existence of silica (SiO_2) in the synthesized materials. In Figure 6.17ai, the diffracted peak at 26.57° is responsible for the (112) crystal plane of silica and whereas the peak at 17.64° for alumina (Al_2O_3) are well-matched with the JCPDS file no. 01-079-2403, 01-082-0511 [41]. In Figure 6.17aii, the intense peaks at 12.25° and 22.76° are due to (003) and (006) crystal planes of Mg-Al-LDH and Mg-Al-Ti-LDH phases respectively. The brucite structure, $Mg(OH)_2$, where Mg^{2+} cations are octahedrally synchronized with hydroxyl groups in which partial replacement occurred by trivalent and tetravalent ions such as Al^{3+} and Ti^{4+} on the addition of Al (from WPCB derived silica-alumina) and Ti-precursor, respectively; thus, proving the high degree of crystallinity and layered structure [42]. The sharp peak at 36.97° is attributed to the (103) crystal plane of the anatase phase of TiO_2 (JCPDS file no. 01-071-1166). After calcination of LDH at 600 °C, the peaks at 12.25° and 22.76° disappeared and the peaks at 18.36°, 41.35°, and 46.7° can be accounted for MATLS$_W$-5 ($MgAl_2Ti_3O_{10}$ crystalline phase) as confirmed by the JCPDS file no. 00-005-0450 (Figure 6.17aiii). However, the diffractogram of MATLS$_C$ at 18.31° indicates a similar pattern relative to MATLS$_W$-5 (Figure 6.17aiv). Moreover, the peaks at 26.78° and 38.50° are characteristic of (101) and (103) crystal planes of SiO_2 and TiO_2 (anatase) phases respectively, which ensure the presence of SiO_2 and TiO_2 in all the prepared catalysts.

6.3.1.2 FTIR Study

FTIR spectra of WPCB derived SA$_{(WPCB)}$ (i), MATLS$_W$-5 (iii) and MATLS$_C$ (iv) catalysts were recorded in the region of 4000 to 400 cm^{-1} as depicted in Figure 6.17b. Figure 6.17bi displays the intense adsorption peak at 600 cm^{-1} and the weak adsorption peak at 1000 cm^{-1}, which confirm the bending mode of silica and vibration mode of silica-alumina, respectively. The stretching band corresponding to silica is

also found at 1250 cm^{-1} for both $MATLS_W$-5 and $MATLS_C$ catalysts and support (Figure 6.17bi, iii, iv) [43]. The hydroxyl stretching mode on the support is located at wavenumber 3450 cm^{-1} and the WPCB derived and commercial SiO_2 modified catalysts revealed a small adsorption peak at 3550 cm^{-1} due to the presence of a minimal amount of hydroxyl groups in the brucite layer. The shift of the peak position from 3550 cm^{-1} to broad peak at 3450 cm^{-1} is adapted by Ti $^{4+}$ and Al $^{3+}$ ions present in the catalysts' layer i.e., Ti-OH-MgAl (Figure 6.17biii, iv). Nevertheless, a low-frequency band at 1640 cm^{-1} (Figure 6.17biii, iv) is attributed to the interlayer water molecules and anions [44]. Moreover, the band around ~440 cm^{-1} could be ascribed to metal-oxygen (metals viz. Mg, Al, Ti) stretching vibrations in the catalyst layers.

6.3.1.3 TGA Analysis

The thermal stability of the WPCB derived silica-alumina ($SA_{(WPCB)}$) and synthesized catalysts with varying proportions of constituent species were analyzed by TGA (in Figure 6.17c). The mass loss of SiO_{2W} has been detected to be about 14 % in between 300 to 345 °C due to the desorption of adsorbed water. Second decomposition (about ~5% loss) from 345 to 380 °C occurred due to the condensation and dehydration of silanol groups present in the silica [41]. The catalysts viz. $MATLS_W$-1, $MATLS_W$-2, $MATLS_W$-4, $MATLS_W$-7 exhibited ~5.47 % mass loss around 261 °C owing to desorption of water while further ~11.8 wt.% loss was observed due to dehydroxylation of brucite-like layers from 261 to 400 °C, [45]. An additional ~20.77% mass loss (400 to 750 °C) indicated the removal of carbonate anions could be intercalated with the LDH. On the other hand, the rest of the catalysts ($MATLS_W$-3, $MATLS_W$-5, $MATLS_W$-6, $MATLS_W$-8, $MATLS_W$-9) revealed three stages of decomposition, as elaborated in Figure 6.17c. Primarily, for $MATLS_W$-5 catalyst, the release of interlamellar water molecules was found from 25 to 300 °C with 10.88%

mass loss. Subsequently, dehydroxylation (300 - 355 °C) led to ~12.51% mass loss. Finally, ~21.47% loss occurred due to the decomposition of the strongly bound carbonate anions from the interlayer region between 355 and 600 °C, Notably, from Figure 6.17c, it can be visualized that the mass loss in case of MATLS$_W$-1, MATLS$_W$-2, MATLS$_W$-4, MATLS$_W$-7 was relatively lower in comparison with the other catalysts as the total mass loss was observed to decline with the reduction of TiO_2 in the composites [46, 47]. TGA analysis of WPCB has also been done before removal of brominated epoxy resin. It is observed from Figure 6.18 that the maximum rate of mass loss for untreated WPCB was found at 272 °C due to the presence of BER [48]. The weight loss at 399 °C could be ascribed to the polymers of the WPCBs other than flame retardants. The intense weight loss might be attributed at around 450-600 °C due to the combustion of polymeric fraction [49].

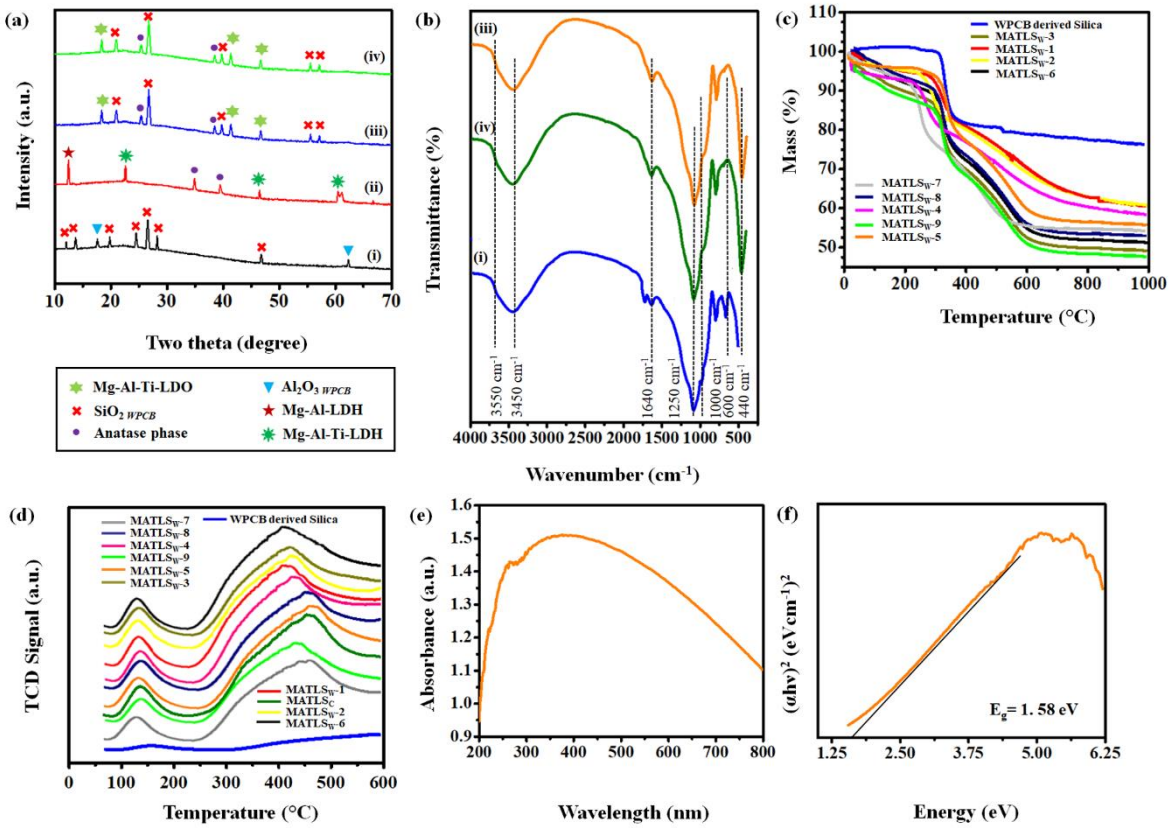

Figure 6.17. (a) XRD configuration of (i) WPCB derived SA$_{(WPCB)}$, (ii) uncalcined

MATLS$_W$-5, (iii) calcined MATLS$_W$-5, (iv) calcined MATLS$_C$ (b) FTIR spectra (c) TGA (d) CO_2-TPD of MATLS$_W$ catalysts, WPCB derived SA$_{(WPCB)}$, MATLS$_C$ catalysts and (e) UV-Vis Diffuse Reflectance Spectra (DRS) (f) Tauc Plot of MATLS$_W$-5

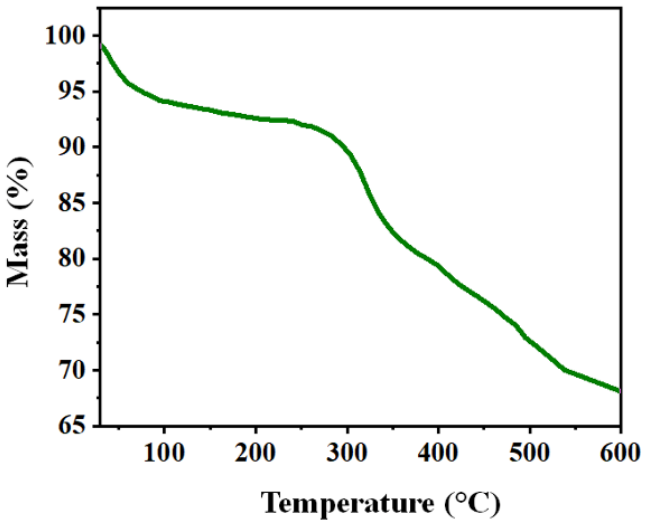

Figure 6.18. TGA analysis of WPCB with brominated epoxy resin

6.3.1.4 CO_2 TPD

The basic strength of the different synthesized MATLS$_W$ catalysts was determined by CO_2-TPD and the results are shown in Figure 6.17d. Two main CO_2 desorption peaks could be detected, one between 50 and 300 °C and another between 300 and 500 °C; henceforth, ascribed to the weak basic sites and moderately strong basic sites respectively. The typical desorption of CO_2 with small peak at 124.7 °C indicated the weak Brønsted basic site of MATLS$_W$-5 catalyst. Hence, this site denotes the bidentate carbonate anions, which is related to the surface hydroxyl groups in the structure [50]. The broad peak located at 475.15 °C denotes the strong Lewis base site of MATLS$_W$-5 catalyst. Moreover, the incorporation of Ti^{4+} and Al^{3+} ions in the LDO matrix could beneficially reduce the basic sites of the catalyst [51] as strong basic sites of LDO catalysts are disadvantageous to transesterification reaction resulting in low yield

(Figure 6.22d, e). The relative basic site strength of the various catalysts are as follows; WPCB derived $SA_{(WPCB)}$ <$MATLS_W$-6 < $MATLS_W$-3 < $MATLS_W$-1 <$MATLS_W$-2 < $MATLS_W$-4 <$MATLS_W$-9 < $MATLS_W$-7 <$MATLS_W$-8 < $MATLS_C$ <$MATLS_W$-5. Thus, CO_2-TPD profile of $MATLS_W$-5 catalyst signifies desirable basic characteristics as compared to other prepared catalysts (Figure 6.17d).

6.3.1.5 UV-Vis DRS Spectra

The optical property of the $MATLS_W$-5 was observed by UV-Vis DRS spectra (200 to 800 nm) as illustrated in Figure 6.17e. From the literature, it was learned that the TiO_2 exhibited an intense peak in the UV region <385 nm, which influenced the photon energy transfer between electron-holes from ligand to metal [52]. In comparison with TiO_2, $MATLS_W$-5 exhibited longer absorption of light in the visible region (400-800 nm). The shift might happen due to the incorporation of a partial amount of tetravalent Ti^{4+} ions in the brucite-like layers [45], which induced the excited state of TiO_2 towards the visible range with a high-pitched edge prominent at 800 nm wavelength. The direct bandgap energy (E_g) was determined using Kubelka-Munk expression ($F(R)$) as stated by the following equations:

$$(\alpha h\nu)^n = A(h\nu - E_g) \tag{6.6}$$

$$(F(R)h\nu)^n = A(h\nu - E_g) \tag{6.7}$$

$$F(R) = \frac{(1-R)^2}{2R} = \frac{K}{S} \tag{6.8}$$

where, α : absorption co-efficient, h : Planck's constant, ν : light frequency, A : Absorption constant, E_g : Bandgap, n : 2 for indirect transition, $F(R)$: Kubelba-Munk function, R : reflectance of $MATLS_W$-5, K : molar absorption co-efficient, S :

Scattering factor

The calculation of bandgap energy was done by Tauc plot: $(F(R)h\nu)^2$ vs. $h\nu$ as revealed in Figure 6.17f. It could be found that the bandgap energy (E_g) of MATLS$_W$-5 was 1.58 eV, which was remarkably less compared to that of nano-TiO_2 (3.35 eV). Concurrently, the MATLS$_W$-5 catalyst with the optimal proportions of SA:Mg:Ti (mole ratio of 12:5:3) can facilitate much improved photocatalytic activity in the transesterification reaction with less energy consumption under SSQLBR.

6.3.1.6 Morphological Analysis

The FESEM image (Figure 6.19a) depicts the rod-like morphology of the SA$_{(WPCB)}$. From Figure 6.19b, it is observed that the rod-like morphology of SiO_{2W} support is covered with Mg-Al-Ti based LDO. The elemental composition of unimpregnated SA$_{(WPCB)}$ is: 21.14% Si, 6.47% Al, and 72.39% O (Figure 6.19c). Whereas, the EDS analysis of the SiO_{2W} supported MATLS$_W$-5 catalyst reveals a significant presence of Mg and Ti along with Al, Si and O (1.33%, 8.70%, 0.89%, 36.17%, and 52.91%, respectively), as shown in Figure 6.19d.

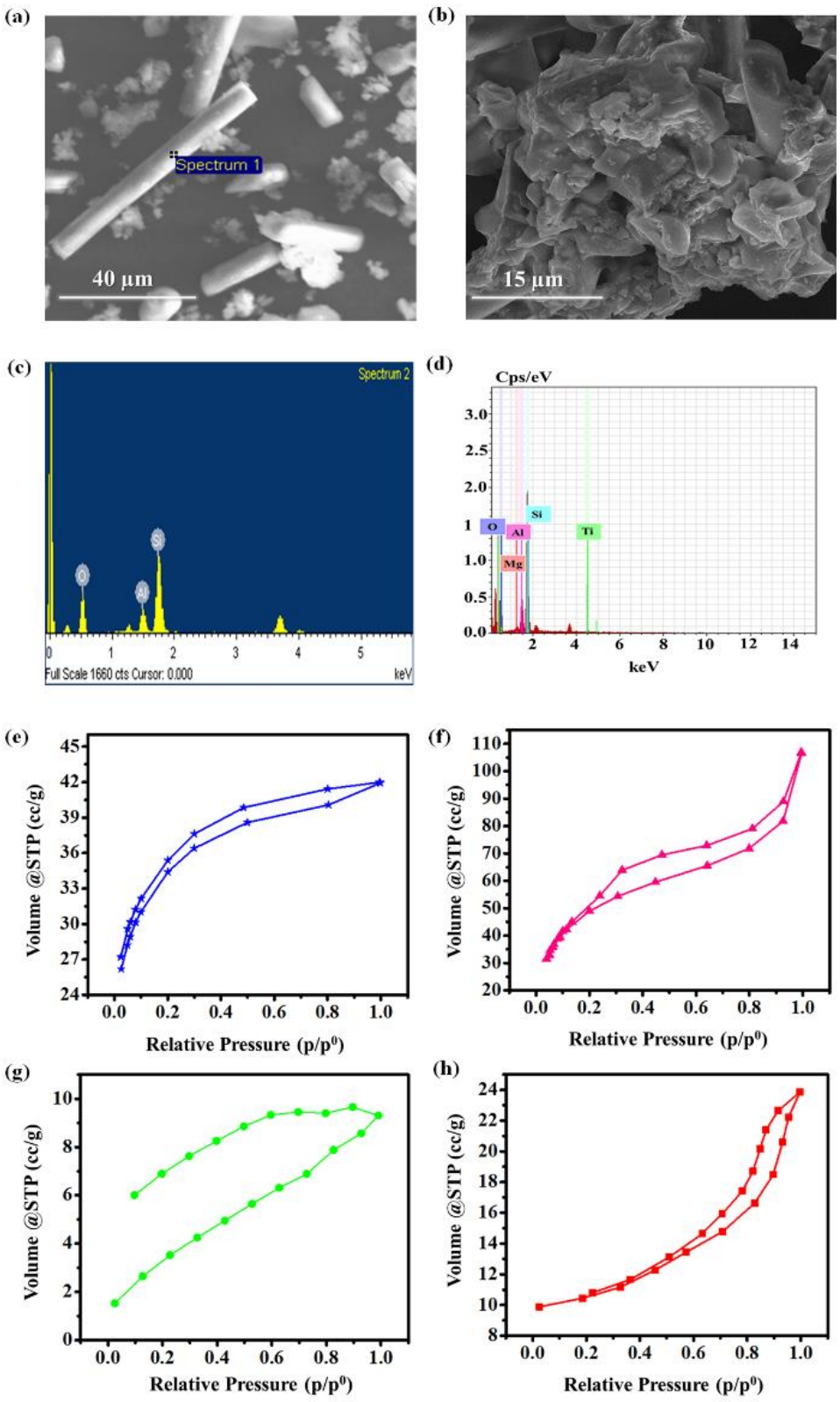

Figure 6.19. FESEM and EDS: (a,c) WPCB derived $SA_{(WPCB)}$ (b,d) MATLSW-5 ; BET N_2-sorption isotherm: (e) WPCB derived $SA_{(WPCB)}$ (f) $MATLS_W$-5 (g) commercial silica (h) $MATLS_C$

6.3.1.7 BET Analysis

The textural property of $SA_{(WPCB)}$, optimal $MATLS_W$-5 catalyst, commercial $SA_{(C)}$, and $MATLS_C$ were analyzed using BET method (Figure 6.19e-h). The $SA_{(WPCB)}$ exhibited type I isotherm with H_4 type hysteresis loop indicating the microporous characteristics (Figure 6.19e). The N_2 sorption isotherm of optimal catalyst $MATLS_W$-5 represented H_3 type hysteresis loop (p/p° in the range of 0.2-0.8) implied mesoporous morphology (Figure 6.19f); while the type IV (IUPAC classification) isotherm of $MATLS_W$-5 could be ascribed to monolayer-multilayer adsorption [53]. The BET specific surface area of $SA_{(WPCB)}$ and $MATLS_W$-5 are 160.349 m^2/g and 126.295 m^2/g, respectively. In contrast, the $SA_{(C)}$ and $MATLS_C$ possessed appreciably lower surface area of 26 m^2/g and 56 m^2/g respectively. It is evident (Figure 6.19g, h) that $MATLS_C$ displays type III isotherm indicating microporous structure in the $SA_{(C)}$ and $MATLS_C$. Thus, the SiO_{2W} supported catalyst with high specific surface area and mesoporous morphology would be advantageous for the transesterification reaction for GC synthesis.

6.3.1.8 XPS Analysis

The electronic states of the constituent species of the optimum synthesized catalyst $MATLS_W$-5 is revealed through XPS analysis (Figure 6.20a-g). The electronic state of the elements present in the catalyst was obtained by X-ray photoelectron spectrometry (XPS, VG ESCALAB 220i, Thermo Fisher, UK) analysis with the binding energies for the catalyst compositions calibrated using C1s at 284.6 eV (Figure 6.20b). Si 2p unravels three peaks as shown in Figure 6.20c. The primary peak at 102 eV is assigned to Al-O-Si bonds of the $SA_{(WPCB)}$. The binding energy at 103.5 eV indicates Si-O bond, while 99.3 eV resembles Si. The binding energy of Mg 2p could be ascribed to Mg-OH at 50.8 eV.; whereas, the peak of Mg 2p at 49.9 eV binding energy

is associated to the metallic state (Figure 6.20d). In this approach, the spectra of Al 2p could be divided into two peaks (Figure 6.20e). The Al 2p binding energy at 74.1 eV represents the octahedrally coordinated Al^{3+} in LDO framework, as 74.3 eV indicates the high interaction between Al^{3+} and Mg^{2+} caused by scattering. The deconvolution of the XPS spectra of TiO_2 demonstrates the high-resolution peak of Ti $2p_{3/2}$ and weak peak of Ti $2p_{1/2}$ located at 458.1 and 463.8 eV respectively. These are responsible for the strong electron transfer between Ti^{4+} and Brucite layers (Figure 6.20f). Such interactions could be advantageous for generating electron-hole pairs during photocatalysis [54]. The XPS spectra for O 1s demonstrate four different peaks (Figure 6.20g). O1s spectrum at 530.4 eV relates to the lattice oxygen confined to Mg^{2+}, Al^{3+}, Ti^{4+} or Si^{2+} of the $MATLS_W$-5, considered as more active basic sites [55]. Besides, the other two peaks at 531.4 and 532.7 eV are ascribed to CO_3^{2-} and H_2O, respectively.

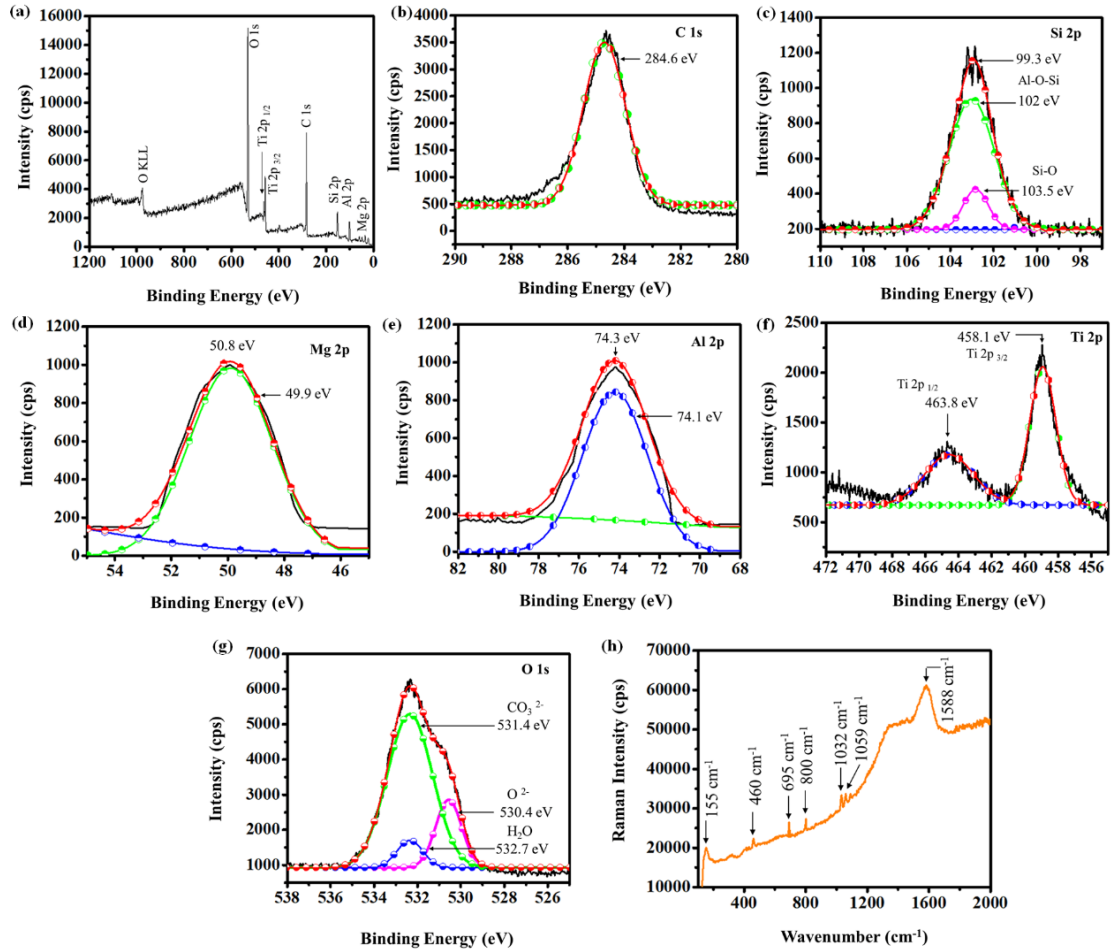

Figure 6.20. (a-g) XPS analysis, (h) Raman spectra of MATLS$_W$-5

6.3.1.9 Raman Spectra

To achieve more information of various bands in FTIR absorption spectra, the Raman scattering effect was observed in the range of 100-2000 cm^{-1} for the optimum synthesized catalyst MATLS$_W$-5 (Figure 6.20h). In the Raman spectra, the strong band recorded at ~155 cm^{-1} due to the anti-symmetric stretching vibration of hydrogen bond in both brucite-like octahedral layers and interlayer water molecules. The band at 460 cm^{-1} could be attributed to the Mg-OH and Al-OH bond. Moreover, the peak at ~695 cm^{-1} (ν_4) and 1059 cm^{-1} (ν_1) corroborates well with the interlayer CO_3^{2-} symmetric stretching mode, which is associated with brucite hydroxyl surface of the MATLS$_W$-5 catalyst [56, 57]. Besides, an intense band at ~800 cm^{-1} occurred due to

Ti-O vibrations in the catalyst phase [58]. Finally, owing to water bending modes, the higher wavenumber band at 1588 cm^{-1} was detected [59].

6.3.2 Optimization

6.3.2.1 ANOVA Analysis of the Transesterification Parameters and Model Validation

Table 6.12 represents the 'Model Fit Summary', obtained from the transesterification data, which could be represented using three statistical correlations such that is linear, 2FI, and quadratic models. Among these models, the quadratic model could best predict the GC yield compared to linear and 2FI models, as the quadratic model displayed the lowest standard deviation (0.24), highest R^2 (0.99), and adjusted R^2 (0.99). ANOVA results for the quadratic model were found to be statistically significant due to acceptable p-value <0.0001 (at 95% confidence level) and high model F value of 271.3278. Based on the ANOVA results (Table 6.13), it is observed that all three process parameters were statistically effective (p-value <0.05); further, catalyst concentration has the highest influence (max F value) on GC yield followed by reaction time and reaction temperature. The significant model terms γ_{CC}, γ_T, γ_t, $\gamma_{CC}\gamma_T$, $\gamma_{CC}\gamma_t$, $\gamma_T\gamma_t$, γ_T^2, γ_t^2 were considered in the quadratic model (Eq. 6.9) that adequately established the relationship between the response and process parameters in coded form.

$$\gamma_{GC} = 95.67 + 2.60\gamma_{CC} + 1.69\gamma_T + 2.46\gamma_t - 0.55\gamma_{CC}\gamma_T - 0.67\gamma_{CC}\gamma_t + 0.32\gamma_T\gamma_t - 0.35\gamma_T^2 - 1.98\gamma_t^2$$

$$(R^2 = 0.99) \qquad (6.9)$$

Table 6.12 Model fit summary of linear, 2FI, and quadratic model for GC yield

Source	Prob > F	Std. Dev.	R^2	Adjusted R^2	Predicted R^2	PRESS
Linear	< 0.0001	1.2994	0.8517	0.8175	0.7375	38.8669
2FI	0.6175	1.3603	0.8750	0.8001	0.5567	65.6390
Quadratic	< 0.0001	0.2459	0.9971	0.9934	0.9542	6.7732

The perturbation plot (Figure 6.21) illustrates that the enhanced GC yield (γ_{GC}) could be achieved at higher γ_{CC} (A), γ_T (B), and γ_t (C); thus, reiterating the findings of ANOVA analysis. Notably, with an increase in γ_{CC}, a higher number of basic reaction sites became available, which eventually positively affected the transesterification of GL and DMC leading to higher γ_{GC}. As evident from Eq. 6.9, all 2FI and quadratic terms have a negative effect; thus, higher values of the parameters B and C demonstrate an antagonistic effect on γ_{GC}.

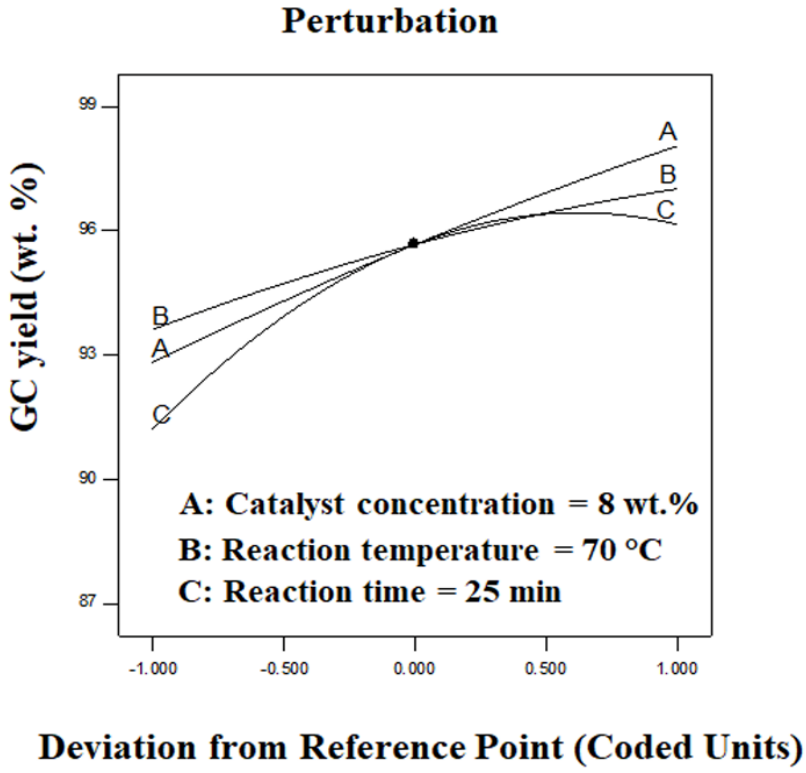

Figure 6.21. Individual influence of process parameters

6.3.2.2 Interactive Parametric Effects on GC Yield

The contour plot (Figure 6.22a) elucidates the interactive effects of γ_{CC} and γ_T on γ_{GC}. The γ_{CC} was varied from 2 to 8 wt.% and γ_T was varied from 50 to 70 °C by keeping the reaction time fixed at 25 min. Evidently, the γ_{GC} increased monotonically from 91.55 wt.% to 97.39 wt.% with the corresponding rise in γ_{CC} from 2 wt.% to 8 wt.% due to availability of increased basic sites of catalyst; indicating surface reaction kinetics controlling regime. Further increase in γ_{CC}, it renders high γ_{GC} but the mass transfer limitation might occur in the reaction process [60]. Figure 6.22b shows the interaction of γ_{CC} and γ_t at the constant value of γ_T at upper level. Mostly, γ_{CC} with 2 wt.% to 8 wt.% concentration resulted in high GC yield (more than 95 %) between 15 min and 25 min. However, prolong reaction time might diminish the γ_{GC} via glycidol formation in reaction mixture [61]. Figure 6.22b exhibits that the maximum yield could be obtained within 25 min employing 8 wt.% catalyst concentration. Figure 6.22c depicts the interaction between γ_T and γ_t indicating that an elevated temperature (up to 70 °C) could enhance the γ_{GC} in between 15 to 25 min, but an additional time and higher temperature (>70 °C) could lessen γ_{GC} owing to overheating of reaction system [62]. Accordingly, the optimal parametric values concerning the maximum γ_{GC} was achieved at 70 °C, 8 wt.% γ_{CC}, and 25 min.

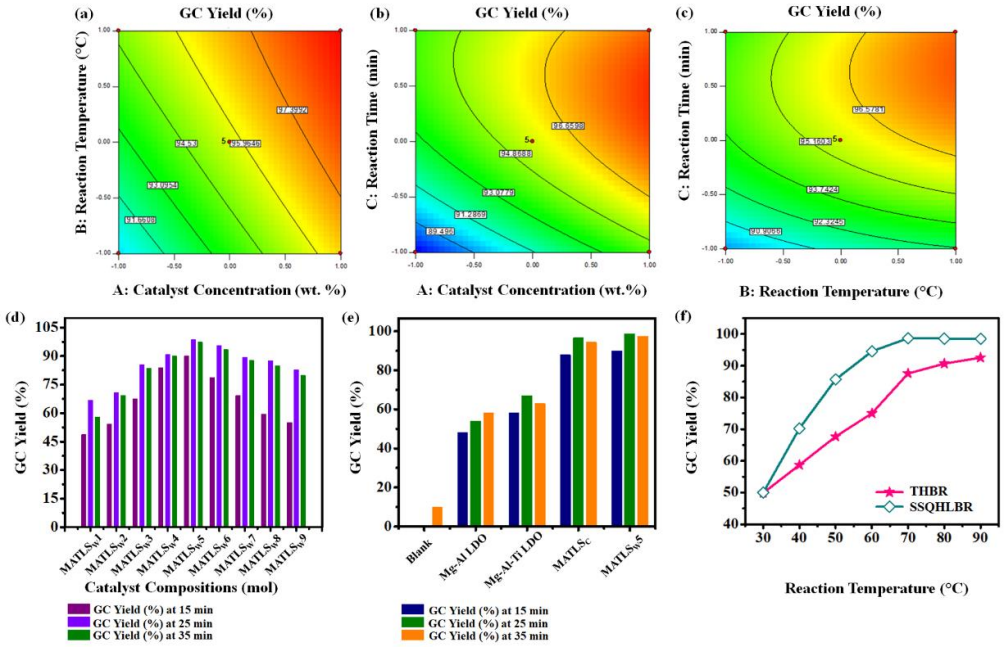

Figure 6.22 (a), (b) & (c) Interactive effects of catalyst concentration with reaction temperature, catalyst concentration with reaction time & reaction temperature with reaction time; (d) Effect of catalyst composition on GC yield; (e) Effect of reaction time on GC yield; (f) Effect of reaction temperature on GC yield at optimal parametric condition

Table 6.13. ANOVA results for quadratic model corresponding to Eq. 6.9

Source	Sum of Squares	df	Mean Square	F Value	p-value Prob > F	
Model	147.6769	9	16.4085	271.3278	< 0.0001	significant
γ_{CC} -catalyst concentration	54.3403	1	54.3403	898.5583	< 0.0001	
γ_T -reaction temperature	23.0521	1	23.0521	381.1831	< 0.0001	
γ_t -reaction time	48.7578	1	48.7578	806.2474	< 0.0001	
$\gamma_{CC}\gamma_T$	1.2210	1	1.2210	20.1906	0.0028	
$\gamma_{CC}\gamma_t$	1.7956	1	1.7956	29.6916	0.0010	
$\gamma_T\gamma_t$	0.4290	1	0.4290	7.0943	0.0323	
γ_{CC}^2	0.2276	1	0.2276	3.7636	0.0935	
γ_T^2	0.5306	1	0.5306	8.7744	0.0210	
γ_t^2	16.6322	1	16.6322	275.0267	< 0.0001	
Residual	0.4233	7	0.0604			
Lack of Fit	0.4233	3	0.1411			
Pure Error	0	4	0			
Cor Total	148.1002	16				

6.3.2.3. Effects of Catalyst Composition on GC Yield

A series of trimetallic MATLS$_W$ catalysts were prepared (by varying the composition of support within the range from 10 to 15 mol %) deploying the SSQHLBR to study the catalytic performance on transesterification reaction at various time by keeping the other process conditions at optimal level (70 °C temperature and 8 wt.% catalyst concentration). As shown in Figure 6.22d, all catalysts shows impressive activity rendering γ_{GC} in the range of 47.67-98.68 wt.%. Among those, 12 mol% of SA$_{(WPCB)}$ augmented the γ_{GC}, whereas 15 mol % of SA$_{(WPCB)}$ diminished the γ_{GC}. Thereafter, further increase in mol% i.e., basicity of the catalyst might be reduced at the expenses of glycidol formation [63]. The best catalytic performance was observed for 12:5:3 mole ratio of Si:Mg:Ti which showed maximum yield of GC (98.68 %) under SSQHLBR. To get more insight about the interrelation between the nature and reactivity of the synthesized catalyst MATLS$_W$-5, different heterogeneous base catalysts namely conventional Mg-Al LDO catalyst (5:1 mole ratio), Mg-Al-Ti LDO catalyst (5:1:3 mole ratio), commercially modified MATLS$_C$ were used for GC synthesis under SSQHLBR (Figure 6.22e). Apparently, the reaction when carried out under blank condition resulted a maximum 10 wt.% γ_{GC} at 35 min while the Mg-Al LDO and Mg-Al-Ti LDO catalysts displayed 48 to 67 wt.% γ_{GC}. Evidently, the MATLS$_C$-5 (more expensive than MATLS$_W$-5) exhibited 90 wt.% γ_{GC} which was significantly less than that (98 wt.% γ_{GC}) rendered by MATLS$_W$-5.

Outstandingly, the MATLS$_W$-5 was highly photoactive, stable, and prepared in a facile manner. Besides, leaching of the active sites in the reaction mixture was insignificant (< 1 ppm Ti/Mg after 5th batch confirmed through ICP); thus, implying appreciable

stability and reusability (98.68% to 96.12%) of the catalyst (Figure 6.24).

6.3.3 Effects of Thermal Heating and Electromagnetic Radiation on GC Yield

The effect of γ_T on the GC yield (Figure 6.22f) in presence of MATLS$_W$-5 catalyst in both the *THBR* and *SSQHLBR* was explored at the derived optimal condition. At room temperature (30 °C), the GC yield was only 48 wt.% under dark condition (no radiation/heating). Under SSQHLBR (40-70 °C), MATLS$_W$-5 catalyst displayed remarkably higher GC yield primarily due to its photoexcitation caused by solar simulated radiation. Further, SSQHLBR could demonstrate outstanding performance at moderate temperature owing to the strong molecular stretching and bending vibrations created due to interaction between reaction mix and the impinging solar simulated radiation (wavelength: 300-1100 nm) that provided higher GC yield within a noticeably shorter time with 90.38% less energy consumption than THBR (Table 6.14).

Table 6.14 Energy analysis for THBR and SSQHLBR promoted transesterification reaction

Reactor type	Power (W)	GC yield (wt.%)	Energy consumption (kJ)
THBR	650	87.56	1560
SSQHLBR	100	98.68	150

6.3.4 Characterization of Synthesized GC by GC-MS

At optimal condition under *SSQHLBR*, all peaks of the product were detected up to retention time of 25 min for both MATLS$_W$-5 and MATLS$_C$-5 catalysts. Figure 6.23 shows a strong peak of GC at retention time 9.5 min and 21 min. The mass spectra of GC are detected by GC-MS with the mass range (m/z) 44.07 and 86.92.

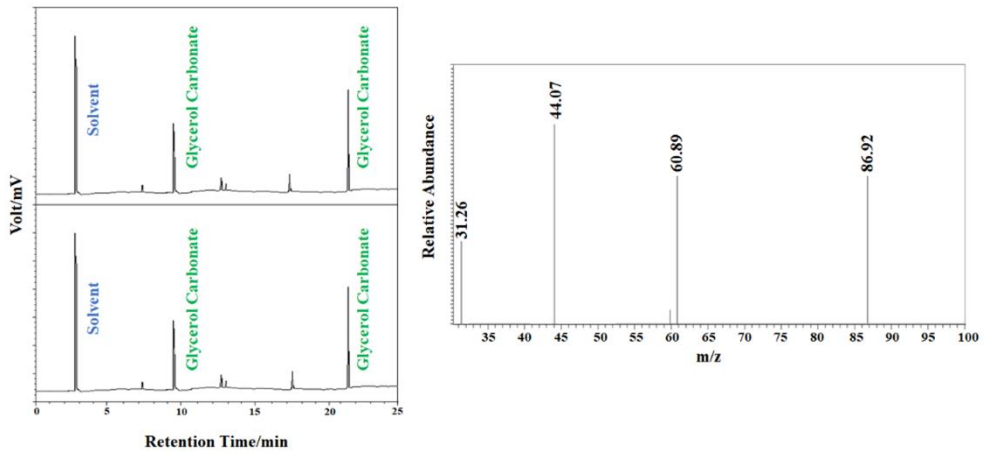

Figure 6.23. Gas chromatography and mass spectroscopy of GC

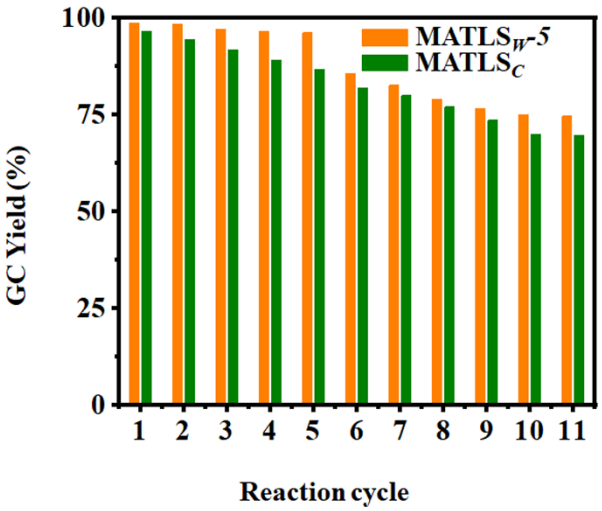

Figure 6.24. Recyclability of the catalyst

6.3.5 Life Cycle Assessment

The environmental impact assessment vis-à-vis LCA results corresponding to the ReCiPe midpoint (H) method are depicted in Figure 6.25a-d. The impact categories mainly GWP 100, FDP, HTP_inf illustrate (Figure 6.25a) more impacts due to acid water, shredded fraction of materials, suspended matters disposal in the air in comparison with other criteria i.e., FETP inf, IRP_HE, METP_inf, MDP, ODP_inf, POFP, TAP100, WDP for GC synthesis under the two reactor configurations namely SSQHLBR and THBR. GC synthesis in SSQHLBR had seemingly revealed 5.78%

less GWP, 3.60% less FDP, and 5.72% less HTP_inf compared to THBR, as shown in Table 5.12. Due to the higher carbon intensity in the Indian electricity mix, the GWP is relatively higher [64]. Remarkably, SSQHLBR consumed lower energy (0.4656 kWh electricity), whereas THBR utilized higher energy (1.074 kWh electricity); thus, SSQHLBR significantly reduced the energy demand during the GC production process. In addition, Figure 6.25b depicts the comparative environmental advantages of MATLS$_W$-5 over its conventional counterpart (MATLS$_C$-5) when used in the SSQHLBR. The LCIA midpoint assessment results (ReCiPe (H) method) exhibited a significant positive contribution of the waste-derived MATLS$_W$-5 catalyst in mitigating harmful environmental impacts than MATLS$_C$-5 (commercial silica-alumina-based catalyst). MATLS$_W$-5 catalyst has a markedly favorable potential on GWP 100, FDP, HTP_inf due to the lower energy usage in the extraction process and treatment of e-waste. Significantly, the novel MATLS$_W$-5 catalyst in conjunction with the SSQHLBR could significantly reduce the environmental damage i.e., preventing 21.56% climate change, 17.63% fossil depletion, and 15.19% human toxicity.

Additionally, in comparison with laboratory scale, a scale-up study of the same process for 1MT (functional unit) of GC synthesis was performed using LCA. Table 5.12 depicts the impact categories where GWP, FDP, HTP_inf, IRP_HE, MDP showed some differences in laboratory-scale results compared with those on a larger scale. These might occur due to the consumption patterns for the creation of the product using the novel protocol. Moreover, at larger scale, additional energy and transportation were required from ‘cradle to gate’.

Based on LCA results, a global perspective on WPCB extraction, WPCB derived MATLS$_W$-5 catalyst preparation and GC synthesis in SSQHLBR have been implemented (Figure 6.25c-e). The graphical presentation aims to demonstrate the

fact that variations in locations have notable impacts on the above-mentioned processes. The GWP, POFP and TAP 100 for WPCB extraction in India, West Bengal (IN-WB) i.e., 0.85386 kg CO_2-Eq, 0.00194 kg NMVOC and 0.00264 kg SO_2-Eq, respectively contributed (Figure 6.25c) higher impacts than the other locations mainly due to higher consumption of electricity; notably, 40.73% of the electricity was consumed for the extraction process. Meanwhile, all over India GWP rendered less impact (0.07525 kg CO_2-Eq) in comparison with the others. Similarly, in the preparation of $MATLS_W$-5, the GWP, POFP, and TAP (Figure 6.25d) showed deleterious impacts i.e., 2.51531kg CO_2-Eq, 0.00571 kg NMVOC, and 0.00779 kg SO_2-Eq, respectively on environment because of high electricity consumption.

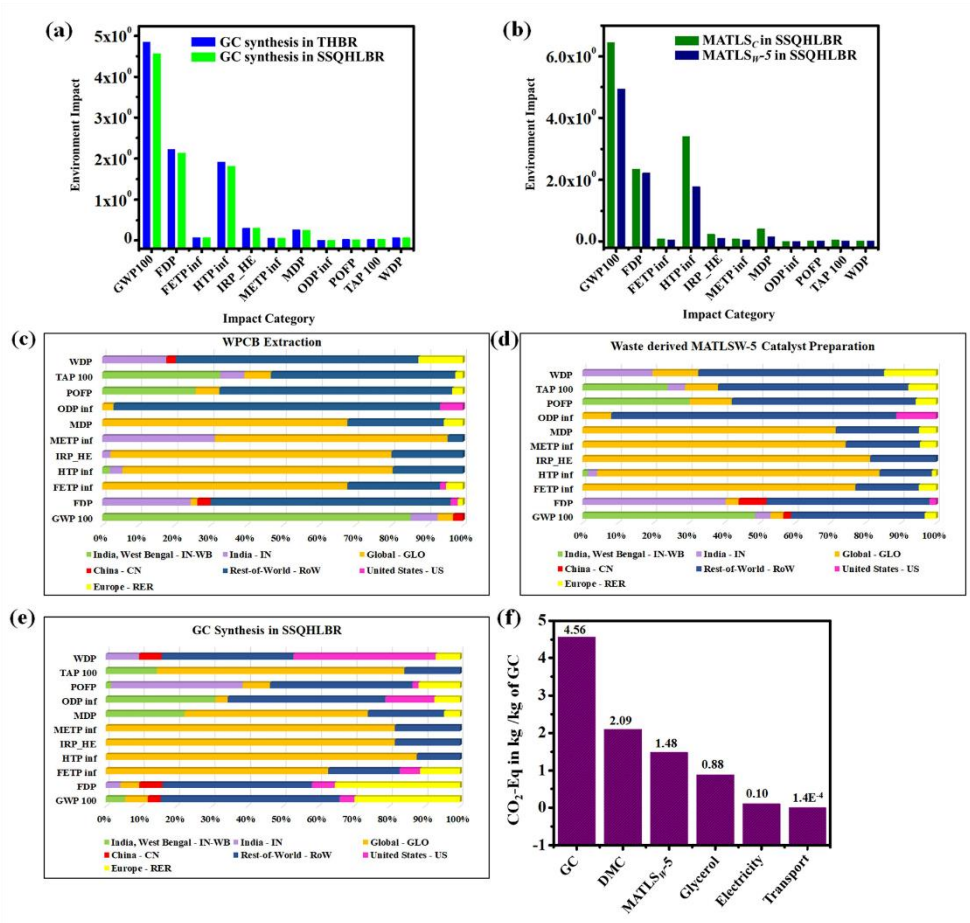

Figure 6.25. Comparative environmental impact assessments for the GC synthesis process: (a) THBR and SSQHLBR using $MATLS_W$-5 catalyst (b) $MATLS_W$-5 and

$MATLS_C$-5 catalyst preparation under SSQHLBR (c)-(e) 'cradle to gate' worldwide scenario, (f)Total GWP incorporating the involvement of product, raw materials, catalyst, reactor, electricity, transport

On the other hand, the GC synthesis in SSQHLBR could reduce the impact of GWP, POFP, and TAP (Figure 6.25e) i.e., 0.09706 kg CO_2-Eq, 0.00022 kg NMVOC, and 0.03168 kg SO_2-Eq, respectively on the ecosystem by consuming only 2.27 % of electricity. Noticeably, the SSQHLBR has remarkably exacerbated the GC production process making it more environmentally benign.

In this study, cost analysis has been adopted using the default ReCiPe Midpoint (H) method to derive the environmental impacts associated with WPCB extraction, $MATLS_W$-5 catalyst preparation, and GC synthesis in SSQHLBR. The cost of WPCB extracted $SA_{(WPCB)}$ powder is only INR 38.17 per 1.5 kg, while the cost of commercial silica-alumina is much higher [INR 475/kg (*www.indiamart.com*)]. Overall costs of 1 kg $MATLS_W$-5 catalyst and 1 kg GC preparation have been estimated to be INR 163.05 and INR 101.62 respectively; which indicate the cost-effectiveness of the present protocol. If each of the raw materials needs to be picked up from source/market, transportation cost could eventually increase the overall production cost. Accordingly, based on the sensitivity analysis, the present process analyzed at the derived optimal condition makes the 'cradle to gate' analysis more realistic, environmentally, and economically viable.

The carbon footprint estimation for the 1 kg GC synthesis process is exposed in Figure 6.25f. The feedstock DMC and GL (in mole ratio 5:3) content in GC is approximately 45.86 wt.% and 19.45 wt.%. However, the major CO_2 load is associated with DMC and catalyst. A 2.09 kg CO_2-eq is connected to the DMC, and 1.48 kg CO_2-eq is accompanied with $MATLS_W$-5 catalyst for the preparation of 1 kg

GC. This accounts for 78% of the total GWP. Whereas, 1.76 kg CO_2-eq is related to $MATLS_C$-5 catalyst for the production of 1 kg GC which accounts for 84% of the total GWP of the process. Therefore, it could be inferred from the results that the GWP could be reduced by 6% for the GC synthesis using the e-waste derived optimal $MATLS_W$-5 catalyst.

The LCA evidently implied superior environmental and economical sustainability of the GC production process due to employment of the e-waste derived novel $MATLS_W$ catalyst compared to the catalyst prepared using commercially available chemicals.

6.3.6 Electrochemical Properties of Product GC

The electrochemical impedance spectroscopy (EIS) (Nyquist plot Z) represents the real part of impedance and Z" imaginary part of the impedance; a charge transfer resistance could be achieved from the diameter of the semicircle of the curve. At low-frequency region, the impedance plot displays a semicircle region. From Figure 6.26a it is clear that the product GC has low charge transfer resistance at high temperature (at 80 °C) than that at room temperature, which depicts the acceptability of the produced GC as a better electrolyte solvent at higher temperature. The electrochemical performance of the ESD with GC electrolyte comprising LiTFSI (1 M) was quantified by a coin cell arrangement. A near-rectangular CV curve was achieved for the supercapacitor with the GC electrolyte and a decent EDLC (electric double layer capacitor) capacitive nature was also obtained. The fabricated supercapacitor with the GC electrolyte produced almost zero current at room temperature. Nevertheless, the CV response of the supercapacitor differed from the EDLC nature, exhibiting a reductive peak at around 1.06 V. The reductive peak is due to the fact of Li-intercalation of the electrodes on charging and discharging process. The viscosity of the electrolyte affects the ion transference in between the electrode

and electrolyte medium which results in the electrochemical performance of the system.

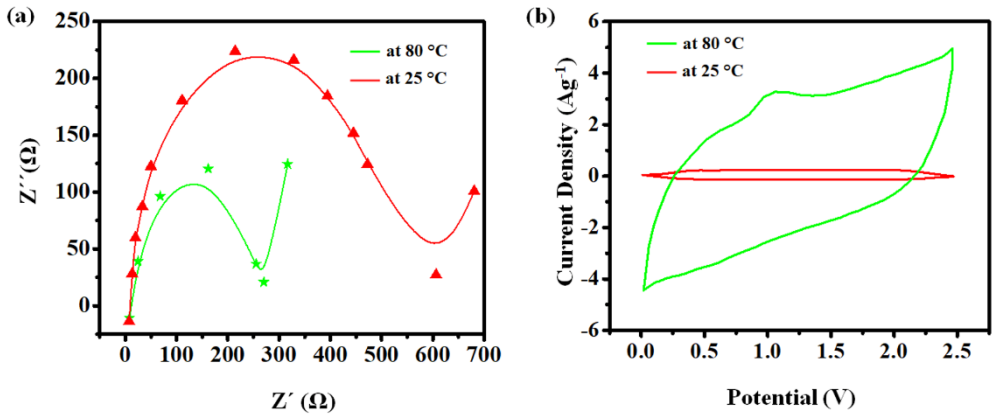

Figure 6.26. Electrochemical properties of product GC: (a) Nyquist plot and (b) cyclic voltammetry at different temperatures.

At higher temperature, the mobility of Li ions in the GC electrolyte becomes higher than at room temperature. Thus, at higher temperature, the Li ions got enough time to get transferred through the liquid and solid interphase showing a pseudocapacitive behavior during the charging-discharge process of each electrode in GC electrolyte. The demonstration of pseudocapacitive behavior of the fabricated cell has been given in Figure 6.26b which states that the fabricated cell exhibited greater storage capability at higher temperature than room temperature. Hence, these results suggest that the produced GC can find its promising applicability as an admirable electrolyte in ESD.

6.4 ACTIVITY IV

6.4.1. Characterization of Catalyst

The detailed diffraction pattern, phase purity, and crystal structure of all the prepared BMZTO samples were evaluated using powder HR-XRD. Figure 6.27a shows progressive peak intensity with a noticeably broadened peak attributed after ball

milling for 10, 20, 40, and 60 min. The sharp diffraction pattern of pristine ZnO/TiO_2 (UMZTO) exhibits the characteristic peak of the rutile phase of TiO_2; hexagonal ZnO displays the ZnO phase, which matches very well with the JCPDS card no. 98-000-0375, 10-73-8765, respectively, as shown in Figure 6.27a.A. In addition, in the UMZTO (Figure 6.27a.A), only one small intensity new peak shift of hexagonal $ZnTiO_3$ is evident in the XRD pattern (JCPDS card no. 26-1500). However, from Figure 6.27a.B, it could be illustrated that after 10 min of ball milling, a high-intensity diffraction peak of hexagonal $ZnTiO_3$ was observed with 2θ and lattice planes at 32.7 (104), 35.2 (110), 48.9 (024), 53.4 (116), 61.77 (214), 63.3 (300) corresponding to lattice constant $a = b = 5.076$Å, $c = 13.92$Å are agreed to $ZnTiO_3$ phase. All the characteristic peaks are well-established with the reported data JCPDS card no. 25-0671. On the other hand, by increasing the ball milling time up to 20 min, the diffraction pattern of BMZTO-20 follows clear characteristic peak positions of cubic Zn_2TiO_4 in accordance to JCPDS card no. 13-0536 as obtained in Figure 6.27a.C. The peaks are assigned at positions 29.6, 34.97, 56.26, and 62.8, representing (220), (311), (511), and (440) crystal planes, respectively. The lattice constants are identified to be $a = b = c = 8.456$Å. The fraction of the cubic phase decreased with an increase in ball milling time. Figure 6.27a.D demonstrates that BMZTO-40 can be effortlessly indexed to an Ecandrewsite phase of $ZnTiO_3$. No obvious peaks are observed from TiO_2 and ZnO which indicates that the synthesized samples are free from unwanted impurities. On the contrary, Figure 6.27a.E precisely confirms similar a diffraction peak of BMZTO-60 with the Ecandrewsite phase of $ZnTiO_3$, justifying the peak positions at 32.75 (104), 35.3 (110), 40.44 (113), 48.93 (024), 53.42 (116), 61.78 (214), 63.38 (300) with no extra peak patterns corresponding to BMZTO-40 because of more milling time. Further attention should be attributed that these diffraction

patterns (Figure 6.27a. D, E) suggest that the hexagonal $ZnTiO_3$ are crystallographically pure Ecandrewsite phase with grain size 52.34 nm (using Scherer's equation). This result unveils the mechano-chemical effect in the formation of $ZnTiO_3$ due to the mechanical energy of the ball mill, which resulted in the fracture of ZnO and TiO_2 and propagates defects in the framework.

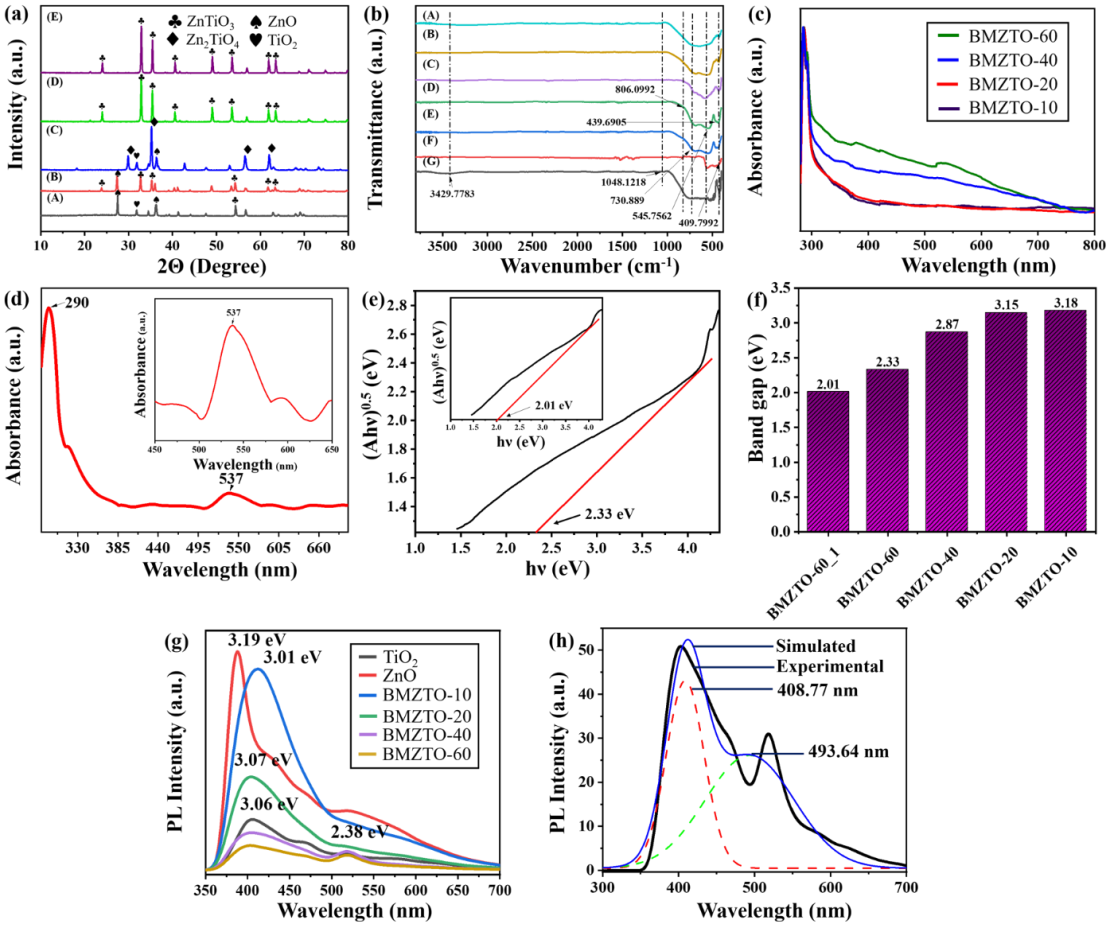

Figure 6.27. a) HR-XRD of (A) UMZTO, (B) BMZTO-10, (C) BMZTO-20, (D) BMZTO-40, (E) BMZTO-60; b) FT-IR spectrum (A) UMZTO, (B) BMZTO-10, (C) BMZTO-20, (D) BMZTO-40, (E) BMZTO-60 (F) ZnO, (G) TiO_2; (c) UV-Vis spectrum of all prepared catalysts (d) UV-Vis spectrum of BMZTO-60 (e) Tauc Plot to determine the direct band gap of BMZTO-60 (f) direct band gap energy calculation for different BMZTO ($ZnTiO_3$); Photoluminescence spectrum of (g) various ball-milled catalysts (h) deconvolution of the BMZTO-60

FT-IR spectra of UMZTO, BMZTO-10, BMZTO-20, BMZTO-40, BMZTO-60, ZnO, and TiO_2 samples at different ball milling time at fixed calcination temperature are measured in the range of 4000-400 cm^{-1} as shown in Figure 6.27b. UMZTO, BMZTO-10, BMZTO-20, BMZTO-40, and BMZTO-60 show a vibration band around 3429 cm^{-1}, characterized as O-H stretching modes of water. The peak at 1048 cm^{-1} denotes the bending vibrations of H-O-H molecules represented in Figure 6.27b(A-G). As shown in Figure 6.27b(A-G), a broad stretching band was detected across 1000 to 400 cm^{-1}. This denotes the metal-oxygen characteristic bands. The peaks at 409 and 545 cm^{-1} wavenumbers of both the ball-milled and nonmilled samples portray the Ti-O and Zn-O stretching vibration, which are the characteristic peak of TiO_2 and ZnO, respectively. The vibration bond at 730 and 806 cm^{-1} are attributed to the Zn-O-Ti bond structure in the cubic phase of Zn_2TiO_4 and Ecandrewsite phase of $ZnTiO_3$, respectively, in Figure 6.27b(A-E) [65]. This is well observed from Figure 6.27b (D, E) that an intense peak at 439 and 545 cm^{-1} are attributed to the stretching vibrations for the Ti-O and Zn-O bonds corresponding to the formation of the Ecandrewsite phase of the $ZnTiO_3$ [66]. Hence, the vibrational bands that appeared in FT-IR elucidate the formation of $ZnTiO_3$.

In order to identify the high photocatalytic activity of the prepared catalysts, it is of utmost importance to evident the catalysts' optical absorption ability in both the UV and visible regions. The UV-Vis spectrum of all the ball-milled samples is recorded in the range of 280-800 nm (UV to the visible range), as shown in Figure 6.27c, d. The absorption spectra of BMZTO for various ball milling periods are shown in Figure 6.27c. The absorption edge of the hexagonal/cubic phase of BMZTO-60, BMZTO-40, BMZTO-20, and BMZTO-10 is about 290, 432, 393, and 389 nm for the 60, 40, 20, and 10 min of the ball milling samples, respectively. However, it can be displayed in

Figure 6.27d that the UV absorption edge of the Ecandrewsite phase of hexagonal $ZnTiO_3$ (BMZTO-60) has a redshift at 537 nm compared to other samples. The respective normalized BMZTO-60 not only shows the intense absorption peak (λ_{max}) in the ultraviolet region at 290 nm, but also has a strong absorption (λ_{max}) in the visible region at 537 nm. This new absorption edge at a higher wavelength (537 nm) is the trigger point that BMZTO-60 might absorb lights in the higher wavelength. Thus, it could increase the affinity to absorb more photons in the visible range. This should facilitate using an inexpensive solar simulated radiation source to induce the active sites of the catalyst surface and enhance the esterification in the forward direction. The optical band gap was evaluated using the Tauc plot (Figure 6.27e), according to Kubelka-Munk theory: $\alpha h\upsilon = A\left(h\upsilon - E_g\right)^{0.5}$; E_g is the band gap energy, α is absorption co-efficient, $h\upsilon$ stands for photon energy, and A is the proportionality constant. The direct band gap of $ZnTiO_3$-based catalysts is appraised from the intercept of the tangents to the plots. The band gap energy values of BMZTO-40, BMZTO-20, and BMZTO-10 are 2.87, 3.15, and 3.18 eV, respectively. Meanwhile, BMZTO-60 manifested two absorption edges appeared at 290 and 537 nm with the corresponding band gap of 2.33 and 2.01 eV, respectively, as shown in Figure 6.27f. The two band gaps ascribed to the presence of two phases of $ZnTiO_3$, where 2.33 eV is attributed to the hexagonal phase, and 2.01 eV occurred due to the existence of cubic phase [67]. Hence, reducing the bandgap energy by increasing the percentage of Ecandrewsite/hexagonal phase of the photocatalyst $ZnTiO_3$ is more conducive to the quantum jump. Therefore, the stronger oxidative holes present in ZnO and reductive electrons in TiO_2 are exposed to visible range, which leads to an enhanced photoelectric catalytic behavior [68].

The PL spectrum of different ball-milled samples is performed in steady-state

fluorescence spectroscopy at room temperature in the wavelength range of 300-700 nm, as shown in Figure 6.27g, h. In order to identify the charge recombination, the intensity of the PL peaks infer the quality of the prepared samples. Remarkably, compared to other synthesized catalysts and pristine ZnO and TiO_2, BMZTO-60 and BMZTO-40 exhibit two spectral ranges, as shown in Figure 6.27g. From Figure 6.27h this is evident that the wavelength of emission is augmented with the rise of the excitation wavelength. The ball-milled samples were excited by the wavelength at 350 nm, giving the strong greenish-blue emission in a similar peak position (around 3.09 eV energy) with different intensities. A broad band grows in the PL spectrum at ~519 nm for BMZTO-40 and BMZTO-60. The deconvolutions of the bands for the prepared BMZTO-60 into Gaussian type lines affirm its emission at 408.77 and 493.64 nm. These peaks are formed due to the presence of lattice defects and oxygen vacancies in BMZTO-60 corresponds to the violet emissions. Interestingly, the low-intensity luminescence spectra of BMZTO-60 endorse an effective decrease in the recombination rate under visible light irradiation and are highly efficient for the separation of photogenerated electron-hole pairs [69]. Moreover, hindered recombination is one of the crucial factors for superior photocatalytic properties. However, the results for BMZTO-60 are in good agreement with performing esterification under the hybrid effect of NIR-MW irradiation in the packed bed reactor system.

The surface morphology of the prepared BMZTO samples was observed by FESEM analysis, as shown in Figure 6.28a. From Figure 6.28a, b, it could be seen that the morphology of the particles was spherical, and the average particle size distribution was 23.03 and 28 nm for BMZTO-60 and BMZTO-40, respectively. However, Figure 6.28c, d shows agglomerated particles having irregular shapes of BMZTO-20 and

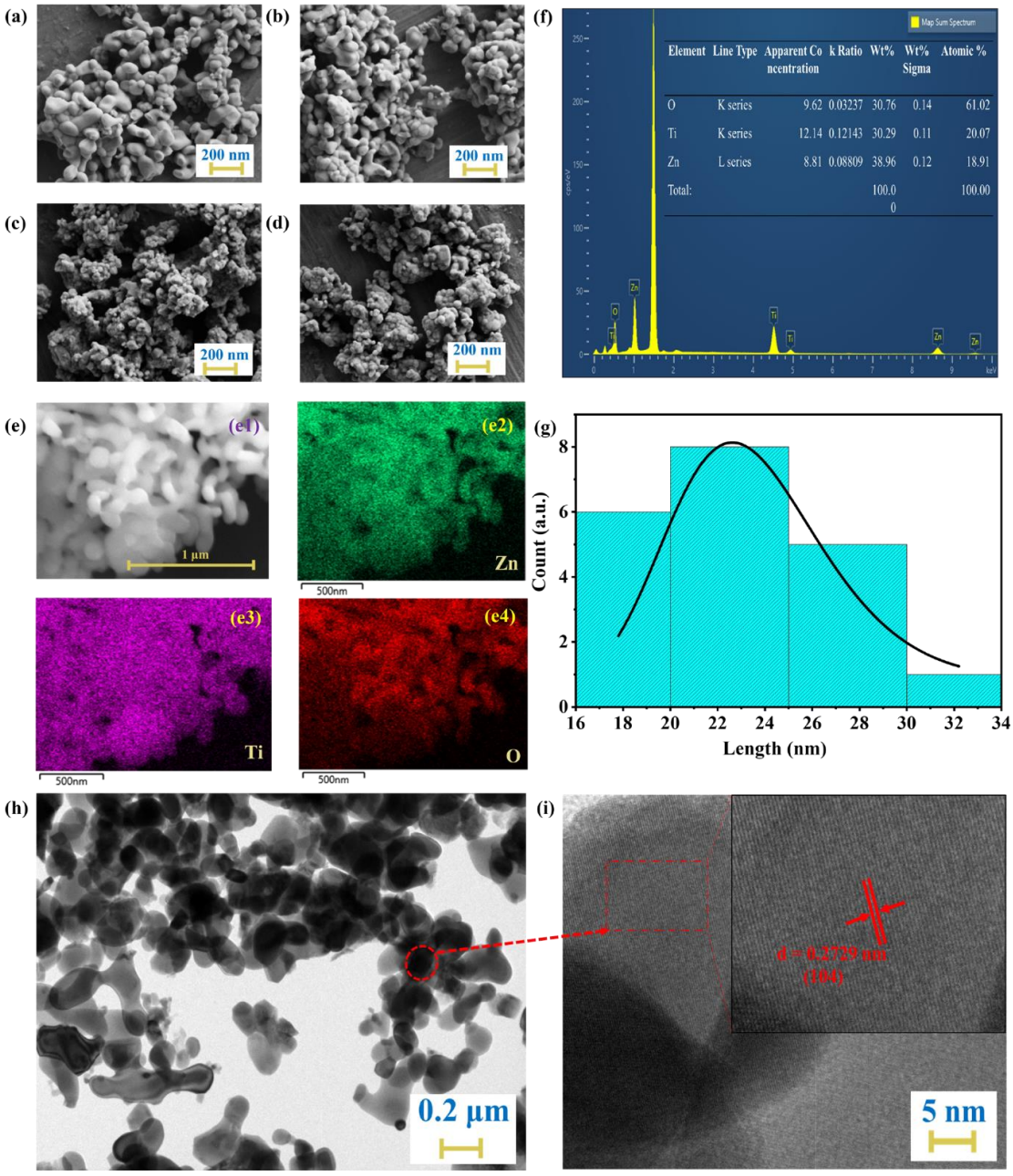

Figure 6.28. FESEM images of (a) BMZTO-60, (b) BMZTO-40, (c) BMZTO-20, (d) BMZTO-10; (e) EDX elemental mapping (e1-e4) Zn (green), Ti (pink), O (red) (f) Energy Dispersive X-ray (EDX) spectrum; (g) particle size distribution of BMZTO-60; (h) low magnification TEM; (i) HR-TEM image of BMZTO-60

BMZTO-10. A clear conclusion might be drawn from the high magnification images that due to the increase in ball milling time, the particle size of the catalysts was drastically changed while the calcination temperature remained fixed at 973 K. In

order to ascertain the composition of the nanoparticles, EDX analysis was studied. The representative EDX mapping and spectrum (Figure 6.28e, f) approve the presence of the estimated amount of Zn (green), Ti (pink), and O (red) in the BMZTO-60 catalyst. The particle size distribution has been calculated using *ImageJ* software, and the histogram of the particle size distribution is exhibited in Figure 6.28g.

TEM analysis further revealed more details about the nano-spherical morphology of the $ZnTiO_3$ sample. Figure 6.28h depicts the typical TEM image of BMZTO-60 nanospheres obtained at 973 K. The morphological characteristics of the catalyst sample are reliable with the FESEM analysis. The HRTEM image of the sample is represented in Figure 6.28i. To verify the diffraction pattern of the catalyst revealed by HR-XRD results, HR-TEM was performed. The d-spacing i.e., the distance between two adjacent lattice fringes is 0.2729 nm, corresponding to (104) interplanar spacing of the BMZTO-60, has been calculated using *ImageJ* software which is well matched with HR-XRD data.

The properties and activities of the prepared catalysts have been compared with relevant previous studies (Table 6.15) to highlight the advantages of the present investigation. It can also be obtained that the optimum BMZTO-60 catalyst prepared by simple ball milling method have shown two adsorption edges appeared at 290 and 537 nm with the corresponding band gap of 2.33 and 2.01 eV, due to the presence of hexagonal phase and cubic phase of the catalyst, respectively. This property made the catalyst more efficient to act as photocatalyst under NIR irradiation, as NIR uses 50% of the solar light energy to induce the heat energy as well as the photocatalyst activity of the catalyst. Moreover, this as-prepared BMZTO-60 have the advantages of high crystallinity (23.03 nm), high BET surface area (standard deviation: 18.90), low bandgap, and highly energy efficient to use for MO production in MRPBR under the

combined effect of NIR and MW irradiation.

Table 6.15. Comparison of photocatalytic activity and property of prepared catalyst for reaction over reported in literature

Catalyst	Method	BET surface area [m^2/g]	Crystallite size [nm]	Band Gap (eV)	Temperature [K]	Applications	Ref.
La_3+/ZnO-TiO_2	sol–gel method	3.27	11.5	3.3	308	Trans/ esterification	[70]
$ZnTiO_3$	chemical vapor deposition	-	-	3.3	338	acetone sensors	[71]
Fe_2O_3/ ZnTi	sol–gel technique	10	23	2.82	353	4-chlorophenol degradation	[72]
$Zn_2Ti_3O_8$/ $ZnTiO_3$	Hydrothermal	12.4	-	3.50	453	CO_2 reduction with H_2O	[73]
$ZnTiO_3$	sol-gel method	low	-	2.9	333	quantum dot sensitized solar cells	[74]
$ZnTiO_3$	**Ball-milling method**	**24.70**	**23.03**	**2.33**	**298**	**Esterification in MRPBR**	**This work**

6.4.2 Optimization of Reaction Conditions and Model Validation

The experimental results were analyzed meticulously. Table 6.16 represents the 'Model Summary Statistics,' which unveiled the best fitting of the quadratic model associating response and significant variables displayed the lowest standard deviation (1.31) and highest R^2 value $R^2 = 0.99$ compared to linear and 2FI models. The analysis of variance (ANOVA) method was carried out to verify the accuracy of the model. ANOVA (Table 6.17) results of the response variable articulated by the quadratic model with a significant p-value <0.0001 (95% confidence level) might precisely predict that there was no significant fit as p > 0.05. Therefore, this model was proficient in predicting MO synthesis yields within the range of variables employed. The results indicated that all four independent variables had an eminent effect on MO yield (p<0.05). Among them, Table 6.17 shows that one linear term

(ψ_T), three interactions and three square co-efficient of quadratic terms ($\psi_{CC}\psi_{LHSV}$, $\psi_T\psi_{LHSV}$, $\psi_{MR}\psi_{LHSV}$, ψ_{CC}^2, ψ_{MR}^2, ψ_{LHSV}^2) were the main operating variables due to a high model F value of 102.26 under the condition "Probability > F" p-value <0.0001 indicating a significant model term in this continuous study with the standard deviation value of 20.086. The polynomial model to describe the mathematical relationship between the MO yield content (ψ_{MO}) in terms of the independent process variables is given in Eq. 6.10

$$\psi_{MO} = 75.85 - 1.23\psi_{CC} + 12.03\psi_T - 1.30\psi_{MR} - 1.67\psi_{LHSV} - 2.03\psi_{CC}\psi_T - 1.81\psi_{CC}\psi_{MR} + 4.43\psi_{CC}\psi_{LHSV} - 1.02\psi_T\psi_{MR} + 4.89\psi_T\psi_{LHSV} - 3.7\psi_{MR}\psi_{LHSV} - 5.10\psi_{CC}^2 + 1.52\psi_T^2 - 4.85\psi_{MR}^2 - 3.5\psi_{LHSV}^2$$
$$R^2 = 0.99 \qquad (6.10)$$

positive sign indicates a synergistic effect, while an antagonistic effect is denoted by negative sign [75].

Table 6.16. Model summary statistics

Source	Prob > F	Std. Dev.	R-Squared	Adj. R-Squared	Pred. R-Squared	Press Value
Linear	<0.0001	5.26	0.7314	0.6866	0.6036	981.11
2FI	0.1235	4.72	0.8379	0.7479	0.5732	1056.28
Quadratic	<0.0001	1.31	0.9903	0.9806	0.9442	138.06

6.4.2.1. Verification of the Optimal Model

In order to corroborate the accuracy of the quadratic polynomial model, the comparison between the experimental values and the predicted values on MO yield was assessed in the study, as shown in Figure 6.29a. The plot conforms that the applicability of the quadratic model was high corresponding to a 1.31 standard deviation (less than 5%) represented with a subsequent expression of the response variable MO yield within 0.13 min^{-1} of LHSV. Details of the analysis of the perturbation plot, which shows the influence of all the independent variables on the MO yield and response surface plots for individual process parameters were provided

in the following section.

6.4.2.2 Analysis of the Response for the Effect of Variables on the Production of MO Yield

The perturbation plot shows the influence of all the independent variables on the MO yield, as presented in Figure 6.30. The curvature of the variables from the centre point indicates the importance of each variable which confirms the statistical results obtained from the ANOVA table. The response is plotted by changing individual factors at a time over its range possessing all other factors constant. The steepest slope showed the most influencing factor, and the response was sensitive to that factor. From the plot, reaction temperature (ψ_T) has the most significant influence on the MO yield. Increasing the temperature from 323 to 333 °C, the ester yield ψ_{MO} increases. However, the other variables showed minimal effect on the amount. Increasing the amount of catalyst loading (ψ_{CC}), the yield of ester increases initially and reaches a maximum yield level at intermediate catalyst loading. At higher temperature, the conversion of OA become faster, which leads to a high conversion of OA with a high concentration of product yield. Moreover, when the mole ratio was increased, there was only a marginal increase in the ester yield. On the other hand, in the case of LHSV, MO yield slightly decreased with the increase of space-time. OA conversion in the MPBR depends on the experimental conditions, which consequently influence the residence time. Due to the rotating action in the packed bed reactor, micromixing intensity rises with rotating speed due to contact between the catalyst and the reactants at a reasonable LHSV, resulting in a high MO yield.

6.4.2.3 Response Surface Plots for Individual Process Parameter

To find the optimal condition with maximum MO yield, the graphical response of 3D surface curves was plotted by Design Expert 7.0 software using the derived Eq. 6.10.

It demonstrates the interactive effect of independent process variables on maximum MO yield, as discussed in the following segment.

Figure 6.29b indicates the interactive influence of catalyst loading and reaction temperature on ψ_{MO} for MPBR when the other two variables remained constant. It is observed that the ψ_{MO} increases (from 59 to 79.04 %) with the temperature rise (50-60 °C). The catalyst loading was varied over the range of 20-40 wt.%. The yield amount of MO proportionally increased with catalyst loading due to the increase in the number of active sites on the catalyst surface. Nevertheless, no such difference was evident beyond the catalyst concentration of 30 wt.%. Increasing the catalyst loading might decrease the reaction rate, which could lead to a reduction in ψ_{MO}. Higher loading of catalyst resulted in lowering the interaction between the immiscible reactants and offering the mass transfer limitation. Thus, the optimal condition for the esterification reaction could be achieved at a catalyst loading of 20 wt.%, and the reaction temperature should be 333 K. However, ANOVA results in Table 6.17 show minimal impact between the interactive parameters due to the p-value <0.007, which is less than 0.5 but greater than 0.0001.

The interaction of catalyst loading and the mole ratio of methanol to OA on ψ_{MO} is represented in Figure 6.29c. The 3D surface response plot is concave in nature which indicates a relatively less impact on ψ_{MO}. It could be considered from the plot that the maximum ψ_{MO} might be obtained at the temperature of 333 K and LHSV of 0.20 min^{-1}. Lower loading of catalyst results in less active sites to adsorb methanol and consequently lower the yield value. On the other hand, an excess amount of catalyst loading may cause increasing viscosity of the reaction mixture, revealing irregular mixing in the reaction medium [76]. As a result, 30 wt.% of catalyst loading is found to be advantageous in shifting the chemical equilibrium of the esterification reaction

toward the product MO. However, the excess mole ratio of methanol to OA slightly reduces the OA conversion and MO yield. The plausible reason might be the excess methanol that infers the yield by changing the flow pattern of the reactants in the reactor, and as a result, micromixing efficiency also decreased [77]. Therefore, the suggested methanol to OA mole ratio range for esterification reaction in MPBR is 11:1. Although, ANOVA results (Table 6.17) show the negligible influence of the two parameters on MO yield as the p-value was less than 0.015.

Aimed to achieve the maximum yield of MO, Figure 6.29d shows the influence of catalyst loading and LHSV. At low levels of both catalyst loading (20 wt.%) and LHSV at 0.44 min^{-1}, the graphical representation displays a minimum yield of MO (52.4%). This can be observed due to the minimum availability of the catalyst's active sites and the short reaction period. However, increasing the catalyst loading alone and similarly decreasing the LHSV alone lessens the product yield by 61.65 to 64.12%. This signifies that at high space-time, the yield decreased because of a change in the flow pattern of the reactant liquids resulting in a reversible reaction. Likewise, it should be noted that high catalyst loading leads to poor mixing of reactants; consequently, yield amount decreases. The result might be attributed that using moderate catalyst loading (30 wt.%), providing more active sites of catalyst surface for the completion of the reaction within 12 min, and achieving maximum MO yield. From ANOVA results in Table 6.17, it was observed that the interaction between catalyst loading and LHSV is very significant for MPBR owing to its very low p-value (<0.0001).

The relationship between reaction temperature and LHSV is significant on MO yield as it was recognized from ANOVA Table 6.17 that other variables, viz., mole ratio of methanol to OA (11:1) and catalyst loading (30 wt.%), were kept constant at the middle point. Decreasing the LHSV alone beyond 0.22 min^{-1} with respect to

minimum reaction temperature (323 K) results in the reduction of MO yield (55%), and it signifies that at a low temperature, no reaction had occurred, which leads to poor mixing of reactants. In the meanwhile, a drastic increment of yield (75%) has been detected at high LHSV (0.44 min^{-1}) and high reaction temperature (333 K). An increase in the reaction temperature from 328 to 333 K not only enhanced the intrinsic kinetic rate of reaction significantly but also reduced the activation energy of the esterification reaction with the aid of non-ionizing radiation, as can be seen in Figure 6.29e. The highest ψ_{MO} was obtained at 79.04% due to high reaction temperature (333 K) and low LHSV (0.13 min^{-1}). From ANOVA Table 6.17, it is identified that the impact of reaction temperature and LHSV plays an important role on ψ_{MO} since the corresponding P-value was <0.0001.

Figure 6.29f displays the impact of the mole ratio of methanol to OA and LHSV on ψ_{MO}, while the other two variables, viz., catalyst loading (30 wt.%) and reaction temperature (328 K), were kept constant at the center point. From ANOVA Table 6.17, it is observed that the interaction between the two parameters was highly significant due to its low p-value (<0.0001) and high F value (32.29). The mole ratio of methanol to OA (7:1) and the LHSV (0.44 min^{-1}) was attributed to a reduction in conversion and product yield (62.8%). This indicates that an excess amount of methanol is favorable to accelerating the reaction toward the forwarding direction. A gradual increase in MO yield was noticed when the mole ratio was increased from 7:1 to 11:1. Correspondingly, the LHSV from 0.44 to 0.13 min^{-1} was appreciable for the increase in MO yield (79.04%). This might be due to the interaction between the reactants and catalyst, which enhances the collision leading to the drastic improvement in OA conversion. However, at a high level of both variables, the mole ratio of methanol to OA and LHSV resulted in decreased MO yield. This reduction might be associated

with excess solubility of methanol or the dilution of catalyst loading in the presence of excess methanol in the reaction medium.

Table 6.17. ANOVA results

Source	Sum of Squares	df	Mean Square	F Value	p-value Probability > F	Std. Deviation	
Model	2450.99	14	175.07	102.26	< 0.0001	1.31	significant
ψ_{CC} -catalyst concentration	18.25	1	18.25	10.66	0.0056		
ψ_{T} -reaction temperature	1738.09	1	1738.09	1015.19	< 0.0001		
ψ_{MR} -methanol: OA mole ratio	20.36	1	20.36	11.89	0.0039		
ψ_{LHSV} -LHSV	33.5	1	33.5	19.57	0.0006		
$\psi_{CC}\psi_{T}$	16.56	1	16.56	9.68	0.0077		
$\psi_{CC}\psi_{MR}$	13.14	1	13.14	7.68	0.015		
$\psi_{CC}\psi_{LHSV}$	78.77	1	78.77	46.01	< 0.0001		
$\psi_{T}\psi_{MR}$	4.14	1	4.14	2.42	0.1422		
$\psi_{T}\psi_{LHSV}$	95.75	1	95.75	55.92	< 0.0001		
$\psi_{MR}\psi_{LHSV}$	55.28	1	55.28	32.29	< 0.0001		
ψ_{CC}^{2}	168.8	1	168.8	98.59	< 0.0001		
ψ_{T}^{2}	15.16	1	15.16	8.85	0.01		
ψ_{MR}^{2}	152.58	1	152.58	89.12	< 0.0001		
ψ_{LHSV}^{2}	81.29	1	81.29	47.48	< 0.0001		
Residual	23.97	14	1.71				
Lack of Fit	23.97	10	2.4				
Pure Error	0	4	0				
Corrected Total	2474.96	28					

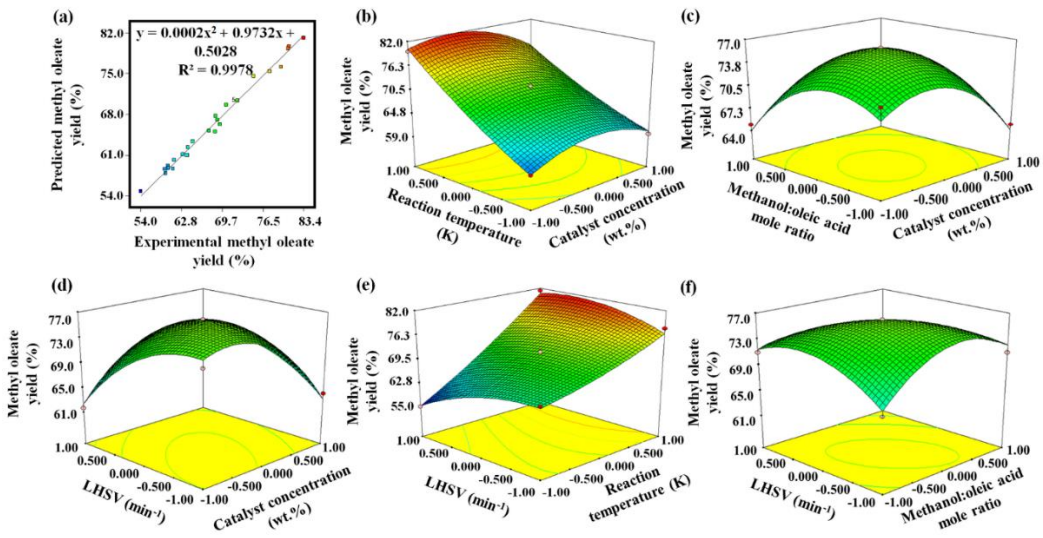

Figure 6.29. (a) Quadratic relationship between the predicted and experimental MO yield (%); Interactive plot of (b) catalyst loading and reaction temperature; (c) catalyst loading and the mole ratio of methanol: OA; (d) catalyst concentration and LHSV; (e) reaction temperature and LHSV; (f) mole ratio of methanol: OA and LHSV; on MO yield

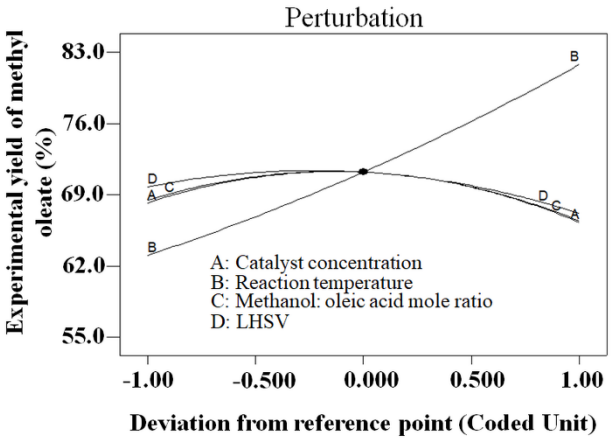

Figure 6.30. Perturbation plot

6.4.3 Influence of Electromagnetic Radiation

The selection of a proper heating system ensures adequate interaction of the reactants present in the reactor with the catalyst at a shorter reaction time. Conventional heating from the surface of the reactor wall to the reaction mixture makes the process unsuitable with prolonged reaction time. To benchmark the reactor performance,

esterification has been done under the adiabatic condition by maintaining the feed flow at 333 K has been chosen to operate the esterification. From Figure 6.31a, it could be observed that the formation of MO yield was very low (33.57%) under adiabatic condition. In order to overcome this condition, electromagnetic radiation plays an indispensable function in the esterification process. MW involved two mechanisms, dipolar polarization and ionic conduction. Methanol is supersensitive to MWs because of having lower gyradius and molecular inertia [78]. The polar molecules might selectively absorb MW energy and non-polar molecules are inactive in MW due to dielectric loss [79]. Since $ZnTiO_3$ (BMZTO-60) is a useful candidate for MW resonators due to its excellent dielectric properties [80]; resulting in good reaction performance under MW irradiation. On the contrary, MW power absorption might be highly inconsistent based on the dimension and dielectric properties of the materials. Thus, the limitation of heat and mass transfer in the presence of MW may affect the overall progress of endothermic esterification [81]. The heat of reaction (delta H) has been calculated using the Eyring-Polanyi equation, which can be written in Eq. 6.11

$$k = \kappa \frac{k_B T}{h} \exp\left(-\frac{\Delta G}{RT}\right) \tag{6.11}$$

where, k = reaction rate, κ =transmission coefficient=1, k_B =Boltzmann constant=1.38×10^{-23} $J.K^{-1}$, h =Planck's constant=6.63×10^{-34} J.s Taking the natural logarithm of Eq. (6.11) and substituting $\Delta G = \Delta H - T\Delta S$ gives

$$\ln\left(\frac{k}{T}\right) = \frac{-\Delta H}{R}\left(\frac{1}{T}\right) + \left[\ln\kappa + \ln\left(\frac{k_B}{h}\right) + \frac{\Delta S}{R}\right] \tag{6.12}$$

Eq. (6.12) describes the relationship between enthalpy and entropy with the

connection of reaction rate. The values of these two thermodynamic parameters can be obtained from the slope and the intercept of the linear plot of 1/T vs. ln (k/T). The enthalpy and entropy were found to be 13.812 $kJ.mol^{-1}$ and -0.066 $kJ.mol^{-1}.K^{-1}$, respectively; implying that the esterification is endothermic.

The value of the calculated heat of reaction and entropy are found to be 13.812 $kJ.mol^{-1}$ and -0.066 $kJ.mol^{-1}.K^{-1}$, respectively; implying that the esterification is endothermic. From Figure 6.31a, it is evident that at the optimum operating condition, MO yield results in a maximum value of 69.8% at the LHSV of 0.13 min^{-1} under MW irradiation. On the other hand, NIR (100W) at the molecular level caused robust molecular collision due to bending and stretching vibration of bonds leading to product yield maximization. Since NIR uses 50% of the solar light energy, it is responsive not only to induce the thermal/heat energy but also enhance the photocatalytic activity [82]. Moreover, from UV-Vis spectra, a clear absorption edge in the visible range at 537 nm is obtained which is assigned for the cubic phase of BMZTO-60. From the esterification, it might be attributed that the optical absorption of as-prepared BMZTO-60 ($ZnTiO_3$) catalyst has shifted from the UV to the visible spectra range and (NIR) photon absorption capacity has enhanced with the energy greater than the band gap energy, which excites the electrons from valence band to conduction band and leaves the hole in the valence band. The photogenerated electron-hole pairs are separated in the bulk materials and then the esterification took place under NIR irradiation. As a result of NIR, the yield of MO reached up to 73.5% at the LHSV of 0.13 min^{-1}, as demonstrated in Figure 6.31a. From Figure 6.31a, it is observed that the MO yield increased from 49% to 79.04% under hybrid electromagnetic radiation within the LHSV of 1-0.2 min^{-1}. After 0.20 min^{-1} of LHSV, no further improvement in OA conversion has been detected significantly, so it is considered from a Box-Behnken optimum condition that within LHSV of 0.2-0.08

min^{-1}, the conversions of OA/yield of MO became more stable and reached the steady-state condition. It is evident from Table 6.18 that the individual effect of NIR (100W) was superior compared to the individual effect of MW (750W) [83]. However, the combination of MW+NIR (850 W) resulted in a synergistic effect, which rendered 52% of increase in MO yield at optimum LHSV at non-recycling conditions with minimal increase in power input of about 13.33%. In the production of MO in recycle reactor, one extra peristaltic pump (220 W) has been used to control the power by remaining the others' power same, the yield amount of MO was increased up to 2.52% per unit watt of electrical power usage. The yield per used electrical unit has been calculated for each system and depicted in Table 6.18.

Table 6.18. Effect of energy input on MO yield at a fixed LHSV

Power source	**% increment of Power input w.r.t MW at optimal 0.20 min^{-1} LHSV**	**MO Yield%**	**Yield% per used Electrical Unit (W)**
MW (750W)[#] non-recycle	-	-	0.055
NIR (100W)[#] non-recycle	86.66% decrease[#]	67% (28.84% increase[#])	0.12
NIR-MW (850W) non-recycle	13.33% increase[#]	79.04% (52% increase[#])	0.058
NIR-MW (850W) recycle	13.33% increase[#]	93% (78.84% increase[#])	0.059

[#] in comparison with MW radiation non-recycle mode

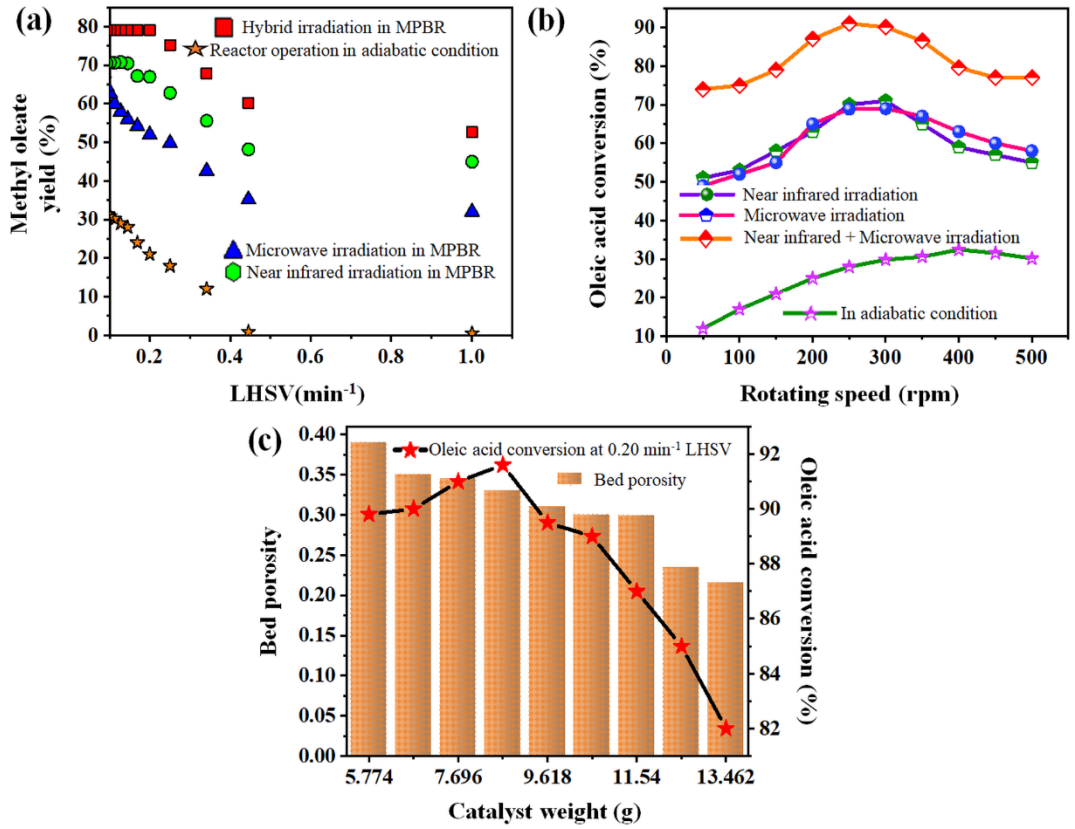

Figure 6.31. Effects of (a) electromagnetic radiation on MO yield; (b) rotating speed (c) catalyst weight on bed porosity as well as on OA conversion

6.4.4 Influence of Rotating Action and Bed Porosity

The effect of rotating speed on OA conversion has been obtained from Figure 6.31b. The results show that with the increase of rotational speed, firstly the OA conversion increased. While the rotating speed was in the range of 230-245 rpm, the OA conversion reached the maximum value (90.25%) under hybrid radiation. In that range, chemical reactions promoted by individual electromagnetic irradiation performed a 68-71% MO yield. On the other hand, the OA conversion amount decreased as the rotating speed increased > 250 rpm for each system. The possible reason for it is based on the fact that, at low rotating speed, severe liquid flow misallocation and rivulet flow have occurred inside the packing of the reactor. Besides, at high rotating speed, the rivulet flow has been replaced by more even droplet flow

[84, 85]. Nevertheless, further increase in rotating speed resulted in central vortex formation correspond to an ineffective mixing of the reactants [60]. Thus, from Figure 6.31b it might be observed that at optimum rotating speed of 235 rpm has significantly eliminated the mass transfer hindrance by the centrifugal acceleration in the reactor medium, as well as maximizes the MO yield. The rotating effect has also been studied under the adiabatic condition with a feed temperature of around 333 K to investigate the reactor performance under continuous flow with/without recycling. Figure 6.31b attributes that the rotating speed has influenced the ester formation by increasing its speed up to 410 rpm.

In general, bed porosity depends on the particle to reactor bed diameter, shape, and size of the particle. From Figure 6.31c, it could be identified that with the increase of catalyst weight, the porosity decreases at a fixed LHSV (0.20 min^{-1}). At optimum reaction temperature (333 K) and 0.39 porosity, the OA conversion reached up to 89% at a LHSV of 0.21 min^{-1}. In contrast, at 0.33 bed porosity, it was observed that the OA conversion was increased up to ~91%. That means the decrease in bed porosity advocates the miscibility of the reaction mixture resulting in higher conversion as well as MO yield. This observation is validated by the previously reported data [86]. Further increase in catalyst weight creates lower bed porosity of supported BMZTO coated glass bead catalyst. Hence, the effective volume of the reaction decreased. Thus, the OA conversion was reduced to ~81.97% at the same space time. Nevertheless, a homogeneous reaction has also been observed at optimal reactor condition in MPBR in comparison with the heterogeneously catalyzed esterification, resulted in much less MO yield amount of 43.58%, as shown in Figure 6.32.

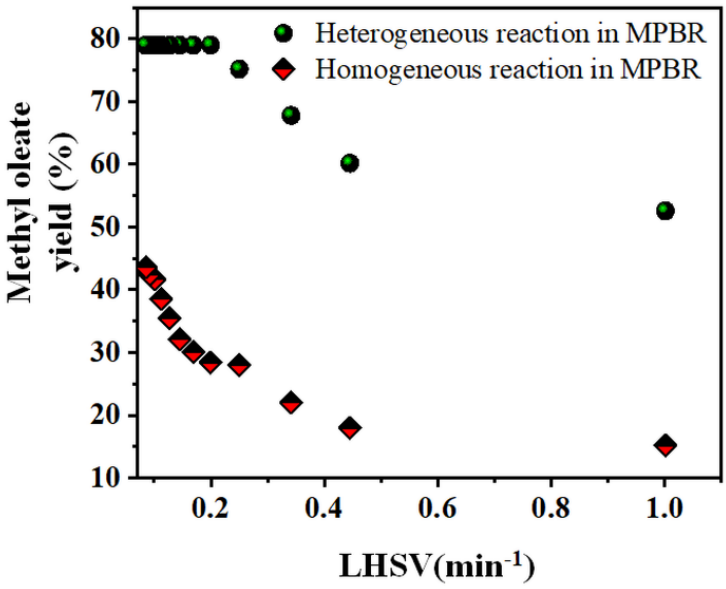

Figure 6.32. Esterification in MPBR through homogeneous and heterogeneous catalyses

6.4.5 Simulation of the Radiation Heat Transfer

A global coordinate system has been used in the simulation module. To reduce the computational load, the model consists of 4 spherical catalysts with a diameter of 5 mm, arranged in a 3D cylindrical lattice of 3 mm in radius and 20 mm in length. The simulation was coupled with NIR irradiation and MW electromagnetic wave, and the heat transfer in porous media was conducted using a heat transfer module. To investigate the effect of the temperature and total temperature gradient, the spheres are arranged inside the cylinder in such a manner that they are in contact with each other. Figure 6.33a shows the temperature distribution (K) in the model catalyst bed under combined MW and NIR irradiation, whereas Figure 6.33c and e show temperature distribution (K) under individual MW and NIR separately. Figure 6.33a shows that after reaching steady state condition, the temperature distribution in the MPBR under combined radiation resulted in uniform temperature in all directions of the reaction medium (333 K). This also shows the time independency toward the effect of

temperature and temperature gradient. However, for MW and IR separate irradiation, the temperature distribution shows a slight decrease toward the packed bed's edges, as shown in Figure 6.33c and e. Furthermore, the temperature gradient (K/m) for MW-NIR shows the value of 50 K/m which is exactly similar to the experimentally obtained value (Figure 6.33b). MW and NIR show higher temperature gradient [87] than the combined irradiation. Meanwhile, among the MW and NIR, MW irradiation shows the lower temperature gradient than NIR (Figure 6.33d and f). This result might attribute the presence of BMZTO-60 and the penetration depth of MW have influenced the reaction though the temperature distribution is non-uniform. Moreover, the NIR has confirmed that the radiation heat transfer has taken place along with conduction/convection. Therefore, from the simulation, it could be concluded that the combined NIR-MW shows uniformity in the temperature distribution with no heat dissipation along with a lower temperature gradient revealing uniform heat transfer, which makes the liquid flow almost identical throughout the catalyst bed in comparison with individual NIR and MW. Hence, the simulation agrees well with the experimental data that the reaction has conducted in steady-state and isothermal conditions.

6.4.6 External and Internal Mass Transfer Resistance

Consider a heterogeneous catalytic isothermal esterification in MPBR and MRPBR packed with a supported BMZTO-60 coated spherical glass bead catalyst Mears criterion (Eq. 5.30) and Weisz-Prater parameter (Eq. 5.37) were adopted to check the external and internal mass transfer resistance, respectively. Firstly, the packed bed reactor is effective at $600 > Re > 50$. It could be exhibited from Figure 6.34a that the k_C value was low (5.40×10^{-5} m/s) at a lower flow rate (3.28 mL min^{-1}). Significantly, the value of k_C was raised with an increasing flow rate. Since an increased feed flow

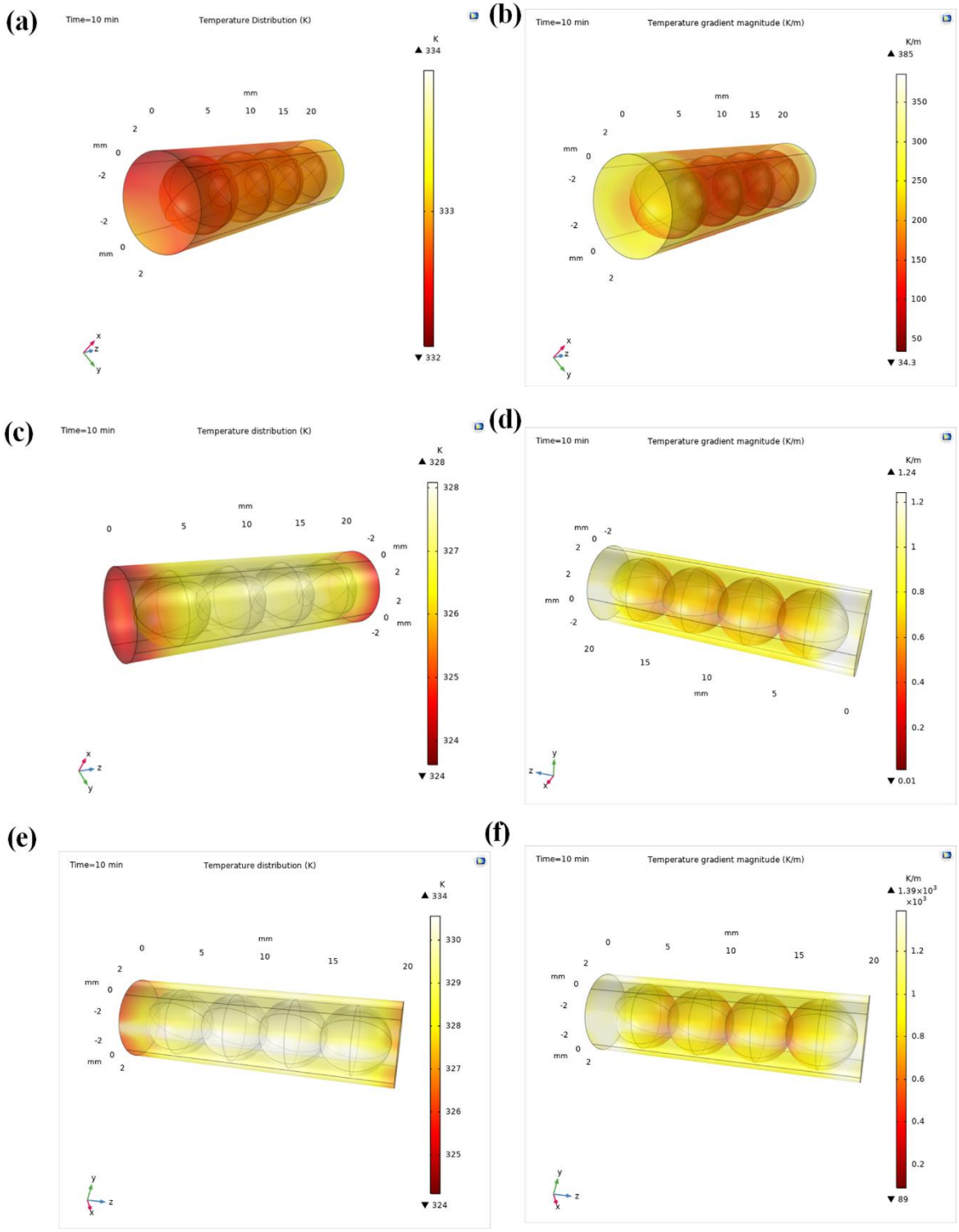

Figure 6.33. Simulated temperature distribution and temperature gradient in MPBR in (a,b) MW-NIR, (c,d) MW, (e,f) NIR irradiated MPBR

(>7.892 mL/min) rate reduces the mass transfer limitation, which resulted in a faster reaction rate and obtained maximum MO yield. However, further increases in flow

rate produced turbulence in the reactor bed; as a result, the reactants only pass through the catalyst without interacting with the active sites of the catalyst yielding lower MO production. Furthermore, within the range of flow rates of 3.28 and 39.46 mL/min, insignificant mass transfer resistance occurred with a minimum value of $C_m = 6.03\times10^{-4} < 0.15$ as depicted in Figure 6.34b. To estimate the internal diffusion resistance Thiele Modulus (ϕ_{TM}) has been calculated for different bed porosity. The value of ϕ_{TM} is 0.326<2 indicates the overall esterification was not limited by internal mass transfer, which could be neglected completely. The effectiveness factor for all the catalyst sizes approaches 1 (0.992), as shown in Figure 6.34c.

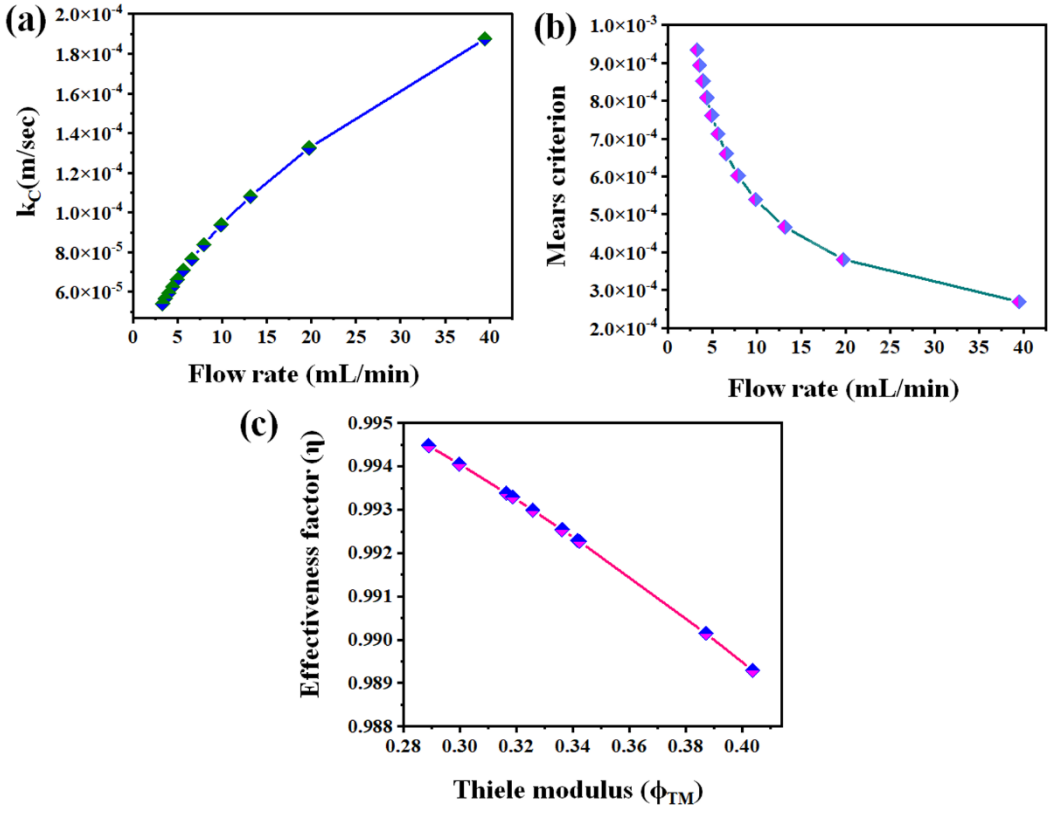

Figure 6.34. (a) Relationship between the external mass transfer coefficient (k_C) and feed flow rate (b) relationship between Mears criterion (C_m) and feed flowrate (3.28-39.46 mL/min) (c) calculated effectiveness factor (η) and Thiele modulus (ϕ_{TM}) for estimation of external and internal mass transfer diffusion

This value designates no limitation in internal diffusion within the reaction medium due to the size of the catalyst particles. It could also be attributed to the Weisz-Prater parameter, with the value $C_{WP} = 5.27 \times 10^{-2} < 1$ showing the significant influence of catalyst size corroborating negligible internal mass transfer resistance. Likewise, for recycle reactor also, the mass transfer resistance has been neglected significantly, as mentioned in Table 6.19. In the present study, dispersion number ($D_a \leq 0$) confirms that there is no dispersion or radial variation in feed concentration of the reactor bed. Thus, these interpretations particularized that the esterification is surface kinetic controlled and follows ideal reactor behavior at the optimal reaction condition with negligible external and internal diffusional resistance.

Table 6.19. Mass transfer correlation in rotating catalytic packed bed

	MRPBR	**MPBR**
Optimum feed flow rate	**9.785 mL/min**	**7.892 mL/min**
Re	149.83	120.84
Sc	1.4	1.4
Sh	13.7	12.3
Pe	2.09×10^{2}	1.69×10^{2}
k_C	9.33×10^{-5}	8.38×10^{-5}
C_m	4.61×10^{-3}	6.03×10^{-4}
C_{WP}	3.93×10^{-2}	5.27×10^{-2}
D_a	3.85×10^{-6}	6.41×10^{-7}

6.4.7 Effect of Recycle

In comparison with non-recycle mode, the yield of MO increased in recycle reactor from 79.04% to 93% within 0.20 min^{-1} LHSV. A deeper investigation of recycle reactor has been carried out to analyze the effect of recycle with LHSV, as shown in Figure 6.35. At optimal LHSV, recycling further increases the MO yield amount to 93%. However, at recycle condition by changing the optimal value of LHSV 0.25 min^{-1}, the MO yield increased monotonously from 93% to 93.55%. In this condition,

the reactor has acted as recycle reactor by following the mechanism of an autocatalytic parallel reaction along with the recycle ratio of 1.27. However, Figure 6.35 reveals that even at higher LHSV of 0.25 min^{-1} (lower space time), MO yield increased from 79.04% to 93.55%. To get the maximum MO yield, recycle ratio reveals a minimum value at minimum space time (3.99 min). Hence, it might be stated from the result in Figure 6.35 that the recycled packed bed reactor with optimum recycle ratio shows a higher yield than the pristine packed bed reactor for minimum space time at optimal condition.

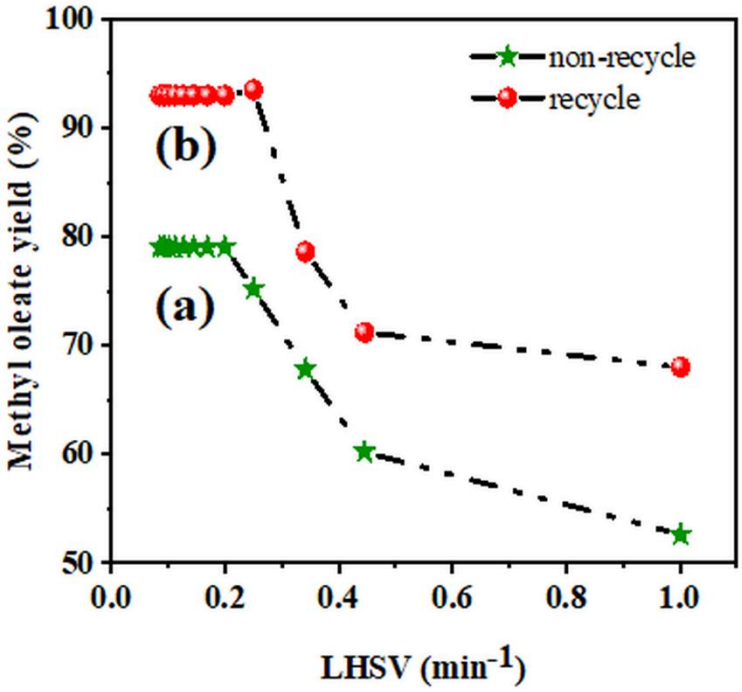

Figure 6.35. MO yield as a function of LHSV under optimal process condition: (a) non-recycle (b) recycle at optimal recycle ratio in MRPBR

6.4.8 Kinetic Analysis

LH and ER models' parameters were determined using the experimental data (Table 6.20) for solving the coupled system of differential (Eq. 5.45, 5.46) and linear/non-linear algebraic (Eq. 5.47-5.55) equation. The kinetic analysis of the esterification

process was performed by varying the catalyst weight. From Table 6.20, it is observed that at isothermal steady-state conditions, the RSSQ value for the LH model in MPBR equipped with a hybrid reactor system (NIR-MW) was much less than the other two models at a space time of 4.87 min. This could be endorsed by the fact that the hybrid effect caused the advantageous effect of the adsorption of reactants on the catalyst surface, thus providing a higher yield. At considerable space time, better propagation capacity of NIR irradiation caused the vigorous molecular collision of the reactant molecules emerging strong molecular stretching and bending vibrations on account of this faster reaction rate and higher MO yield. On the other hand, MW irradiation elevated the superheating of the reaction species, as vibration around the C=O bond is stronger under MW irradiation, which triggers the enrichment of the reaction rate [80]. Meanwhile, EROA and ERM had an adverse effect on the individual adsorption on the catalyst surface. Hence, producing model fit with RSSQ=1.47×10^{-8}, 8.24×10^{-9}, and 7.72×10^{-9} for LH, EROA, and ERM, respectively.

To verify the superiority of the recycle reactor system, the kinetic models LH, EROA, and ERM, ERMO were also estimated for MRPBR (Table 6.20). The reaction rate for Eq. 5.43 (non-recycling) reaction was 2.80×10^{-4} mol/gcat.s, whereas reaction rate was 7.25×10^{-4} mol/gcat.s for Eq. 5.44 (recycling) demonstrates that reaction rate in autocatalytic mode was playing predominant role due to high value among Eq. 5.43 and 5.44. Thus, the esterification follows parallel reaction in recycle system sequentially with autocatalytic behavior in recycle stream, has been evaluated by kinetic analyses. From Table 6.20, it could be observed that at steady-state isothermal conditions LH kinetic model has fitted best, giving less error with RSSQ value of 1.52×10^{-7} for fixed LHSV of 0.20 min^{-1}.

Table 6.20. Kinetic parameters for M-OA esterification in hybrid electromagnetic radiated MRPBR

Reactor type	**Model type**	**LHSV (min^{-1})**	k_1 **(mol/gcat.min)**	k_2 **(mol/gcat.min)**	$K_{OA}\times10^3$ **(L/mol)**	$K_M\times10^3$ **(L/mol)**	$K_{MO'}\times10^3$ **(mol/L)**	$K_{MO}\times10^3$ **(mol/L)**	*RSSQ*
NIR+MW (non-recycle)	LH	0.20	15.038±0.54		8.51±0.31	5.95±0.22	3.35×10^{-4}±9.16×10^{-6}		**1.47×10^{-8}**
	EROA		20.18±0.72		18.82±0.67		1.66×10^{-4}±7.28×10^{-6}		**8.24×10^{-9}**
	ERM		20.18±0.72			18.38±0.69	1.80×10^{-4}±8.52×10^{-6}		**7.72×10^{-9}**
	PH		29.68±0.03						**6.03×10^{-9}**
NIR+MW (Recycle)	LH	0.25	0.002±0.001	108.56±0.01	4.15±5.73×10^{-4}	5.51±8.17×10^{-4}	38.11±0.01	0.001±3.36×10^{-7}	**1.52×10^{-7}**
	EROA		3.64±0.01	202.99±0.73	96.08±0.15		0.04±5.98×10^{-4}	0.03±0.01	**1.35×10^{-7}**
	ERM		7.34±0.001	374.69±0.15		112.09±0.04	0.02±4.73×10^{-4}	0.14±0.02	**1.28×10^{-7}**
	ERMO'		8.25±0.003	415.09±0.48	0.96±3.93×10^{-4}	73.68±0.05	32.07±0.04	0.013±3.18×10^{-4}	**9.26×10^{-8}**
	PH		6.71						**1.45×10^{-7}**

Significantly, from Table 6.20, it might be observed that for all the reactors, the PH model gives better fit with less error of RSSQ=1.45×10^{-7}, which shows better fit in recycle reactor than the non-recycle reactor system. Thus, the autocatalytic parallel reaction mechanism in esterification commendably follows heterogeneous kinetics than supported BMZTO coated glass bead catalyst after adding recycle stream under the influence of hybrid irradiation. For the comparison of experimental and calculated rate value, parity plot has been obtained for both non-recycle and recycle MPBR performance as shown in Figure 6.36a,c. The parity plot of non-recycling and recycling MPBR revealed that LH kinetic model for MRPBR had illustrated more accuracy of the experimental rate than LH kinetic model obtained for non-recyling rate. Similarly, residual plot has also been observed from the difference of

experimental and calculated rate value (Figure 6.36 b,d). Residual plot for recycle MPBR under optimal reaction condition demonstrated that the range between the highest positive and lowest negative residual values, LH kinetic model for MRPBR shows the lower value than the MPBR. Thus, the parity plot and residual plot corroborated well with the LH kinetics performed in MRPBR.

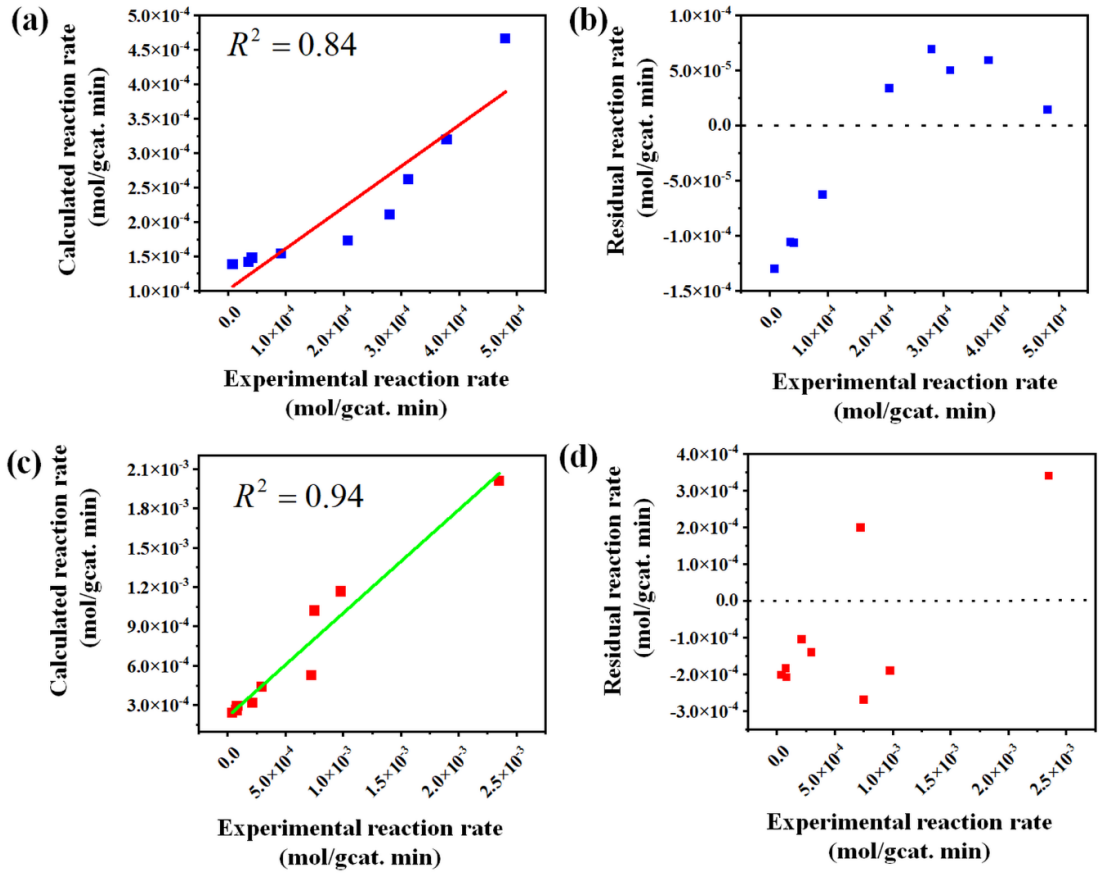

Figure 6.36. Parity plot (a, c) and residual analysis (b, d) of the LH kinetic model in non-recycle and recycle MPBR, respectively.

6.4.9 ASPEN PLUS Simulation for MRPBR Scale-up

The process flowsheet describes the developed process, as shown in Figure 6.37a. To verify the experimental laboratory unit of biodiesel production, a computational modeling was done on the basis of throughput scale-up factor of 1000 by ASPEN PLUS considering geometric similarity. The feed flowrate consists of 6.252 kmol/h of

methanol (methanol stream) and 0.589 kmol/h of OA (OA stream). The product effluent of MO is formed by 2.387 kmol/h (PRDTMO stream). The esterification was done in MRPBR by fixing the ratio of reactor length to diameter by keeping the reaction temperature at 333 K and at 1 atm pressure. All pumps in the simulation process have been used only to transfer fluid in an adequate manner. At the output of the reactor, MIXPRDT1 stream contains both the recycled (stream RECYCLE2) and fresh (stream FRSHFEED) product mix. The splitter was connected to recycle stream where the liquid effluent was recycled without further purification. At the end of the flow sheet separator was attached to separate the main product MO at the bottom and the by-product water and trace amount of methanol and OA from the top of the separator. Heat duty of heater was 1412.96 cal/s. Stream PRDTMO represents the purified product MO produced from the separator with a yield amount of 91.08% within the residence time of 3.09 h (Figure 6.37b). There is a difference of ±2.58% in between the experimental result (93.55% of MO yield) and large-scale production capacity. This could be due to the possibilities of generation of two-phase flow present in the industrial scale real reactor system and not pondered in simulation. Herein, the reaction pathway and the development of the reaction mechanism were followed by LH kinetics to elucidate the significance of each step of the process flow sheet. Hence, the results manifested the simulation combined with an experimentally verified kinetic model is a commanding tool for designing the process. The stream conditions and product qualities of reactor performance are mentioned in Table 6.21. Therefore, these results improve not only the modeling methodology of esterification on lab-scale but also for predicting the optimization of the performance and understanding of the autocatalytic parallel kinetics for the design of new processes to produce MO at the industrial level.

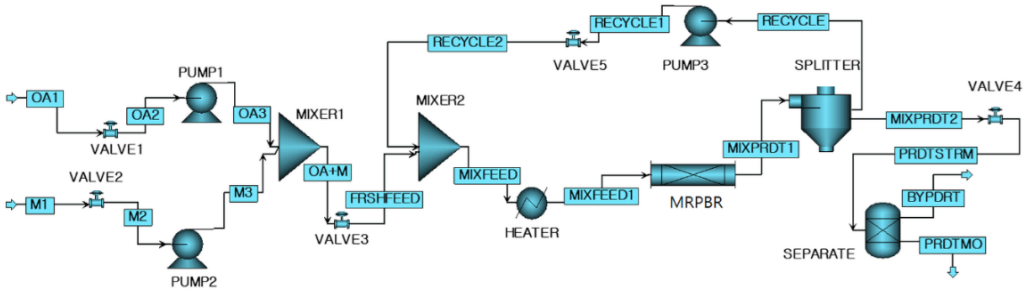

Figure 6.37. (a) Process flow diagram of the MO production in ASPEN PLUS

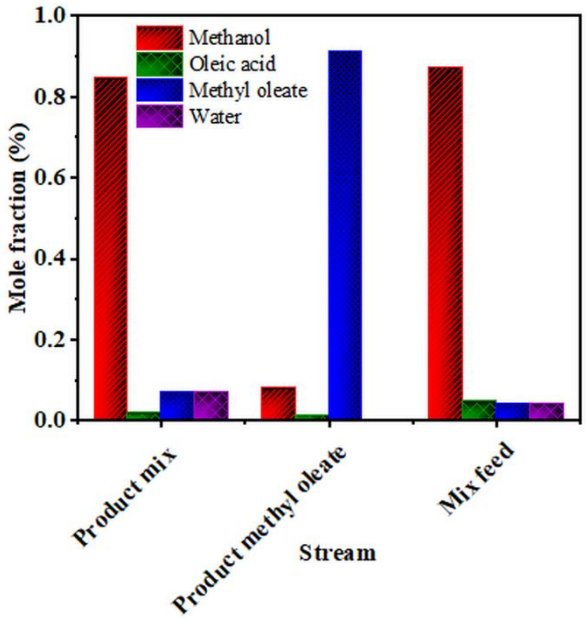

Figure 6.37. (b) Summary of mole fraction in various stream

Table 6.21. Summary of all streams used in the process flow diagram.

		Material																
Stream Name	**Units**	**BYPDRT**	**FRSHFEED**	**Methanol(M1)**	**Methanol(M2)**	**Methanol(M3)**	**MIXFEED**	**MIXFEED1**	**MIXPRDT1**	**MIXPRDT2**	**OA1(OA1)**	**OA2(OA2)**	**OA3(OA3)**	**OA+methanol (OA+M)**	**PRDTMO**	**PRDTSTRM**	**RECYCLE**	**RECYCLE1**	**RECYCLE2**
		Description																
From		SEPARATE	VALVE3		VALVE2	PUMP2	MIXER2	HEATER	MRPBR	SPLITTER		VALVE1	PUMP1	MIXER1	SEPARATE	VALVE4	SPLITTER	PUMP3	VALVE5
To		MIXER2	VALVE2		PUMP2	MIXER1	HEATER	CFRRR	SPLITTER	VALVE4	VALVE1	PUMP1	MIXER1	VALVE3		SEPARATE	PUMP3	VALVE5	MIXER2

Stream Class		CONVEN	CONVEN	CONVEN	CONVEN	CONVEN	CONVEN	CONVEN	CONVEN	CONVEN	CONVEN	CONVEN	CONVEN	CONVEN	CONVEN	CONVEN	CONVEN	CONVEN	CONVEN
MIXED Substream																			
Phase		Vapor Phase	Liquid Phase	Liquid Phase	Liquid Phase	Liquid Phase	Liquid Phase	Liquid Phase	Liquid Phase	Liquid Phase	Liquid Phase	Liquid Phase	Liquid Phase	Liquid Phase	Liquid Phase	Liquid Phase	Liquid Phase	Liquid Phase	Liquid Phase
Temperature	K	333	311.5	313	313	313	324.5	333	333	333	333	333	333	333	311.5	333	333	333	333
Pressure	bar	1.013	1.013	1.013	1.013	1.013	1.013	1.013	1.013	1.013	1.013	1.013	1.013	1.013	1.013	1.013	1.013	1.013	1.013
Molar Enthalpy	cal/mol	-6.02E+04	-6.85E+04	-5.66E+04	-5.66E+04	-5.66E+04	-6.76E+04	-6.73E+04	-6.70E+04	-6.70E+04	-6.70E+04	-1.95E+05	-1.95E+05	-1.95E+05	-6.85E+04	-1.61E+05	-6.70E+04	-6.70E+04	-6.70E+04
Mass Enthalpy	cal/gm	-1.14E+03	-1.28E+03	-1.77E+03	-1.77E+03	-1.77E+03	-1.26E+03	-1.25E+03	-1.25E+03	-1.25E+03	-1.25E+03	-6.89E+02	-6.89E+02	-6.89E+02	-1.28E+03	-5.83E+02	-1.25E+03	-1.25E+03	-1.25E+03
Molar Entropy	cal/mol-K	-5.70E+01	-8.81E+01	-5.63E+01	-5.63E+01	-5.63E+01	-8.64E+01	-8.55E+01	-8.55E+01	-8.55E+01	-8.55E+01	-4.29E+02	-4.29E+02	-4.29E+02	-8.81E+01	-4.08E+02	-8.55E+01	-8.55E+01	-8.55E+01
Mass Entropy	cal/gm-K	-1.08E+00	-1.64E+00	-1.76E+00	-1.76E+00	-1.76E+00	-1.61E+00	-1.59E+00	-1.59E+00	-1.59E+00	-1.59E+00	-1.52E+00	-1.52E+00	-1.52E+00	-1.64E+00	-1.48E+00	-1.59E+00	-1.59E+00	-1.59E+00
Molar Density	mol/cc	3.66E-05	1.51E-02	2.42E-02	2.42E-02	2.42E-02	1.48E-02	1.47E-02	1.46E-02	1.46E-02	1.46E-02	3.09E-03	3.09E-03	3.09E-03	1.51E-02	3.07E-03	1.46E-02	1.46E-02	1.46E-02
Mass Density	gm/cc	1.94E-03	8.12E-01	7.75E-01	7.75E-01	7.75E-01	7.96E-01	7.87E-01	7.85E-01	7.85E-01	7.85E-01	8.74E-01	8.74E-01	8.74E-01	8.12E-01	8.46E-01	7.85E-01	7.85E-01	7.85E-01
Enthalpy Flow	cal/sec	-7.75E+00	-1.30E+05	-9.83E+04	-9.83E+04	-9.83E+04	-3.12E+05	-3.11E+05	-3.09E+05	-1.27E+05	-3.19E+04	-3.19E+04	-3.19E+04	-3.19E+04	-1.30E+05	-1.17E+05	-1.27E+05	-1.82E+05	-1.82E+05
Mole Flows	kmol/hr	4.63E-04	6.84E+00	6.25E+00	6.25E+00	6.25E+00	1.66E+01	1.66E+01	1.66E+01	6.84E+00	5.90E-01	5.90E-01	5.90E-01	5.90E-01	6.84E+00	2.62E+00	6.84E+00	9.78E+00	9.78E+00
METHA-01	kmol/hr	3.44E-04	6.25E+00	6.25E+00	6.25E+00	6.25E+00	1.45E+01	1.45E+01	1.40E+01	5.78E+00	0.00E+00	0.00E+00	0.00E+00	0.00E+00	6.25E+00	2.04E-01	5.78E+00	8.26E+00	8.26E+00
OLEIC-01	kmol/hr	4.30E-05	5.90E-01	0.00E+00	0.00E+00	0.00E+00	7.57E-01	7.57E-01	2.84E-01	1.17E-01	5.90E-01	5.90E-01	5.90E-01	5.90E-01	5.90E-01	2.96E-02	1.17E-01	1.67E-01	1.67E-01

METHY-01	kmol/hr	0.00E+00	0.00E+00	0.00E+00	0.00E+00	0.00E+00	6.76E-01	6.76E-01	1.15E+00	4.73E-01	0.00E+00	0.00E+00	0.00E+00	0.00E+00	2.39E+00	4.73E-01	6.76E-01	6.76E-01	6.76E-01
WATER	kmol/hr	7.61E-05	0.00E+00	0.00E+00	0.00E+00	0.00E+00	6.76E-01	6.76E-01	1.15E+00	4.73E-01	0.00E+00	0.00E+00	0.00E+00	0.00E+00	0.00E+00	4.73E-01	6.76E-01	6.76E-01	6.76E-01
Mole Fractions																			
METHA-01		7.43E-01	9.14E-01	1.00E+00	1.00E+00	1.00E+00	8.73E-01	8.73E-01	8.45E-01	8.45E-01	0.00E+00	0.00E+00	0.00E+00	9.14E-01	7.79E-02	8.45E-01	8.45E-01	8.45E-01	8.45E-01
OLEIC-01		9.28E-02	8.62E-02	0.00E+00	0.00E+00	0.00E+00	4.55E-02	4.55E-02	1.71E-02	1.71E-02	1.00E+00	1.00E+00	1.00E+00	8.62E-02	1.13E-02	1.71E-02	1.71E-02	1.71E-02	1.71E-02
METHY-01		0.00E+00	0.00E+00	0.00E+00	0.00E+00	0.00E+00	4.06E-02	4.06E-02	6.91E-02	6.91E-02	0.00E+00	0.00E+00	0.00E+00	0.00E+00	***9.11E-01***	6.91E-02	6.91E-02	6.91E-02	6.91E-02
WATER		1.64E-01	0.00E+00	0.00E+00	0.00E+00	0.00E+00	4.06E-02	4.06E-02	6.91E-02	6.91E-02	0.00E+00	0.00E+00	0.00E+00	0.00E+00	0.00E+00	6.91E-02	6.91E-02	6.91E-02	6.91E-02
ZINC--01		0	0	0	0	0	0	0	0	0	0	0	0	0	0	0	0	0	0
TITAN-01		0	0	0	0	0	0	0	0	0	0	0	0	0	0	0	0	0	0
Volume Flow	l/min	2.11E-01	7.53E+00	4.31E+00	4.31E+00	4.31E+00	1.87E+01	1.89E+01	1.89E+01	7.79E+00	3.18E+00	3.18E+00	3.18E+00	7.53E+00	1.42E+01	7.79E+00	1.11E+01	1.11E+01	1.11E+01

6.4.10 Repeated Cycle Reactions for MO Formation

As the operational stability of the supported BMZTO-60 coated glass bead photocatalyst is one of the important aspects of the industrial application, a reusability study of the catalyst has been performed. Figure 6.38a-c represents the image of the supported BMZTO-60 coated glass bead catalyst before and after the reaction that placed in the reactor. After repeated use of the photocatalyst in esterification continuously for more than 36 h of reaction, the sphere catalysts have successfully demonstrated that the photocatalytic efficiency has been maintained up to 3 cycles. This suggests that the catalysts could be recycled for continuous use in the esterification process while maintaining their photocatalytic efficiency and negligibly dissolved into the solution. However, after each cycle, proper washing and drying

were carried out. The affinity of the washed catalyst for OA conversion had an observed drop of 5 to 7%, as shown in Figure 6.38c (after the 2nd cycle). The treatment conditions might have to be wisely handled to minimize damage.

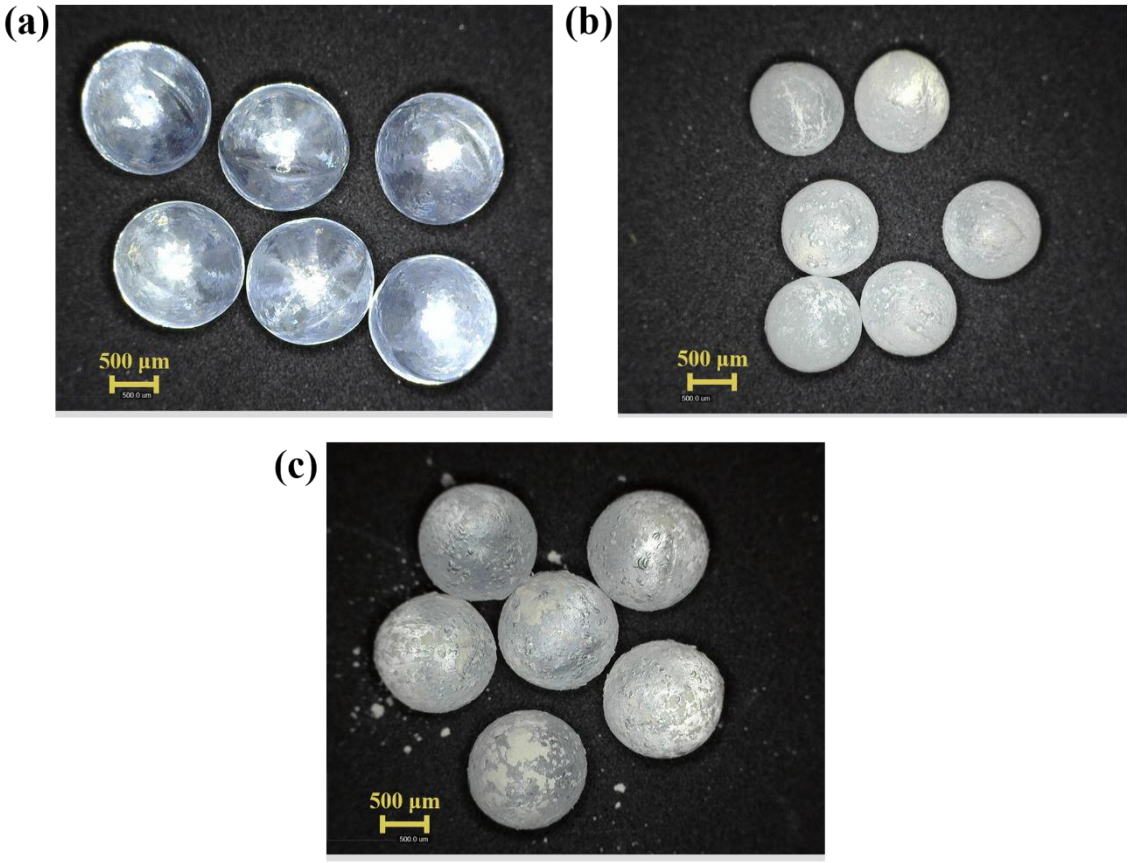

Figure 6.38. Microscopic images of (a) bulk glass bead (b,c) BMZTO-60 before and after reaction at a magnification of 500 µm

6.5 ACTIVITY V

6.5.1 Physical Characterization

6.5.1.1 XRD Analysis

The XRD patterns of as-synthesized CH, MWNT, FMWNT-CH, W@FMWNT-CH, and Al_1/W_2@FMWNT-CH were measured in the diffraction angles of 10-80°, as depicted in Figure 6.39a. The XRD pattern of the CH that appeared at 2θ ~20.18° has been allocated as the characteristic CH peak caused by hydrogen bonds comprising

many –NH_2 and –OH groups, which agrees with the previous literature [88], as shown in Figure 6.39ai. The characteristic peak at approximately 25.72° and 42.84° are associated with the pristine MWNT (Figure 6.39aii) corresponding to the (002) and (100) lattice planes of carbon in MWNT, respectively. Figure 6.39aiii shows that all the characteristic peaks of CH and MWCNTs are present, suggesting an effective combination of FMWNT-CH. Significantly, the peak intensities at 21.24° dramatically increase, elevating crystallinity, accompanied by the structure of FMWNT-CH support [89]. In Figure 6.39aiv, the 2θ values of 28.26° (002) and 39.83° (110) indicate the characteristic diffraction peak of W metal for as-synthesized W@FMWNT-CH catalyst, which is in good agreement with the previous study [90] and at 21.62° for FMWNT-CH phase. However, the XRD pattern of the $A1_1/W_2$ alloy anchored on the support of FMWNT-CH (Figure 6.39av) indicates that Al grains are randomly oriented without having any preferred crystalline phase. The primary change in the diffraction patterns with a high amount of W (Al: W= 1:2) composition recognized a broad halo around 2θ of about 13.38 to 39.54° which indicates the presence of an amorphous phase of Al/W alloy supported on FMWNT-CH [91]. The obtained peak pattern of the as-synthesized Al_1/W_2@FMWNT-CH catalyst proves that the modification of MWNT with CH and following the chemical reduction process for growing Al and W have resulted in good dispersion on the carbon filler-biopolymer support and the metal alloy and hybrid support co-exists in a single amorphous phase. Similar kind of XRD patterns have been observed for the prepared catalysts with different Al: W content.

6.5.1.2. BET Analysis

Figure 6.39b displays the N_2-adsorption/desorption isotherms of the catalyst Al_1/W_2@FMWNT-CH recorded at 77 K. According to IUPAC classification, the

obtained isotherm was classified as type IV. Further, the isotherm suggests that Al_1/W_2@FMWNT-CH has mesoporous textural properties. The BET surface area and BJH pore size distribution of Al/W, CH, and MWNT are reported in the Figure 3.40a,b.

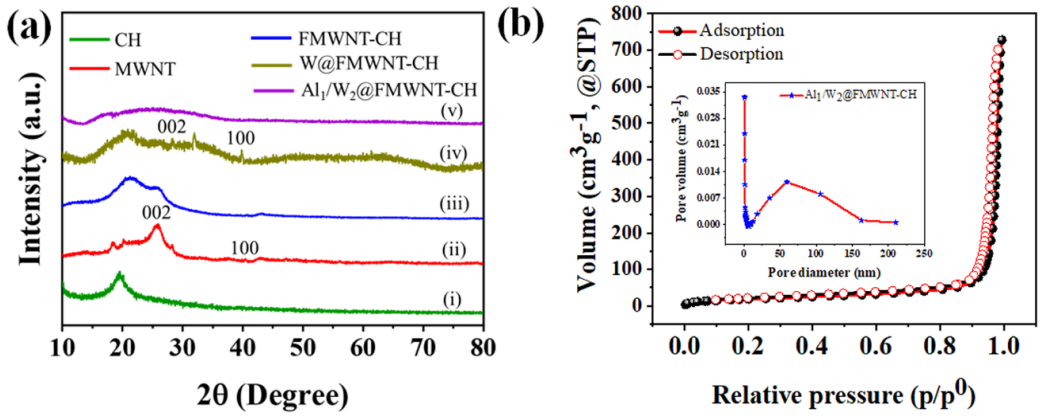

Figure 6.39. (a) XRD analysis of (i) CH, (ii) MWNT, (iii) FMWNT-CH, (iv) W@FMWNT-CH, (v) Al_1/W_2@FMWNT-CH; (b) BET-BJH analysis of Al_1/W_2@FMWNT-CH.

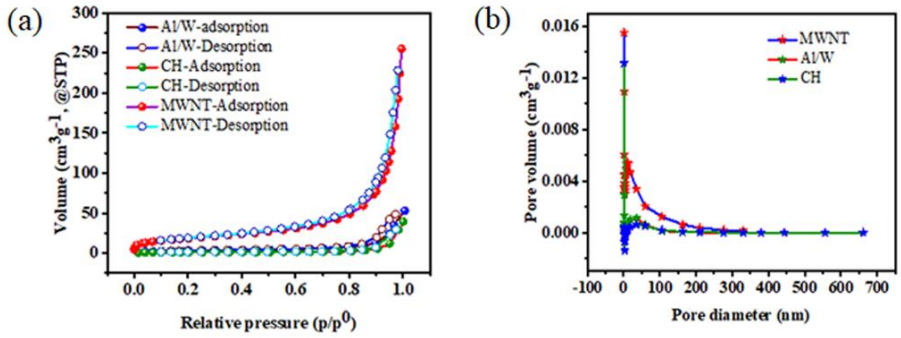

Figure 6.40. (a) BET (b) BJH analyses of Al/W, CH, and MWNT

The textural properties of all the samples are summarized in Table 6.22. As-prepared Al_1/W_2@FMWNT-CH has the highest specific surface area of 122.79 m^2g^{-1} among the others. The synthesized catalyst's average pore size (BJH method), measured using N_2 desorption isotherm, is 1.045 nm, as shown in Figure 6.39b. Al_1/W_2@FMWNT-CH composite led to a decrease in average pore diameter with a

value of 18.41 nm and with the highest increase in the pore volume of 1.09 cm^3g^{-1}, as depicted in Table 6.22.

Table 6.22. Textural properties of various as synthesized catalysts.

Sample	BET-specific surface area (m^2g^{-1})	Average pore diameter (nm)	Total pore volume (cm^3g^{-1})	Pore diameter (nm)
Al/W	10.89	26.05	0.07	1.4950
CH	4.02	17.64	0.06	1.3654
MWNT	70	62.20	0.35	1.0454
Al_1/W_2@FMWNT-CH	122.79	18.41	1.09	1.0452

The larger specific surface area and pore volume might be attributed to the chemical-reduction process to grow and uniform dispersion of the amorphous alloy on the filler-biopolymer support [92]. The synergistic effect of filler and biopolymer can provide more surface for easy adsorption of many reactant molecules for electrochemical reactions and inhibit corrosion. Thus, the overall electrochemical oxidation-reduction performance would improve, rapidly converting bio-GL to glyceric acid and H_2 generation.

6.5.1.3. FT-IR Analysis

FTIR analysis has been used for CH, MWNT, and Al_1/W_2@FMWNT-CH to identify the intermolecular interactions between the molecules, as demonstrated in Figure 6.41a. The strong absorbance peak at 1663 cm^{-1} in the spectrum indicates the -C=O stretching of MWNT and at 1579 cm^{-1} attributed to N-H bending vibration from the primary amine group of CH. During the modification process, the C=O group of MWNT reacted with the amine group of CH and turned it into –NHCO–, as indicated by the peak at 1636 cm^{-1} [93] in the spectrum of Figure 6.41aiii. A broad band at 3465 cm^{-1} corresponds to the stretching vibration of the surface –OH group for the

amorphous phase. C–H stretching at 2880 cm^{-1} and C–N vibrations at 1073 cm^{-1} infer the presence of CH in the FMWNT-CH support and Al_1/W_2@FMWNT-CH materials. Moreover, the peak at 765 cm^{-1} in Figure 6.41aiii might be associated with Al-C bonds [94]. No such stretching band for Al-O has been observed at 550 cm^{-1}. This reveals that the reduction reaction using ascorbic acid had occurred successfully. No sharp band at 941 cm^{-1} arose from W-O and W=O stretching vibration. Moreover, no broad band at 702 cm^{-1} has appeared for W-O-W [95]. Lack of W-O and Al-O bands reveal that reducing Al and W was crowned over the support FMWNT-CH.

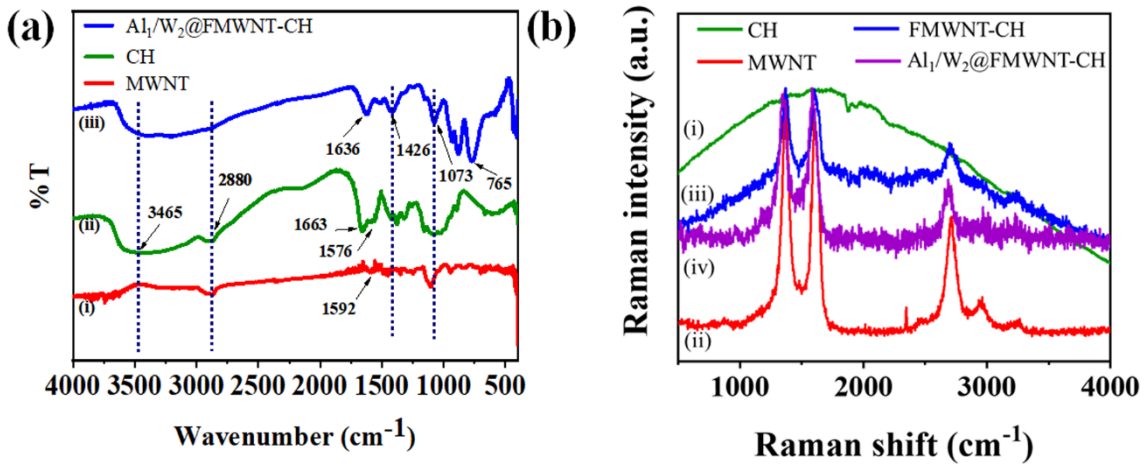

Figure 6.41. (a) FTIR spectra of (i) FMWNT, (ii) CH, (iii) Al_1/W_2@FMWNT-CH; (b) Raman spectrum of (i) CH, (ii) MWNT, (iii) FMWNT-CH, (iv) Al_1/W_2@FMWNT-CH.

6.5.1.4. Raman Spectroscopy

Raman spectroscopy was used to verify the presence of FMWNT and CH in the composite, and it can detect distinct peaks in the nanocomposite material favorable for the electrolysis of bio-GL. Figure 6.41b shows the Raman spectral analysis of the CH, MWNT, FMWNT-CH, and Al_1/W_2@FMWNT-CH nanocomposites. The bands at 1347.8 cm^{-1}, 1582.7 cm^{-1}, and 2689.7 cm^{-1} correspond to the D, G, and G´-bands, respectively, responsible for disordered structure or defects in MWNT [96]. The D-

band indicates disordered carbon with a sp^3 electronic structure of carbon atoms present in the functional groups of the nanocomposite, while the G-band is attributed to the tangential stretching vibration of C=C bonds originating from the in-plane vibrations of sp^2 graphitic carbon [97]. To determine the structural disorder and defect I_D/I_G ratio is calculated. The I_D/I_G ratios of MWNT, FMWNT-CH, and Al_1/W_2@FMWNT-CH are 1.14, 1.14, and 1.19, respectively, in Figure 6.41b. No changes have occurred in the MWNT and FMWNT-CH, whereas structural defects are identified for Al_1/W_2@FMWNT-CH nanocomposite. This might be observed due to the existence of Al-W alloy in the structure of FMWNT-CH.

6.5.1.5 Morphological Analysis

The morphology of the synthesized FMWNT-CH, Al/W, and Al_1/W_2@FMWNT-CH hybrid nanocomposites was analyzed using FESEM, STEM, TEM, and HRTEM techniques. Figure 6.42a exhibits the morphology of the coated Al_1/W_2@FMWNT-CH nanocomposite on Ni-foam. FESEM images of CH-renovated FMWNTs (Figure 6.42b) show that the FMWNTs are well dispersed throughout the CH matrix. It is also clear that the FMWNT and CH are highly interconnected and formed spaghetti-like structures. The formation of a spaghetti-like structure proves the existence of excellent compatibility between the biopolymer and nanofiller. No bead formation occurred during the preparation of CH renovated FMWNT support. On the other hand, bright spots indicate the formation of nano-sized aggregation of Al/W amorphous alloy particles (Figure 6.42c). Al/W amorphous alloys were grown on the rough surface of CH-renovated FMWNTs through a chemical reduction process. Hence, the bead-like alloy nanoparticles are anchored to the spaghetti-like structure and uniformly distributed, enhancing the roughness of the composite system. This rough surface avoids the diffusional limitations in solutions and allows easy ion access by making the active site of the catalyst more electro-conductive, as shown in Figure

6.42d. Incorporating alloy particles within the negatively charged MWNTs, and the positively charged polycation of CH reduced the van der Waals forces due to the interactions of FMWNTs renovated with CH [98]. HAADF-STEM analysis was conducted for Al_1/W_2@FMWNT-CH to identify the distribution of various elements. The dark field image of the substrate demonstrates the homogeneous spread of elements C, N, Al, W, and O, as illustrated by elemental mapping in Figure 6.42(e-e5). This confirms alloy formation and is uniform distribution in the FMWNT-CH framework (Figure 6.42e-f). Energy dispersive X-ray spectroscopy (EDS) was employed to evaluate the sample composition. Figure 6.42g represents the EDS spectrum of Al_1/W_2@FMWNT-CH nanocomposite, which indicates the presence of elements W, Al, C, N, and O in the nanocomposite. As confirmed from the EDS spectrum, no other impurities were detected in the samples. The size histogram of the alloy particles was seen from 90 random spots in an arbitrarily chosen area using *ImageJ* software. The dimensions of alloy nanoparticles lie between 5-30 nm, as presented in Figure 6.42h. TEM analysis of the Al_1/W_2@FMWNT-CH was accomplished in accordance with the FESEM images. Figure 6.42i shows that the FMWNTs are well and uniformly interconnected with CH, and the outer surface of CH-renovated FMWNT is decorated with Al-W alloy nanoparticles. High-resolution TEM of Al_1/W_2@FMWNT-CH (Figure 6.42j) with their inverse fast Fourier transform (IFFT) images (Figure 6.42k) shows the lattice fringes of existing FMWNT merged with CH as indicated by the bars and arrows. The d-spacing value of 0.17 nm in accordance with (002) crystal planes might be adapted to the CH-renovated FMWNT, inferring CH merged with FMWNT at this plane. The SAED pattern (Figure 6.42l) follows an amorphous nature. These results confirm the existence of highly rough surface morphology of Al/W alloy nanoparticles over the support

FMWNT-CH, leading to vastly active electrocatalytic activity toward bio-GL electrolysis and agree with the XRD pattern.

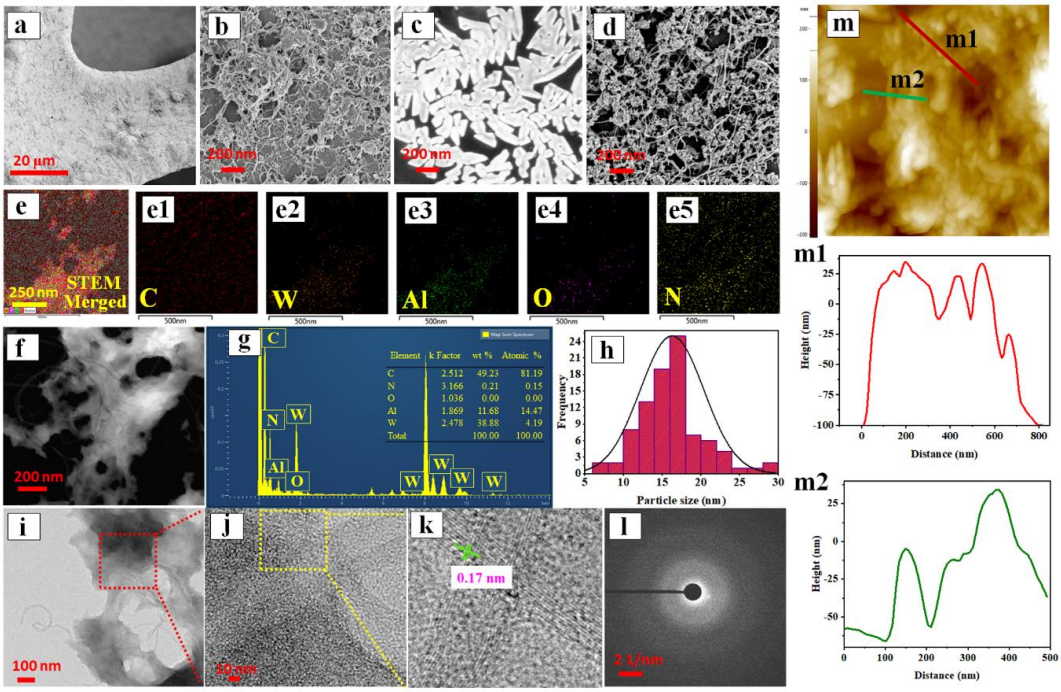

Figure 6.42. FESEM images of (a) Al_1/W_2@FMWNT-CH/Ni-foam, (b) FMWNT-CH, (c) Al/W,(d) Al_1/W_2@FMWNT-CH; (e)-(f) STEM images of Al_1/W_2@FMWNT-CH(with high angle annular dark field detector-HAADF); EDX elemental maps respectively showing the spatial distributions of (e1) C, (e2) W, (e3) O, (e4) Al, (e5) N in the selected area; (g) EDS spectrum (h) size distribution; (i) TEM image of Al_1/W_2@FMWNT-CH (j)-(k) HRTEM image with lattice fringes of FMWNT-CH; (l) SAED pattern of FMWNT-CH; (m-m2) AFM analysis of Al_1/W_2@FMWNT-CH nanocomposite.

In addition, AFM analysis was accomplished using tapping mode to investigate the structures of synthesized nanocomposites. AFM images of Al_1/W_2@FMWNT-CH are displayed in Figure 6.42m. The results confirm the product's high surface roughness due to the presence of Al/W alloy on the FMWNT-CH surface. The average roughness of the composite is 25 nm throughout the surface of the nanocomposite.

Figure 6.42 (m1-m2) reveals the uniform wrapping of CH onto FMWNT and the even distribution of metal alloys (Al/W) on the support material. Therefore, the abovementioned results are consistent with FESEM, STEM, and HRTEM images and XRD, confirming the formation of Al_1/W_2@FMWNT-CH nanocomposite.

6.5.1.6 XPS Analysis

XPS analysis was conducted to get more evidence about the formation of Al_1/W_2@FMWNT-CH, and the full scan spectrum of the supported alloy nanocomposite has been shown in (Figure 6.43). The high-resolution XPS spectra of C1s, O1s, Al2p, Al2s, W4f, and N1s are shown in Figure 6.44a-f. The C1s spectrum was deconvoluted into five bands at 283.8, 284.6, 286.1, 288, and 289.9 eV corresponding to C–M (M: Al, W), C=C/C–H, C–N/C–O, O=C–NH, and π–π^*, respectively (Figure 6.44a). Meanwhile, the O1s spectrum was observed at about 530.4 eV, representing adsorbed oxygen (O_{Ads}), O-containing functional groups, and hydroxyl radicals in the CH. Peaks at 531.6 and 532.6 eV are attributed to C=O and C–OH, respectively, as depicted in Figure 6.44b. Moreover, in Figure 6.44c, the N1s signal consists of two deconvoluted peaks at 400.9 and 402.8 eV, indicating the existence of $–NH_2$ and C–N in the system, respectively. These spectra demonstrate the successful formation of CH-renovated FMWNT in the nanocomposite. Figure 6.44d shows the two high-intensity peaks, $W4f_{7/2}$ (35.4 eV) and $W4f_{5/2}$ (37.7 eV), corresponding to W in the metallic state [99]. Other distinctive peaks of Al are determined in Figure 6.44e, f, where the metallic peaks of Al2p and Al2s fall within the binding energy ranges of 73-79.3 eV and 119.4 eV, respectively. These peaks are concomitant with the metallic state of Al rather than the possible oxide layer [100]. Hence, the XPS patterns of W4f (area=273298.7 cps. eV), Al2s (area=2457.61 cps. eV), O1s (area=305455.2 cps. eV), and C1s (area=216337.64 cps. eV) imply the

existence of W (45.12%), Al (23%), O (3%), C (25.31%), and N (3.57%) and reveal the presence of Al and W in the metallic state in Al_1/W_2@FMWNT-CH.

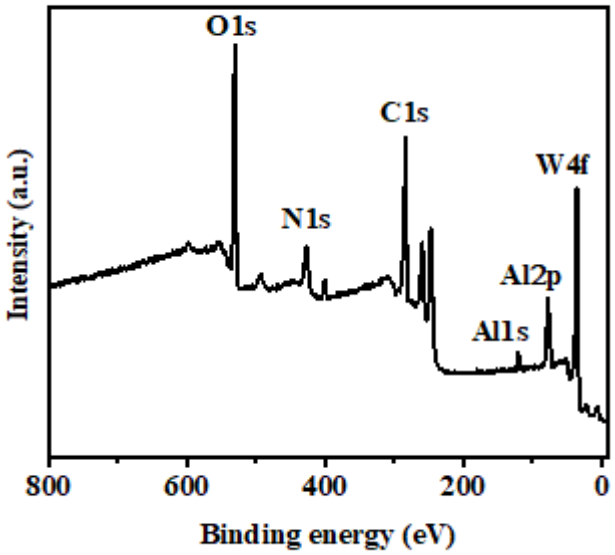

Figure 6.43. XPS survey scan of Al_1/W_2@FMWNT-CH in full spectrum

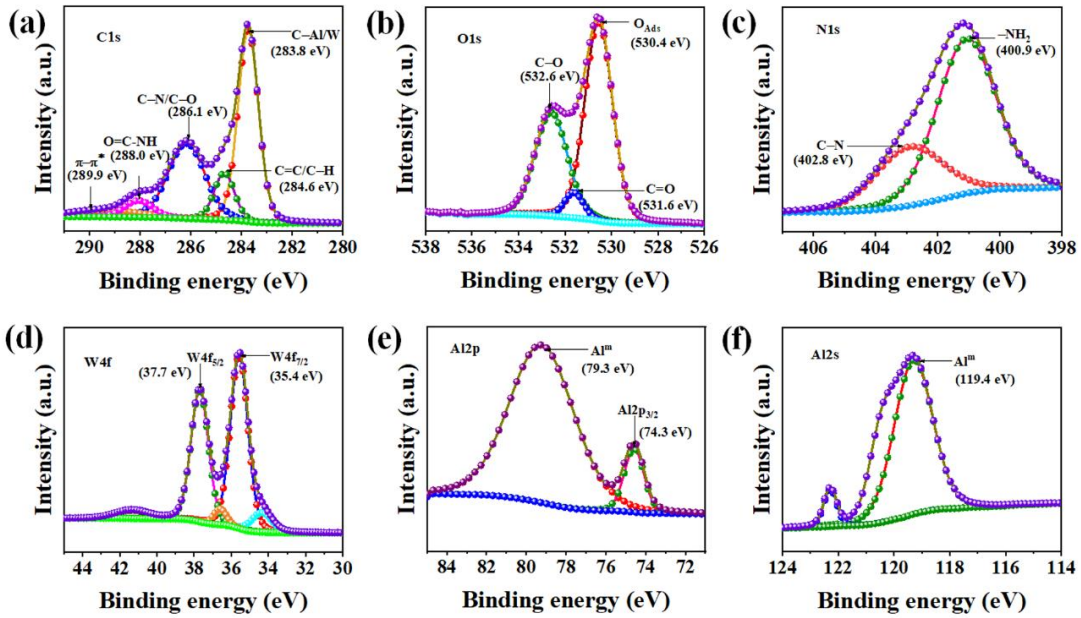

Figure 6.44. XPS analyses of (a) C1s, (b) O1s, (c) N1s, (d) W4f, (e) Al2p, (f) Al2s for Al_1/W_2@FMWNT-CH

6.5.2 Electrocatalytic Performance

The electrocatalytic GOR performance of all prepared catalysts, namely, Al/W, Al@MWNT, W@MWNT, Al/W@MWNT, Al@FMWNT-CH, Al_1/W_2@FMWNT-CH, Al/W@CH, and W@FMWNT-CH over Ni-foam were measured by a three-electrode system in a membrane-less electrolyzer, as shown in Figure 6.45a. The CV curve in the presence of 1 M NaOH and 0.5 M bio-GL electrolyte solution at 80 mV s^{-1} scan rate represents the electrochemical reactivity of the as-prepared catalysts toward GOR as depicted in Figure 6.45b to understand the bio-GL electrooxidation reaction pathway. When the current density reached 10 mA cm^{-2}, the potentials of monometallic pristine and modified supported catalysts considering Al@MWNT, W@MWNT, Al@FMWNT-CH, and W@FMWNT-CH were 1.23, 1.24, 1.20, and 1.33 V *v*s. RHE, respectively. The potential for single-supported bimetallic alloy catalysts such as Al/W@MWNT and Al/W@CH were 1.22 and 1.24 V *v*s. RHE, respectively. Subsequently, the potentials for unsupported and hybrid support-based alloy catalysts Al/W and Al_1/W_2@FMWNT-CH were 1.20 and 1.17 V *v*s. RHE, respectively. To identify the effect of Ni-foam on the electrooxidation performance, GOR has also been performed for Ni-Foam. Figure 6.45b shows Ni-foam substrate has no such activity for GOR until 1.31 V vs. RHE under the reaction conditions. Moreover, no oxidation or reduction peaks were noticed for the bare Ni-foam substrate when bio-GL was present in the electrolyte solution. The CV of GOR for Al_1/W_2@FMWNT-CH at potentials beyond ca. 0.95 V *v*s. RHE shows neither bio-GL nor the electrode surface has been oxidized. During the forward scan, a single peak region was detected in the potential range from 0.95 to 1.67 V *v*s. RHE. This significantly supports that the forward anodic peak is developed due to the electrooxidation of chemisorbed bio-GL by the Al_1/W_2@FMWNT-CH and oxidation

of bio-GL to glyceraldehyde, which is the intermediate of product glyceric acid. On the other side, the reverse anodic peak disappears entirely during the backward scan, as obtained in Figure 6.45b. This is a strong indication of indirect bio-GL oxidation. At higher concentrations (>0.1 M), bio-GL is chemically consumed, leading to reverse anodic peak disappearance known as an indirect mechanism [101]. Fleischmann et al. have proposed this indirect electron transfer mechanism in an alkaline solution [102]. GL oxidation occurred via the indirect alcohol oxidation mechanism, involving the three mentioned initial elementary steps

$$M(OH)_2 + OH^- \rightarrow MOOH + H_2O + e^- \quad (6.13)$$

$$MOOH + RCH_2OH + OH^- \rightarrow M(OH)_2 + H_2O + RCHO + e^- \quad (6.14)$$

$$RCHO + 3OH^- \rightarrow RCOO^- + 2H_2O + 2e^- \quad (6.15)$$

This finding corroborates that the omnipresent primary step is the oxidation of M^{II} to M^{III} (Eq. 6.13). According to Eq. 6.14, this transformation concurred with the bio-GL oxidation mediated by the generated MOOH, regenerating the $M(OH)_2$. At higher potentials, the glyceraldehyde formed from Eq. 6.14 could be further oxidized to glyceric acid (Eq. 6.15). This bio-GL indirect oxidation mechanism conforms to the literature elucidated elsewhere [103]. The electrooxidation of bio-GL was further explored using all seven catalysts (Al@MWNT, W@MWNT, Al@FMWNT-CH, W@FMWNT-CH, Al/W@MWNT, Al/W@CH, and Al/W) in 1 M NaOH containing 0.5 M bio-GL electrolyte solution at a scan rate of 80 mV s^{-1}. It is worth mentioning that every prepared unsupported or supported catalyst followed the indirect electron transfer mechanism. Likewise, the peak obtained in the forward scan of all catalysts corresponded to bio-GL electro-oxidation. As shown in Figure 6.45b, for Al_1/W_2@FMWNT-CH catalyst, glyceraldehyde oxidation has been detected at an

applied potential of 1.13 V *vs*. RHE. Meanwhile, glyceraldehyde has been oxidized to glyceric acid. The onset potential for glyceric acid oxidation has been detected at 1.35 V *vs*. RHE. This designates the cleavage of C-C bond at this stage. The first oxidation peak in glyceraldehyde oxidation was for the conversion of glyceraldehyde to glyceric acid, and the second oxidation peak starting from 1.35 V *vs.* RHE was for glyceric acid oxidation. During the C-C bond cleavage, formic acid might be formed, preventing their further oxidation as no oxidation peak around 1.6 V *vs.* RHE was observed. These results are precisely endorsed with previous results stated elsewhere [104]. A comparison table for all prepared catalysts that participated in GOR performance was depicted in Table 6.23. From Table 6.23, it is observed that the values of the oxidation potentials for Al@MWNT, W@MWNT, W@FMWNT-CH, Al/W@CH, and Al/W correspond to CO-poisoning with less current density toward GOR. However, Al@FMWNT-CH, and Al/W@MWNT expressed an anti-CO-poisoning effect for only bio-GL to glyceraldehyde conversion at higher current densities. Thus, the results obtained for Al_1/W_2@FMWNT-CH modified electrode have endorsed the best catalytic activity not only for the subsequent investigation of bio-GL electrooxidation to glyceric acid and formic acid but also an efficient catalytic property having the anti-CO-poisoning ability. The relatively low potential of Al_1/W_2@FMWNT-CH compared to the other prepared catalysts indicates that the introduction of barnacle carapace-derived CH-renovated FMWNT support and Al/W alloy exhibited a synergistic role in enhancing the charge transfer resistance to achieve the highest GOR performance (119.61 mA cm^{-2} current density reached at 1.74 V *vs*. RHE potential).

Further, in this study, the potent functional groups like -NH, -OH present in the novel hybrid support positively impact the growth of the alloy nanoparticles. Hence, uniform distribution and better dispersion of metal alloy on support lead to a

significant influence on GOR. In addition, to portray the superiority of GOR over OER, the LSV curve of the Al_1/W_2@FMWNT-CH catalyst in 0.1 M NaOH solution was categorized for OER. Compared with the LSV curve for OER (1.52 V *vs.* RHE), the onset potential for Al_1/W_2@FMWNT-CH catalyst (1.04 V *vs.* RHE) shifted cathodically, revealing that GOR is more favorable than the OER over the catalyst at 80 mV s^{-1} scan rate (Figure 6.45c). Thus, replacing OER with GOR might save energy input for H_2 generation up to 0.42 V *vs.* RHE.

Table 6.23. The catalytic activity of all catalysts toward GOR in an alkaline solution

Catalyst	Onset potential (V *vs.* RHE)	Current density (mA cm^{-2})	Glyceraldehyde oxidation potential (V *vs.* RHE)	Glyceric acid oxidation potential (V *vs.* RHE)	Formic acid oxidation potential (V *vs.* RHE)	Oxalic acid oxidation potential (V *vs.* RHE)	Carbonate potential (V *vs.* RHE)	Remarks
Al@MWNT	0.98	48.86	1.17	-	-	1.71	2.01	CO-poisoning
W@MWNT	0.99	33.37	1.16	-	-	1.63	2.00	CO-poisoning
Al@FMWNT-CH	1.04	72.61	1.19	-	-	-	-	-
W@FMWNT-CH	1.00	15.92	1.14	-	-	1.61	1.94	CO-poisoning
Al/W@MWNT	1.01	55.43	-	-	-	-	-	-
Al/W@CH	1.00	26.1	1.14	-	-	1.61	1.94	CO-poisoning
Al/W	1.03	72.58	1.15	-	-	1.64	1.81	CO-poisoning
Al_1/W_2@FMWNT-CH	**0.95**	**119.61**	**1.13**	**1.35**	**-**	**-**	**-**	**-**

The effect of bio-GL concentration on the GOR was investigated on Al_1/W_2@FMWNT-CH catalyst, as illustrated in Figure 6.45d. The CV curve was recorded at 80 mVs^{-1} scan rates in 1 M NaOH aqueous electrolyte containing several bio-GL concentrations ranging from 0.1 to 0.75 M. The catalytic activity upsurges with a concentration of up to 0.5 M of bio-GL, followed by an abrupt drip at 0.75 M. The peak current density for 0.75 M concentration on GOR decreased to 95.81 mA cm^{-2}. The oxidation peak current for various bio-GL concentrations are as follows: 0.1 M: 51.22 mA cm^{-2} <0.35 M: 72.97 mA cm^{-2} <0.5 M: 119.61 mA cm^{-2}. The catalyst's oxidation peak current density increases monotonically, and the corresponding peak

potentials shift negatively. The drop of peak current at 0.75 M might explain that the Al_1/W_2@FMWNT-CH surface is being camouflaged with excess bio-GL, preventing the adsorption of OH and resulting in inadequate $(OH)_{ads}$ coverage [105]. Simultaneously, for each concentration, no reverse anodic peak was detected. This is an indication that the indirect electron transfer pathway took place during the reaction. To understand the mass-transport phenomenon of bio-GL, the kinetics of the Al_1/W_2@FMWNT-CH modified electrode has been further studied at various scan rates (5 to 80 mVs^{-1}) (Figure 6.45e). From Figure 6.45e, it could be explained that the peak currents of the catalyst increased gradually with the increase in scan rates. From the plot between the oxidation current densities (j_{pa}) versus the square root of the scan rates ($V^{1/2}$) in Figure 6.45f, a linear relationship has well-fitted with a regression co-efficient value of 0.96 that could confirm the GOR is a diffusion-controlled reaction process. At the same time, various combinations for Al/W alloy corresponding to fixed FMWNT-CH were studied to establish the superiority of catalysts' anodic GOR catalytic behavior. The activity of Al_1/W_2@FMWNT-CH showed best oxidation current performance than the other catalysts (Al_1/W_3@FMWNT-CH: 88.41 mA cm^{-2}, Al/W@FMWNT-CH: 72.97 mA cm^{-2}, Al_3/W_1@FMWNT-CH: 59.83 mA cm^{-2}, Al_2/W_1@FMWNT-CH: 58.66 mA cm^{-2}), as depicted in Figure 6.45g. The prepared optimal catalyst's activity was compared with the relevant previous literature (Table 6.24) to highlight the advantages of barnacle-carapace derived CH-renovated FMWNT support and non-noble alloy-based catalysts in the present study. Although noble metal-based catalysts namely, FeCo@Fe@Pd/MWCNT-COOH, Pt/CNTs-CeO_2, Pt_5Ru_5/C, Pd-(Ni-Zn)/C exhibited lower potential, conquered lower GL conversion at a lengthy reaction time. Moreover, from Table 6.24, it could be observed that the transition metal-based catalysts showed higher onset potential than the prepared optimal catalyst. It was well observed that the optimum catalyst, Al_1/W_2@FMWNT-

CH revealed higher GL conversion (79.5%) at room temperature (25 °C), and lower reaction time (1 h) employing 0. 5 M GL in 1 M NaOH solution at a minimum onset potential of 0.95 V *vs.* RHE. Therefore, the optimum catalyst's activity conformed the advocacy in evaluating higher current density and glyceric acid selectivity (79.92%) in comparison with the previous studies.

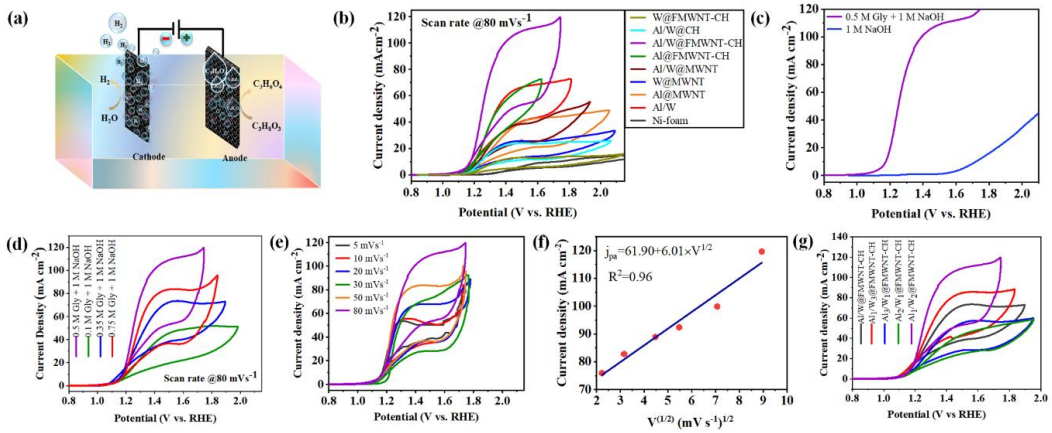

Figure 6.45. (a) Schematic diagram of bio-GL electrolysis using Al_1/W_2@FMWNT-CH catalyst; (b) CV of different catalysts in 1 M NaOH + 0.5 M bio-GL at 80 mVs^{-1} scan rate, Al_1/W_2@FMWNT-CH catalyst; (c) LSV of GOR and OER; CV (d) at various concentration of bio-GL at a scan rate of 80 mVs^{-1}; (e) at various scan rate of 5 to 80 mVs^{-1}; (f) anodic peak currents versus the square root of scan rates; (g) at various molar ratio Al and W at a scan rate of 80 mVs^{-1}

Tafel slope analysis was carried out to identify the kinetics involved in the GOR [overpotential (η) *vs.* log I from $\eta = a + b\log j$, b Tafel slope, a : constant an j : current density]. Al_1/W_2@FMWNT-CH catalyst exhibited a lower Tafel slope (108.38 mV dec^{-1}) than Al/W (175.02 mV dec^{-1}), Al@MWNT (158.69 mV dec^{-1}), W@MWNT (234.54 mV dec^{-1}), Al/W@MWNT (150.75 mV dec^{-1}), Al@FMWNT-CH (143.6 mV dec^{-1}), and Al/W@CH (176.71 mV dec^{-1}), W@FMWNT-CH (224.82 mV dec^{-1}) in bio-GL oxidation (Figure 6.46a). This indicates that the alloy and surface modification of support has been kinetically advantageous in alkaline solution

over a series of prepared catalysts, suggesting intrinsic activity for the bio-GL electrooxidation.

Table 6.24. Comparison of electrocatalytic activity and property of prepared W-based catalyst for GOR over reported in literature.

Catalyst	Feed solution	Applied potential	Reaction condition	GL Conversion (%)	Ref.
FeCo@Fe@Pd/MWCNT-COOH	0.5 M GL+1 M KOH	-0.58 V	60 °C, 4.68 h	16	[106]
Pt/C	0.1 M GL+0.5M H_2SO_4	1.097 V *vs.* SHE	60 °C, 10 h	91.80	[107]
Pd-(Ni-Zn)/C	5 wt% GL+2 M KOH	0.42 V *vs.* RHE	25 °C, 10.2 h	77.1	[108]
$Rh_{0.3}(Ni(OH)_2)_{0.7}$/C	0.5 M GL+1 M KOH	1.29 V *vs.* RHE	25 °C, 1 h	23.40	[109]
$CuCo_2O_4$/Carbon fiber	0.1 M GL+0.1 M KOH	1.14 V *vs.* RHE	25 °C, 5 h	79.7	[110]
Pt_5Ru_5/C	0.1 M GL+0.5 M H_2SO_4	0.44 V *vs.* SHE	60 °C, 7 h	31.5	[111]
Pt/FeNC	5 M GL+8 M KOH	0.85 V *vs.* RHE	60 °C, 12 h	94	[112]
Pt/CNTs-CeO_2	0.1 M GL+1.0 M KOH	0.8 V	50 °C, 4 h	55.30	[113]
Al_1/W_2@FMWNT-CH	**0. 5 M GL+1 M NaOH**	**0.95 V *vs.* RHE**	**25 °C, 1 h**	**79.5**	**This work**

EIS study was carried out to investigate the corrosion inhibition property and charge transfer across the electrode and electrolyte interface. The results of the EIS study were considered as Nyquist and Bode plots in Figure 6.46b-d. EIS data reflects the electrochemical information, including Faradic processes (e.g., the electrode reaction) and non-Faradaic processes (e.g., the charging and discharging processes of the electrical double layer) amid the electrode and electrolyte solution [114]. From the Nyquist plot of all electrode samples (Figure 6.46b-c), it can clearly be distinguished that the Al_1/W_2@FMWNT-CH catalyst has the highest impedance value with the largest semicircle diameter at the higher frequency in comparison with the counterpart, indicating that it is more resistant to corrosion, where a charge transfer process controls the corrosion mechanism. Among the others, Al@FMWNT-CH,

W@FMWNT-CH, and Al/W@MWNT showed the lowest corrosion resistance as described by the low impedance value and small semicircle diameter. Besides, Table 6.25 describes all catalysts' R_S (electrolyte solution resistance) and R_{ct} (charge transfer resistance) values. The Al_1/W_2@FMWNT-CH catalyst with the largest R_{ct} (17304 Ω) and smallest R_S (5.47 Ω) values illustrated the stronger corrosion resistance. Furthermore, the ESCA was determined to estimate the active surface area of the catalyst. According to CV curves at non-faradaic regions for the optimum catalyst, Al_1/W_2@FMWNT-CH, ECSA value was 42.28 cm^2, whereas the value for unsupported Al/W was very low i.e., 39.71 cm^2, which confirmed the superiority in catalytic activity of the optimum catalyst toward GOR and HER over other as-synthesized catalysts. Among all prepared catalysts, optimum Al_1/W_2@FMWNT-CH catalyst shows the largest current density after normalized by ECSA, thus, confirming the enhanced activity over other catalyst. On the one hand, it is clear from Table 6.25 that with the low corrosion current density (I_{corr}: 0.43 mA cm^{-2}) and high corrosion potential (E_{corr}: -0.604 V vs. RHE), Al_1/W_2@FMWNT-CH catalyst signifies best corrosion resistance in comparison with the other prepared catalysts toward electrochemical reaction.

There are many reasons behind the corrosion resistance of the best catalyst, Al_1/W_2@FMWNT-CH. Firstly, without any incorporation of CH in MWNT, what is endangered for the electrode surface alone due to its electric conductivity.

Table 6.25. Corrosion measurement and equivalent circuit parameters determined by modeling impedance spectra for all catalysts

Catalysts	I_{corr} (mA cm^{-2})	E_{corr} (V vs. RHE)	R_S (Ω)	R_{ct} (Ω)
Al/W	1.34	-0.339	6.91	6854.33
Al@MWNT	1.315	-0.55	7.62	5841.40
W@MWNT	0.055	-0.67	7.02	1443.95
Al/W@MWNT	1.65	-0.581	7.00	3066.03
Al@FMWNT-CH	1.96	-0.24	7.64	1303.02
Al_1/W_2@FMWNT-CH	**0.43**	**-0.604**	**5.47**	**17304.68**
Al/W@CH	0.965	-0.469	23.73	3658.02
W@FMWNT-CH	0.923	-0.652	13.86	1588.84

The results indicate that modification of nanofiller MWNT using barnacle carapace derived biopolymer CH has provided a passive layer to protect the Al-W alloy, leading to an excellent corrosion resistance property [115]. The formation of an amorphous alloy employing a reduction process using ascorbic acid could also be motivated by the catalytic activity toward corrosion inhibition. Moreover, from the Bode plots in Figure 6.46d, the log |z| value of the catalyst in the low-frequency region is more extensive than in the high-frequency region. The broad phase diagram with phase angle ~75° indicates that more absorbed bio-GL molecules were rapidly oxidized at a lower frequency to generate a faster interfacial charge transfer [116], i.e., highly capacitive behavior of Al_1/W_2@FMWNT-CH. These findings are consistent with the aforementioned electrochemical analysis.

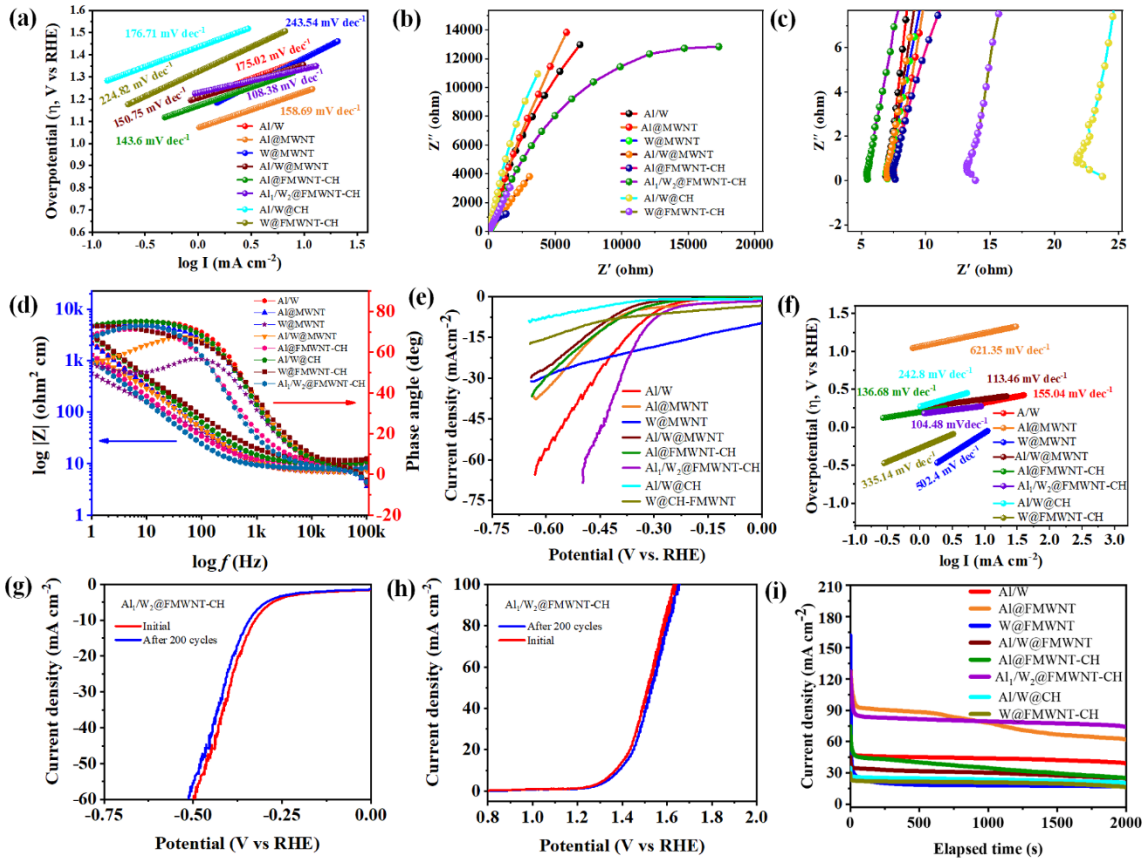

Figure 6.46. (a) Tafel slope plots for GOR; (b-c) Nyquist diagram for bio-GL electro-oxidation; (d); Bode diagrams and phase angle; (e) LSV plot of various catalysts for HER; (f) Tafel slope plots for HER; LSV plot after 200 cycles for (g) GOR (h) HER; (i) chronoamperometry test for all suitable catalysts on Ni-foam in 0.5M bio-GL-1M NaOH solution.

In addition to the noteworthy GOR activity, the HER activity of all prepared catalysts was also measured in the same alkaline solution. LSV polarization curves for all the working electrodes mentioned above were obtained with 0.5 M bio-GL in 1 M NaOH electrolyte at 1 mV s^{-1} scan rate. The outcome in Figure 6.46e shows that the catalysts, Al/W, Al@MWNT, W@MWNT, Al/W@MWNT, Al@FMWNT-CH, Al_1/W_2@FMWNT-CH, Al/W@CH, and W@FMWNT-CH require overpotentials of 0.273, 0.326, 0.266, 0.349, 0.302, 0.253, 0.445, and 0.112 V, respectively, to reach a current density of 5 mA cm^{-2}. It is evident from the LSV curve that the catalyst

Al_1/W_2@FMWNT-CH shows a lower overpotential as compared to the other electrodes performed in the system. Although W@FMWNT-CH shows the lowest overpotential to reach 5 mA cm^{-2} current density, at 0.439 V *vs.* RHE overpotential, Al_1/W_2@FMWNT-CH ascribed to 45.93 mA cm^{-2}, while at same overpotential, W@FMWNT-CH reached only 17.35 mA cm^{-2} current density. A comparison table (Table 6.26) has illustrated where non-noble W with noble Pt-based electrodes demonstrated higher overpotential for HER in acid electrolyte. Concerning previous literature, Al_1/W_2@FMWNT-CH has shown high efficacy in H_2 production in alkaline electrolyte compared to unsupported WC and W catalysts. At the same time, in presence of barnacle carapace derived CH renovated FMWNT supported Al/W alloy needs far less overpotential (5 mA cm^{-2} current density produced only at 0.253 V overpotential), accrediting the electrocatalytic activity for HER. Accordingly, it ensures its enormously effectual H_2 production in the bio-GL electrolyzer.

Table 6.26. Comparison of electrocatalytic activity and property of prepared catalyst over W-based catalyst for HER reported in the literature.

Sample	electrolyte	Current density/mA cm^{-2}	Overpotential (V)	Application	Ref.
W	0.5 M H_2SO_4	10	0.32	HER	[90]
Pt/WC-PME	0.5 M H_2SO_4	4.42	0.250	HER	[117]
WC	neutral pH	8.8	0.300	HER	[118]
Pt/C	0.5 M H_2SO_4	10	0.277	HER	[119]
Al_1/W_2@FMWNT-CH	**1 M NaOH**	**5**	**0.253**	**HER**	**This work**

The optimal Al_1/W_2@FMWNT-CH catalyst confirms lowest Tafel slope of 104.48 mV dec^{-1} among Al/W (155.04 mV dec^{-1}), Al@MWNT (621.35 mV dec^{-1}), W@MWNT (502.40 mV dec^{-1}), Al/W@MWNT (113.46 mV dec^{-1}), Al@FMWNT-CH (136.68 mV dec^{-1}), and Al/W@CH (242.8 mV dec^{-1}), W@FMWNT-CH (335.14 mV dec^{-1}) catalyst (Figure 6.46f). A Tafel plot has been constructed to predict the

rate-limiting step of HER. The calculated value suggests that H_2 generation followed the Volmer–Heyrovsky mechanism, and its rate is well-established by the Volmer step [120]. Furthermore, after 200 continuous cycles of CV, the LSV curve of Al_1/W_2@FMWNT-CH almost overlaps with the initial one for both HER and GOR (Figure 6.46g-h). To investigate the long-term stability of the Al_1/W_2@FMWNT-CH catalyst compared to the other prepared catalyst, a chronoamperometry test over 2000 s was carried out at constant potential of 1.25 V *vs.* RHE. The result for the optimum catalyst is quite encouraging by showing a constant current density of >88 mA cm^{-2} (Figure 6.46i). Meanwhile, the behavior of other prepared catalysts as obtained from the chronoamperometry study (Figure 6.46i) showed a gradual decay in current densities over a fixed time scale (2000 s). Hence, the chronoamperometry result for the optimum catalyst agrees with the abovementioned LSV curve (Figure 6.46g-h) leading to the highest current density inferring the stronger capacity to anti-CO-poisoning and better stability.

At the end of the electrolysis, the ^{13}C NMR technique was performed to characterize the products formed during GOR. In the carbon spectrum, it was observed that the bio-GL has been converted to intermediate product glyceraldehyde to glyceric acid with a little amount of formic acid. The signal of $C(1)-OH$ carbon atoms corresponding to the bio-GL, glyceraldehyde, glyceric acid, and formic acid were located in the 62.0-63.6 ppm range, as mentioned in Figure 6.47. Meanwhile, the small peak shift around δ= 90.2 ppm could be attributed to the carbon atom ($C=O$). The peaks around 71.6-74.3 ppm confirm the presence of $C(II)-OH$ carbon atoms for intermediate products glyceraldehyde and glyceric acid. The reduction of the characteristic peak shift of bio-GL after electrooxidation ensures bio-GL oxidation. Furthermore, glyceric acid and formic acid were detected in the carbon NMR spectra

at δ= 175.8 and 162.6 ppm, respectively, for the carbon atom $O=C-OH$. The Faradaic efficiency for the production of glyceric acid shows ~90% at 119.61 $mAcm^{-2}$ current density. Thus, the formation of glyceric acid with a little amount of formic acid was confirmed from the ^{13}C NMR spectrum, revealing the breakage of bio-GL's C-C bond. H_2 produced in the cathode was determined by gas chromatography equipped with a thermal conductivity detector. Argon (purity: 99.999 %) was used as a carrier gas with a constant flow rate of 20 mL min^{-1}. No standard H_2 curve was noticed before the reaction. In contrast, a stable flow rate of gas was attained after 60 min of reaction [121], as shown in Figure 6.48. Notably, in the GC-MS spectra only the H_2 peak was detected, indicating that the OER was efficiently suppressed by GOR. Besides, anodic glyceric acid and formic acid production reached 6.65 mmol cm^{-2} h^{-1}, and 1.67 mmol cm^{-2} h^{-1}, respectively; and the cathodic H_2 production rate of 28.55 ml cm^{-2} h^{-1} over the optimum catalyst. From Table 6.27, it could be established that H_2 production using the optimal catalyst was much higher than the other prepared catalysts.

In summary, it can be emphasized that all the analyses techniques are in good correlation, indicating the C-C bond breakage and formation of glyceric acid as a significant product with a small amount of formic acid at the anode Al_1/W_2@FMWNT-CH coupled with cathodic H_2 production. Additionally, it is noteworthy to mention that instead of unsupported Alloy Al/W, Al_1/W_2@FMWNT-CH would possibly reduce the electricity consumption of cathodic H_2 production in bio-GL electrolyzer from 3.2 to 2.9 kWh/m^3H_2 at 50 mA cm^{-2}. Therefore, the electricity consumption might be minimized for bio-GL electrooxidation coupled with H_2 production using the optimum catalyst.

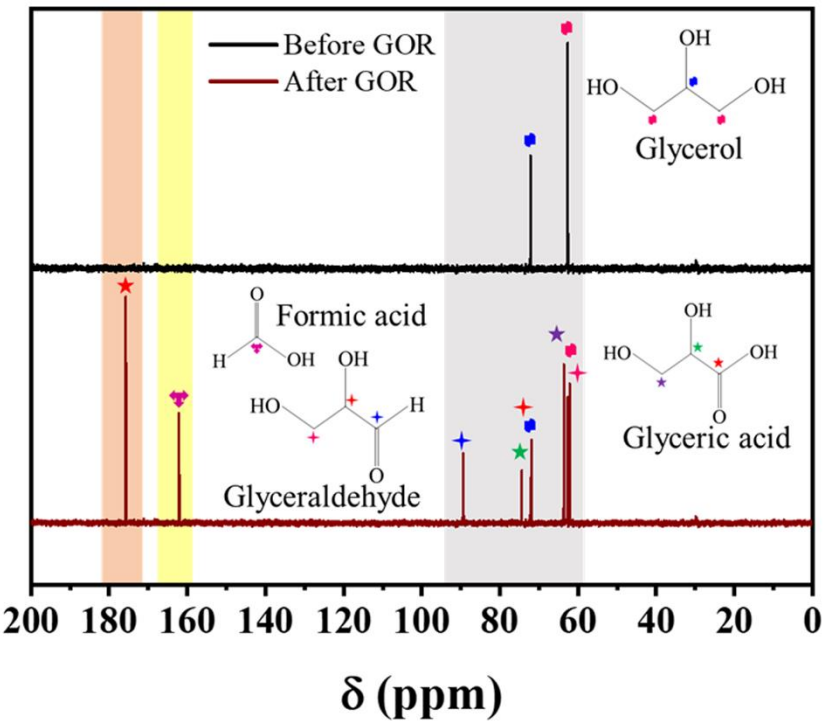

Figure 6.47. ^{13}C NMR spectra before and after GOR

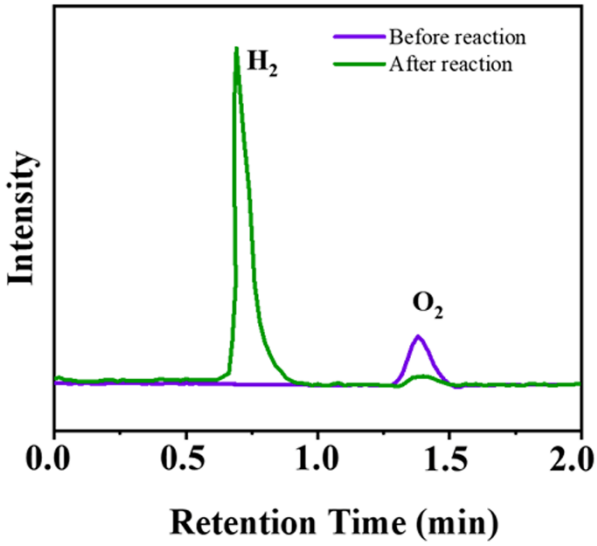

Figure 6.48. Gas chromatography analysis during chronoamperometry for the HER using optimum Al_1/W_2@FMWNT-CH catalyst

Table 6.27. Comparison of H_2 production rate for all prepared catalysts

Catalyst	H_2 production rate (mL cm^{-2} h^{-1})
Al/W	27.11
Al@FMWNT	15.22
W@FMWNT	13
Al/W@FMWNT	12.44
Al@FMWNT-CH	14.44
Al/W@CH	3.7
W@FMWNT-CH	7.25
Al_1/W_2@FMWNT-CH	28.55

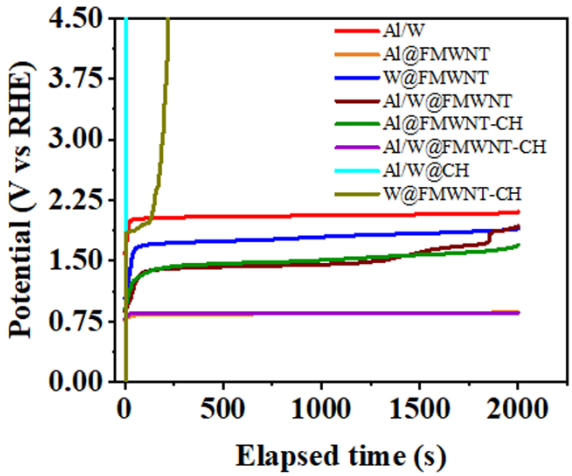

Figure 6.49. Chronopotentiometry curves of different catalysts in 0.5 M bio-GL and 1 M NaOH solution

To study the anti-poisoning ability and electrocatalytic durability of the different electrocatalysts for bio-GL electrolysis, chronopotentiometry study has been employed. At fixed applied current density of 50 mA cm^{-2} the chronopotentiometric curves of Al/W, Al@MWNT, W@MWNT, Al/W@MWNT, Al@FMWNT-CH, Al/W@FMWNT-CH, Al/W@CH, and W@FMWNT-CH electrocatalysts in 0.5 M bio-GL in 1 M NaOH solution were obtained as shown in Figure 6.49. The potential value at which the electrode potential shifts to a higher potential could be considered as an indicator of the poisoning tolerance ability. It is worth mentioning that Al_1/W_2@FMWNT-CH could operate at longer times without any jump in the higher potential leading to higher stability and anti-poisoning ability. Meanwhile, Al/W@CH,

and W@FMWNT-CH confirmed poisoning by reducing the activity of the electrocatalyst. This result provides the advantage of both alloy and hybrid support material in the catalyst admired the better stability than other prepared catalysts.

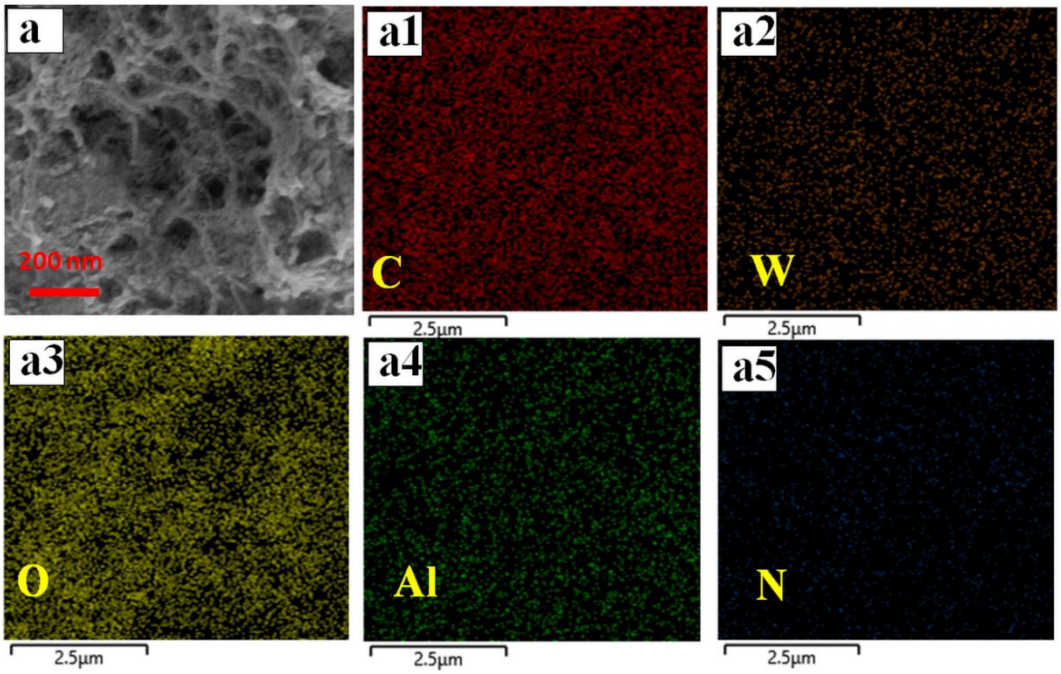

Figure 6.50. (a) FESEM image, elemental mapping of (a1) C, (a2) W, (a3) O, (a4) Al, (a5) N of Al_1/W_2@FMWNT-CH after stability test

Finally, a FESEM image (Figure 6.50a) of the catalyst was taken after the 200 reaction cycles, assessing the stability by chronopotentiometry. As depicted in Figure 6.50(a1-a5), the results demonstrated insignificant changes in the morphology after the stability test. Additionally, the elemental maps of the catalyst indicate the presence of Al, W, C, N, and O, validating the strength of the catalyst.

6.5.3 Environmental Impact Assessment

The concept of sustainability in combination of LCIA and LCC has received increasing scientific interest nowadays [122]. To investigate and compare the impact categories, the ReCiPe midpoint (H) indicator was used for the environmental

assessment of WPLG and commercial GL electrolysis using optimal Al_1/W_2@FMWNT-CH catalyst preparation (as shown in Figure 5.6) for the scale-up production of 1 kg of glyceric acid and 0.5 kg of H_2. The impact categories for CH (1st boundary) and the Al_1/W_2@FMWNT-CH catalyst (2nd boundary) consumed 11-24% of the GWP100, 16-27% of FDP, 2-8% of HTPinf, 4-27% of PMFP, 3-16% of TETPinf, 3-8% of ALOP, and 14-21% of WDP, 1-10% of METPinf (as given in Table 6.28). Among all the steps, 1 kg of glyceric acid and 0.5 kg of H_2 resulted from WPLG electrolysis, showed a higher greenhouse emission (30-34%) than CH and catalyst preparation. The main reason might be using large quantities of electricity, raw material, and waste treatment.

Table 6.28. Results for waste-derived and commercial GL electrolysis using ReCiPe midpoint (H)

Impact category	Unit	Chitosan	Al_1/W_2@FMWNT-CH	WPLG electrolysis	Commercial GL electrolysis
Climate change	kg CO_2-eq	2.69	5.93	7.35	8.38
Fossil depletion	kg oil-eq	1.23	2.04	2.16	2.20
Human toxicity	kg 1,4-DCB-eq	1.44	7.18	35.28	46.12
Particulate matter formation	kg PM10-eq	0.01	0.07	0.07	0.11
Terrestrial ecotoxicity	kg 1,4-DCB-eq	0.002	0.01	0.01	0.04
Agricultural land occupation	m^2a	0.13	0.36	0.97	3.17
Water depletion	m^3	0.06	0.09	0.13	0.15
Marine ecotoxicity	Kg 1,4 DCB-eq	0.16	1.79	7.20	9.34

Further, Figure 6.51a-h shows the five midpoint assessment categories viz. GWP100, FDP, HTPinf, METPinf, and ALOP associated with bio-GL electrolysis from WPLG and commercial GL. In WPLG electrolysis, biodiesel synthesis and bio-GL separation

might be consumed more electricity. However, a less environmental burden has been observed for WPLG electrolysis, whereas electrolysis using commercial GL showed higher ecological effects as depicted in Table 6.28. Electricity consumption, reactors, chemicals used in the reaction, and waste released are the dominant factors affecting these impact categories. Therefore, it is necessary to improve the waste emission in air and soil to reduce the greenhouse effect, human toxicity, and marine ecotoxicity effects in glyceric acid and H_2 production. Significantly, the midpoint indicator assessment analysis results for the WPLG and commercial GL electrolysis revealed that WPLG electrolysis is more environmentally friendly than commercial electrolysis. Thus, WPLG electrolysis provides possible environmental benefits by producing renewable H_2 energy and reducing energy consumption.

Table 6.29. Environmental impact from the production process using ReCiPe Endpoint (H, A)

Damage category	Unit	WPLG electrolysis	Commercial GL electrolysis
Ecosystem	points	0.18	0.63
Human health	points	1.09	1.47
resources	points	0.25	0.26

The endpoint indicator assessment was also performed via ReCiPe Endpoint (H, A) to identify the damage category. Table 6.29 shows that bio-GL electrolysis using WPLG encompasses fewer points (<35.59%) in the total ecosystem. Ecosystem quality includes climate change, agricultural land occupation, freshwater ecotoxicity, eutrophication, and terrestrial acidification. Besides, human health, which is associated with human toxicity, ionizing radiation, ozone depletion, particulate matter formation, and photochemical oxidant formation, occupied 1.09 points for WPLG electrolysis. In contrast, this point was 25.85% high in commercial GL electrolysis.

On the resource side, ecosystem quality is related to fossil depletion and metal depletion. The results observed from the endpoint indicator assessment for GL electrolysis using WPLG and commercial GL are depicted in Table 6.29. In every case, electrolysis using WPLG shows superiority to commercial GL electrolysis in lowering the environmental burden. The results obtained from the endpoint indicator are consistent with those mentioned results from the midpoint indicator impact assessment. Thus, to reduce fossil-based greenhouse gas emissions, WPLG might be the key component with new electrode technology (Al_1/W_2@FMWNT-CH) to help in producing valuable chemicals and renewable H_2 energy production.

6.5.4 Economic Assessment

LCC constitutes a valuable assessment tool for determining the economic analysis. The study aims to assess and compare the economic performances of glyceric acid and H_2 production from WPLG and commercial GL electrolysis obtained through the entire life cycle process. LCC was used to identify the cost which was directly and indirectly related to the production. Directly related costs are raw material costs and reactants used in the reaction. These are WPLG and commercial GL, NaOH, water, Ni-foam, and many other chemicals, as mentioned in Table 6.30. It also includes the transportation and electricity cost. Next, the electricity and transportation costs are 50-52% increased, as mentioned in Table 6.30. Indirectly related costs are the various emissions (CO_2, CO, N_2O, CH_4, VOC, SO_2, NO_X) as depicted in Table 6.31. Among the two paths, GL electrolysis using commercial GL has the maximum production cost. The raw materials cost is a little high due to the cost of GL used in commercial GL electrolysis. On the other hand, the indirect cost related to waste emissions is less in WPLG electrolysis. Although the selling price of the product glyceric acid (L-glyceric acid sodium salt) produced from WPLG and commercial GL electrolysis is

the same, the added value is 5.25% higher for WPLG than for commercial GL electrolysis.

Table 6.30. Assumptions for the estimation of the raw material cost, operating cost, revenue, added value of the WPLG, and commercial GL electrolysis.

Component	WPLG electrolysis ($/kg)	Commercial GL electrolysis ($/kg)
Raw material cost	3626.52	3626.52
GL	-	631.18
NaOH	56.52	56.52
Water	4.26	4.26
Nickel foam	545.45	545.45
Other chemicals	867.5	867.5
Transportation cost	0.08	0.17
Electricity	0.84	1.68
External costs	0.10	0.12
Revenue	10084.07	10084.07
Added Value		
Glyceric acid	6148.53	5825.49
H_2	6.59	6.59

Table 6.31. The amount and cost of different emission substances in air

Emissions	CO_2	CO	N_2O	CH_4	VOC	SO_2	NOx
$/kg	0.032	0.68	4.5	0.24	3.58	4.01	5.23
Chitosan	1.28	0.00094	0.00325	5.04E-9	0.00011	0.00484	5.49E-11
Al_1/W_2@FMWNT-CH	2.94	0.00198	0.00771	0.01212	6.09E-5	0.29	0.00771
WPLG electrolysis	1.59	0.0021	0.0042	2.56E-8	1.11E-5	0.0075	1.15E-10
Commercial GL electrolysis	3.77	0.0026	0.01061	0.1316	1.38E-5	0.39	1.27E-10

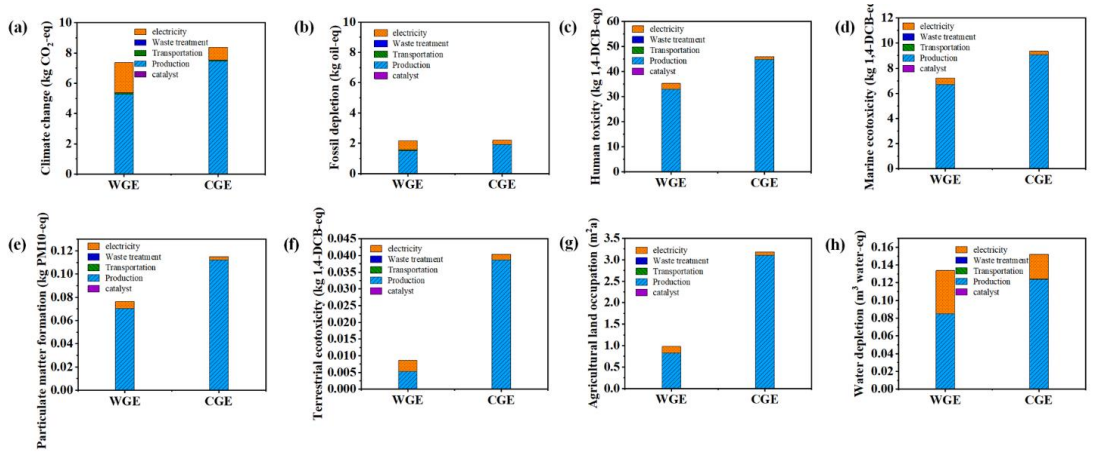

Figure 6.51. Environmental impact assessment for (a) climate change, (b) fossil depletion, (c) human toxicity, (d) marine ecotoxicity, (e) particulate matter formation, (f) terrestrial ecotoxicity, (g) agricultural land occupation, (h) water depletion of catalyst preparation, electricity, transportation, bio-GL electrolysis production and waste treatment for WPLG electrolysis (WGE) and commercial GL electrolysis (CGE) using ReCiPe midpoint (H)

The reason might be the consumption of less raw material, payment of tax, operating cost, and maintenance cost. Therefore, compared to commercial GL electrolysis, WPLG electrolysis is more economically feasible than the other.

References

[1] P. Pradhan, S. Chakraborty, R. Chakraborty, Optimization of infrared radiated fast and energy-efficient biodiesel production from waste mustard oil catalyzed by Amberlyst 15: Engine performance and emission quality assessments, Fuel 173 (2016) 60-68.

[2] M. Veillette, A. Giroir-Fendler, N. Faucheux, M. Heitz, Esterification of free fatty acids with methanol to biodiesel using heterogeneous catalysts: From model acid oil to microalgae lipids, Chemical Engineering Journal 308 (2017) 101-109.

[3] K. Saravanan, B. Tyagi, H.C. Bajaj, Nano-crystalline, mesoporous aerogel sulfated zirconia as an efficient catalyst for esterification of stearic acid with methanol, Applied Catalysis B: Environmental 192 (2016) 161-170.

[4] D. Singh, P. Patidar, A. Ganesh, S. Mahajani, Esterification of oleic acid with glycerol in the presence of supported zinc oxide as catalyst, Industrial & Engineering Chemistry Research 52(42) (2013) 14776-14786.

[5] C.C. Yu, Y.-S. Lee, B.S. Cheon, S.H. Lee, Synthesis of glycerol monostearate with high purity, Bulletin-Korean Chemical Society 24(8) (2003) 1229-1231.

[6] Z. Wang, W. Du, L. Dai, D. Liu, Study on Lipozyme TL IM-catalyzed esterification of oleic acid and glycerol for 1, 3-diolein preparation, Journal of Molecular Catalysis B: Enzymatic 127 (2016) 11-17.

[7] F. Ataya, M.A. Dubé, M. Ternan, Acid-catalyzed transesterification of canola

oil to biodiesel under single-and two-phase reaction conditions, Energy & Fuels 21(4) (2007) 2450-2459.

[8] M. Olutoye, S. Wong, L. Chin, H. Amani, M. Asif, B. Hameed, Synthesis of fatty acid methyl esters via the transesterification of waste cooking oil by methanol with a barium-modified montmorillonite K10 catalyst, Renewable Energy 86 (2016) 392-398.

[9] P. Hoo, A.Z. Abdullah, Kinetics modeling and mechanism study for selective esterification of glycerol with lauric acid using 12-tungstophosphoric acid post-impregnated SBA-15, Industrial & Engineering Chemistry Research 54(32) (2015) 7852-7858.

[10] P. Siril, H.E. Cross, D. Brown, New polystyrene sulfonic acid resin catalysts with enhanced acidic and catalytic properties, Journal of Molecular Catalysis A: Chemical 279(1) (2008) 63-68.

[11] J. Xu, C. Liu, M. Wang, L. Shao, L. Deng, K. Nie, F. Wang, Rotating packed bed reactor for enzymatic synthesis of biodiesel, Bioresource technology 224 (2017) 292-297.

[12] A. Busciglio, F. Scargiali, F. Grisafi, A. Brucato, Oscillation dynamics of free vortex surface in uncovered unbaffled stirred vessels, Chemical Engineering Journal 285 (2016) 477-486.

[13] R. Chakraborty, E. Mandal, Fast and energy efficient glycerol esterification with lauric acid by near and far-infrared irradiation: Taguchi optimization and kinetics evaluation, Journal of the Taiwan Institute of Chemical Engineers 50 (2015) 93-99.

[14] M. Blanco, D. Zamora, M. Mir, R. Mulero, Study of the lipase-catalyzed esterification of stearic acid by glycerol using in-line near-infrared spectroscopy, Industrial & engineering chemistry research 48(15) (2009) 6957-6960.

[15] Y. Pouilloux, S. Métayer, J. Barrault, Synthesis of glycerol monooctadecanoate from octadecanoic acid and glycerol. Influence of solvent on the catalytic properties of basic oxides, Comptes Rendus de l'Académie des Sciences-Series IIC-Chemistry 3(7) (2000) 589-594.

[16] Z. Ziobrowski, K. Kiss, A. Rotkegel, N. Nemestóthy, R. Krupiczka, L. Gubicza, Pervaporation aided enzymatic production of glycerol monostearate in organic solvents, Desalination 241(1-3) (2009) 212-217.

[17] I.B. Ju, H.-W. Lim, W. Jeon, D.J. Suh, M.-J. Park, Y.-W. Suh, Kinetic study of catalytic esterification of butyric acid and n-butanol over Dowex 50Wx8-400, Chemical Engineering Journal 168(1) (2011) 293-302.

[18] Y.S. Huang, K. Sundmacher, Kinetics study of propyl acetate synthesis reaction catalyzed by Amberlyst 15, International Journal of Chemical Kinetics 39(5) (2007) 245-253.

[19] S. Akyalçın, M.R. Altıokka, Kinetics of esterification of acetic acid with 1-octanol in the presence of Amberlyst 36, Applied Catalysis A: General 429 (2012) 79-84.

[20] A. Sarı, A. Bicer, A. Karaipekli, C. Alkan, A. Karadag, Synthesis, thermal energy storage properties and thermal reliability of some fatty acid esters with glycerol as novel solid–liquid phase change materials, Solar Energy Materials and Solar Cells 94(10) (2010) 1711-1715.

[21] T. Hussain, T. Saeed, A.M. Mumtaz, Z. Javaid, K. Abbas, A. Awais, H.A. Idrees, Effect of two hydrophobic polymers on the release of gliclazide from their matrix tablets, ACTA poloniae pharmaceutica-drug research 70 (2013) 749-757.

[22] H. Ke, D. Li, X. Wang, H. Wang, Y. Cai, Y. Xu, F. Huang, Q. Wei, Thermal and mechanical properties of nanofibers-based form-stable PCMs consisting of glycerol monostearate and polyethylene terephthalate, Journal of thermal analysis and calorimetry 114 (2013) 101-111.

[23] B. Xu, Z. Li, Paraffin/diatomite composite phase change material incorporated cement-based composite for thermal energy storage, Applied energy 105 (2013) 229-237.

[24] G. Suppes, M. Goff, S. Lopes, Latent heat characteristics of fatty acid derivatives pursuant phase change material applications, Chemical Engineering Science 58(9) (2003) 1751-1763.

[25] M. Ojanen, P. Kärhä, E. Ikonen, Spectral irradiance model for tungsten halogen lamps in 340–850 nm wavelength range, Applied optics 49(5) (2010) 880-886.

[26] S. Sandesh, P. Manjunathan, A.B. Halgeri, G.V. Shanbhag, Glycerol acetins: fuel additive synthesis by acetylation and esterification of glycerol using cesium phosphotungstate catalyst, RSC advances 5(126) (2015) 104354-104362.

[27] M. Xing, J. Zhang, F. Chen, B. Tian, An economic method to prepare vacuum activated photocatalysts with high photo-activities and photosensitivities, Chemical Communications 47(17) (2011) 4947-4949.

[28] A.V. Mohod, P.R. Gogate, Intensified synthesis of medium chain triglycerides using ultrasonic reactors at a capacity of 4L, Ultrasonics Sonochemistry 42 (2018) 347-355.

[29] M.R. Esfahani, M. Azin, Pretreatment of sugarcane bagasse by ultrasound energy and dilute acid, Asia-Pacific Journal of Chemical Engineering 7(2) (2012) 274-278.

[30] P. Karan, R. Chakraborty, Intensification of autocatalytic methyl oleate synthesis in continuous flow rotating recycle reactor under hybrid radiation: Process optimization and Scale-up, Chemical Engineering Journal 455 (2023) 140032.

[31] A. Hykkerud, J.M. Marchetti, Esterification of oleic acid with ethanol in the presence of Amberlyst 15, Biomass and Bioenergy 95 (2016) 340-343.

[32] Y. Xia, Y. Fang, K. Zhang, G. Shi, J. Brown, Enzymatic synthesis of partial glycerol caprate in solvent-free media, Journal of Molecular Catalysis B: Enzymatic 23(1) (2003) 3-8.

[33] A. Asfour, Diffusion: Mass transfer in fluid systems By EL Cussler, Cambridge University Press, 1984, 525 pp., $49.50, Wiley Online Library, 1985.

[34] M. Mekala, S.K. Thamida, V.R. Goli, Pore diffusion model to predict the kinetics of heterogeneous catalytic esterification of acetic acid and methanol, Chemical Engineering Science 104 (2013) 565-573.

[35] J.M. Aragon, J.M. Vegas, L.G. Jodra, Self-condensation of cyclohexanone catalyzed by Amberlyst-15. Study of diffusional resistances and deactivation of the catalyst, Industrial & engineering chemistry research 33(3) (1994) 592-599.

[36] M. Patel, A. Chavda, I. Mukhopadhyay, J. Kim, A. Ray, Nanostructured SnS with inherent anisotropic optical properties for high photoactivity, Nanoscale 8(4) (2016) 2293-2303.

[37] V. Kumar, S.K. Sharma, T. Sharma, V. Singh, Band gap determination in thick films from reflectance measurements, Optical materials 12(1) (1999) 115-119.

[38] Z. Zeng, L. Cui, W. Xue, J. Chen, Y. Che, Recent developments on the

mechanism and kinetics of esterification reaction promoted by various catalysts, Chemical kinetics 2 (2012) 255-282.

[39] M.C. Manique, A.P. Silva, A.K. Alves, C.P. Bergmann, Application of hydrothermally produced TiO_2 nanotubes in photocatalytic esterification of oleic acid, Materials Science and Engineering: B 206 (2016) 17-21.

[40] M. Ma, X. Wen, Y. Xie, Z. Guo, R. Zhao, P. Yu, D. Gong, S. Deng, Z. Zeng, Antifungal activity and mechanism of monocaprin against food spoilage fungi, Food Control 84 (2018) 561-568.

[41] S.-D. Jiang, Z.-M. Bai, G. Tang, L. Song, A.A. Stec, T.R. Hull, Y. Hu, W.-Z. Hu, Synthesis of mesoporous silica@ Co–Al layered double hydroxide spheres: layer-by-layer method and their effects on the flame retardancy of epoxy resins, ACS applied materials & interfaces 6(16) (2014) 14076-14086.

[42] R. Lu, X. Xu, J. Chang, Y. Zhu, S. Xu, F. Zhang, Improvement of photocatalytic activity of TiO2 nanoparticles on selectively reconstructed layered double hydroxide, Applied Catalysis B: Environmental 111 (2012) 389-396.

[43] N.H. Shalaby, R.A. Elsalamony, A.M. El Naggar, Mesoporous waste-extracted SiO_2–Al_2O_3-supported Ni and Ni–H_3 $PW_{12}O_{40}$ nano-catalysts for photo-degradation of methyl orange dye under UV irradiation, New Journal of Chemistry 42(11) (2018) 9177-9186.

[44] K. Mahmoudi, K. Hosni, N. Hamdi, E. Srasra, Kinetics and equilibrium studies on removal of methylene blue and methyl orange by adsorption onto activated carbon prepared from date pits-A comparative study, Korean Journal of Chemical Engineering 32(2) (2015) 274-283.

[45] E. Seftel, M. Mertens, P. Cool, The influence of the Ti4+ location on the formation of self-assembled nanocomposite systems based on TiO_2 and Mg/Al-LDHs with photocatalytic properties, Applied Catalysis B: Environmental 134 (2013) 274-285.

[46] R. Djeda, G. Mailhot, V. Prevot, Porous layered double hydroxide/TiO_2 photocatalysts for the photocatalytic degradation of orange II, ChemEngineering 4(2) (2020) 39.

[47] A.E. Awadallah, M.S. Mostafa, A.A. Aboul-Enein, S.A. Hanafi, Hydrogen production via methane decomposition over Al_2O_3–TiO_2 binary oxides supported Ni catalysts: Effect of Ti content on the catalytic efficiency, Fuel

129 (2014) 68-77.

[48] J. Guo, X. Luo, S. Tan, O.A. Ogunseitan, Z. Xu, Thermal degradation and pollutant emission from waste printed circuit boards mounted with electronic components, Journal of hazardous materials 382 (2020) 121038.

[49] R. Panda, K.K. Pant, T. Bhaskar, S.N. Naik, Dissolution of brominated epoxy resin for environment friendly recovery of copper as cupric oxide nanoparticles from waste printed circuit boards using ammonium chloride roasting, Journal of Cleaner Production 291 (2021) 125928.

[50] D.N. Thanh, O. Kikhtyanin, R. Ramos, M. Kothari, P. Ulbrich, T. Munshi, D. Kubička, Nanosized TiO_2-A promising catalyst for the aldol condensation of furfural with acetone in biomass upgrading, Catalysis Today 277 (2016) 97-107.

[51] C. Autthanit, W. Chatkaew, P. Praserthdam, B. Jongsomjit, Effect of different phase composition in titania on catalytic behaviors of $AgLi/TiO_2$ catalysts via ethanol dehydrogenation, Journal of Environmental Chemical Engineering 8(2) (2020) 103547.

[52] Y. Xiaodan, W. Qingyin, J. Shicheng, G. Yihang, Nanoscale ZnS/TiO_2 composites: preparation, characterization, and visible-light photocatalytic activity, Materials Characterization 57(4-5) (2006) 333-341.

[53] K.S. Sing, Reporting physisorption data for gas/solid systems with special reference to the determination of surface area and porosity (Recommendations 1984), Pure and applied chemistry 57(4) (1985) 603-619.

[54] R. Chong, C. Su, Z. Wang, Z. Chang, L. Zhang, D. Li, Enhanced Photocatalytic Reduction of CO_2 on Rutile TiO_2/MgAl Layered Double Oxides with H_2O Under Ambient Temperature, Catalysis Letters 150 (2020) 1061-1071.

[55] [55] J. Chen, Y. Song, D. Shan, E.-H. Han, In situ growth of Mg–Al hydrotalcite conversion film on AZ31 magnesium alloy, Corrosion Science 53(10) (2011) 3281-3288.

[56] J.T. Kloprogge, L. Hickey, R.L. Frost, FT-Raman and FT-IR spectroscopic study of synthetic Mg/Zn/Al-hydrotalcites, Journal of Raman Spectroscopy 35(11) (2004) 967-974.

[57] H. Panda, R. Srivastava, D. Bahadur, Stacking of lamellae in Mg/Al hydrotalcites: Effect of metal ion concentrations on morphology, Materials

Research Bulletin 43(6) (2008) 1448-1455.

[58] T. Chuvaeva, O. Dymshits, V. Petrov, M.Y. Tsenter, A. Shashkin, A. Zhilin, V. Golubkov, Low-frequency Raman scattering of magnesium aluminosilicate glasses and glass-ceramics, Journal of non-crystalline solids 282(2-3) (2001) 306-316.

[59] S.J. Palmer, R.L. Frost, G. Ayoko, T. Nguyen, Synthesis and Raman spectroscopic characterisation of hydrotalcite with CO_3^{2-} and $(MoO_4)^{2-}$ anions in the interlayer, Journal of Raman Spectroscopy: An International Journal for Original Work in all Aspects of Raman Spectroscopy, Including Higher Order Processes, and also Brillouin and Rayleigh Scattering 39(3) (2008) 395-401.

[60] P. Karan, P. Mukhopadhyay, R. Chakraborty, Intensification of monostearin (phase change material) synthesis in infrared radiated rotating reactor: Optimization and heterogeneous kinetics, Energy Conversion and Management 138 (2017) 577-586.

[61] C. Wang, H. Wang, Y. Cao, Waste printed circuit boards as novel potential engineered catalyst for catalytic degradation of orange II, Journal of Cleaner Production 221 (2019) 234-241.

[62] N. Mariam, I. Zainab, S. Hoong, Synthesis of glyceryl carbonate via microwave irradiation, Journal of Oil Palm Research 28(1) (2016) 131-141.

[63] D. Singh, B. Reddy, A. Ganesh, S. Mahajani, Zinc/lanthanum mixed-oxide catalyst for the synthesis of glycerol carbonate by transesterification of glycerol, Industrial & Engineering Chemistry Research 53(49) (2014) 18786-18795.

[64] M. Munagala, Y. Shastri, K. Nalawade, K. Konde, S. Patil, Life cycle and economic assessment of sugarcane bagasse valorization to lactic acid, Waste Management 126 (2021) 52-64.

[65] P. Tahay, Y. Khani, M. Jabari, F. Bahadoran, N. Safari, A. Zamanian, Synthesis of cubic and hexagonal $ZnTiO_3$ as catalyst support in steam reforming of methanol: Study of physical and chemical properties of copper catalysts on the H_2 and CO selectivity and coke formation, International Journal of Hydrogen Energy 45(16) (2020) 9484-9495.

[66] N. Pal, M. Paul, A. Bhaumik, New mesoporous perovskite $ZnTiO_3$ and its excellent catalytic activity in liquid phase organic transformations, Applied

Catalysis A: General 393(1-2) (2011) 153-160.

[67] L. Nikam, R. Panmand, S. Kadam, S. Naik, B. Kale, Enhanced hydrogen production under a visible light source and dye degradation under natural sunlight using nanostructured doped zinc orthotitanates, New Journal of Chemistry 39(5) (2015) 3821-3834.

[68] J. Zhao, S. Ge, D. Pan, Y. Pan, V. Murugadoss, R. Li, W. Xie, Y. Lu, T. Wu, E.K. Wujcik, Microwave hydrothermal synthesis of In_2O_3-ZnO nanocomposites and their enhanced photoelectrochemical properties, Journal of the Electrochemical Society 166(5) (2019) H3074-H3083.

[69] L.K. Munguti, F.B. Dejene, Sol pH-induced zinc–titanium mixed-oxide multi-phase composite and its photocatalytic properties, Nano-Structures & Nano-Objects 27 (2021) 100772.

[70] M. Guo, W. Jiang, C. Chen, S. Qu, J. Lu, W. Yi, J. Ding, Process optimization of biodiesel production from waste cooking oil by esterification of free fatty acids using La^{3+}/ZnO-TiO_2 photocatalyst, Energy Conversion and Management 229 (2021) 113745.

[71] S.S.A. Abdul Haroon Rashid, Y.M. Sabri, A.E. Kandjani, C.J. Harrison, R.K. Canjeevaram Balasubramanyam, E. Della Gaspera, M.R. Field, S.K. Bhargava, A. Tricoli, W. Wlodarski, Zinc titanate nanoarrays with superior optoelectrochemical properties for chemical sensing, ACS Applied Materials & Interfaces 11(32) (2019) 29255-29267.

[72] B. Ozturk, G.S.P. Soylu, Promoting role of transition metal oxide on $ZnTiO_3$–TiO_2 nanocomposites for the photocatalytic activity under solar light irradiation, Ceramics International 42(9) (2016) 11184-11192.

[73] J. Lu, D. Li, Y. Chai, L. Li, M. Li, Y. Zhang, J. Liang, Rational design and preparation of nanoheterostructures based on zinc titanate for solar-driven photocatalytic conversion of CO_2 to valuable fuels, Applied Catalysis B: Environmental 256 (2019) 117800.

[74] A. Sahu, R. Chaurashiya, K. Hiremath, A. Dixit, Nanostructured zinc titanate wide band gap semiconductor as a photoelectrode material for quantum dot sensitized solar cells, Solar Energy 163 (2018) 338-346.

[75] V. Mahdavi, A. Monajemi, Optimization of operational conditions for biodiesel production from cottonseed oil on CaO–MgO/Al_2O_3 solid base catalysts, Journal of the Taiwan Institute of Chemical Engineers 45(5) (2014)

2286-2292.

[76] R.S. Malani, H. Sardar, Y. Malviya, A. Goyal, V.S. Moholkar, Ultrasound-intensified biodiesel production from mixed nonedible oil feedstock using heterogeneous acid catalyst supported on rubber de-oiled cake, Industrial & Engineering Chemistry Research 57(44) (2018) 14926-14938.

[77] Y.-H. Chen, L.-C. Wang, C.-H. Tsai, N.-C. Shang, Continuous-flow esterification of free fatty acids in a rotating packed bed, Industrial & engineering chemistry research 49(9) (2010) 4117-4122.

[78] A. Mazubert, M. Poux, J. Aubin, Intensified processes for FAME production from waste cooking oil: a technological review, Chemical engineering journal 233 (2013) 201-223.

[79] Y. Ning, S. Niu, Preparation and catalytic performance in esterification of a bamboo-based heterogeneous acid catalyst with microwave assistance, Energy Conversion and Management 153 (2017) 446-454.

[80] S. Lei, H. Fan, X. Ren, J. Fang, L. Ma, Z. Liu, Novel sintering and band gap engineering of $ZnTiO_3$ ceramics with excellent microwave dielectric properties, Journal of Materials Chemistry C 5(16) (2017) 4040-4047.

[81] M. Bhattacharya, T. Basak, R. Senagala, A comprehensive theoretical analysis for the effect of microwave heating on the progress of a first order endothermic reaction, Chemical engineering science 66(23) (2011) 5832-5851.

[82] Y. Sang, H. Liu, A. Umar, Photocatalysis from UV/Vis to near-infrared light: towards full solar-light spectrum activity, ChemCatChem 7(4) (2015) 559-573.

[83] K.-S. Chen, Y.-C. Lin, K.-H. Hsu, H.-K. Wang, Improving biodiesel yields from waste cooking oil by using sodium methoxide and a microwave heating system, Energy 38(1) (2012) 151-156.

[84] J. Burns, C. Ramshaw, Process intensification: visual study of liquid maldistribution in rotating packed beds, Chemical Engineering Science 51(8) (1996) 1347-1352.

[85] X. Shi, Y. Xiang, L.-X. Wen, J.-F. Chen, CFD analysis of liquid phase flow in a rotating packed bed reactor, Chemical Engineering Journal 228 (2013) 1040-1049.

[86] L.E. Santiago, E.r.G. Rebouças, M.G. Silva, K.C. Oliveira, A.A. Jesus, E.M.

Aguiar, J.A. Oliveira, D.F. Souza, Influence of porosity in a packed-bed tubular reactor on biodiesel production from soybean oil and supercritical ethanol: an experimental and phenomenological investigation, Energy & Fuels 33(9) (2019) 8649-8656.

[87] P. Yan, A.I. Stankiewicz, F.E. Sarabi, H. Nigar, Microwave heating in heterogeneous catalysis: Modelling and design of rectangular traveling-wave microwave reactor, Chemical Engineering Science 232 (2021) 116383.

[88] M. Pan, Z. Weng, J. Liu, Effect of positive bias on properties of chitosan coating prepared on micro-arc oxidation surface of Ti–6Al–4V alloy by electrophoretic deposition, Materials Chemistry and Physics 275 (2022) 125257.

[89] Y. Jian, J. Zhang, C. Yang, L. Qi, X. Wang, H. Deng, X. Shi, Biological MWCNT/chitosan composite coating with outstanding anti-corrosion property for implants, Colloids and Surfaces B: Biointerfaces 225 (2023) 113227.

[90] G.M. Abd El-Hafez, N.H. Mahmoud, A. Walcarius, A.M. Fekry, Evaluation of the electrocatalytic properties of Tungsten electrode towards hydrogen evolution reaction in acidic solutions, International Journal of Hydrogen Energy 44(31) (2019) 16487-16496.

[91] S. Higashino, M. Miyake, A. Takahashi, Y. Matamura, H. Fujii, R. Kasada, T. Hirato, Evaluation of the hardness and Young's modulus of electrodeposited Al–W alloy films by nano-indentation, Surface and Coatings Technology 325 (2017) 346-351.

[92] Z. Yang, D. Jia, Y. Wu, D. Song, X. Sun, C. Wang, L. Yang, Y. Zhang, J. Gao, T. Ohsaka, Novel lithium-chalcogenide batteries combining S, Se and C characteristics supported by chitosan-derived carbon intertwined with CNTs, Chemical Engineering Journal 427 (2022) 131790.

[93] Z. Wu, W. Feng, Y. Feng, Q. Liu, X. Xu, T. Sekino, A. Fujii, M. Ozaki, Preparation and characterization of chitosan-grafted multiwalled carbon nanotubes and their electrochemical properties, Carbon 45(6) (2007) 1212-1218.

[94] L. Yate, J. Caicedo, A.H. Macias, F. Espinoza-Beltrán, G. Zambrano, J. Muñoz-Saldaña, P. Prieto, Composition and mechanical properties of AlC, AlN and AlCN thin films obtained by rf magnetron sputtering, Surface and

Coatings Technology 203(13) (2009) 1904-1907.

[95] S.K. Kamal, P. Sahoo, J. Vimala, B. Shanker, P. Ghosal, L. Durai, Synthesis of high purity tungsten nanoparticles from tungsten heavy alloy scrap by selective precipitation and reduction route, Journal of Alloys and Compounds 678 (2016) 403-409.

[96] H.-M. Yi, G. Yu, Z.-L. Lv, H.-F. Li, X. Lin, H.-H. Li, H.-D. Zheng, Simultaneously elevating the resistive switching performance and thermal/irradiative stabilities of biomemorizer based on twisted carboxylated multi-walled carbon nanotube-chitosan composites, Journal of Alloys and Compounds 952 (2023) 169934.

[97] J.H. Advani, K. Ravi, D.R. Naikwadi, H.C. Bajaj, M.B. Gawande, A.V. Biradar, Bio-waste chitosan-derived N-doped CNT-supported Ni nanoparticles for selective hydrogenation of nitroarenes, Dalton Transactions 49(30) (2020) 10431-10440.

[98] M. Malekkiani, A. Heshmati Jannat Magham, F. Ravari, M. Dadmehr, Facile fabrication of ternary MWCNTs/ZnO/Chitosan nanocomposite for enhanced photocatalytic degradation of methylene blue and antibacterial activity, Scientific reports 12(1) (2022) 5927.

[99] R. Juškėnas, I. Valsiūnas, V. Pakštas, A. Selskis, V. Jasulaitienė, V. Karpavičienė, V. Kapočius, XRD, XPS and AFM studies of the unknown phase formed on the surface during electrodeposition of Ni–W alloy, Applied Surface Science 253(3) (2006) 1435-1442.

[100] J. Van den Brand, W. Sloof, H. Terryn, J. De Wit, Correlation between hydroxyl fraction and O/Al atomic ratio as determined from XPS spectra of aluminium oxide layers, Surface and Interface Analysis: An International Journal devoted to the development and application of techniques for the analysis of surfaces, interfaces and thin films 36(1) (2004) 81-88.

[101] M.S. Houache, M.G. Sandoval, R. Safari, F. Gaztañaga, F. Escudero, A. Hernández-Laguna, C.I. Sainz-Díaz, G.A. Botton, P.V. Jasen, E.A. González, Morphology alteration of nickel microstructures for glycerol electrooxidation, Journal of Catalysis 404 (2021) 348-361.

[102] M. Fleischmann, K. Korinek, D. Pletcher, The oxidation of organic compounds at a nickel anode in alkaline solution, Journal of Electroanalytical Chemistry and Interfacial Electrochemistry 31(1) (1971) 39-49.

[103] T. Andreu, M. Mallafré, M. Molera, M. Sarret, R. Oriol, I. Sirés, Effect of thermal treatment on nickel-cobalt electrocatalysts for glycerol oxidation, ChemElectroChem 9(9) (2022) e202200100.

[104] C. Liu, M. Hirohara, T. Maekawa, R. Chang, T. Hayashi, C.-Y. Chiang, Selective electro-oxidation of glycerol to dihydroxyacetone by a non-precious electrocatalyst–CuO, Applied Catalysis B: Environmental 265 (2020) 118543.

[105] J. Zhao, W. Jing, T. Tan, X. Liu, Y. Kang, W. Wang, Etching high-Fe-content PtPdFe nanoparticles as efficient catalysts towards glycerol electrooxidation, New Journal of Chemistry 44(11) (2020) 4604-4612.

[106] O.O. Fashedemi, H.A. Miller, A. Marchionni, F. Vizza, K.I. Ozoemena, Electro-oxidation of ethylene glycol and glycerol at palladium-decorated FeCo@ Fe core–shell nanocatalysts for alkaline direct alcohol fuel cells: functionalized MWCNT supports and impact on product selectivity, Journal of Materials Chemistry A 3(13) (2015) 7145-7156.

[107] H.J. Kim, J. Lee, S.K. Green, G.W. Huber, W.B. Kim, Selective glycerol oxidation by electrocatalytic dehydrogenation, ChemSusChem 7(4) (2014) 1051-1056.

[108] A. Marchionni, M. Bevilacqua, C. Bianchini, Y.X. Chen, J. Filippi, P. Fornasiero, A. Lavacchi, H. Miller, L. Wang, F. Vizza, Electrooxidation of ethylene glycol and glycerol on Pd-(Ni-Zn)/C anodes in direct alcohol fuel cells, ChemSusChem 6(3) (2013) 518-528.

[109] F.F. Xavier, A.C. Cunha, T.W. Napporn, P. Olivi, Replacing oxygen evolution reaction by glycerol electrooxidation on Rh modified Ni (OH) 2/C for energy-efficient hydrogen production, International Journal of Hydrogen Energy (2023).

[110] X. Han, H. Sheng, C. Yu, T.W. Walker, G.W. Huber, J. Qiu, S. Jin, Electrocatalytic oxidation of glycerol to formic acid by $CuCo_2O_4$ spinel oxide nanostructure catalysts, ACS Catalysis 10(12) (2020) 6741-6752.

[111] Y. Kim, H.W. Kim, S. Lee, J. Han, D. Lee, J.R. Kim, T.W. Kim, C.U. Kim, S.Y. Jeong, H.J. Chae, The role of ruthenium on carbon-supported PtRu catalysts for electrocatalytic glycerol oxidation under acidic conditions, ChemCatChem 9(9) (2017) 1683-1690.

[112] J. Li, K. Jiang, S. Bai, C. Guan, H. Wei, H. Chu, High productivity of tartronate from electrocatalytic oxidation of high concentration glycerol

through facilitating the intermediate conversion, Applied Catalysis B: Environmental 317 (2022) 121784.

[113] X. Liu, C. Yang, Electrocatalytic selective oxidation of glycerol to glyceric acid over efficient Pt/CNTs-CeO_2 catalysts, Materials Letters 324 (2022) 132658.

[114] F. Guan, X. Zhai, J. Duan, J. Zhang, K. Li, B. Hou, Influence of sulfate-reducing bacteria on the corrosion behavior of 5052 aluminum alloy, Surface and Coatings Technology 316 (2017) 171-179.

[115] R.A. Ahmed, A.M. Fekry, R. Farghali, A study of calcium carbonate/multiwalled-carbon nanotubes/chitosan composite coatings on Ti–6Al–4V alloy for orthopedic implants, Applied surface science 285 (2013) 309-316.

[116] Q. Qian, X. He, Z. Li, Y. Chen, Y. Feng, M. Cheng, H. Zhang, W. Wang, C. Xiao, G. Zhang, Electrochemical Biomass Upgrading Coupled with Hydrogen Production under Industrial-Level Current Density, Advanced Materials (2023) 2300935.

[117] C. Ma, J. Sheng, N. Brandon, C. Zhang, G. Li, Preparation of tungsten carbide-supported nano Platinum catalyst and its electrocatalytic activity for hydrogen evolution, International journal of hydrogen energy 32(14) (2007) 2824-2829.

[118] F. Harnisch, G. Sievers, U. Schröder, Tungsten carbide as electrocatalyst for the hydrogen evolution reaction in pH neutral electrolyte solutions, Applied Catalysis B: Environmental 89(3-4) (2009) 455-458.

[119] U. Phungjit, M. Hunsom, K. Pruksathorn, Effect of Temperature for Platinum/Carbon Electrocatalyst Preparation on Hydrogen Evolution Reaction, Engineering Journal 25(4) (2021) 105-113.

[120] U.N. Pan, D.R. Paudel, A.K. Das, T.I. Singh, N.H. Kim, J.H. Lee, Ni-nanoclusters hybridized 1T–Mn–VTe_2 mesoporous nanosheets for ultra-low potential water splitting, Applied Catalysis B: Environmental 301 (2022) 120780.

[121] X. Du, M. Tan, T. Wei, H. Kobayashi, J. Song, Z. Peng, H. Zhu, Z. Jin, R. Li, W. Liu, Highly efficient and robust nickel-iron bifunctional catalyst coupling selective methanol oxidation and freshwater/seawater hydrogen evolution via CO-free pathway, Chemical Engineering Journal 452 (2023) 139404.

[122] A. Di Maria, J. Eyckmans, K. Van Acker, Downcycling versus recycling of co nstruction and demolition waste: Combining LCA and LCC to support sustain able policy making, Waste management 75 (2018) 3-21.

CHAPTER 7

Conclusion and New Findings

ACTIVITY I

GL esterification was conducted with Amberlyst 36 (wet) catalyst which led to a promising SA conversion coupled with good MSN yield within a distinctive short reaction time through the application of the novel infrared radiated RBR. The rotating effect had caused a much faster esterification reaction compared to SBR in terms of SA conversion and desired ester yield. Besides, LH model firmly represented the heterogeneous mechanism for prediction of reaction kinetics of the esterification under rotating condition. The computed activation energy for the RBR indicated its superior energy-efficiency over the SBR. The evaluated kinetic parameters were utilized for scale-up purposes. The MSN prepared through this energy-efficient green route exhibited a promising phase change properties.

ACTIVITY II

GMC has been proficiently synthesized using energy-efficient inclusive QHRUERR. The synergistic effects of QHR and US expedited the GMC selectivity by escalating 9 ± 1 times more than the action of QHR radiated rotating reactor and ultrasonically energized rotating reactor operated independently. Moreover, to enhance the effect of QHR on esterification reaction, NT-P25 catalyst was employed along with A15catalyst. The combination of photocatalytic activity by Lewis acid sites (nano-TiO_2P25) and Brønsted acid groups (A15) rendered 7% GMC selectivity enhancement comparing with individual catalytic effects. Besides, from the comparative performance analyses among the conventionally energized, ultrasonically energized, quartz halogen energized, and the hybrid reactor (QHRUERR), it was evident that the integrated reactor exhibited the esterification process much more energy efficient (93% ± 0.16% less energy consumption compare to other reactor) besides rendering maximum GMC yield (20% more than conventional reactor). For

all types of reactors, LH kinetic model was observed to be the best mechanism representing CA-GL esterification. Further, the reusability of the catalyst also signified the fact that the catalyst reusability was highest in integrated reactor than conventional one because of efficient intermixing. Thus, the hybrid QHRUERR demonstrated superior efficacy in terms of intensification of reaction rate, energy efficiency, and greater catalytic reusability. The produced GMC also exhibited a good food preservation properties in comparison with pure substance. The prepared product displayed 144 h endurance toward *A. Niger* growth. Moreover, the evaluated esterification kinetic parameters were useful for reactor scale-up enabling design of large scale sustainable green synthesis of GMC and similar fine chemicals.

ACTIVITY III

The SSQHLBR facilitated extraction of silica (as support) and alumina (as precursor) from e-waste for the preparation of novel layered double oxide photocatalyst evinced superior environmental and economical sustainability compared to its conventional counterpart in the synthesis of GC. Environmental impact assessment and cost analysis of the entire process revealed that the e-waste-derived novel photocatalyst is eco-friendlier and more cost-effective (cost INR 25.77/kg less) compared to its commercially derived counterpart. Notably, the photocatalytic nature of $MATLS_W$-5 catalyst becomes more pronounced under the influence of SSR in SSQHLBR, providing a significant reduction in the environmental impacts such as GWP, FDP, HTP by 0.28 kg CO_2-Eq, 0.08 kg oil-Eq, 0.11 kg 1,4-DCB-Eq, respectively owing to 56.64% less electricity consumption per kg GC synthesis as revealed by LCIA. The GWP burden has been remarkably reduced by 6% for the GC synthesis using the novel photocatalyst in comparison with $MATLS_C$. The optimally synthesized GC unveiled its practical use as an efficient electrolyte in the energy storage device. Such

approaches mitigated the consumption of resources by substituting the conventional process inputs with waste-derived inputs along with the applications of efficient reactor systems. Scale-up study of the developed process for 1 MT of GC synthesis implied that this process could be accomplished with overall sustainability. Thus, imbibing the idea of 'Circular Economy', this activity effectively reduced the environmental impacts through the sustainable valorization of the hazardous e-wastes for the production of cost-effective energy storage materials towards a greener and healthier mother earth.

ACTIVITY IV

MO synthesis in a MRBR revealed the advantages of the synergistic effect of combined microwave-near infrared irradiated mode in comparison with individual applications of near-infrared and microwave irradiations in terms of both power requirement and MO yield in presence of the prepared nano-$ZnTiO_3$ spherical photocatalyst. Furthermore, the implementation of recycling mode in the continuous flow reactor has played a crucial role in rendering the autocatalytic parallel reaction mechanism which resulted in an impulsive increase in MO yield (93.55 %) and COMSOL simulation implied uniform radiation heat transfer/ temperature distribution throughout the reactor system at optimal conditions. Moreover, LH kinetics parameters were evaluated under negligible internal and external mass transfer regimes. The scale-up study has been performed meticulously through ASPEN PLUS simulation with a 1000 throughput scale-up factor that predicted 91.08 % MO yield which corroborates well with the lab-scale experimental MO yield (93.55 %). Thus, the highly effective synergistic radiation system in combination with the rotating recycle reactor operation, resulted in a significantly intensified continuous MO (a biodiesel blending stock) synthesis, portraying an energy-proficient biorefinery viable

process to produce clean fuel.

ACTIVITY V

A facile and eco-friendly protocol was followed to improve the electrochemical efficacy of biopolymer CH renovated functional MWNT supported non-noble metal-based catalyst compared to precious noble metal toward bio-GL electrolysis. The chronoamperometry and chronopotentiometry studies ascertained that the optimal catalyst viz. barnacle carapace waste-derived CH-renovated FMWNT-supported Al/W alloy catalyst displayed higher chemical stability and durability than unsupported one. The synergistic effect of the combined support barnacle carapace derived CH renovated FMWNT and Al/W alloy showed excellent economical catalytic properties (higher added value of $6148.53/kg for glyceric acid) following the indirect bio-GL oxidation mechanism with the minimum onset potentials (1.17 V *vs*. RHE) coupled with cathodic H_2 production with minimum overpotential (0.270 V) to reach 10 mA cm^{-2} current density. Moreover, the fabricated optimal catalyst outperformed prepared unsupported and supported catalysts demonstrating promising corrosion resistance with the low corrosion current density (I_{corr}: 0.43 mA cm^{-2}) and high corrosion potential (E_{corr}: -0.604 V *vs.* RHE). The obtained results were concordant and allowed accurate determination of the composition of the oxidized products, containing glyceric acid as a leading product, with glyceraldehyde intermediate, and formic acid as a byproduct revealing the anodic glyceric acid and formic acid production rate of 6.65 mmol cm^{-2} h^{-1}, and 1.67 mmol cm^{-2} h^{-1}, respectively; and the cathodic H_2 production rate of 28.55 mL cm^{-2} h^{-1}. Moreover, according to the LCA coupled with LCC results, in the production of 1 kg glyceric acid and 0.5 kg H_2 energy using WPLG electrolysis, the GWP100, FDP, HTPinf, and METPinf burdens were reduced by 12.29%, 1.81%, 23.50%, and 22.91%, respectively; in comparison with

commercial GL electrolysis. Therefore, in summary, this work revealed an economical pathway toward the fabrication and application of a novel hybrid-supported non-noble metal alloy-based electrocatalyst for efficient production of glyceric acid and H_2 through a sustainable pathway in futuristic application.

❖ **Contribution to the Society**

1. Value-added products of bio-GL are important synthetic chemicals that find their application in various fields such as energy storage material, food additive, fuel additive, H_2 production etc., thus encouraging extensive economic growth and attenuating environmental effects of climate change.

2. Utilization of e-waste can mitigate the crucial issue of human health and the ecosystem. Moreover, naturally occuring biowaste resources viz. barnacle carapace shells are the main resources of bio-polymer CH. The use of these wastes as support material can meticulously reduce the catalyst preparation cost. Besides, the sustainable application of these wastes as green catalyst support can effectively prevent the hazardous waste generated throughout the largest populated country. These will further set up a new era for entrepreneurship/start-up initiatives in rural/urban society.

3. Commercialization and market growth of the value-added products obtained through GL conversion will drive a consumer economy and help boost the revenue and profits of the biodiesel industry, thus contributing to the economic growth of the society.

❖ **Novelty:**

- Energy-efficient infrared radiated rotating reactor intensified MSN synthesis.

- Rotating reactor resulted in faster MSN yield than conventionally stirred reactor.
- Optimally synthesized product possesses properties suitable for phase change material.
- Lower reaction activation energy for rotating reactor.
- Heterogeneous kinetics with mass transfer and surface reaction-controlled regimes.
- Valorization of e-waste (PCB) for preparation of inexpensive silica and alumina.
- Green synthesis of optimal GC via cost-effective, eco-friendly protocol.
- LCIA and scale-up of the overall process and Substantial reductions in GWP, FDP and HTP by 5.78%, 3.60% and 5.72% respectively.
- Intensified MO synthesis in continuous-flow-rotating-recycle-reactor.
- Near-infrared-microwave combined radiation was found superior to individual microwaves.
- Temperature profile and LH kinetic simulation of the parallel-autocatalytic-esterification.
- Reactor scale-up prediction in ASPEN PLUS simulator corroborates with lab-scale yield.
- Anti-corrosive, highly stable supported alloy catalyst for bio-GL electrolysis
- Synergistic effect of barnacle carapace-derived chitosan-CNT support and Al-W alloy

- Simultaneous production of glyceric acid and H_2 in a membrane-less electrolytic-cell
- Crude bio-GL electrolysis could minimize cost over commercial GL electrolysis.

❖ **Challenges and Opportunities for Scale-Up**

Challenges

1. Commercialization of the product obtained through GL valorization is still not yet explored
2. Due to a lack of infrastructure, and reluctance to set rules, waste valorization on a large scale is still a challenge.
3. P&ID in addition to PFD is necessary to scale up the reactor configurations for GL valorization.
4. Application of electromagnetic radiation is still in the lab scale stage due to the uneven distribution of penetration depth; dielectric property and no standard data of electromagnetic radiation are available based on which the economic assessment of these developed technologies could be done on pilot scale.
5. Large-scale reactor faces a lack of appropriate selection of operating parameters which causes pressure drop, clogging, heat and mass transfer hindrance. More research work in continuous flow reactors is required to avoid the losses.

Opportunities

1. The synergistic effect of hybrid energy (electromagnetic energy and ultrasonic energy) has the potential to reduce the operating conditions, resulting in a high yield of the desired products, and low by-product formation.

2. Mild reaction conditions excluded the requirement for costly material of construction for reactors.

3. In the case of a continuous flow reactor autocatalytic reaction takes place with the employment of recycle mode and enhances the product yield. This could open up a new platform, portraying an energy-proficient biorefinery viable process for the production of clean energy.

4. Environmental impact assessment for end-to-life disposal implicates waste management for the development of eco-friendly, energy-efficient and economically sustainable processes.

5. Employing theoretical simulations considering COMSOL, ASPEN PLUS could design the model and show the validation with the experimental results and therefore confirm their ability for application of the large-scale reactor performance.

❖ **Future Recommendations**

Previous chapters illustrate elaborate descriptions of the work conducted while focusing on the preparation and application of green cost-effective catalysts for the synthesis of environment-friendly value-added products of GL and H_2 energy in energy-efficient reactors. However, this final chapter suggests a few future recommendations in which further investigations could be carried out.

1. Study of GL fuel cells can not only achieve electricity output but also produce high value-added products in the anode with the aid of lower applied potential using non-noble metal catalysts. It can be done in continuous flow reactor.

2. Studies on other continuous reactors viz. continuous stirred tank reactor for continuous production of such valuable esters using waste-derived supported catalyst.

3. Production of hydrogen energy through GL electrolysis should be explored with the effect of electromagnetic energy sources.

Poulami Karan
26.09.2023

Prof. Rajat Chakraborty
Chemical Engineering Department
Jadavpur University
Kolkata-700032
26.09.2023

ELSEVIER LICENSE
TERMS AND CONDITIONS

Apr 25, 2024

This Agreement between Ms. POULAMI KARAN ("You") and Elsevier ("Elsevier") consists of your license details and the terms and conditions provided by Elsevier and Copyright Clearance Center.

License Number	5775970359408
License date	Apr 25, 2024
Licensed Content Publisher	Elsevier
Licensed Content Publication	Journal of Colloid and Interface Science
Licensed Content Title	Synergistic effect of p-n heterojunction, supporting and zeolite nanoparticles in enhanced photocatalytic activity of NiO and SnO2
Licensed Content Author	Hadis Derikvandi,Alireza Nezamzadeh-Ejhieh
Licensed Content Date	Mar 15, 2017
Licensed Content Volume	490
Licensed Content Issue	n/a
Licensed Content Pages	14
Start Page	314
End Page	327

Type of Use	reuse in a thesis/dissertation
Portion	figures/tables/illustrations
Number of figures/tables/illustrations	1
Format	both print and electronic
Are you the author of this Elsevier article?	No
Will you be translating?	No
Title of new work	Intensification and Optimization of Bio-glycerol conversion into Valuable Chemicals using Electromagnetic Radiation promoted Reactor
Institution name	Jadavpur University
Expected presentation date	May 2024
Portions	Figure 5(B) on page 322
Requestor Location	Ms. POULAMI KARAN Jadavpur University Kolkata, West Bengal 700032 India Attn: Ms. POULAMI KARAN
Publisher Tax ID	GB 494 6272 12
Billing Type	Invoice
Billing Address	Ms. POULAMI KARAN Jadavpur University

Kolkata, India 700032
Attn: POULAMI KARAN

Total 0.00 USD

Terms and Conditions

INTRODUCTION

1. The publisher for this copyrighted material is Elsevier. By clicking "accept" in connection with completing this licensing transaction, you agree that the following terms and conditions apply to this transaction (along with the Billing and Payment terms and conditions established by Copyright Clearance Center, Inc. ("CCC"), at the time that you opened your RightsLink account and that are available at any time at https://myaccount.copyright.com).

GENERAL TERMS

2. Elsevier hereby grants you permission to reproduce the aforementioned material subject to the terms and conditions indicated.

3. Acknowledgement: If any part of the material to be used (for example, figures) has appeared in our publication with credit or acknowledgement to another source, permission must also be sought from that source. If such permission is not obtained then that material may not be included in your publication/copies. Suitable acknowledgement to the source must be made, either as a footnote or in a reference list at the end of your publication, as follows:

"Reprinted from Publication title, Vol /edition number, Author(s), Title of article / title of chapter, Pages No., Copyright (Year), with permission from Elsevier [OR APPLICABLE SOCIETY COPYRIGHT OWNER]." Also Lancet special credit - "Reprinted from The Lancet, Vol. number, Author(s), Title of article, Pages No., Copyright (Year), with permission from Elsevier."

4. Reproduction of this material is confined to the purpose and/or media for which permission is hereby given. The material may not be reproduced or used in any other way, including use in combination with an artificial intelligence tool (including to train an algorithm, test, process, analyse, generate output and/or develop any form of artificial intelligence tool), or to create any derivative work and/or service (including resulting from the use of artificial intelligence tools).

5. Altering/Modifying Material: Not Permitted. However figures and illustrations may be altered/adapted minimally to serve your work. Any other abbreviations, additions, deletions and/or any other alterations shall be made only with prior written authorization of Elsevier Ltd. (Please contact Elsevier's permissions helpdesk here). No modifications can be made to any Lancet figures/tables and they must be reproduced in full.

6. If the permission fee for the requested use of our material is waived in this instance, please be advised that your future requests for Elsevier materials may attract a fee.

7. Reservation of Rights: Publisher reserves all rights not specifically granted in the combination of (i) the license details provided by you and accepted in the course of this

licensing transaction, (ii) these terms and conditions and (iii) CCC's Billing and Payment terms and conditions.

8. License Contingent Upon Payment: While you may exercise the rights licensed immediately upon issuance of the license at the end of the licensing process for the transaction, provided that you have disclosed complete and accurate details of your proposed use, no license is finally effective unless and until full payment is received from you (either by publisher or by CCC) as provided in CCC's Billing and Payment terms and conditions. If full payment is not received on a timely basis, then any license preliminarily granted shall be deemed automatically revoked and shall be void as if never granted. Further, in the event that you breach any of these terms and conditions or any of CCC's Billing and Payment terms and conditions, the license is automatically revoked and shall be void as if never granted. Use of materials as described in a revoked license, as well as any use of the materials beyond the scope of an unrevoked license, may constitute copyright infringement and publisher reserves the right to take any and all action to protect its copyright in the materials.

9. Warranties: Publisher makes no representations or warranties with respect to the licensed material.

10. Indemnity: You hereby indemnify and agree to hold harmless publisher and CCC, and their respective officers, directors, employees and agents, from and against any and all claims arising out of your use of the licensed material other than as specifically authorized pursuant to this license.

11. No Transfer of License: This license is personal to you and may not be sublicensed, assigned, or transferred by you to any other person without publisher's written permission.

12. No Amendment Except in Writing: This license may not be amended except in a writing signed by both parties (or, in the case of publisher, by CCC on publisher's behalf).

13. Objection to Contrary Terms: Publisher hereby objects to any terms contained in any purchase order, acknowledgment, check endorsement or other writing prepared by you, which terms are inconsistent with these terms and conditions or CCC's Billing and Payment terms and conditions. These terms and conditions, together with CCC's Billing and Payment terms and conditions (which are incorporated herein), comprise the entire agreement between you and publisher (and CCC) concerning this licensing transaction. In the event of any conflict between your obligations established by these terms and conditions and those established by CCC's Billing and Payment terms and conditions, these terms and conditions shall control.

14. Revocation: Elsevier or Copyright Clearance Center may deny the permissions described in this License at their sole discretion, for any reason or no reason, with a full refund payable to you. Notice of such denial will be made using the contact information provided by you. Failure to receive such notice will not alter or invalidate the denial. In no event will Elsevier or Copyright Clearance Center be responsible or liable for any costs, expenses or damage incurred by you as a result of a denial of your permission request, other than a refund of the amount(s) paid by you to Elsevier and/or Copyright Clearance Center for denied permissions.

LIMITED LICENSE

The following terms and conditions apply only to specific license types:

15. **Translation**: This permission is granted for non-exclusive world **English** rights only unless your license was granted for translation rights. If you licensed translation rights you may only translate this content into the languages you requested. A professional translator must perform all translations and reproduce the content word for word preserving the integrity of the article.

16. **Posting licensed content on any Website**: The following terms and conditions apply as follows: Licensing material from an Elsevier journal: All content posted to the web site must maintain the copyright information line on the bottom of each image; A hyper-text must be included to the Homepage of the journal from which you are licensing at http://www.sciencedirect.com/science/journal/xxxxx or the Elsevier homepage for books at http://www.elsevier.com; Central Storage: This license does not include permission for a scanned version of the material to be stored in a central repository such as that provided by Heron/XanEdu.

Licensing material from an Elsevier book: A hyper-text link must be included to the Elsevier homepage at http://www.elsevier.com . All content posted to the web site must maintain the copyright information line on the bottom of each image.

Posting licensed content on Electronic reserve: In addition to the above the following clauses are applicable: The web site must be password-protected and made available only to bona fide students registered on a relevant course. This permission is granted for 1 year only. You may obtain a new license for future website posting.

17. **For journal authors:** the following clauses are applicable in addition to the above:

Preprints:

A preprint is an author's own write-up of research results and analysis, it has not been peer-reviewed, nor has it had any other value added to it by a publisher (such as formatting, copyright, technical enhancement etc.).

Authors can share their preprints anywhere at any time. Preprints should not be added to or enhanced in any way in order to appear more like, or to substitute for, the final versions of articles however authors can update their preprints on arXiv or RePEc with their Accepted Author Manuscript (see below).

If accepted for publication, we encourage authors to link from the preprint to their formal publication via its DOI. Millions of researchers have access to the formal publications on ScienceDirect, and so links will help users to find, access, cite and use the best available version. Please note that Cell Press, The Lancet and some society-owned have different preprint policies. Information on these policies is available on the journal homepage.

Accepted Author Manuscripts: An accepted author manuscript is the manuscript of an article that has been accepted for publication and which typically includes author-incorporated changes suggested during submission, peer review and editor-author communications.

Authors can share their accepted author manuscript:

- immediately
  - via their non-commercial person homepage or blog
  - by updating a preprint in arXiv or RePEc with the accepted manuscript

- via their research institute or institutional repository for internal institutional uses or as part of an invitation-only research collaboration work-group
- directly by providing copies to their students or to research collaborators for their personal use
- for private scholarly sharing as part of an invitation-only work group on commercial sites with which Elsevier has an agreement

- After the embargo period
  - via non-commercial hosting platforms such as their institutional repository
  - via commercial sites with which Elsevier has an agreement

In all cases accepted manuscripts should:

- link to the formal publication via its DOI
- bear a CC-BY-NC-ND license - this is easy to do
- if aggregated with other manuscripts, for example in a repository or other site, be shared in alignment with our hosting policy not be added to or enhanced in any way to appear more like, or to substitute for, the published journal article.

Published journal article (JPA): A published journal article (PJA) is the definitive final record of published research that appears or will appear in the journal and embodies all value-adding publishing activities including peer review co-ordination, copy-editing, formatting, (if relevant) pagination and online enrichment.

Policies for sharing publishing journal articles differ for subscription and gold open access articles:

Subscription Articles: If you are an author, please share a link to your article rather than the full-text. Millions of researchers have access to the formal publications on ScienceDirect, and so links will help your users to find, access, cite, and use the best available version.

Theses and dissertations which contain embedded PJAs as part of the formal submission can be posted publicly by the awarding institution with DOI links back to the formal publications on ScienceDirect.

If you are affiliated with a library that subscribes to ScienceDirect you have additional private sharing rights for others' research accessed under that agreement. This includes use for classroom teaching and internal training at the institution (including use in course packs and courseware programs), and inclusion of the article for grant funding purposes.

Gold Open Access Articles: May be shared according to the author-selected end-user license and should contain a CrossMark logo, the end user license, and a DOI link to the formal publication on ScienceDirect.

Please refer to Elsevier's posting policy for further information.

18. **For book authors** the following clauses are applicable in addition to the above: Authors are permitted to place a brief summary of their work online only. You are not allowed to download and post the published electronic version of your chapter, nor may you scan the printed edition to create an electronic version. **Posting to a repository:** Authors are permitted to post a summary of their chapter only in their institution's repository.

19. **Thesis/Dissertation**: If your license is for use in a thesis/dissertation your thesis may be submitted to your institution in either print or electronic form. Should your thesis be

published commercially, please reapply for permission. These requirements include permission for the Library and Archives of Canada to supply single copies, on demand, of the complete thesis and include permission for Proquest/UMI to supply single copies, on demand, of the complete thesis. Should your thesis be published commercially, please reapply for permission. Theses and dissertations which contain embedded PJAs as part of the formal submission can be posted publicly by the awarding institution with DOI links back to the formal publications on ScienceDirect.

Elsevier Open Access Terms and Conditions

You can publish open access with Elsevier in hundreds of open access journals or in nearly 2000 established subscription journals that support open access publishing. Permitted third party re-use of these open access articles is defined by the author's choice of Creative Commons user license. See our open access license policy for more information.

Terms & Conditions applicable to all Open Access articles published with Elsevier:

Any reuse of the article must not represent the author as endorsing the adaptation of the article nor should the article be modified in such a way as to damage the author's honour or reputation. If any changes have been made, such changes must be clearly indicated.

The author(s) must be appropriately credited and we ask that you include the end user license and a DOI link to the formal publication on ScienceDirect.

If any part of the material to be used (for example, figures) has appeared in our publication with credit or acknowledgement to another source it is the responsibility of the user to ensure their reuse complies with the terms and conditions determined by the rights holder.

Additional Terms & Conditions applicable to each Creative Commons user license:

CC BY: The CC-BY license allows users to copy, to create extracts, abstracts and new works from the Article, to alter and revise the Article and to make commercial use of the Article (including reuse and/or resale of the Article by commercial entities), provided the user gives appropriate credit (with a link to the formal publication through the relevant DOI), provides a link to the license, indicates if changes were made and the licensor is not represented as endorsing the use made of the work. The full details of the license are available at http://creativecommons.org/licenses/by/4.0.

CC BY NC SA: The CC BY-NC-SA license allows users to copy, to create extracts, abstracts and new works from the Article, to alter and revise the Article, provided this is not done for commercial purposes, and that the user gives appropriate credit (with a link to the formal publication through the relevant DOI), provides a link to the license, indicates if changes were made and the licensor is not represented as endorsing the use made of the work. Further, any new works must be made available on the same conditions. The full details of the license are available at http://creativecommons.org/licenses/by-nc-sa/4.0.

CC BY NC ND: The CC BY-NC-ND license allows users to copy and distribute the Article, provided this is not done for commercial purposes and further does not permit distribution of the Article if it is changed or edited in any way, and provided the user gives appropriate credit (with a link to the formal publication through the relevant DOI),

provides a link to the license, and that the licensor is not represented as endorsing the use made of the work. The full details of the license are available at http://creativecommons.org/licenses/by-nc-nd/4.0. Any commercial reuse of Open Access articles published with a CC BY NC SA or CC BY NC ND license requires permission from Elsevier and will be subject to a fee.

Commercial reuse includes:

- Associating advertising with the full text of the Article
- Charging fees for document delivery or access
- Article aggregation
- Systematic distribution via e-mail lists or share buttons

Posting or linking by commercial companies for use by customers of those companies.

20. **Other Conditions**:

v1.10

Questions? customercare@copyright.com.

ELSEVIER LICENSE
TERMS AND CONDITIONS

Apr 25, 2024

This Agreement between Ms. POULAMI KARAN ("You") and Elsevier ("Elsevier") consists of your license details and the terms and conditions provided by Elsevier and Copyright Clearance Center.

License Number	5775970799405
License date	Apr 25, 2024
Licensed Content Publisher	Elsevier
Licensed Content Publication	International Journal of Hydrogen Energy
Licensed Content Title	Mesoporous silica supported Ni-based catalysts for methane dry reforming: A review of recent studies
Licensed Content Author	Bernard Chukwuemeka Ekeoma,Mohammad Yusuf,Khairiraihanna Johari,Bawadi Abdullah
Licensed Content Date	Dec 19, 2022
Licensed Content Volume	47
Licensed Content Issue	98
Licensed Content Pages	25
Start Page	41596
End Page	41620

Type of Use	reuse in a thesis/dissertation
Portion	figures/tables/illustrations
Number of figures/tables/illustrations	1
Format	both print and electronic
Are you the author of this Elsevier article?	No
Will you be translating?	No
Title of new work	Intensification and Optimization of Bio-glycerol conversion into Valuable Chemicals using Electromagnetic Radiation promoted Reactor
Institution name	Jadavpur University
Expected presentation date	May 2024
Portions	Fig.6. on page 41604
Requestor Location	Ms. POULAMI KARAN Jadavpur University Kolkata, West Bengal 700032 India Attn: Ms. POULAMI KARAN
Publisher Tax ID	GB 494 6272 12
Total	0.00 USD
Terms and Conditions	

INTRODUCTION

1. The publisher for this copyrighted material is Elsevier. By clicking "accept" in connection with completing this licensing transaction, you agree that the following terms and conditions apply to this transaction (along with the Billing and Payment terms and conditions established by Copyright Clearance Center, Inc. ("CCC"), at the time that you opened your RightsLink account and that are available at any time at https://myaccount.copyright.com).

GENERAL TERMS

2. Elsevier hereby grants you permission to reproduce the aforementioned material subject to the terms and conditions indicated.

3. Acknowledgement: If any part of the material to be used (for example, figures) has appeared in our publication with credit or acknowledgement to another source, permission must also be sought from that source. If such permission is not obtained then that material may not be included in your publication/copies. Suitable acknowledgement to the source must be made, either as a footnote or in a reference list at the end of your publication, as follows:

"Reprinted from Publication title, Vol /edition number, Author(s), Title of article / title of chapter, Pages No., Copyright (Year), with permission from Elsevier [OR APPLICABLE SOCIETY COPYRIGHT OWNER]." Also Lancet special credit - "Reprinted from The Lancet, Vol. number, Author(s), Title of article, Pages No., Copyright (Year), with permission from Elsevier."

4. Reproduction of this material is confined to the purpose and/or media for which permission is hereby given. The material may not be reproduced or used in any other way, including use in combination with an artificial intelligence tool (including to train an algorithm, test, process, analyse, generate output and/or develop any form of artificial intelligence tool), or to create any derivative work and/or service (including resulting from the use of artificial intelligence tools).

5. Altering/Modifying Material: Not Permitted. However figures and illustrations may be altered/adapted minimally to serve your work. Any other abbreviations, additions, deletions and/or any other alterations shall be made only with prior written authorization of Elsevier Ltd. (Please contact Elsevier's permissions helpdesk here). No modifications can be made to any Lancet figures/tables and they must be reproduced in full.

6. If the permission fee for the requested use of our material is waived in this instance, please be advised that your future requests for Elsevier materials may attract a fee.

7. Reservation of Rights: Publisher reserves all rights not specifically granted in the combination of (i) the license details provided by you and accepted in the course of this licensing transaction, (ii) these terms and conditions and (iii) CCC's Billing and Payment terms and conditions.

8. License Contingent Upon Payment: While you may exercise the rights licensed immediately upon issuance of the license at the end of the licensing process for the transaction, provided that you have disclosed complete and accurate details of your proposed use, no license is finally effective unless and until full payment is received from you (either by publisher or by CCC) as provided in CCC's Billing and Payment terms and conditions. If full payment is not received on a timely basis, then any license preliminarily granted shall be deemed automatically revoked and shall be void as if never granted. Further, in the event that you breach any of these terms and conditions or any of CCC's Billing and Payment terms and conditions, the license is automatically revoked and

shall be void as if never granted. Use of materials as described in a revoked license, as well as any use of the materials beyond the scope of an unrevoked license, may constitute copyright infringement and publisher reserves the right to take any and all action to protect its copyright in the materials.

9. Warranties: Publisher makes no representations or warranties with respect to the licensed material.

10. Indemnity: You hereby indemnify and agree to hold harmless publisher and CCC, and their respective officers, directors, employees and agents, from and against any and all claims arising out of your use of the licensed material other than as specifically authorized pursuant to this license.

11. No Transfer of License: This license is personal to you and may not be sublicensed, assigned, or transferred by you to any other person without publisher's written permission.

12. No Amendment Except in Writing: This license may not be amended except in a writing signed by both parties (or, in the case of publisher, by CCC on publisher's behalf).

13. Objection to Contrary Terms: Publisher hereby objects to any terms contained in any purchase order, acknowledgment, check endorsement or other writing prepared by you, which terms are inconsistent with these terms and conditions or CCC's Billing and Payment terms and conditions. These terms and conditions, together with CCC's Billing and Payment terms and conditions (which are incorporated herein), comprise the entire agreement between you and publisher (and CCC) concerning this licensing transaction. In the event of any conflict between your obligations established by these terms and conditions and those established by CCC's Billing and Payment terms and conditions, these terms and conditions shall control.

14. Revocation: Elsevier or Copyright Clearance Center may deny the permissions described in this License at their sole discretion, for any reason or no reason, with a full refund payable to you. Notice of such denial will be made using the contact information provided by you. Failure to receive such notice will not alter or invalidate the denial. In no event will Elsevier or Copyright Clearance Center be responsible or liable for any costs, expenses or damage incurred by you as a result of a denial of your permission request, other than a refund of the amount(s) paid by you to Elsevier and/or Copyright Clearance Center for denied permissions.

LIMITED LICENSE

The following terms and conditions apply only to specific license types:

15. **Translation**: This permission is granted for non-exclusive world **English** rights only unless your license was granted for translation rights. If you licensed translation rights you may only translate this content into the languages you requested. A professional translator must perform all translations and reproduce the content word for word preserving the integrity of the article.

16. **Posting licensed content on any Website**: The following terms and conditions apply as follows: Licensing material from an Elsevier journal: All content posted to the web site must maintain the copyright information line on the bottom of each image; A hyper-text must be included to the Homepage of the journal from which you are licensing at http://www.sciencedirect.com/science/journal/xxxxx or the Elsevier homepage for books at http://www.elsevier.com; Central Storage: This license does not include permission for

a scanned version of the material to be stored in a central repository such as that provided by Heron/XanEdu.

Licensing material from an Elsevier book: A hyper-text link must be included to the Elsevier homepage at http://www.elsevier.com . All content posted to the web site must maintain the copyright information line on the bottom of each image.

Posting licensed content on Electronic reserve: In addition to the above the following clauses are applicable: The web site must be password-protected and made available only to bona fide students registered on a relevant course. This permission is granted for 1 year only. You may obtain a new license for future website posting.

17. **For journal authors:** the following clauses are applicable in addition to the above:

Preprints:

A preprint is an author's own write-up of research results and analysis, it has not been peer-reviewed, nor has it had any other value added to it by a publisher (such as formatting, copyright, technical enhancement etc.).

Authors can share their preprints anywhere at any time. Preprints should not be added to or enhanced in any way in order to appear more like, or to substitute for, the final versions of articles however authors can update their preprints on arXiv or RePEc with their Accepted Author Manuscript (see below).

If accepted for publication, we encourage authors to link from the preprint to their formal publication via its DOI. Millions of researchers have access to the formal publications on ScienceDirect, and so links will help users to find, access, cite and use the best available version. Please note that Cell Press, The Lancet and some society-owned have different preprint policies. Information on these policies is available on the journal homepage.

Accepted Author Manuscripts: An accepted author manuscript is the manuscript of an article that has been accepted for publication and which typically includes author-incorporated changes suggested during submission, peer review and editor-author communications.

Authors can share their accepted author manuscript:

- immediately
  - via their non-commercial person homepage or blog
  - by updating a preprint in arXiv or RePEc with the accepted manuscript
  - via their research institute or institutional repository for internal institutional uses or as part of an invitation-only research collaboration work-group
  - directly by providing copies to their students or to research collaborators for their personal use
  - for private scholarly sharing as part of an invitation-only work group on commercial sites with which Elsevier has an agreement
- After the embargo period
  - via non-commercial hosting platforms such as their institutional repository
  - via commercial sites with which Elsevier has an agreement

In all cases accepted manuscripts should:

- link to the formal publication via its DOI

- bear a CC-BY-NC-ND license - this is easy to do
- if aggregated with other manuscripts, for example in a repository or other site, be shared in alignment with our hosting policy not be added to or enhanced in any way to appear more like, or to substitute for, the published journal article.

Published journal article (JPA): A published journal article (PJA) is the definitive final record of published research that appears or will appear in the journal and embodies all value-adding publishing activities including peer review co-ordination, copy-editing, formatting, (if relevant) pagination and online enrichment.

Policies for sharing publishing journal articles differ for subscription and gold open access articles:

Subscription Articles: If you are an author, please share a link to your article rather than the full-text. Millions of researchers have access to the formal publications on ScienceDirect, and so links will help your users to find, access, cite, and use the best available version.

Theses and dissertations which contain embedded PJAs as part of the formal submission can be posted publicly by the awarding institution with DOI links back to the formal publications on ScienceDirect.

If you are affiliated with a library that subscribes to ScienceDirect you have additional private sharing rights for others' research accessed under that agreement. This includes use for classroom teaching and internal training at the institution (including use in course packs and courseware programs), and inclusion of the article for grant funding purposes.

Gold Open Access Articles: May be shared according to the author-selected end-user license and should contain a CrossMark logo, the end user license, and a DOI link to the formal publication on ScienceDirect.

Please refer to Elsevier's posting policy for further information.

18. **For book authors** the following clauses are applicable in addition to the above: Authors are permitted to place a brief summary of their work online only. You are not allowed to download and post the published electronic version of your chapter, nor may you scan the printed edition to create an electronic version. **Posting to a repository:** Authors are permitted to post a summary of their chapter only in their institution's repository.

19. **Thesis/Dissertation**: If your license is for use in a thesis/dissertation your thesis may be submitted to your institution in either print or electronic form. Should your thesis be published commercially, please reapply for permission. These requirements include permission for the Library and Archives of Canada to supply single copies, on demand, of the complete thesis and include permission for Proquest/UMI to supply single copies, on demand, of the complete thesis. Should your thesis be published commercially, please reapply for permission. Theses and dissertations which contain embedded PJAs as part of the formal submission can be posted publicly by the awarding institution with DOI links back to the formal publications on ScienceDirect.

Elsevier Open Access Terms and Conditions

You can publish open access with Elsevier in hundreds of open access journals or in nearly 2000 established subscription journals that support open access publishing. Permitted third party re-use of these open access articles is defined by the author's choice of Creative Commons user license. See our open access license policy for more information.

Terms & Conditions applicable to all Open Access articles published with Elsevier:

Any reuse of the article must not represent the author as endorsing the adaptation of the article nor should the article be modified in such a way as to damage the author's honour or reputation. If any changes have been made, such changes must be clearly indicated.

The author(s) must be appropriately credited and we ask that you include the end user license and a DOI link to the formal publication on ScienceDirect.

If any part of the material to be used (for example, figures) has appeared in our publication with credit or acknowledgement to another source it is the responsibility of the user to ensure their reuse complies with the terms and conditions determined by the rights holder.

Additional Terms & Conditions applicable to each Creative Commons user license:

CC BY: The CC-BY license allows users to copy, to create extracts, abstracts and new works from the Article, to alter and revise the Article and to make commercial use of the Article (including reuse and/or resale of the Article by commercial entities), provided the user gives appropriate credit (with a link to the formal publication through the relevant DOI), provides a link to the license, indicates if changes were made and the licensor is not represented as endorsing the use made of the work. The full details of the license are available at http://creativecommons.org/licenses/by/4.0.

CC BY NC SA: The CC BY-NC-SA license allows users to copy, to create extracts, abstracts and new works from the Article, to alter and revise the Article, provided this is not done for commercial purposes, and that the user gives appropriate credit (with a link to the formal publication through the relevant DOI), provides a link to the license, indicates if changes were made and the licensor is not represented as endorsing the use made of the work. Further, any new works must be made available on the same conditions. The full details of the license are available at http://creativecommons.org/licenses/by-nc-sa/4.0.

CC BY NC ND: The CC BY-NC-ND license allows users to copy and distribute the Article, provided this is not done for commercial purposes and further does not permit distribution of the Article if it is changed or edited in any way, and provided the user gives appropriate credit (with a link to the formal publication through the relevant DOI), provides a link to the license, and that the licensor is not represented as endorsing the use made of the work. The full details of the license are available at http://creativecommons.org/licenses/by-nc-nd/4.0. Any commercial reuse of Open Access articles published with a CC BY NC SA or CC BY NC ND license requires permission from Elsevier and will be subject to a fee.

Commercial reuse includes:

- Associating advertising with the full text of the Article
- Charging fees for document delivery or access
- Article aggregation
- Systematic distribution via e-mail lists or share buttons

Posting or linking by commercial companies for use by customers of those companies.

20. **Other Conditions**:

v1.10

Questions? customercare@copyright.com.

ELSEVIER LICENSE
TERMS AND CONDITIONS

Apr 25, 2024

This Agreement between Ms. POULAMI KARAN ("You") and Elsevier ("Elsevier") consists of your license details and the terms and conditions provided by Elsevier and Copyright Clearance Center.

License Number	5775991460734
License date	Apr 25, 2024
Licensed Content Publisher	Elsevier
Licensed Content Publication	Elsevier Books
Licensed Content Title	Handbook of Chitin and Chitosan
Licensed Content Author	Suneeta Kumari,Rupak Kishor
Licensed Content Date	Jan 1, 2020
Licensed Content Pages	33
Start Page	1
End Page	33
Type of Use	reuse in a thesis/dissertation
Portion	figures/tables/illustrations
Number of	1

figures/tables/illustrations

Format	both print and electronic
Are you the author of this Elsevier chapter?	No
Will you be translating?	No
Title of new work	Intensification and Optimization of Bio-glycerol conversion into Valuable Chemicals using Electromagnetic Radiation promoted Reactor
Institution name	Jadavpur University
Expected presentation date	May 2024
Portions	Figue 1.1 on page 3
Requestor Location	Ms. POULAMI KARAN Jadavpur University Kolkata, West Bengal 700032 India Attn: Ms. POULAMI KARAN
Publisher Tax ID	GB 494 6272 12
Total	0.00 USD

Terms and Conditions

INTRODUCTION

1. The publisher for this copyrighted material is Elsevier. By clicking "accept" in connection with completing this licensing transaction, you agree that the following terms and conditions apply to this transaction (along with the Billing and Payment terms and conditions established by Copyright Clearance Center, Inc. ("CCC"), at the time that you opened your RightsLink account and that are available at any time at https://myaccount.copyright.com).

GENERAL TERMS

2. Elsevier hereby grants you permission to reproduce the aforementioned material subject to the terms and conditions indicated.

3. Acknowledgement: If any part of the material to be used (for example, figures) has appeared in our publication with credit or acknowledgement to another source, permission must also be sought from that source. If such permission is not obtained then that material may not be included in your publication/copies. Suitable acknowledgement to the source must be made, either as a footnote or in a reference list at the end of your publication, as follows:

"Reprinted from Publication title, Vol /edition number, Author(s), Title of article / title of chapter, Pages No., Copyright (Year), with permission from Elsevier [OR APPLICABLE SOCIETY COPYRIGHT OWNER]." Also Lancet special credit - "Reprinted from The Lancet, Vol. number, Author(s), Title of article, Pages No., Copyright (Year), with permission from Elsevier."

4. Reproduction of this material is confined to the purpose and/or media for which permission is hereby given. The material may not be reproduced or used in any other way, including use in combination with an artificial intelligence tool (including to train an algorithm, test, process, analyse, generate output and/or develop any form of artificial intelligence tool), or to create any derivative work and/or service (including resulting from the use of artificial intelligence tools).

5. Altering/Modifying Material: Not Permitted. However figures and illustrations may be altered/adapted minimally to serve your work. Any other abbreviations, additions, deletions and/or any other alterations shall be made only with prior written authorization of Elsevier Ltd. (Please contact Elsevier's permissions helpdesk here). No modifications can be made to any Lancet figures/tables and they must be reproduced in full.

6. If the permission fee for the requested use of our material is waived in this instance, please be advised that your future requests for Elsevier materials may attract a fee.

7. Reservation of Rights: Publisher reserves all rights not specifically granted in the combination of (i) the license details provided by you and accepted in the course of this licensing transaction, (ii) these terms and conditions and (iii) CCC's Billing and Payment terms and conditions.

8. License Contingent Upon Payment: While you may exercise the rights licensed immediately upon issuance of the license at the end of the licensing process for the transaction, provided that you have disclosed complete and accurate details of your proposed use, no license is finally effective unless and until full payment is received from you (either by publisher or by CCC) as provided in CCC's Billing and Payment terms and conditions. If full payment is not received on a timely basis, then any license preliminarily granted shall be deemed automatically revoked and shall be void as if never granted. Further, in the event that you breach any of these terms and conditions or any of CCC's Billing and Payment terms and conditions, the license is automatically revoked and shall be void as if never granted. Use of materials as described in a revoked license, as well as any use of the materials beyond the scope of an unrevoked license, may constitute copyright infringement and publisher reserves the right to take any and all action to protect its copyright in the materials.

9. Warranties: Publisher makes no representations or warranties with respect to the licensed material.

10. Indemnity: You hereby indemnify and agree to hold harmless publisher and CCC, and their respective officers, directors, employees and agents, from and against any and all claims arising out of your use of the licensed material other than as specifically authorized pursuant to this license.

11. No Transfer of License: This license is personal to you and may not be sublicensed, assigned, or transferred by you to any other person without publisher's written permission.

12. No Amendment Except in Writing: This license may not be amended except in a writing signed by both parties (or, in the case of publisher, by CCC on publisher's behalf).

13. Objection to Contrary Terms: Publisher hereby objects to any terms contained in any purchase order, acknowledgment, check endorsement or other writing prepared by you, which terms are inconsistent with these terms and conditions or CCC's Billing and Payment terms and conditions. These terms and conditions, together with CCC's Billing and Payment terms and conditions (which are incorporated herein), comprise the entire agreement between you and publisher (and CCC) concerning this licensing transaction. In the event of any conflict between your obligations established by these terms and conditions and those established by CCC's Billing and Payment terms and conditions, these terms and conditions shall control.

14. Revocation: Elsevier or Copyright Clearance Center may deny the permissions described in this License at their sole discretion, for any reason or no reason, with a full refund payable to you. Notice of such denial will be made using the contact information provided by you. Failure to receive such notice will not alter or invalidate the denial. In no event will Elsevier or Copyright Clearance Center be responsible or liable for any costs, expenses or damage incurred by you as a result of a denial of your permission request, other than a refund of the amount(s) paid by you to Elsevier and/or Copyright Clearance Center for denied permissions.

LIMITED LICENSE

The following terms and conditions apply only to specific license types:

15. **Translation**: This permission is granted for non-exclusive world **English** rights only unless your license was granted for translation rights. If you licensed translation rights you may only translate this content into the languages you requested. A professional translator must perform all translations and reproduce the content word for word preserving the integrity of the article.

16. **Posting licensed content on any Website**: The following terms and conditions apply as follows: Licensing material from an Elsevier journal: All content posted to the web site must maintain the copyright information line on the bottom of each image; A hyper-text must be included to the Homepage of the journal from which you are licensing at http://www.sciencedirect.com/science/journal/xxxxx or the Elsevier homepage for books at http://www.elsevier.com; Central Storage: This license does not include permission for a scanned version of the material to be stored in a central repository such as that provided by Heron/XanEdu.

Licensing material from an Elsevier book: A hyper-text link must be included to the Elsevier homepage at http://www.elsevier.com . All content posted to the web site must maintain the copyright information line on the bottom of each image.

Posting licensed content on Electronic reserve: In addition to the above the following

clauses are applicable: The web site must be password-protected and made available only to bona fide students registered on a relevant course. This permission is granted for 1 year only. You may obtain a new license for future website posting.

17. **For journal authors:** the following clauses are applicable in addition to the above:

Preprints:

A preprint is an author's own write-up of research results and analysis, it has not been peer-reviewed, nor has it had any other value added to it by a publisher (such as formatting, copyright, technical enhancement etc.).

Authors can share their preprints anywhere at any time. Preprints should not be added to or enhanced in any way in order to appear more like, or to substitute for, the final versions of articles however authors can update their preprints on arXiv or RePEc with their Accepted Author Manuscript (see below).

If accepted for publication, we encourage authors to link from the preprint to their formal publication via its DOI. Millions of researchers have access to the formal publications on ScienceDirect, and so links will help users to find, access, cite and use the best available version. Please note that Cell Press, The Lancet and some society-owned have different preprint policies. Information on these policies is available on the journal homepage.

Accepted Author Manuscripts: An accepted author manuscript is the manuscript of an article that has been accepted for publication and which typically includes author-incorporated changes suggested during submission, peer review and editor-author communications.

Authors can share their accepted author manuscript:

- immediately
    - via their non-commercial person homepage or blog
    - by updating a preprint in arXiv or RePEc with the accepted manuscript
    - via their research institute or institutional repository for internal institutional uses or as part of an invitation-only research collaboration work-group
    - directly by providing copies to their students or to research collaborators for their personal use
    - for private scholarly sharing as part of an invitation-only work group on commercial sites with which Elsevier has an agreement
- After the embargo period
    - via non-commercial hosting platforms such as their institutional repository
    - via commercial sites with which Elsevier has an agreement

In all cases accepted manuscripts should:

- link to the formal publication via its DOI
- bear a CC-BY-NC-ND license - this is easy to do
- if aggregated with other manuscripts, for example in a repository or other site, be shared in alignment with our hosting policy not be added to or enhanced in any way to appear more like, or to substitute for, the published journal article.

Published journal article (JPA): A published journal article (PJA) is the definitive final record of published research that appears or will appear in the journal and embodies all value-adding publishing activities including peer review co-ordination, copy-editing, formatting, (if relevant) pagination and online enrichment.

Policies for sharing publishing journal articles differ for subscription and gold open access articles:

Subscription Articles: If you are an author, please share a link to your article rather than the full-text. Millions of researchers have access to the formal publications on ScienceDirect, and so links will help your users to find, access, cite, and use the best available version.

Theses and dissertations which contain embedded PJAs as part of the formal submission can be posted publicly by the awarding institution with DOI links back to the formal publications on ScienceDirect.

If you are affiliated with a library that subscribes to ScienceDirect you have additional private sharing rights for others' research accessed under that agreement. This includes use for classroom teaching and internal training at the institution (including use in course packs and courseware programs), and inclusion of the article for grant funding purposes.

Gold Open Access Articles: May be shared according to the author-selected end-user license and should contain a CrossMark logo, the end user license, and a DOI link to the formal publication on ScienceDirect.

Please refer to Elsevier's posting policy for further information.

18. **For book authors** the following clauses are applicable in addition to the above: Authors are permitted to place a brief summary of their work online only. You are not allowed to download and post the published electronic version of your chapter, nor may you scan the printed edition to create an electronic version. **Posting to a repository:** Authors are permitted to post a summary of their chapter only in their institution's repository.

19. **Thesis/Dissertation**: If your license is for use in a thesis/dissertation your thesis may be submitted to your institution in either print or electronic form. Should your thesis be published commercially, please reapply for permission. These requirements include permission for the Library and Archives of Canada to supply single copies, on demand, of the complete thesis and include permission for Proquest/UMI to supply single copies, on demand, of the complete thesis. Should your thesis be published commercially, please reapply for permission. Theses and dissertations which contain embedded PJAs as part of the formal submission can be posted publicly by the awarding institution with DOI links back to the formal publications on ScienceDirect.

Elsevier Open Access Terms and Conditions

You can publish open access with Elsevier in hundreds of open access journals or in nearly 2000 established subscription journals that support open access publishing. Permitted third party re-use of these open access articles is defined by the author's choice of Creative Commons user license. See our open access license policy for more information.

Terms & Conditions applicable to all Open Access articles published with Elsevier:

Any reuse of the article must not represent the author as endorsing the adaptation of the article nor should the article be modified in such a way as to damage the author's honour or reputation. If any changes have been made, such changes must be clearly indicated.

The author(s) must be appropriately credited and we ask that you include the end user license and a DOI link to the formal publication on ScienceDirect.

If any part of the material to be used (for example, figures) has appeared in our publication with credit or acknowledgement to another source it is the responsibility of the user to ensure their reuse complies with the terms and conditions determined by the rights holder.

Additional Terms & Conditions applicable to each Creative Commons user license:

CC BY: The CC-BY license allows users to copy, to create extracts, abstracts and new works from the Article, to alter and revise the Article and to make commercial use of the Article (including reuse and/or resale of the Article by commercial entities), provided the user gives appropriate credit (with a link to the formal publication through the relevant DOI), provides a link to the license, indicates if changes were made and the licensor is not represented as endorsing the use made of the work. The full details of the license are available at http://creativecommons.org/licenses/by/4.0.

CC BY NC SA: The CC BY-NC-SA license allows users to copy, to create extracts, abstracts and new works from the Article, to alter and revise the Article, provided this is not done for commercial purposes, and that the user gives appropriate credit (with a link to the formal publication through the relevant DOI), provides a link to the license, indicates if changes were made and the licensor is not represented as endorsing the use made of the work. Further, any new works must be made available on the same conditions. The full details of the license are available at http://creativecommons.org/licenses/by-nc-sa/4.0.

CC BY NC ND: The CC BY-NC-ND license allows users to copy and distribute the Article, provided this is not done for commercial purposes and further does not permit distribution of the Article if it is changed or edited in any way, and provided the user gives appropriate credit (with a link to the formal publication through the relevant DOI), provides a link to the license, and that the licensor is not represented as endorsing the use made of the work. The full details of the license are available at http://creativecommons.org/licenses/by-nc-nd/4.0. Any commercial reuse of Open Access articles published with a CC BY NC SA or CC BY NC ND license requires permission from Elsevier and will be subject to a fee.

Commercial reuse includes:

- Associating advertising with the full text of the Article
- Charging fees for document delivery or access
- Article aggregation
- Systematic distribution via e-mail lists or share buttons

Posting or linking by commercial companies for use by customers of those companies.

20. **Other Conditions**:

v1.10

Questions? customercare@copyright.com.

RightsLink

PK

Exploring the Promotional Effects of K, Sr, and Mg on the Catalytic Stability of Red Mud for the Synthesis of Glycerol Carbonate from Renewable Glycerol

Author: Bikashbindu Das, Kaustubha Mohanty
Publication: Industrial & Engineering Chemistry Research
Publisher: American Chemical Society
Date: Sep 1, 2019

PERMISSION/LICENSE IS GRANTED FOR YOUR ORDER AT NO CHARGE

This type of permission/license, instead of the standard Terms and Conditions, is sent to you because no fee is being charged for your order. Please note the following:

- Permission is granted for your request in both print and electronic formats, and translations.
- If figures and/or tables were requested, they may be adapted or used in part.
- Please print this page for your records and send a copy of it to your publisher/graduate school.
- Appropriate credit for the requested material should be given as follows: "Reprinted (adapted) with permission from {COMPLETE REFERENCE CITATION}. Copyright {YEAR} American Chemical Society." Insert appropriate information in place of the capitalized words.
- One-time permission is granted only for the use specified in your RightsLink request. No additional uses are granted (such as derivative works or other editions). For any uses, please submit a new request.

If credit is given to another source for the material you requested from RightsLink, permission must be obtained from that source.

BACK CLOSE WINDOW

ELSEVIER LICENSE
TERMS AND CONDITIONS

Apr 25, 2024

This Agreement between Ms. POULAMI KARAN ("You") and Elsevier ("Elsevier") consists of your license details and the terms and conditions provided by Elsevier and Copyright Clearance Center.

License Number	5775990010807
License date	Apr 25, 2024
Licensed Content Publisher	Elsevier
Licensed Content Publication	Chemical Engineering Science
Licensed Content Title	Production of glycerol carbonate from carboxylation of glycerol with CO2 using ZIF-67 as a catalyst
Licensed Content Author	Chechia Hu,Masaaki Yoshida,Ho-Cheng Chen,Shun Tsunekawa,Yi-Feng Lin,Jun-Hao Huang
Licensed Content Date	May 18, 2021
Licensed Content Volume	235
Licensed Content Issue	n/a
Licensed Content Pages	1
Start Page	116451
End Page	0

Type of Use	reuse in a thesis/dissertation
Portion	figures/tables/illustrations
Number of figures/tables/illustrations	1
Format	both print and electronic
Are you the author of this Elsevier article?	No
Will you be translating?	No
Title of new work	Intensification and Optimization of Bio-glycerol conversion into Valuable Chemicals using Electromagnetic Radiation promoted Reactor
Institution name	Jadavpur University
Expected presentation date	May 2024
Portions	Fig. 3 (a-d), Fig.5d on page 5 and 6
Requestor Location	Ms. POULAMI KARAN Jadavpur University Kolkata, West Bengal 700032 India Attn: Ms. POULAMI KARAN
Publisher Tax ID	GB 494 6272 12
Total	0.00 USD
Terms and Conditions	

INTRODUCTION

1. The publisher for this copyrighted material is Elsevier. By clicking "accept" in connection with completing this licensing transaction, you agree that the following terms and conditions apply to this transaction (along with the Billing and Payment terms and conditions established by Copyright Clearance Center, Inc. ("CCC"), at the time that you opened your RightsLink account and that are available at any time at https://myaccount.copyright.com).

GENERAL TERMS

2. Elsevier hereby grants you permission to reproduce the aforementioned material subject to the terms and conditions indicated.

3. Acknowledgement: If any part of the material to be used (for example, figures) has appeared in our publication with credit or acknowledgement to another source, permission must also be sought from that source. If such permission is not obtained then that material may not be included in your publication/copies. Suitable acknowledgement to the source must be made, either as a footnote or in a reference list at the end of your publication, as follows:

"Reprinted from Publication title, Vol /edition number, Author(s), Title of article / title of chapter, Pages No., Copyright (Year), with permission from Elsevier [OR APPLICABLE SOCIETY COPYRIGHT OWNER]." Also Lancet special credit - "Reprinted from The Lancet, Vol. number, Author(s), Title of article, Pages No., Copyright (Year), with permission from Elsevier."

4. Reproduction of this material is confined to the purpose and/or media for which permission is hereby given. The material may not be reproduced or used in any other way, including use in combination with an artificial intelligence tool (including to train an algorithm, test, process, analyse, generate output and/or develop any form of artificial intelligence tool), or to create any derivative work and/or service (including resulting from the use of artificial intelligence tools).

5. Altering/Modifying Material: Not Permitted. However figures and illustrations may be altered/adapted minimally to serve your work. Any other abbreviations, additions, deletions and/or any other alterations shall be made only with prior written authorization of Elsevier Ltd. (Please contact Elsevier's permissions helpdesk here). No modifications can be made to any Lancet figures/tables and they must be reproduced in full.

6. If the permission fee for the requested use of our material is waived in this instance, please be advised that your future requests for Elsevier materials may attract a fee.

7. Reservation of Rights: Publisher reserves all rights not specifically granted in the combination of (i) the license details provided by you and accepted in the course of this licensing transaction, (ii) these terms and conditions and (iii) CCC's Billing and Payment terms and conditions.

8. License Contingent Upon Payment: While you may exercise the rights licensed immediately upon issuance of the license at the end of the licensing process for the transaction, provided that you have disclosed complete and accurate details of your proposed use, no license is finally effective unless and until full payment is received from you (either by publisher or by CCC) as provided in CCC's Billing and Payment terms and conditions. If full payment is not received on a timely basis, then any license preliminarily granted shall be deemed automatically revoked and shall be void as if never granted. Further, in the event that you breach any of these terms and conditions or any of CCC's Billing and Payment terms and conditions, the license is automatically revoked and

shall be void as if never granted. Use of materials as described in a revoked license, as well as any use of the materials beyond the scope of an unrevoked license, may constitute copyright infringement and publisher reserves the right to take any and all action to protect its copyright in the materials.

9. Warranties: Publisher makes no representations or warranties with respect to the licensed material.

10. Indemnity: You hereby indemnify and agree to hold harmless publisher and CCC, and their respective officers, directors, employees and agents, from and against any and all claims arising out of your use of the licensed material other than as specifically authorized pursuant to this license.

11. No Transfer of License: This license is personal to you and may not be sublicensed, assigned, or transferred by you to any other person without publisher's written permission.

12. No Amendment Except in Writing: This license may not be amended except in a writing signed by both parties (or, in the case of publisher, by CCC on publisher's behalf).

13. Objection to Contrary Terms: Publisher hereby objects to any terms contained in any purchase order, acknowledgment, check endorsement or other writing prepared by you, which terms are inconsistent with these terms and conditions or CCC's Billing and Payment terms and conditions. These terms and conditions, together with CCC's Billing and Payment terms and conditions (which are incorporated herein), comprise the entire agreement between you and publisher (and CCC) concerning this licensing transaction. In the event of any conflict between your obligations established by these terms and conditions and those established by CCC's Billing and Payment terms and conditions, these terms and conditions shall control.

14. Revocation: Elsevier or Copyright Clearance Center may deny the permissions described in this License at their sole discretion, for any reason or no reason, with a full refund payable to you. Notice of such denial will be made using the contact information provided by you. Failure to receive such notice will not alter or invalidate the denial. In no event will Elsevier or Copyright Clearance Center be responsible or liable for any costs, expenses or damage incurred by you as a result of a denial of your permission request, other than a refund of the amount(s) paid by you to Elsevier and/or Copyright Clearance Center for denied permissions.

LIMITED LICENSE

The following terms and conditions apply only to specific license types:

15. **Translation**: This permission is granted for non-exclusive world **English** rights only unless your license was granted for translation rights. If you licensed translation rights you may only translate this content into the languages you requested. A professional translator must perform all translations and reproduce the content word for word preserving the integrity of the article.

16. **Posting licensed content on any Website**: The following terms and conditions apply as follows: Licensing material from an Elsevier journal: All content posted to the web site must maintain the copyright information line on the bottom of each image; A hyper-text must be included to the Homepage of the journal from which you are licensing at http://www.sciencedirect.com/science/journal/xxxxx or the Elsevier homepage for books at http://www.elsevier.com; Central Storage: This license does not include permission for

a scanned version of the material to be stored in a central repository such as that provided by Heron/XanEdu.

Licensing material from an Elsevier book: A hyper-text link must be included to the Elsevier homepage at http://www.elsevier.com . All content posted to the web site must maintain the copyright information line on the bottom of each image.

Posting licensed content on Electronic reserve: In addition to the above the following clauses are applicable: The web site must be password-protected and made available only to bona fide students registered on a relevant course. This permission is granted for 1 year only. You may obtain a new license for future website posting.

17. **For journal authors:** the following clauses are applicable in addition to the above:

Preprints:

A preprint is an author's own write-up of research results and analysis, it has not been peer-reviewed, nor has it had any other value added to it by a publisher (such as formatting, copyright, technical enhancement etc.).

Authors can share their preprints anywhere at any time. Preprints should not be added to or enhanced in any way in order to appear more like, or to substitute for, the final versions of articles however authors can update their preprints on arXiv or RePEc with their Accepted Author Manuscript (see below).

If accepted for publication, we encourage authors to link from the preprint to their formal publication via its DOI. Millions of researchers have access to the formal publications on ScienceDirect, and so links will help users to find, access, cite and use the best available version. Please note that Cell Press, The Lancet and some society-owned have different preprint policies. Information on these policies is available on the journal homepage.

Accepted Author Manuscripts: An accepted author manuscript is the manuscript of an article that has been accepted for publication and which typically includes author-incorporated changes suggested during submission, peer review and editor-author communications.

Authors can share their accepted author manuscript:

- immediately
  - via their non-commercial person homepage or blog
  - by updating a preprint in arXiv or RePEc with the accepted manuscript
  - via their research institute or institutional repository for internal institutional uses or as part of an invitation-only research collaboration work-group
  - directly by providing copies to their students or to research collaborators for their personal use
  - for private scholarly sharing as part of an invitation-only work group on commercial sites with which Elsevier has an agreement
- After the embargo period
  - via non-commercial hosting platforms such as their institutional repository
  - via commercial sites with which Elsevier has an agreement

In all cases accepted manuscripts should:

- link to the formal publication via its DOI

- bear a CC-BY-NC-ND license - this is easy to do
- if aggregated with other manuscripts, for example in a repository or other site, be shared in alignment with our hosting policy not be added to or enhanced in any way to appear more like, or to substitute for, the published journal article.

Published journal article (JPA): A published journal article (PJA) is the definitive final record of published research that appears or will appear in the journal and embodies all value-adding publishing activities including peer review co-ordination, copy-editing, formatting, (if relevant) pagination and online enrichment.

Policies for sharing publishing journal articles differ for subscription and gold open access articles:

Subscription Articles: If you are an author, please share a link to your article rather than the full-text. Millions of researchers have access to the formal publications on ScienceDirect, and so links will help your users to find, access, cite, and use the best available version.

Theses and dissertations which contain embedded PJAs as part of the formal submission can be posted publicly by the awarding institution with DOI links back to the formal publications on ScienceDirect.

If you are affiliated with a library that subscribes to ScienceDirect you have additional private sharing rights for others' research accessed under that agreement. This includes use for classroom teaching and internal training at the institution (including use in course packs and courseware programs), and inclusion of the article for grant funding purposes.

Gold Open Access Articles: May be shared according to the author-selected end-user license and should contain a CrossMark logo, the end user license, and a DOI link to the formal publication on ScienceDirect.

Please refer to Elsevier's posting policy for further information.

18. **For book authors** the following clauses are applicable in addition to the above: Authors are permitted to place a brief summary of their work online only. You are not allowed to download and post the published electronic version of your chapter, nor may you scan the printed edition to create an electronic version. **Posting to a repository:** Authors are permitted to post a summary of their chapter only in their institution's repository.

19. **Thesis/Dissertation**: If your license is for use in a thesis/dissertation your thesis may be submitted to your institution in either print or electronic form. Should your thesis be published commercially, please reapply for permission. These requirements include permission for the Library and Archives of Canada to supply single copies, on demand, of the complete thesis and include permission for Proquest/UMI to supply single copies, on demand, of the complete thesis. Should your thesis be published commercially, please reapply for permission. Theses and dissertations which contain embedded PJAs as part of the formal submission can be posted publicly by the awarding institution with DOI links back to the formal publications on ScienceDirect.

Elsevier Open Access Terms and Conditions

You can publish open access with Elsevier in hundreds of open access journals or in nearly 2000 established subscription journals that support open access publishing. Permitted third party re-use of these open access articles is defined by the author's choice of Creative Commons user license. See our open access license policy for more information.

Terms & Conditions applicable to all Open Access articles published with Elsevier:

Any reuse of the article must not represent the author as endorsing the adaptation of the article nor should the article be modified in such a way as to damage the author's honour or reputation. If any changes have been made, such changes must be clearly indicated.

The author(s) must be appropriately credited and we ask that you include the end user license and a DOI link to the formal publication on ScienceDirect.

If any part of the material to be used (for example, figures) has appeared in our publication with credit or acknowledgement to another source it is the responsibility of the user to ensure their reuse complies with the terms and conditions determined by the rights holder.

Additional Terms & Conditions applicable to each Creative Commons user license:

CC BY: The CC-BY license allows users to copy, to create extracts, abstracts and new works from the Article, to alter and revise the Article and to make commercial use of the Article (including reuse and/or resale of the Article by commercial entities), provided the user gives appropriate credit (with a link to the formal publication through the relevant DOI), provides a link to the license, indicates if changes were made and the licensor is not represented as endorsing the use made of the work. The full details of the license are available at http://creativecommons.org/licenses/by/4.0.

CC BY NC SA: The CC BY-NC-SA license allows users to copy, to create extracts, abstracts and new works from the Article, to alter and revise the Article, provided this is not done for commercial purposes, and that the user gives appropriate credit (with a link to the formal publication through the relevant DOI), provides a link to the license, indicates if changes were made and the licensor is not represented as endorsing the use made of the work. Further, any new works must be made available on the same conditions. The full details of the license are available at http://creativecommons.org/licenses/by-nc-sa/4.0.

CC BY NC ND: The CC BY-NC-ND license allows users to copy and distribute the Article, provided this is not done for commercial purposes and further does not permit distribution of the Article if it is changed or edited in any way, and provided the user gives appropriate credit (with a link to the formal publication through the relevant DOI), provides a link to the license, and that the licensor is not represented as endorsing the use made of the work. The full details of the license are available at http://creativecommons.org/licenses/by-nc-nd/4.0. Any commercial reuse of Open Access articles published with a CC BY NC SA or CC BY NC ND license requires permission from Elsevier and will be subject to a fee.

Commercial reuse includes:

- Associating advertising with the full text of the Article
- Charging fees for document delivery or access
- Article aggregation
- Systematic distribution via e-mail lists or share buttons

Posting or linking by commercial companies for use by customers of those companies.

20. **Other Conditions**:

v1.10

Questions? customercare@copyright.com.

ELSEVIER LICENSE
TERMS AND CONDITIONS

Apr 25, 2024

This Agreement between Ms. POULAMI KARAN ("You") and Elsevier ("Elsevier") consists of your license details and the terms and conditions provided by Elsevier and Copyright Clearance Center.

License Number	5775990316343
License date	Apr 25, 2024
Licensed Content Publisher	Elsevier
Licensed Content Publication	Fuel
Licensed Content Title	Microwave-assisted synthesis of glycerol carbonate by transesterification of glycerol using Mangifera indica peel calcined ash as catalyst
Licensed Content Author	Arpita Das,Da Shi,Gopinath Halder,Samuel Lalthazuala Rokhum
Licensed Content Date	Dec 15, 2022
Licensed Content Volume	330
Licensed Content Issue	n/a
Licensed Content Pages	1
Start Page	125511
End Page	0

Type of Use	reuse in a thesis/dissertation
Portion	figures/tables/illustrations
Number of figures/tables/illustrations	1
Format	both print and electronic
Are you the author of this Elsevier article?	No
Will you be translating?	No
Title of new work	Intensification and Optimization of Bio-glycerol conversion into Valuable Chemicals using Electromagnetic Radiation promoted Reactor
Institution name	Jadavpur University
Expected presentation date	May 2024
Portions	Fig.3 on page 5
Requestor Location	Ms. POULAMI KARAN Jadavpur University Kolkata, West Bengal 700032 India Attn: Ms. POULAMI KARAN
Publisher Tax ID	GB 494 6272 12
Total	0.00 USD
Terms and Conditions	

INTRODUCTION

1. The publisher for this copyrighted material is Elsevier. By clicking "accept" in connection with completing this licensing transaction, you agree that the following terms and conditions apply to this transaction (along with the Billing and Payment terms and conditions established by Copyright Clearance Center, Inc. ("CCC"), at the time that you opened your RightsLink account and that are available at any time at https://myaccount.copyright.com).

GENERAL TERMS

2. Elsevier hereby grants you permission to reproduce the aforementioned material subject to the terms and conditions indicated.

3. Acknowledgement: If any part of the material to be used (for example, figures) has appeared in our publication with credit or acknowledgement to another source, permission must also be sought from that source. If such permission is not obtained then that material may not be included in your publication/copies. Suitable acknowledgement to the source must be made, either as a footnote or in a reference list at the end of your publication, as follows:

"Reprinted from Publication title, Vol /edition number, Author(s), Title of article / title of chapter, Pages No., Copyright (Year), with permission from Elsevier [OR APPLICABLE SOCIETY COPYRIGHT OWNER]." Also Lancet special credit - "Reprinted from The Lancet, Vol. number, Author(s), Title of article, Pages No., Copyright (Year), with permission from Elsevier."

4. Reproduction of this material is confined to the purpose and/or media for which permission is hereby given. The material may not be reproduced or used in any other way, including use in combination with an artificial intelligence tool (including to train an algorithm, test, process, analyse, generate output and/or develop any form of artificial intelligence tool), or to create any derivative work and/or service (including resulting from the use of artificial intelligence tools).

5. Altering/Modifying Material: Not Permitted. However figures and illustrations may be altered/adapted minimally to serve your work. Any other abbreviations, additions, deletions and/or any other alterations shall be made only with prior written authorization of Elsevier Ltd. (Please contact Elsevier's permissions helpdesk here). No modifications can be made to any Lancet figures/tables and they must be reproduced in full.

6. If the permission fee for the requested use of our material is waived in this instance, please be advised that your future requests for Elsevier materials may attract a fee.

7. Reservation of Rights: Publisher reserves all rights not specifically granted in the combination of (i) the license details provided by you and accepted in the course of this licensing transaction, (ii) these terms and conditions and (iii) CCC's Billing and Payment terms and conditions.

8. License Contingent Upon Payment: While you may exercise the rights licensed immediately upon issuance of the license at the end of the licensing process for the transaction, provided that you have disclosed complete and accurate details of your proposed use, no license is finally effective unless and until full payment is received from you (either by publisher or by CCC) as provided in CCC's Billing and Payment terms and conditions. If full payment is not received on a timely basis, then any license preliminarily granted shall be deemed automatically revoked and shall be void as if never granted. Further, in the event that you breach any of these terms and conditions or any of CCC's Billing and Payment terms and conditions, the license is automatically revoked and

shall be void as if never granted. Use of materials as described in a revoked license, as well as any use of the materials beyond the scope of an unrevoked license, may constitute copyright infringement and publisher reserves the right to take any and all action to protect its copyright in the materials.

9. Warranties: Publisher makes no representations or warranties with respect to the licensed material.

10. Indemnity: You hereby indemnify and agree to hold harmless publisher and CCC, and their respective officers, directors, employees and agents, from and against any and all claims arising out of your use of the licensed material other than as specifically authorized pursuant to this license.

11. No Transfer of License: This license is personal to you and may not be sublicensed, assigned, or transferred by you to any other person without publisher's written permission.

12. No Amendment Except in Writing: This license may not be amended except in a writing signed by both parties (or, in the case of publisher, by CCC on publisher's behalf).

13. Objection to Contrary Terms: Publisher hereby objects to any terms contained in any purchase order, acknowledgment, check endorsement or other writing prepared by you, which terms are inconsistent with these terms and conditions or CCC's Billing and Payment terms and conditions. These terms and conditions, together with CCC's Billing and Payment terms and conditions (which are incorporated herein), comprise the entire agreement between you and publisher (and CCC) concerning this licensing transaction. In the event of any conflict between your obligations established by these terms and conditions and those established by CCC's Billing and Payment terms and conditions, these terms and conditions shall control.

14. Revocation: Elsevier or Copyright Clearance Center may deny the permissions described in this License at their sole discretion, for any reason or no reason, with a full refund payable to you. Notice of such denial will be made using the contact information provided by you. Failure to receive such notice will not alter or invalidate the denial. In no event will Elsevier or Copyright Clearance Center be responsible or liable for any costs, expenses or damage incurred by you as a result of a denial of your permission request, other than a refund of the amount(s) paid by you to Elsevier and/or Copyright Clearance Center for denied permissions.

LIMITED LICENSE

The following terms and conditions apply only to specific license types:

15. **Translation**: This permission is granted for non-exclusive world **English** rights only unless your license was granted for translation rights. If you licensed translation rights you may only translate this content into the languages you requested. A professional translator must perform all translations and reproduce the content word for word preserving the integrity of the article.

16. **Posting licensed content on any Website**: The following terms and conditions apply as follows: Licensing material from an Elsevier journal: All content posted to the web site must maintain the copyright information line on the bottom of each image; A hyper-text must be included to the Homepage of the journal from which you are licensing at http://www.sciencedirect.com/science/journal/xxxxx or the Elsevier homepage for books at http://www.elsevier.com; Central Storage: This license does not include permission for

a scanned version of the material to be stored in a central repository such as that provided by Heron/XanEdu.

Licensing material from an Elsevier book: A hyper-text link must be included to the Elsevier homepage at http://www.elsevier.com . All content posted to the web site must maintain the copyright information line on the bottom of each image.

Posting licensed content on Electronic reserve: In addition to the above the following clauses are applicable: The web site must be password-protected and made available only to bona fide students registered on a relevant course. This permission is granted for 1 year only. You may obtain a new license for future website posting.

17. **For journal authors:** the following clauses are applicable in addition to the above:

Preprints:

A preprint is an author's own write-up of research results and analysis, it has not been peer-reviewed, nor has it had any other value added to it by a publisher (such as formatting, copyright, technical enhancement etc.).

Authors can share their preprints anywhere at any time. Preprints should not be added to or enhanced in any way in order to appear more like, or to substitute for, the final versions of articles however authors can update their preprints on arXiv or RePEc with their Accepted Author Manuscript (see below).

If accepted for publication, we encourage authors to link from the preprint to their formal publication via its DOI. Millions of researchers have access to the formal publications on ScienceDirect, and so links will help users to find, access, cite and use the best available version. Please note that Cell Press, The Lancet and some society-owned have different preprint policies. Information on these policies is available on the journal homepage.

Accepted Author Manuscripts: An accepted author manuscript is the manuscript of an article that has been accepted for publication and which typically includes author-incorporated changes suggested during submission, peer review and editor-author communications.

Authors can share their accepted author manuscript:

- immediately
  - via their non-commercial person homepage or blog
  - by updating a preprint in arXiv or RePEc with the accepted manuscript
  - via their research institute or institutional repository for internal institutional uses or as part of an invitation-only research collaboration work-group
  - directly by providing copies to their students or to research collaborators for their personal use
  - for private scholarly sharing as part of an invitation-only work group on commercial sites with which Elsevier has an agreement
- After the embargo period
  - via non-commercial hosting platforms such as their institutional repository
  - via commercial sites with which Elsevier has an agreement

In all cases accepted manuscripts should:

- link to the formal publication via its DOI

- bear a CC-BY-NC-ND license - this is easy to do
- if aggregated with other manuscripts, for example in a repository or other site, be shared in alignment with our hosting policy not be added to or enhanced in any way to appear more like, or to substitute for, the published journal article.

Published journal article (JPA): A published journal article (PJA) is the definitive final record of published research that appears or will appear in the journal and embodies all value-adding publishing activities including peer review co-ordination, copy-editing, formatting, (if relevant) pagination and online enrichment.

Policies for sharing publishing journal articles differ for subscription and gold open access articles:

Subscription Articles: If you are an author, please share a link to your article rather than the full-text. Millions of researchers have access to the formal publications on ScienceDirect, and so links will help your users to find, access, cite, and use the best available version.

Theses and dissertations which contain embedded PJAs as part of the formal submission can be posted publicly by the awarding institution with DOI links back to the formal publications on ScienceDirect.

If you are affiliated with a library that subscribes to ScienceDirect you have additional private sharing rights for others' research accessed under that agreement. This includes use for classroom teaching and internal training at the institution (including use in course packs and courseware programs), and inclusion of the article for grant funding purposes.

Gold Open Access Articles: May be shared according to the author-selected end-user license and should contain a CrossMark logo, the end user license, and a DOI link to the formal publication on ScienceDirect.

Please refer to Elsevier's posting policy for further information.

18. **For book authors** the following clauses are applicable in addition to the above: Authors are permitted to place a brief summary of their work online only. You are not allowed to download and post the published electronic version of your chapter, nor may you scan the printed edition to create an electronic version. **Posting to a repository:** Authors are permitted to post a summary of their chapter only in their institution's repository.

19. **Thesis/Dissertation**: If your license is for use in a thesis/dissertation your thesis may be submitted to your institution in either print or electronic form. Should your thesis be published commercially, please reapply for permission. These requirements include permission for the Library and Archives of Canada to supply single copies, on demand, of the complete thesis and include permission for Proquest/UMI to supply single copies, on demand, of the complete thesis. Should your thesis be published commercially, please reapply for permission. Theses and dissertations which contain embedded PJAs as part of the formal submission can be posted publicly by the awarding institution with DOI links back to the formal publications on ScienceDirect.

Elsevier Open Access Terms and Conditions

You can publish open access with Elsevier in hundreds of open access journals or in nearly 2000 established subscription journals that support open access publishing. Permitted third party re-use of these open access articles is defined by the author's choice of Creative Commons user license. See our open access license policy for more information.

Terms & Conditions applicable to all Open Access articles published with Elsevier:

Any reuse of the article must not represent the author as endorsing the adaptation of the article nor should the article be modified in such a way as to damage the author's honour or reputation. If any changes have been made, such changes must be clearly indicated.

The author(s) must be appropriately credited and we ask that you include the end user license and a DOI link to the formal publication on ScienceDirect.

If any part of the material to be used (for example, figures) has appeared in our publication with credit or acknowledgement to another source it is the responsibility of the user to ensure their reuse complies with the terms and conditions determined by the rights holder.

Additional Terms & Conditions applicable to each Creative Commons user license:

CC BY: The CC-BY license allows users to copy, to create extracts, abstracts and new works from the Article, to alter and revise the Article and to make commercial use of the Article (including reuse and/or resale of the Article by commercial entities), provided the user gives appropriate credit (with a link to the formal publication through the relevant DOI), provides a link to the license, indicates if changes were made and the licensor is not represented as endorsing the use made of the work. The full details of the license are available at http://creativecommons.org/licenses/by/4.0.

CC BY NC SA: The CC BY-NC-SA license allows users to copy, to create extracts, abstracts and new works from the Article, to alter and revise the Article, provided this is not done for commercial purposes, and that the user gives appropriate credit (with a link to the formal publication through the relevant DOI), provides a link to the license, indicates if changes were made and the licensor is not represented as endorsing the use made of the work. Further, any new works must be made available on the same conditions. The full details of the license are available at http://creativecommons.org/licenses/by-nc-sa/4.0.

CC BY NC ND: The CC BY-NC-ND license allows users to copy and distribute the Article, provided this is not done for commercial purposes and further does not permit distribution of the Article if it is changed or edited in any way, and provided the user gives appropriate credit (with a link to the formal publication through the relevant DOI), provides a link to the license, and that the licensor is not represented as endorsing the use made of the work. The full details of the license are available at http://creativecommons.org/licenses/by-nc-nd/4.0. Any commercial reuse of Open Access articles published with a CC BY NC SA or CC BY NC ND license requires permission from Elsevier and will be subject to a fee.

Commercial reuse includes:

- Associating advertising with the full text of the Article
- Charging fees for document delivery or access
- Article aggregation
- Systematic distribution via e-mail lists or share buttons

Posting or linking by commercial companies for use by customers of those companies.

20. **Other Conditions**:

v1.10

Questions? customercare@copyright.com.

ELSEVIER LICENSE
TERMS AND CONDITIONS

Apr 25, 2024

This Agreement between Ms. POULAMI KARAN ("You") and Elsevier ("Elsevier") consists of your license details and the terms and conditions provided by Elsevier and Copyright Clearance Center.

License Number	5776000412007
License date	Apr 25, 2024
Licensed Content Publisher	Elsevier
Licensed Content Publication	Journal of Energy Chemistry
Licensed Content Title	Bifunctional Mn-doped CoSe2 nanonetworks electrode for hybrid alkali/acid electrolytic H2 generation and glycerol upgrading
Licensed Content Author	Linfeng Fan,Yaxin Ji,Genxiang Wang,Zhifang Zhang,Luocai Yi,Kai Chen,Xi Liu,Zhenhai Wen
Licensed Content Date	Sep 1, 2022
Licensed Content Volume	72
Licensed Content Issue	n/a
Licensed Content Pages	8
Start Page	424
End Page	431

Type of Use	reuse in a thesis/dissertation
Portion	figures/tables/illustrations
Number of figures/tables/illustrations	1
Format	both print and electronic
Are you the author of this Elsevier article?	No
Will you be translating?	No
Title of new work	Intensification and Optimization of Bio-glycerol conversion into Valuable Chemicals using Electromagnetic Radiation promoted Reactor
Institution name	Jadavpur University
Expected presentation date	May 2024
Portions	Fig. 6 on page 429
Requestor Location	Ms. POULAMI KARAN Jadavpur University Kolkata, West Bengal 700032 India Attn: Ms. POULAMI KARAN
Publisher Tax ID	GB 494 6272 12
Total	0.00 USD
Terms and Conditions	

INTRODUCTION

1. The publisher for this copyrighted material is Elsevier. By clicking "accept" in connection with completing this licensing transaction, you agree that the following terms and conditions apply to this transaction (along with the Billing and Payment terms and conditions established by Copyright Clearance Center, Inc. ("CCC"), at the time that you opened your RightsLink account and that are available at any time at https://myaccount.copyright.com).

GENERAL TERMS

2. Elsevier hereby grants you permission to reproduce the aforementioned material subject to the terms and conditions indicated.

3. Acknowledgement: If any part of the material to be used (for example, figures) has appeared in our publication with credit or acknowledgement to another source, permission must also be sought from that source. If such permission is not obtained then that material may not be included in your publication/copies. Suitable acknowledgement to the source must be made, either as a footnote or in a reference list at the end of your publication, as follows:

"Reprinted from Publication title, Vol /edition number, Author(s), Title of article / title of chapter, Pages No., Copyright (Year), with permission from Elsevier [OR APPLICABLE SOCIETY COPYRIGHT OWNER]." Also Lancet special credit - "Reprinted from The Lancet, Vol. number, Author(s), Title of article, Pages No., Copyright (Year), with permission from Elsevier."

4. Reproduction of this material is confined to the purpose and/or media for which permission is hereby given. The material may not be reproduced or used in any other way, including use in combination with an artificial intelligence tool (including to train an algorithm, test, process, analyse, generate output and/or develop any form of artificial intelligence tool), or to create any derivative work and/or service (including resulting from the use of artificial intelligence tools).

5. Altering/Modifying Material: Not Permitted. However figures and illustrations may be altered/adapted minimally to serve your work. Any other abbreviations, additions, deletions and/or any other alterations shall be made only with prior written authorization of Elsevier Ltd. (Please contact Elsevier's permissions helpdesk here). No modifications can be made to any Lancet figures/tables and they must be reproduced in full.

6. If the permission fee for the requested use of our material is waived in this instance, please be advised that your future requests for Elsevier materials may attract a fee.

7. Reservation of Rights: Publisher reserves all rights not specifically granted in the combination of (i) the license details provided by you and accepted in the course of this licensing transaction, (ii) these terms and conditions and (iii) CCC's Billing and Payment terms and conditions.

8. License Contingent Upon Payment: While you may exercise the rights licensed immediately upon issuance of the license at the end of the licensing process for the transaction, provided that you have disclosed complete and accurate details of your proposed use, no license is finally effective unless and until full payment is received from you (either by publisher or by CCC) as provided in CCC's Billing and Payment terms and conditions. If full payment is not received on a timely basis, then any license preliminarily granted shall be deemed automatically revoked and shall be void as if never granted. Further, in the event that you breach any of these terms and conditions or any of CCC's Billing and Payment terms and conditions, the license is automatically revoked and

shall be void as if never granted. Use of materials as described in a revoked license, as well as any use of the materials beyond the scope of an unrevoked license, may constitute copyright infringement and publisher reserves the right to take any and all action to protect its copyright in the materials.

9. Warranties: Publisher makes no representations or warranties with respect to the licensed material.

10. Indemnity: You hereby indemnify and agree to hold harmless publisher and CCC, and their respective officers, directors, employees and agents, from and against any and all claims arising out of your use of the licensed material other than as specifically authorized pursuant to this license.

11. No Transfer of License: This license is personal to you and may not be sublicensed, assigned, or transferred by you to any other person without publisher's written permission.

12. No Amendment Except in Writing: This license may not be amended except in a writing signed by both parties (or, in the case of publisher, by CCC on publisher's behalf).

13. Objection to Contrary Terms: Publisher hereby objects to any terms contained in any purchase order, acknowledgment, check endorsement or other writing prepared by you, which terms are inconsistent with these terms and conditions or CCC's Billing and Payment terms and conditions. These terms and conditions, together with CCC's Billing and Payment terms and conditions (which are incorporated herein), comprise the entire agreement between you and publisher (and CCC) concerning this licensing transaction. In the event of any conflict between your obligations established by these terms and conditions and those established by CCC's Billing and Payment terms and conditions, these terms and conditions shall control.

14. Revocation: Elsevier or Copyright Clearance Center may deny the permissions described in this License at their sole discretion, for any reason or no reason, with a full refund payable to you. Notice of such denial will be made using the contact information provided by you. Failure to receive such notice will not alter or invalidate the denial. In no event will Elsevier or Copyright Clearance Center be responsible or liable for any costs, expenses or damage incurred by you as a result of a denial of your permission request, other than a refund of the amount(s) paid by you to Elsevier and/or Copyright Clearance Center for denied permissions.

LIMITED LICENSE

The following terms and conditions apply only to specific license types:

15. **Translation**: This permission is granted for non-exclusive world **English** rights only unless your license was granted for translation rights. If you licensed translation rights you may only translate this content into the languages you requested. A professional translator must perform all translations and reproduce the content word for word preserving the integrity of the article.

16. **Posting licensed content on any Website**: The following terms and conditions apply as follows: Licensing material from an Elsevier journal: All content posted to the web site must maintain the copyright information line on the bottom of each image; A hyper-text must be included to the Homepage of the journal from which you are licensing at http://www.sciencedirect.com/science/journal/xxxxx or the Elsevier homepage for books at http://www.elsevier.com; Central Storage: This license does not include permission for

a scanned version of the material to be stored in a central repository such as that provided by Heron/XanEdu.

Licensing material from an Elsevier book: A hyper-text link must be included to the Elsevier homepage at http://www.elsevier.com . All content posted to the web site must maintain the copyright information line on the bottom of each image.

Posting licensed content on Electronic reserve: In addition to the above the following clauses are applicable: The web site must be password-protected and made available only to bona fide students registered on a relevant course. This permission is granted for 1 year only. You may obtain a new license for future website posting.

17. **For journal authors:** the following clauses are applicable in addition to the above:

Preprints:

A preprint is an author's own write-up of research results and analysis, it has not been peer-reviewed, nor has it had any other value added to it by a publisher (such as formatting, copyright, technical enhancement etc.).

Authors can share their preprints anywhere at any time. Preprints should not be added to or enhanced in any way in order to appear more like, or to substitute for, the final versions of articles however authors can update their preprints on arXiv or RePEc with their Accepted Author Manuscript (see below).

If accepted for publication, we encourage authors to link from the preprint to their formal publication via its DOI. Millions of researchers have access to the formal publications on ScienceDirect, and so links will help users to find, access, cite and use the best available version. Please note that Cell Press, The Lancet and some society-owned have different preprint policies. Information on these policies is available on the journal homepage.

Accepted Author Manuscripts: An accepted author manuscript is the manuscript of an article that has been accepted for publication and which typically includes author-incorporated changes suggested during submission, peer review and editor-author communications.

Authors can share their accepted author manuscript:

- immediately
  - via their non-commercial person homepage or blog
  - by updating a preprint in arXiv or RePEc with the accepted manuscript
  - via their research institute or institutional repository for internal institutional uses or as part of an invitation-only research collaboration work-group
  - directly by providing copies to their students or to research collaborators for their personal use
  - for private scholarly sharing as part of an invitation-only work group on commercial sites with which Elsevier has an agreement
- After the embargo period
  - via non-commercial hosting platforms such as their institutional repository
  - via commercial sites with which Elsevier has an agreement

In all cases accepted manuscripts should:

- link to the formal publication via its DOI

- bear a CC-BY-NC-ND license - this is easy to do
- if aggregated with other manuscripts, for example in a repository or other site, be shared in alignment with our hosting policy not be added to or enhanced in any way to appear more like, or to substitute for, the published journal article.

Published journal article (JPA): A published journal article (PJA) is the definitive final record of published research that appears or will appear in the journal and embodies all value-adding publishing activities including peer review co-ordination, copy-editing, formatting, (if relevant) pagination and online enrichment.

Policies for sharing publishing journal articles differ for subscription and gold open access articles:

Subscription Articles: If you are an author, please share a link to your article rather than the full-text. Millions of researchers have access to the formal publications on ScienceDirect, and so links will help your users to find, access, cite, and use the best available version.

Theses and dissertations which contain embedded PJAs as part of the formal submission can be posted publicly by the awarding institution with DOI links back to the formal publications on ScienceDirect.

If you are affiliated with a library that subscribes to ScienceDirect you have additional private sharing rights for others' research accessed under that agreement. This includes use for classroom teaching and internal training at the institution (including use in course packs and courseware programs), and inclusion of the article for grant funding purposes.

Gold Open Access Articles: May be shared according to the author-selected end-user license and should contain a CrossMark logo, the end user license, and a DOI link to the formal publication on ScienceDirect.

Please refer to Elsevier's posting policy for further information.

18. **For book authors** the following clauses are applicable in addition to the above: Authors are permitted to place a brief summary of their work online only. You are not allowed to download and post the published electronic version of your chapter, nor may you scan the printed edition to create an electronic version. **Posting to a repository:** Authors are permitted to post a summary of their chapter only in their institution's repository.

19. **Thesis/Dissertation**: If your license is for use in a thesis/dissertation your thesis may be submitted to your institution in either print or electronic form. Should your thesis be published commercially, please reapply for permission. These requirements include permission for the Library and Archives of Canada to supply single copies, on demand, of the complete thesis and include permission for Proquest/UMI to supply single copies, on demand, of the complete thesis. Should your thesis be published commercially, please reapply for permission. Theses and dissertations which contain embedded PJAs as part of the formal submission can be posted publicly by the awarding institution with DOI links back to the formal publications on ScienceDirect.

Elsevier Open Access Terms and Conditions

You can publish open access with Elsevier in hundreds of open access journals or in nearly 2000 established subscription journals that support open access publishing. Permitted third party re-use of these open access articles is defined by the author's choice of Creative Commons user license. See our open access license policy for more information.

Terms & Conditions applicable to all Open Access articles published with Elsevier:

Any reuse of the article must not represent the author as endorsing the adaptation of the article nor should the article be modified in such a way as to damage the author's honour or reputation. If any changes have been made, such changes must be clearly indicated.

The author(s) must be appropriately credited and we ask that you include the end user license and a DOI link to the formal publication on ScienceDirect.

If any part of the material to be used (for example, figures) has appeared in our publication with credit or acknowledgement to another source it is the responsibility of the user to ensure their reuse complies with the terms and conditions determined by the rights holder.

Additional Terms & Conditions applicable to each Creative Commons user license:

CC BY: The CC-BY license allows users to copy, to create extracts, abstracts and new works from the Article, to alter and revise the Article and to make commercial use of the Article (including reuse and/or resale of the Article by commercial entities), provided the user gives appropriate credit (with a link to the formal publication through the relevant DOI), provides a link to the license, indicates if changes were made and the licensor is not represented as endorsing the use made of the work. The full details of the license are available at http://creativecommons.org/licenses/by/4.0.

CC BY NC SA: The CC BY-NC-SA license allows users to copy, to create extracts, abstracts and new works from the Article, to alter and revise the Article, provided this is not done for commercial purposes, and that the user gives appropriate credit (with a link to the formal publication through the relevant DOI), provides a link to the license, indicates if changes were made and the licensor is not represented as endorsing the use made of the work. Further, any new works must be made available on the same conditions. The full details of the license are available at http://creativecommons.org/licenses/by-nc-sa/4.0.

CC BY NC ND: The CC BY-NC-ND license allows users to copy and distribute the Article, provided this is not done for commercial purposes and further does not permit distribution of the Article if it is changed or edited in any way, and provided the user gives appropriate credit (with a link to the formal publication through the relevant DOI), provides a link to the license, and that the licensor is not represented as endorsing the use made of the work. The full details of the license are available at http://creativecommons.org/licenses/by-nc-nd/4.0. Any commercial reuse of Open Access articles published with a CC BY NC SA or CC BY NC ND license requires permission from Elsevier and will be subject to a fee.

Commercial reuse includes:

- Associating advertising with the full text of the Article
- Charging fees for document delivery or access
- Article aggregation
- Systematic distribution via e-mail lists or share buttons

Posting or linking by commercial companies for use by customers of those companies.

20. **Other Conditions**:

v1.10

Questions? customercare@copyright.com.

Energy Conversion and Management 138 (2017) 577–586

Contents lists available at ScienceDirect

Energy Conversion and Management

journal homepage: www.elsevier.com/locate/enconman

Intensification of monostearin (phase change material) synthesis in infrared radiated rotating reactor: Optimization and heterogeneous kinetics

Poulami Karan, Punam Mukhopadhyay, Rajat Chakraborty *

Department of Chemical Engineering, Jadavpur University, Kolkata 700032, India

ARTICLE INFO

Article history:
Received 2 January 2017
Received in revised form 9 February 2017
Accepted 10 February 2017
Available online 24 February 2017

Keywords:
Monostearin synthesis
Phase change material
Heterogeneous reaction kinetics
Far infrared radiation
Rotating batch reactor
Energy-efficiency

ABSTRACT

The present article offers an intensification effort for the synthesis of glycerol monostearate (monostearin, a phase change material) using Amberlyst 36 (wet) catalyst. This work demonstrates the superiority of rotating batch reactor (RBR) over the stirred batch reactor (SBR) in glycerol (GL) – stearic acid (SA) esterification under far infrared radiation (FIRR). RBR depicted 92 ± 1% monostearin yield, which is 40% higher than the yield obtained in SBR under optimal process condition viz., 20:1 GL: SA mole ratio, 363 K reaction temperature, and 6.0 wt.% catalyst concentration in only 25 mins. The speed regimes for mass transfer limitation and surface kinetics controlled were determined using Mears criterion. The heterogeneous surface reaction kinetics in RBR followed Langmuir Hinshelwood (LH) mechanism (R^2 = 0.98) under resultant optimal condition. The reaction activation energy for the two different reactor configurations indicated that under identical operating conditions, SBR consumed almost double the energy required for RBR; thus representing superior energy-efficiency of RBR. Notably, the optimally synthesized monostearin demonstrated desirable properties of phase change material as confirmed by FTIR, TGA and DSC analyses.

1. Introduction

The most serious threat to mankind in the 21st century is global warming owing to augmented greenhouse gas emissions [1]. The demand for the energy requirements to achieve a comfortable environment has continuously increased worldwide. Thus, energy consumptions for heating, cooling and air conditioning, have increased the level of greenhouse gas emissions while reducing fossil fuel resources [2]. Therefore, energy-saving through energy-storage has become utmost crucial in engineering applications. Thermal energy-storage plays an important role for an effective energy-utilization through not only reducing the mismatch between supply and demand but also improving the performance and reliability of energy-systems [3].

In past years, several researchers developed monoester of glycerol (GL) through catalytic esterification of GL with stearic acid (SA) which found widespread applications in cosmetic, pharmaceuticals [4] and most significantly as engine lubricants due to its surface-active nature [5]. More recently, researchers have paid attention to the production of SA esters for applications as thermal-storage or phase change material [6]. Notably, fatty acid esters possess solid–liquid phase-change characteristics within a narrow temperature range and portray non-corrosive nature in contrast to fatty acids [7].

Preceding literature revealed the applications of homogeneous catalysts viz. sulfuric acid, nitric acid and p-toluene sulfonic acid for catalyzing esterification reactions [8,9]. The catalytic activity of homogeneous catalysts is high. However, because of their corrosive nature and the occurrences of side reactions, these catalysts cannot be effortlessly separated from the reaction mixture [10]; thus, making their usage economically unfavorable. Hence, in recent years the uses of solid acid catalysts have received noteworthy attentions. Recent studies illuminate the huge applications of Amberlyst-type ion-exchange resin catalysts for heterogeneous esterification reactions [11]. Amberlyst 36(wet) is one of the highly active solid acid catalysts with good ion-exchange capabilities, acceptable endurance towards high temperature, ample surface acidity; thus, demonstrating high efficacy in fatty acid esterification [12]. Furthermore, most of the previous works relevant to glycerol monostearate (monostearin) synthesis depicted requirement of either long reaction time [13] or high reaction temperature [14] coupled with low ester yield [15]. Accordingly, there is an

* Corresponding author.
E-mail addresses: rajat_chakraborty25@yahoo.com, rchakraborty@chemical.jdvu.ac.in (R. Chakraborty).

http://dx.doi.org/10.1016/j.enconman.2017.02.026
0196-8904/

Received: 11 June 2019 | Revised: 15 September 2019 | Accepted: 14 October 2019

DOI: 10.1002/apj.2379

RESEARCH ARTICLE

WILEY Asia-Pacific Journal of Chemical Engineering | Curtin University

Quartz halogen-ultrasonication integrated rotating reactor for efficient photocatalytic-thermocatalytic synthesis of glyceryl monocaprin: Kinetics of heterogeneous esterification

Poulami Karan | Punam Mukhopadhyay | Rajat Chakraborty

Chemical Engineering Department, Jadavpur University, Kolkata, India

Correspondence
Rajat Chakraborty, Chemical Engineering Department, Jadavpur University, Kolkata 700032, India.
Email: rajat_chakraborty25@yahoo.com

Funding information
RUSA 2.0; Jadavpur University, Grant/Award Number: Ref. No. R-11/481/19 11/481/19; Council of Scientific and Industrial Research, Grant/Award Number: 09/096/(0975)/2019-EMR-I

Abstract

A pioneering intensification protocol for glyceryl monocaprin (GMC) synthesis deploying coactive electromagnetic energies,viz. quartz halogen radiation (QHR) and ultrasonication (US) is explored. Concurrently, Amberlyst 15 (A15) and nano-TiO_2 P25 (NT-P25) were applied to achieve capric acid (CA) conversion of 97% ± 0.5%, employing the integrated QHR-US energized rotating reactor (QHRUERR), which was 7.5% ± 0.5% higher than QH energized rotating reactor (QHERR) and 20% ± 1% greater compared to an ultrasonically energized rotating reactor (USERR). Optimal factors, viz., 0.35:1 CA:glycerol mole ratio, 343K temperature, 0.67:1 A15:P25(wt./wt.) dose, resulted maximum GMC selectivity (95% ± 0.3%). Langmuir–Hinshelwood model (R^2 = .99) could best represent the esterification kinetics in QHRUERR under optimal condition. Significantly, reaction activation energy was found minimum in QHRUERR (9.63 kJ/mol) compared with a rotating reactor equipped either with QHR (27.5 kJ/mol) or the US (32.74 kJ/mol), thus implying promising synergy and energy efficiency of QHRUERR. Ultraviolet-visible diffuse reflectance spectra and photoluminescence analyses exhibited the photoactivity of ATO (A15 : NT-P25=0.67: 1 w/w) catalyst possessing lower band gap energy (2.98 eV). The optimal product GMC demonstrated appreciable food preservative attributes toward *Aspergillus Niger* food pathogen. An energy-efficient and sustainable reactor could, thus, be explored in this study for proficient green synthesis of valuable food preservatives.

Nomenclature: A_{CA}, acid number of capric acid; C_G, concentration of glycerol; C_{CA}, concentration of capric acid; f_{ATO}, A15-NT-P25 wt. ratio; f_{MR}, capric acid:glycerol mole ratio; f_{RS}, rotating speed; f_{RT}, reaction temperature; $K_{ads,CA}$, adsorption equilibrium constant for capric acid; $K_{forward,ER}$, kinetic constant for Eley–Rideal; $K_{ads,GMC}$, adsorption equilibrium constant for glycerol; $K_{des,GMC}$, desorption equilibrium constant for glyceryl monocaprin; $k_{forward,LH}$, kinetic constant for Langmuir–Hinshelwood; r_{CA}, reaction rate (mol/gcat·min); θ_{CA}, capric acid conversion; θ_{GMC}, glyceryl monocaprin yield; θ_{SN}, signal noise ratio**Abbreviation:** A15, Amberlyst 15; ATO, Amberlyst 15-nano-TiO_2 P25; CEMR, conventionally energized mechanically stirred reactor; CERR, conventionally energized rotating reactor; ER, Eley–Rideal; FIR, far infrared radiation; G, glycerol; GMC, glyceryl monocaprin; GDC, glyceryl dicaprin; GTC, glyceryl tricaprin; LH, Langmuir–Hinshelwood; NT-P25, TiO_2 P25; PH, pseudo-homogeneous; PL, photoluminescence; QHR, quartz halogen radiation; QH, quartz halogen; QHERR, quartz halogen energized rotating reactor; QHRUERR, quartz halogen radiation and ultrasonication energized rotating reactor; TOD, Taguchi orthogonal design; US, ultrasonication; USERR, ultrasonically energized rotating reactor; UV, ultraviolet; USWE, ultrasonic wave energy

Waste Management 140 (2022) 213–224

Contents lists available at ScienceDirect

Waste Management

journal homepage: www.elsevier.com/locate/wasman

E-waste derived silica-alumina for eco-friendly and inexpensive Mg-Al-Ti photocatalyst towards glycerol carbonate (electrolyte) synthesis: Process optimization and LCA

Poulami Karan, Rajat Chakraborty *

Chemical Engineering Department, Jadavpur University, Kolkata 700032, India

ARTICLE INFO

Keywords:
E-waste Valorization
PCB derived silica-alumina
LDO photocatalyst
Glycerol carbonate
Solar simulated quartz halogen radiation
LCA

ABSTRACT

Valorization of e-waste, i.e. waste printed circuit board (WPCB) through mechano-chemical activation to obtain silica as the catalyst support and alumina as the catalyst precursor for eco-friendly synthesis of inexpensive highly proficient photocatalyst has been explored. The WPCB derived silica-supported layered double oxide photocatalyst ($MATLS_W$) and its counterpart ($MATLS_C$) involving commercial silica and alumina precursors were synthesized through the wet-impregnation method under energy-efficient solar simulated quartz halogen lamp (SSQHL) irradiations to improve its photocatalytic properties compared to conventional methods. The prepared $MATLS_W$ possessed a significantly low band-gap-energy (1.58 eV) that rendered efficient photocatalysis in the green-synthesis of glycerol carbonate (GC) (an effective electrolyte). The catalytic performance of the optimal $MATLS_W$ resulted in a superior yield of GC (98.68%) compared to that rendered by $MATLS_C$ catalyst (GC yield: 96.56%) at optimal process conditions. Detailed life cycle assessment (LCA) of the entire process (deploying Ecoinvent 3.5 database) dictated conducive environmental impacts concerning 1 kg GC synthesis alongside a scale-up study for 1 MT GC synthesis encompassing silica-alumina extraction from WPCB, $MATLS_W$ preparation, and employment of SSQHL-radiated batch reactor (SSQHLBR) (56.64% less energy consumption than conventional). The overall process deploying the novel $MATLS_W$ in conjunction with the effectual reactor demonstrated superiority over the conventional GC synthesis process through appreciable reductions of environmental impact parameters, namely GWP, FDP, and HTP by 5.78%, 3.60%, and 5.72% respectively. The developed green process for e-waste utilization can procreate an effective waste management protocol towards a cleaner world.

1. Introduction

Over the past several decades, a massive 45-million-tons of e-waste (multi-layered FR4, i.e. flame retardant type 4 brominated fiberglass epoxy resin (BER) type printed circuit board) generation has become one of the burning issues owing to the short life-span of various electronic appliances across the globe (Ghosh et al., 2015). E-waste has been a critical issue towards human health and ecosystem (Song and Li, 2014), even though initiatives had been taken for the management of such solid wastes. Currently, India (among the top 4 countries for e-waste generation and second-largest populated country in the world) has been facing many challenges in e-waste management practices, viz. lack of infrastructure, reluctance to set rules, etc. (Arya and Kumar, 2020). The embedded metals (30–40%), non-metals (60–70%), and hazardous toxic substances discarded from cell phones, television, computers are among the main harmful elements to our ecosystem (Wang et al., 2019). Moreover, scanty scientific reports on recovery of the non-metallic part (glass-fiber, BER etc.) from WPCB indicated the technical challenges of retaining the desired quality of porous silica, reinforcing materials, thermoplastic resin matrix composites along with the use of hazardous chemicals making the process economically and environmentally unattractive; which eventually led to a negative impact on the world health management (Ramaswamy et al., 2017). Hence, development of an eco-friendly, energy-efficient, and economical method for WPCB valorization has remained of utmost importance to researchers and practicing technologists.

Importantly, the supply of clean, renewable, and sustainable energy has also become essential for the advancement of mankind. In this regard, the development and innovation of portable energy-storage devices (ESDs) have emerged sharply due to their widespread applications in cell phones, laptops, aerospace electronics, electric vehicles and

* Corresponding author.
E-mail addresses: rajat.chakraborty@jadavpuruniversity.in, rajat_chakraborty25@yahoo.com (R. Chakraborty).

https://doi.org/10.1016/j.wasman.2021.11.022
Received 14 May 2021; Received in revised form 21 October 2021; Accepted 13 November 2021
Available online 24 November 2021

Chemical Engineering Journal 455 (2023) 140032

Contents lists available at ScienceDirect

Chemical Engineering Journal

journal homepage: www.elsevier.com/locate/cej

Intensification of autocatalytic methyl oleate synthesis in continuous flow rotating recycle reactor under hybrid radiation: Process optimization and Scale-up

Poulami Karan, Rajat Chakraborty *

Chemical Engineering Department, Jadavpur University, Kolkata 700032, India

ARTICLE INFO

Keywords:
Methyl oleate
Continuous-flow-rotating-recycle-reactor
Hybrid near infrared-microwave irradiation
Parallel autocatalytic reaction
Mathematical modelling

ABSTRACT

Intensification of the autocatalytic esterification of methanol with oleic acid for producing methyl oleate (biodiesel) was accomplished using a continuous flow rotating reactor under recycle mode. To exaggerate the biodiesel yield, highly efficient hybrid electromagnetic radiation (near-infrared and microwave irradiation) was used as an energy source. Spherical-shaped nano-zinc-titanate photocatalyst (low band-gap energy: 2.01 eV and low recombination rate) was prepared and utilized in the aforementioned novel reactor. Box-Behnken statistical optimization technique was applied to attain the optimum condition (catalyst concentration 30 wt%, reaction temperature 333 K, methanol: oleic acid mole ratio 11:1, LHSV: 0.20 min^{-1}) resulting in maximum biodiesel yield. Moreover, at optimum rotating speed (~235 rpm), high external and internal mass transfer coefficients were achieved which rendered a remarkably augmented reaction rate under ideal reactor behavior (Dispersion number: 6.42×10^{-7}). A geometric-based COMSOL model was simulated which confirmed uniformity of hybrid irradiation and temperature distribution within the rotating catalytic packed bed; which was applied for the development of a parallel-autocatalytic reaction kinetic model. Langmuir Hinshelwood kinetics of the parallel autocatalytic esterification is well represented in the experimental data ($RSSQ = 1.52 \times 10^{-7}$). Without recycle stream, the reaction exhibited a non-autocatalytic reaction with a lower yield of 79.04 % biodiesel within 0.20 min^{-1} LHSV, whereas, under recycle mode, the biodiesel yield was increased up to 93.55 % even at a higher LHSV of 0.25 min^{-1}. For larger-scale production of the methyl oleate, the ASPEN PLUS simulator has been deployed for a throughput scale-up factor of 1000 (geometric similarity), which corroborates well with lab-scale yield/reactor performance.

1. Introduction

Recently, the demand for carbon–neutral and environmentally benign energy resources has emerged as a challenging research topic that can resolve the issues of harmful emissions from non-renewable energy systems. Also, the diminution of fossil fuels and climate deterioration have triggered attention toward the biodiesel industry as a potential alternative to petrodiesel in the global market [1]. In the biodiesel industry, forming several esters through trans/esterification has established a promising approach for futuristic application in the fuel industry.

For instance, the esterification of monohydric alcohol viz. methanol with oleic acid for the formation of methyl oleate using heterogeneous catalysts has fascinated researchers for its use in the biodiesel fuel industry. Regarding reactors, although the conventional batch reactor has achieved a promising research interest in methyl oleate synthesis using heterogeneous catalysts [2], the electromagnetic radiation (MW and NIR) based systems have become an eye-catcher due to their capability of accelerated synthesis and sensational permeability. Theoretically, these radiations not only influence the rotation of dipoles, migration of ions in molecules, and molecular motions of reacting components without disturbing their molecular structure but also decrease the reaction time from hour to minute. For instance, Ning [3], has achieved 97.31 % conversion of oleic acid in biodiesel synthesis under MW irradiation at 338 K for 1 h using 5 wt% of catalyst. Concerning polarity, methanol shows a strong absorption of MW irradiation. Its dipoles' orientation occurs quickly under an electromagnetic field so that they can rotate and align themselves according to the field [4]. Yet, MW irradiation has a few limitations, such as it cannot control the

* Corresponding author.
E-mail addresses: rajat_chakraborty25@yahoo.com, rajat.chakraborty@jadavpuruniversity.in (R. Chakraborty).

https://doi.org/10.1016/j.cej.2022.140032
Received 4 August 2022; Received in revised form 20 October 2022; Accepted 22 October 2022
Available online 23 November 2022

Barnacle carapace-chitosan supported highly-efficient nano Al-W alloy electrocatalyst for sustainable bio-glycerol valorization: Environmental impact and cost analyses

Poulami Karan , Van-Phu Vu , Rajat Chakraborty , Soo-Hyoung Lee

PII: S2666-8211(23)00117-5
DOI: https://doi.org/10.1016/j.ceja.2023.100560
Reference: CEJA 100560

To appear in: *Chemical Engineering Journal Advances*

Received date: 26 July 2023
Revised date: 7 September 2023
Accepted date: 15 September 2023

Please cite this article as: Poulami Karan , Van-Phu Vu , Rajat Chakraborty , Soo-Hyoung Lee , Barnacle carapace-chitosan supported highly-efficient nano Al-W alloy electrocatalyst for sustainable bio-glycerol valorization: Environmental impact and cost analyses, *Chemical Engineering Journal Advances* (2023), doi: https://doi.org/10.1016/j.ceja.2023.100560